

# **Numerical Simulation of Toppling Failure for Jointed Rock Masses**

Hooman Dabirmanesh

A Thesis in the Department of  
Building, Civil, and Environmental Engineering

Presented in Partial Fulfilment of the Requirements  
For the Degree of  
Doctor of Philosophy (Civil Engineering)

at Concordia University  
Montréal, Québec, Canada

May 2024

© Hooman Dabirmanesh, 2024

**CONCORDIA UNIVERSITY**  
**School of Graduate Studies**

This is to certify that the thesis prepared

By: Hooman Dabirmanesh

Entitled: Numerical simulation of toppling failure for jointed  
rock masses

and submitted in partial fulfillment of the requirements for the degree of  
Doctor of Philosophy (Civil Engineering)  
complies with the regulations of the University and meets the accepted standards with  
respect to originality and quality.

Signed by the final examining committee:

\_\_\_\_\_ Chair

Dr. Rene Witte

\_\_\_\_\_ External Examiner

Dr. Hani Mitri

\_\_\_\_\_ External to program

Dr. Hang Xu

\_\_\_\_\_ Examiner

Dr. Emre Erkmen

\_\_\_\_\_ Examiner

Dr. Ciprian Alecsandru

\_\_\_\_\_ Supervisor

Dr. Adel M. Hanna

\_\_\_\_\_ Supervisor

Dr. Biao Li

Approved by \_\_\_\_\_  
Dr. An Chunjiang, Graduate Program Director

May 21, 2024 \_\_\_\_\_  
Dr. M. Debbabi  
Dean of the Gina Cody School of Engineering and Computer Science

## **Abstract**

### **Numerical simulation of toppling failure for jointed rock masses**

**Hooman Dabirmanesh, Ph.D.**

**Concordia University, 2024**

Toppling failure in jointed rock masses presents a complex geological challenge. Conventional numerical methods often struggle to capture its intricacies, particularly when dealing with jointed rock masses. Experimental studies are both time-consuming and financially demanding. To address these challenges, this thesis employs the Discrete Element Method (DEM), a powerful numerical tool capable of accurately simulating toppling failure processes in jointed rock masses, with a specific focus on block-flexural toppling in natural rock slopes. The DEM not only accurately replicates toppling failure but also provides an efficient alternative to expensive experiments.

The research convincingly demonstrates DEM's precision in predicting failure surfaces and its ability to accommodate large deformations and discontinuities make it a powerful tool. The DEM emerges as a potent and cost-effective tool for simulating toppling failure in jointed rock formations, accommodating large deformations, block interactions, and the consideration of discontinuities during failure. The developed DEM code was utilized to simulate and investigate the toppling failure after being validated with experimental test results. The study also explores key parameters like joint friction angles, spacing, and basal joint sets, investigating their influence on failure mechanics and the overall failure surface, a fundamental assumption in the theoretical method for analyzing toppling failure based on the limit equilibrium method. Overall, this study highlights the assumption that a single failure surface used in the limit equilibrium method is not necessarily valid for block-flexural toppling failures.

Utilizing a developed computational code, this research extends its relevance to real-world scenarios, effectively simulating complex rock slope conditions. It emphasizes the importance of particle size calibration in DEM simulations, highlighting the need to strike a balance between accuracy and computational efficiency. The research reveals that the maximum particle size relative to the minimum sub-domain size, represented by joint spacing or block width, is critical for precise simulations.

The findings indicate that DEM excels in capturing the complexities of toppling failures, especially when challenged with large deformations and block separation. In practical scenarios, DEM outperforms traditional theoretical methods by providing a more accurate assessment of safety factors and offering insights into the intricate micro-level interactions within rock slopes.

## Acknowledgments

First and foremost, I would like to express my sincere appreciation and gratitude to Dr. Adel M. Hanna and Dr. Biao Li, my advisors, for their consistent availability, unwavering support, and expert guidance during my academic pursuits. Dr. Adel M. Hanna and Dr. Li's dedication to my research and their willingness to go above and beyond have been invaluable in shaping the culmination of this thesis. Adel and Biao, I am truly thankful for your enduring presence, continuous motivation, patience, and diligent work.

I would like to express my deepest gratitude to my former supervisor, Dr. Attila Michael Zsaki, who provided invaluable assistance during the stages of my research. I'm especially thankful for his involved role in helping me grasp the intricacies of algorithms and coding. His insightful comments and valuable advice significantly contributed to the development of my research. I am grateful for the foundation he laid, which proved crucial in the successful completion of my thesis. Thank you, Attila, for your mentorship and guidance throughout that pivotal period.

I would like to express my genuine gratitude to the individuals on my thesis committee, including Dr. Hani Mitri, Dr. Hang Xu, Dr. Emre Erkmen, and Dr. Ciprian Alecsandru for the valuable insights and suggestions they provided.

I would like to express my deepest gratitude for the invaluable guidance and advice provided by Dr. Mazdak Nikbakht, our former graduate program advisor, and Dr. An Chunjiang, our current graduate program advisor.

I gratefully acknowledge the financial support provided by Concordia University as this endeavor would have been unattainable without it. Furthermore, I would like to express my gratitude to Concordia University for their financial support via Helene Linder Doctoral Fellow Scholarship.

I would like to extend my heartfelt appreciation to Dr. Mehdi Amini for his unwavering support in answering all my questions pertaining to his previous research and for providing invaluable guidance throughout my academic journey.

I am profoundly grateful to my dear friend, Dr. Navid Hajimirza, for his patient and highly effective assistance in guiding me through the intricacies of coding. His mentorship has played a pivotal role in elevating my skills and bolstering my confidence in this critical aspect of my research. His unwavering dedication and support have been irreplaceable, and for that, I am sincerely thankful.

"For a true friend, life is more fulfilling."

My time at Concordia University introduced me to new friends, and I'm sincerely thankful for Dr. Sina Heidari. He has consistently offered support and engaged in inspiring discussions.

Last but certainly not least, I want to express my profound gratitude to my family. My father, Kamran, has been more than just a parent; he has been a mentor and a friend. From a young age, he guided me through the intricacies of engineering and provided unwavering support in all aspects of my life. My mother, Fereshteh, has always been my source of support and encouragement, imparting upon me the invaluable virtues of patience and determination as I pursue my dreams. My sister, Halleh, has been a constant source of motivation, urging me to persevere and generously sharing her engineering knowledge and encouragement. Last but most importantly, my wife, Farzaneh, stood firmly by my side, providing unwavering support during difficult times and creating a serene atmosphere for me to thrive in my PhD journey with unconditional love. I consider myself exceptionally lucky to have each of you in my life. Your love, unwavering encouragement, and unconditional support have been the driving force behind my journey. Your presence, unwavering belief in my abilities, and steadfast support have empowered me to surmount challenges and achieve my aspirations. I will forever be appreciative of the bedrock of love and resilience you have furnished, and I am privileged to have you as my steadfast companions.

“Wherever there's a will, there's a way.”

## **Dedication**

To my beloved family and the eternal spirit of my father

# Table of Contents

List of Figures .....	xi
List of Tables.....	xvi
List of Symbols .....	xvii
Chapter 1. Introduction and problem statement.....	1
1.1 Toppling failure .....	1
1.2 Problem statement .....	2
1.3 Research objectives .....	5
1.3.1 Objectives.....	5
1.4 Outline of the Thesis.....	6
Chapter 2. Literature review and background.....	8
2.1 Introduction .....	8
2.2 Toppling failure .....	9
2.3 Rock slope analysis methods.....	11
2.4 The limit equilibrium method for slope toppling instability .....	12
2.4.1 Flexural toppling .....	19
2.4.2 Block-Flexure Toppling .....	22
2.5 Physical modeling to simulate toppling.....	23
2.6 Numerical analysis of slope toppling .....	25
2.6.1 FEM/BEM/FDM Continuum Methods .....	27
2.6.2 Discrete Element Methods .....	27
2.6.2.1 Discrete Element Method (DEM) formulation .....	29
2.6.2.2 Model initialization .....	31
2.6.2.3 Contact detection.....	31
2.6.2.4 Contact force determination .....	34
2.6.2.5 Total force update.....	36
2.6.2.6 Application of Newton's Laws of motion.....	37
2.6.3 Discontinuous Deformation Analysis (DDA).....	38



2.6.4	Hybrid Methods.....	39
2.7	Application of numerical modeling for rock slope stability.....	40
Chapter 3.	Research methodology, model development, and approach.....	48
3.1	Summary.....	48
3.2	General description and algorithm for model development.....	48
3.2.1	The flowchart of the developed DEM code.....	48
3.2.2	The geometry model generation.....	50
3.2.3	Introduction of joints and boundary conditions.....	55
3.2.4	Determine bonds between particles.....	56
3.2.5	Simulation.....	56
3.2.6	Contact detection and contact resolution.....	58
Chapter 4.	Validation of the DEM framework.....	61
4.1	Case of a particle in free fall.....	61
4.2	Case of a cantilever beam.....	64
4.3	Case of Uniaxial Compressive Strength (UCS).....	66
4.4	Case of slip vs toppling on a surface (The necessity and application of smooth joints).....	70
4.5	Conclusion.....	77
Chapter 5.	Simulation of toppling failure using the Discrete Element Method.....	79
5.1	Introduction.....	79
5.2	Numerical simulation of a rock slope with the potential of block-flexure toppling failure 80	
5.2.1	Experimental tilting test.....	80
5.2.2	Physical model and laboratory test results.....	80
5.2.3	Modeling uniaxial compressive strength (UCS).....	81
5.2.4	Numerical modeling of the slope.....	85
5.2.4.1	Model geometry.....	86
5.2.4.2	Modeling methodology.....	89
5.2.4.3	Modeling results.....	91
5.2.4.4	Conclusion.....	95

5.3	Numerical Simulation of the Equivalent Slope .....	96
5.3.1	The geometry of the equivalent slope .....	97
5.3.2	The numerical simulation.....	100
5.3.3	The effects of joint on a block – flexural toppling failure .....	107
5.3.3.1	Influence of persistence and spacing of discontinuities .....	107
5.3.3.2	Influence of joint base configuration (the joint set persistence) .....	109
5.3.3.3	Effect of joint friction.....	121
5.3.3.4	Discussion .....	128
5.3.3.5	Conclusions .....	131
5.4	Application of the DEM particle-based method to real-world case .....	133
5.4.1	Case 1: A selected section of the Ihlara Valley (Cappadocia, Turkey).....	133
5.4.1.1	Study area.....	133
5.4.1.2	Site Stratigraphy and rock properties and Failure Mechanism in the Valley...	134
5.4.1.3	DEM Modeling .....	136
5.4.1.4	Results and Discussion.....	141
5.4.1.5	Discussions and conclusions .....	146
5.4.2	Case 2: The Rock Slope Facing Galandrood Mine .....	148
5.4.2.1	Study area.....	148
5.4.2.2	Numerical simulation .....	150
Chapter 6.	Conclusion and future works.....	157
6.1	Summary and conclusions .....	157
6.2	Recommendation for analysis and simulation toppling failure .....	159
6.3	Recommendations for Future Research:.....	161
References:	.....	162

## List of Figures

Figure 1-1: Rock slope with a potential for block-flexure toppling failure facing Chalus Road (Amini et al. 2012) .....	1
Figure 1-2: The horrifying moment the canyon cracks and crushes people to death (Twitter: Knox. 2022, from <a href="https://www.thesun.ie/news/8176290/canyon-brazil-crushes-two-people-death-pleasure-boats/">https://www.thesun.ie/news/8176290/canyon-brazil-crushes-two-people-death-pleasure-boats/</a> ) .....	2
Figure 2-1: Possible main toppling failure in rock slopes. a. Flexural. b. Blocky. c. Block-flexural (Amini et al. 2012).....	11
Figure 2-2: Condition for toppling and sliding for a block on an inclined plane (Sagaseta 1986) 13	13
Figure 2-3: Overturning and sliding criteria for a single block on an inclined plane (Sagaseta 1986).....	13
Figure 2-4: Stability criteria (Sagaseta 1986) .....	14
Figure 2-5: Block height/width and a plane dipping (Wyllie and Mah 2004) .....	15
Figure 2-6: Directions of stress and slip directions in a rock slope(left), and condition for interlayer slip(right) (Wyllie and Mah 2004) .....	16
Figure 2-7: Model for limit equilibrium analysis of toppling on a stepped base (Wyllie and Mah 2004).....	17
Figure 2-8: Dilatancy of toppling blocks with base plane coincident with normal to dip of blocks (Zanbak 1983; Wyllie and Mah 2004). .....	17
Figure 2-9: Block toppling failure mode (Liu et al. 2008b).....	18
Figure 2-10: Schematic diagrams showing: a) slope geometry and b) forces acting on a single column. Here $\tau_j$ and $\tau_j - 1$ represents the shear forces acting along the inter-layer boundaries (Adhikary and Dyskin 2007).....	21
Figure 2-11: Illustration of the position of action of normal force on a column for various distributions of normal stress (Aydan and Kawamoto 1992).....	21
Figure 2-12: Block-flexure toppling failure mechanism (Amini et al. 2012) .....	23
Figure 2-13: Plot illustrating the calculation cycle for the discrete element method.....	32
Figure 2-14: Contact notation (a): particle-particle contact, (b): particle-boundary contact (Itasca 2004).....	33
Figure 2-15: Tensile strength and friction angle effects on the failure load (Alzo'ubi et al. 2010) .....	42
Figure 2-16: Comparison of the failure patterns predicted (Lian et al. 2017). .....	43
Figure 2-17: Horizontal displacements at the two monitoring points versus g-level. a) Adhikary and Dyskin's centrifuge test and FEM results; b) Lian et al.'s numerical test results; and c) Alzo'ubi et al.'s numerical test results (Adhikary and Dyskin 2007; Lian et al. 2017; Alzo'ubi et al. 2010).....	44
Figure 2-18: Numerical results for the jointed slope showing (a) displacements of two monitoring points, (b) the corresponding failure surface (Meng et al. 2018).....	45
Figure 3-1: Flowchart representation of the main body of the developed HDPAC.....	49
Figure 3-2: Boundaries and geometry needed for the toppling model.....	50
Figure 3-3: Line segments representing the model's boundary and slope geometry .....	51

Figure 3-4: (a) Generating particles in one large polygon, (b) Removing contacts and bonds between particles where joints are needed in order to generate layers .....	51
Figure 3-5: Particles generated in polygons between parallel joints.....	52
Figure 3-6: The position of the injected particles following settlement due to gravitational load	53
Figure 3-7: Flowchart of the process of generating particles in a domain to produce a model's geometry.....	54
Figure 3-8: Overview of the algorithm of the numerical approach for HDPAC .....	57
Figure 3-9: Typical subdividing of the domain of a model into cells.....	60
Figure 3-10: The problem domain is divided into identical square cells, each large enough to contain the largest particle, so that cell size $d$ is equal to the diameter of the largest particle.....	60
Figure 4-1: Sketch of the freefalling model .....	61
Figure 4-2: The vertical position of the particle's center during time .....	62
Figure 4-3: The velocity of the particle versus time .....	63
Figure 4-4: The cantilever beam model (a) Physical model, (b) DEM model, and (c) Equivalent elastic parallel bonds (PFC3D 2016) .....	65
Figure 4-5: The graphical cantilever beam deformation (a) before, and (b) after applying load at its tip.....	66
Figure 4-6: Summary of the laboratory properties for a Luc du Bonnet granite sample obtained from Cold Spring Quarry, samples taken near the surface (0-200 m) at the Underground Research Laboratory (Modified from Martin 1993).....	68
Figure 4-7: Stress-strain of a) biaxial test results of HDPAC at confinements of $< 0.1\text{MPa}$ for a specimen granite model with $D_{\text{avg}} = 0.745\text{ mm}$ , and b) biaxial test results of the PFC2D at confinements of $0.1\text{MPa}$ for a specimen granite model with $D_{\text{avg}} = 0.72\text{ mm}$ (Potyondy and Cundall 2004).....	69
Figure 4-8: A schematic representation of the smooth joint contact on the realignment of the local particle orientation, and the interface used to adjust the roughness in the contact of the particles in joints: a) Standard contact, b) Smooth joint contact .....	71
Figure 4-9: A single block on an inclined slope.....	72
Figure 4-10: The geometry of a block on an inclined surface made by bonded particles with a parallel bond to each other in the DEM .....	72
Figure 4-11: a) The block's position and state before starting to slip, b) the block's position and state after the block has slipped due to gravity. ....	73
Figure 4-12: The velocity of particles when a smooth joint is not introduced into the model at three different points in time .....	73
Figure 4-13: The position of the block on an inclined slope while slipping due to the gravitational load: a) during the slipping, and b) at the final step of the analysis.....	74
Figure 4-14: The velocity of particles when a smooth joint is introduced into the model at three different points in time .....	74
Figure 4-15: Block height/width on a plane inclined at an angle (Wyllie and Mah 2004).....	75
Figure 4-16: The geometry of the block and the inclined slope used in the DEM simulation .....	76
Figure 4-17: The toppling trajectory movement of the block due to its weight during a time .....	77
Figure 5-1: Typical model geometry for numerical UCS test.....	84

Figure 5-2: (a) Stress-strain curves for three experimental UCS tests conducted by Amini et al. (2015) and the corresponding numerical simulations of UCS tests in HDPAC, and (b) the typical example observed failure mode for numerical UCS tests .....	85
Figure 5-3: (a) A sketch of the model geometry, and (b) the physical model with the ideal arrangement of blocks (Amini et al. 2015) .....	86
Figure 5-4: (a) A sketch of the geometry, and (b) the physical model for the randomly arranged blocks (Amini et al. 2015).....	86
Figure 5-5: The developed slope geometry in the DEM for the ideal arrangement of blocks.....	88
Figure 5-6: The developed slope geometry in the DEM with randomly arranged blocks .....	88
Figure 5-7: The decomposition of the gravitational force represents a tilting angle .....	91
Figure 5-8: (a) Overall failure surface for the ideally arranged blocks model in the numerical simulation, and (b) the overall failure surface angle (15°).....	93
Figure 5-9: Overall failure surface for the ideally arranged blocks model in the physical laboratory tilting table test (Amini et al. 2015).....	93
Figure 5-10: (a) Overall failure surface for the ideally arranged blocks model in the numerical simulation for finer particle sizes (R between 1 and 2.5 mm), and (b) the overall failure surface angle (15°).....	93
Figure 5-11: (a) Overall failure surface for the randomly arranged blocks model in the numerical simulation, and (b) The angles of the overall failure surfaces (14° and 24°).....	94
Figure 5-12: (a) Overall failure surface for the randomly arranged blocks model in the physical laboratory tilting table test, and (b) The angles of the overall failure surfaces (14° and 24°) (Amini et al. 2015) .....	94
Figure 5-13: The model geometry proposed for a rock slope with the potential for block-flexure toppling failure (Amini et al. 2012) .....	97
Figure 5-14: Block configuration used for ideal arrangement experimental test (modified from Amini et al. 2012).....	98
Figure 5-15: Schematic illustration of a rock slope with the potential for toppling failure (Amini et al. 2015).....	98
Figure 5-16: The rotated blocks of the ideal arrangement experimental model .....	99
Figure 5-17: The equivalent geometry used to represent the rotated ideal experiential model in the numerical simulation .....	100
Figure 5-18: a) The geometry of the slope and joint sets used in the numerical simulation of the equivalent slope representing the ideal arrangement of blocks, and b) the corresponding slope model created with particles bonded using parallel bonds and smooth joint contacts.....	101
Figure 5-19: The DEM results: a) the overall post-failure surface and movements of the columns, and b) the angle of the overall failure surface with respect to the normal line of main discontinuities, and the stable, toppling, and sliding zones within the block-flexural toppling failure zone .....	103
Figure 5-20: Measurement point labels and the label number of columns formed by joint sets .	104
Figure 5-21: Data measurements recorded at monitoring points on the slope surface in the base model. (a) Horizontal displacement (X), (b) vertical displacement (Y), (c) vertical displacement over horizontal displacement (dY/dX) over time, (d) vertical displacement (Y) versus horizontal	

(X) displacement, (e) total displacement, and (f) the position of the columns at the end of the simulation .....	106
Figure 5-22: Illustration of the main joint set, base joint set, and joint spacing .....	107
Figure 5-23: The assumptions used in the limit equilibrium method to analyze block–flexural topping failure by Amini et al. (2012).....	108
Figure 5-24: Definition of the parameters used in Figure 5-25.....	116
Figure 5-25: Plot illustrating the normalized horizontal distance between the top of the stable zone and the slope toe (T/H), the normalized horizontal distance between the top of part of the slope without any movements and the slope toe (S/H), and the angle between the total failure plane and the line normal to the discontinuities versus the normalized horizontal distance from the center of the merged joints to the slope toe (D/H) for cases I to XVI.....	116
Figure 5-26: Plot illustrating the total displacement over time at three monitoring points on the slope surface for different friction angles of the main joint set: (a) point C-3, (b) point G-7, (c) point M-13, and (d) overall model configuration showing measurement point labels .....	125
Figure 5-27: Plots illustrating the horizontal (X) displacement over time at three monitoring points on the slope surface for different friction angles of the main joint set: (a) point C-3, (b) point G-7 and (c) point M-13. (d) overall model configuration showing measurement point labels .....	126
Figure 5-28: Plots illustrating the vertical (Y) displacement over time at three monitoring points on the slope surface for different friction angles of the main joint set: (a) point C-3, (b) point G-7 and (c) point M-13. (d) overall model configuration showing measurement point labels.....	127
Figure 5-29: Plot illustrating normalized the horizontal distance between the top of the stable zone and the slope toe (T/H), the normalized horizontal distance between the top of part of the slope without any movements and the slope toe (S/H), and the angle between the total failure plane and the line of normal to discontinuities versus the main joint set friction coefficient (Fric) .....	128
Figure 5-30 : (a) view of the Ihlara Valley, (b) the fallen block, and (c) geological structure of Kizikaya (Sari 2021) .....	133
Figure 5-31: East- West cross-section of the stratigraphy of Ihlara Valley (Sari 2021) .....	134
Figure 5-32: A simplified model proposed by Sari (2009) for the toppling failure mechanism in the Ihlara Valley; (a) the condition of the original slope, (b) weathering at basal Selime tuff, (c) erosion in the toe due to the basal weathering, (d) toppling of the block (Sari 2021) .....	135
Figure 5-33: Rock material and rock mass parameters for the study area (modified Sari 2021).136	
Figure 5-34: General assembly of the DEM model .....	138
Figure 5-35: The geometry of the slope and joint sets used in the numerical simulation.....	139
Figure 5-36: Numerical UCS test results used to calibrate the microparameters of the rock layers .....	140
Figure 5-37: DEM model configurations simulating the toppling failure in the Ihlara Valley: a) degradation of the underlying soft tuff layer due to water infiltration and weathering, and b) removal of the slope toe due to erosion of the weathered tuff zone.....	141
Figure 5-38: The toppling failure process in the slope: a) The toppling failure in the first column of rock and, b) the movements of the other rock column progressing the toppling of the first rock column and overall post-failure.....	142

Figure 5-39: The slope failure and total displacement in the slope modelled using a) FEM for a similar slope to case 1 (Sari 2021) and b) DEM for case 1 (this study)..... 143

Figure 5-40: The progress slope failure in Case 2 while the erosion occurred at the toe of the slope, the mode of the failure is classified as the toppling failure. .... 145

Figure 5-41: The slope failure and total displacement in the slope using (a) a FEM model for a similar slope to case 2 (Sari 2021) and (b) a DEM model for case 2..... 145

Figure 5-42: Mode and progress of the slope failure for case 2 considering the reduction in tensile strength and bond cohesion of the parallel bonds in the weathered tuff..... 146

Figure 5-43: Rock slope facing Galandrood mine (Amini et al. 2012)..... 148

Figure 5-44: Stability analysis results of the Galandrood mine slope (Amini et al. 2012)..... 149

Figure 5-45: Schematic illustration of the slope ..... 151

Figure 5-46: General assembly of the DEM model ..... 152

Figure 5-47: The corresponding slope model created with particles bonded using parallel bonds and smooth joint contacts ..... 153

Figure 5-48: Total displacement of the slope using DEM with reduction factor applied to the strength of the parallel bonds ..... 155

## List of Tables

Table 4-1: Properties of the boundary and the particle .....	62
Table 4-2: The parallel bond model properties .....	65
Table 4-3: The deformation of the tip of the beam by applying F(Force) and M(Moment) at the beam tip .....	66
Table 4-4: Model microproperties for Lac du Bonnet granite .....	68
Table 4-5: The results of the numerical UCS Test of Lac du Bonnet granite, numerical results of PFC, and HDPAC .....	69
Table 4-6: Information about the block and the inclined surface .....	76
Table 5-1: Microparameters values used in the numerical simulation of three numerical UCS tests .....	84
Table 5-2: The calibrated microparameters used in the numerical models.....	90
Table 5-3: Calibrated microparameters for smooth joints used in the models.....	90
Table 5-4: The numerical and physical test results of the tilting table tests .....	92
Table 5-5: Microparameters used in the numerical simulation of the DEM for .....	102
Table 5-6: Microparameters for smooth joints used in numerical simulation .....	102
Table 5-7: Joint set configuration, and the position of the blocks and total failure plane for different joint configurations.....	110
Table 5-8: Joint set configuration, and the position of the blocks and total failure plane for different joint configurations.....	119
Table 5-9: Joint spacing configuration for the main joint set, and the position of the blocks and total failure plane for two different joint configurations.....	121
Table 5-10: Joint friction angle values of the main columnar joint set used in the studied models .....	122
Table 5-11: Total failure plane and deformation patterns of the slope for nine different joint friction angles of the main columnar joints.....	124
Table 5-12: The calibrated microparameters used in the numerical models.....	140
Table 5-13: Calibrated microparameters for smooth joints used in the models.....	141
Table 5-14: The calibrated microparameters used in the numerical models.....	154
Table 5-15: Calibrated microparameters for smooth joints used in the models.....	154
Table 5-16: The parallel bond strength was reduced by a safety factor of 1.62. ....	154



## List of Symbols

$\alpha$	Angle of total failure plane with respect to the horizontal
$\beta$	Angle of an upper surface of a rock slope with respect to the horizontal
$\bar{\beta}_n$	Parallel bond normal critical damping ratio
$\beta_n$	Normal critical damping ratio
$\gamma$	Unit weight
$\delta$	Angle between rock mass stratification and the horizontal
$\theta$	Angle between the face slope and the horizontal
$\theta_T$	Angle of the tilting table at failure point
$k_n$	Normal stiffness of the particle
$k_s$	Shear stiffness of the particle
$\bar{k}^n$	Normal stiffness of parallel bonds
$\bar{k}^s$	Shear stiffness of parallel bonds
$k_{nj}$	Normal stiffness of the joint
$k_{sj}$	Shear stiffness of the joint
$\mu$	Particle friction coefficient
$\bar{\mu}$	Parallel bond friction angle
$\rho$	Density
$\bar{\sigma}$	Parallel bond tensile strength
$\phi$	Angle between the total failure plane and the line of normal to discontinuities
$\bar{c}$	Parallel bond cohesion
D	The horizontal distance from the center of the merged joints to the toe of the slope

$E_c$	Young's modulus of particles
$\bar{E}_c$	Young's modulus of parallel bonds
$g$	Bond gap
$g_j$	Joint gap
$H$	Height of the slope
$J_\varphi$	Joint friction angle
$J_{\varphi b}$	Joint friction coefficient of the base
$S$	Horizontal distance between the top of the slope and the part without any movement
$T$	Horizontal distance between the top of the stable zone and the slope toe
$Fric$	Friction coefficient

## Chapter 1. Introduction and problem statement

---

### 1.1 Toppling failure

The most common failure modes of rock slopes are classified as planer or wedge sliding, toppling, buckling, and bursting depending on their strength and discontinuity (Goodman and Kieffer 2000). The toppling failure mode is a common, hazardous phenomenon encountered by geotechnical and civil engineers when developing and/or restoring construction works that involve joined rock masses. The toppling failure mode was first described by Müller (1968) following his in the Italian Alps, based on which he proposed the theory of the "toppling block".

The toppling failure occurs when rock columns formed by discontinuities in a rock mass rotate around a fixed point (Wyllie and Mah 2004). There are different types of toppling failures in rock slopes, but block-flexure is by far the most common (Amini et al. 2012). Figure 1-1 shows a rock slope that consists of thick sandstone with thin inter-bedded shale layers, subject to the potential failure of block-flexure toppling (Amini et al. 2012).



Figure 1-1: Rock slope with a potential for block-flexure toppling failure facing Chalus Road (Amini et al. 2012)

A recent toppling failure has been reported in the Furnas Canyons, Capit6lio MG, Brazil. "A column of rock crashes down on leisure boats in Furnas Lake, killing 10 and injuring at least 32

people”, Al Jazeera (2022). Figure 1-2 illustrates the separation and toppling of a mass rock in Furnas Lake that killed several people.



Figure 1-2: The horrifying moment the canyon cracks and crushes people to death (Twitter: Knox. 2022, from <https://www.thesun.ie/news/8176290/canyon-brazil-crushes-two-people-death-pleasure-boats/>)

## 1.2 Problem statement

In practice, investigating toppling failures in nature is highly complex and economically impractical in many real cases. Despite many years of rock slope stability assessments, our understanding of the recognition, processing, analysis, and prevention of toppling failure still needs

to develop deeper and more fundamental basic knowledge. Aydan and Kawamoto (Aydan and Kawamoto 1987, 1992), Adhikary et al. (1997), Adhikary and Dyskin (2007), Amini et al. (2015), and Zhu et al. (2020) conducted physical modeling including tilting tables, centrifuge tests, and friction table tests to investigate toppling failure mechanisms. Although physical modeling is an alternative to field study, large-scale experimental tests are often costly and time-consuming if they are to provide comprehensive insights given the inherent complexity of real rock masses (Wyllie 1980). A comprehensive study of toppling failure, therefore, requires a competent numerical method that can profit from its advantages of low cost and high efficiency. Hence, the numerical method used to study toppling failure must account for the complexity of jointed rock masses.

The behavior of rock slopes dominated by discontinuities is not solely determined by the rock mass properties. Therefore, discontinuum-based methods, such as a discrete element method (DEM) can accurately capture the behavior of jointed rock slopes (Lian et al. 2017). In rock-flexural toppling failure, tensile bending stress and block separation from cross-joint surfaces are the main causes of block failure (Amini et al. 2015). Tensile rupture is also a crucial key factor in the process of toppling failure and the finite element method (FEM), cannot simulate a flexural and blocky toppling accurately due to not capturing the crack propagation in intact rock; therefore tensile rupture was not considered across the layers (Alzo'ubi et al. 2010). Toppling failures are characterized by large deformations and displacements; this failure mode involves dynamic processes and continuous complicated contacts are created during toppling failures (Liu et al. 2019). Given this complexity, the discrete element method (DEM) is suitable for modeling toppling failure (Dabirmanesh et al. 2023), given that a priori assumptions about the location and shape of the failure surface are not prescribed in this method, and the failure path can be determined without any assumptions. In addition, discrete element methods (DEMs) can be used to consider fractures and crack propagation inside a zone where the induced stress exceeds the material's strength (Scholtès and Donzé 2015).

While the finite element method (FEM) is widely used in geotechnical design, its limitations become apparent when dealing with large deformations or material separation (Scholtès and Donzé 2015; Dou et al. 2019; Augarde et al. 2021). Furthermore, the slip, rotation, separation, and size of the effects induced by discontinuities cannot be explicitly captured by the Finite element method (FEM) (Hammah et al. 2009). As long as there are relatively few discrete features, special interface (or joint) elements can be incorporated into continuum formulations (Lisjak and Grasselli 2014).

However, compared to continuum approaches, discontinuum-based methods such as the discrete element method (DEM) can effectively capture the large deformations and post-failure problems characteristic of real-world geotechnical engineering (Ishida et al. 1987; Augarde et al. 2021).

Based on the above considerations, studies of the toppling failure mode for jointed rock masses require a numerical method that can consider large deformations of rock masses and account for tensile stress development throughout intact rocks. Such numerical methods must also be able to consider the separations and movements of blocks, as well as crack propagation throughout rock masses.

A limit equilibrium analysis method to analyze block toppling failure was first developed by Goodman and Bray (1976). This approach was later modified for flexural toppling failure (Adhikary et al. 1997; Adhikary and Dyskin 2007; Amini et al. 2009; Aydan and Kawamoto 1992; Majdi and Amini 2011). Amini et al. (2012) developed a block-flexural toppling failure investigation method using limit equilibrium analysis by combining the work of Goodman and Bray (1976), and Aydan and Kawamoto (1992). All the analytical solutions make assumptions to simplify the problem and propose a theoretical model. The assumption of the total failure plane of the instability is an important factor used in the limit equilibrium method to analyze toppling failure. A crucial factor that can influence the results of the limit equilibrium method for toppling failure is that of surface rupture, which many researchers have investigated numerically (Alzo'ubi et al. 2010; Lian et al. 2017; Meng et al. 2018; Zhao 2015). However, none of these numerical methods can consider tensile strength or large deformations; thus, the estimated rupture surface path is not a sufficiently reliable assumption to use for limit equilibrium methods. In addition, the main focus of their studies was based on experimental tests that had the potential of flexural toppling failure. Amini et al. (2012) assumed the total failure plane of instability lies  $10^{\circ}$ – $20^{\circ}$  above the normal line of main discontinuities for block flexural toppling failure.

The other assumption used in theoretical solutions for block–flexural toppling failure is that two adjacent blocks may fail with different potentials of failure, in other words, two blocks with the same failure potential do not stand together. Also, in all of the theoretical solutions evaluated, the thickness of the blocks has been assumed similar. However, rock outcrops will have variable discontinuity spacings. These simplifications are required to be investigated in toppling failures.

In this study, a particle-based discrete element method (DEM) is applied to assess the stability of rock slopes with a potential for toppling failure. The DEM is used to simulate block-flexural

toppling failure based on an experimental tilting table. A validated numerical method is also developed to investigate rock slope stability for toppling failure-prone slopes. Different slope parameters are investigated, including joint friction angles, joint spacing, and joint configuration. Following a thorough investigation into toppling failure, which included verified numerical simulations validated through experimental tests and an in-depth study of small-scale slope behavior, the Discrete Element Method (DEM) is effectively applied to examine real-world cases of toppling failure.

## 1.3 Research objectives

### 1.3.1 Objectives

In this research, a DEM-based particle approach is developed and used to study block-flexural toppling failure. This study uses several algorithms and employs a discrete element code as an approach to simulate toppling failure. A numerical simulation calibrated by experimental testing is extended to simulate a slope representing the theoretical model proposed by Amini et al. (2012). The validated slope based on experimental tests is then later used to investigate the rupture surfaces which is the main assumption in the analytical method to evaluate toppling failure. A discrete element numerical simulation is used to investigate the effect of joint spacing and joint configuration to provide insights into the influence of joint set configurations on the assumptions used in limit equilibrium methods. The main objectives of this study are to:

- 1) **Assessment of Using the Discrete Element Method to Simulate Toppling Failure:** This objective entails evaluating the feasibility of employing a numerical method based on the Discrete Element Method (DEM) for simulating toppling failure. This involves a comprehensive examination of the implemented DEM code to ensure its capacity to accurately depict the toppling failure process. Furthermore, it aims to address identified shortcomings within the existing literature, particularly in relation to determining the overall rupture surface in toppling failure within jointed rock slopes. To accomplish this, a discrete element method that takes into account significant deformations and the role of

tensile stress within rock masses will be utilized. Sub-objectives will encompass the development of algorithms for particle generation and the utilization of algorithms for contact detection, contact resolution, and the establishment of bond and smooth joints to enable realistic interactions among particles.

- 2) **Effectiveness of Smooth Joints:** This objective involves investigating the effectiveness of implementing smooth joints to mitigate issues associated with particle interlocking along interfaces. This approach is designed to eliminate the need for excessively fine particles in simulating toppling failure.
- 3) **Simulation Rock Slope Toppling Failure:** Utilizing the validated numerical DEM-based method, to investigate rock slopes prone to block-flexural toppling failure. This investigation will encompass various slope parameters, including joint friction angles, joint spacing, and the influence of joint configurations, to comprehensively evaluate the resulting failure surface.
- 4) **Real-World Application:** This objective involves the practical application of the numerical DEM-based particle simulation to analyze toppling failure in real-world cases. This practical application is intended to provide valuable insights into the behavior of jointed rock slopes in real-life scenarios.

These objectives collectively serve as the foundation of this research, which seeks to advance our understanding of toppling failure mechanisms in jointed rock slopes and enhance the capabilities of DEM-based simulations in the field of rock mechanics.

## 1.4 Outline of the Thesis

Chapter 2 provides a comprehensive review of prior investigations into toppling failure. These studies are categorized into three main groups: experimental, numerical, and analytical. The chapter introduces the underlying assumptions of theoretical approaches and explains various numerical methodologies. It places particular emphasis on presenting a detailed formulation of the Discrete Element Method (DEM) and its subsequent implementation into a code-based DEM method.

Chapter 3 describes the algorithms and frameworks of the Python object-oriented programming (OOP) based distinct-element method (DEM). The developed code is later used as a simulation tool to investigate toppling failure.



Chapter 4 is dedicated to the confirmation and validation of the developed DEM code. A series of rigorous tests are conducted to validate critical components, including contact detection and resolution, the laws of motion, contact force, parallel bonds, and smooth joints—all of which are indispensable for the final simulation of toppling failure. Numerical uniaxial Compressive Strength (UCS) tests are executed and subsequently validated against experimental results. The numerical UCS results highlight the precision achieved by employing contact detection and resolution, normal contact, tangential force calculation, parallel bond models, boundary conditions, contact forces, and laws of motion.

Chapter 5 presents the efficacy and advantages of using a discrete element-based approach to simulate slopes susceptible to block-flexural toppling failure. Experimental tests are employed to validate the numerical simulations, and the validated model is subsequently used for various parametric studies concerning joint configurations and spacing. Additionally, the chapter explores the investigation of the rupture surface, a fundamental assumption in the analytical method rooted in the limit equilibrium method, through numerical simulations. The proposed theoretical approach for evaluating block-flexural toppling failure is scrutinized and assessed based on numerical simulation outcomes. These results are then employed to evaluate the influence of joint spacing and configuration on toppling failure behavior. Consequently, it is deduced that numerical simulations are imperative for evaluating the analytical method's performance across slopes with varying joint configurations and spacing. This chapter also encompasses the application of the numerical DEM-based method to simulate and analyze real-world cases, demonstrating its utility in studying rock slope toppling failure.

Chapter 6 presents conclusions drawn from the research findings and offers valuable recommendations for future research directions.

## Chapter 2. Literature review and background

---

### 2.1 Introduction

Rock slope failure is a major geotechnical problem that can cause irreparable damage to people, infrastructure, and property. Statistical data indicates that in the 20th century alone, disasters caused by massive rock slope failures killed nearly 50,000 people (Evans 2007). There were 43 landslide disasters in Canada between 1840 and 1998 that resulted in 570 deaths. In British Columbia alone, 21 events occurred (49% of the total) while in Quebec, 17 events took place (39.5% of the total). These two provinces account for the highest proportion of Canada's landslide disasters. There were 239 landslide fatalities in British Columbia (42%), and 213 in Quebec (37%). Between 1841 and 1889, rockslides in Champlain - Quebec caused 91 deaths (Brooks 2001).

Rock slope stability assessment is necessary for many construction fields such as civil engineering, tunnel engineering, and open-pit mining projects. Rock slope failure modes are complex and can be divided into several categories. The strength and discontinuity of rock masses and joints are major factors of failure mode occurrence. Planer or wedge sliding, toppling, buckling, and bursting are some of the major modes of failure (Goodman and Kieffer 2000).

Sliding (plane, wedge, rotational (circular/non-circular)), toppling, and rockfall failure modes are some of the most common types of failures in slopes. Plane sliding is a failure along a single planar surface, which is dipping into an excavation. Its surface strike is parallel or partially parallel to the slope face. Wedge sliding failures occur when the failing slope contains two intersecting discontinuities, so that, both discontinuities dip outward while striking obliquely to the slope face. Wedge sliding thus takes place along the line of the intersection. The analysis of wedges has been discussed extensively in the geotechnical literature, and the analysis methods draw heavily upon the work of Goodman (1964), Wittke (1965), Londe (1965), Londe et al. (1969, 1970), and John (1970) (Wyllie and Mah 2004). Rotational sliding occurs in highly weathered or closely fractured rocks, whereas rockfall occurs when rock masses that have been detached from a steep rock slope descend from the top of the slope by free-falling, leaping, bouncing, or rolling. Toppling failure occurs when rock columns, which are formed in a discontinuous rock mass, rotate around a fixed point (Wyllie and Mah 2004).

The toppling of rock blocks is known as an important potential failure mode, especially for rock slopes, and toppling can occur in civil structures such as foundations, tunnels, and underground chambers. Moreover, it can occur on a small scale in any rocky landscape due to frost, creep, or hydrostatic forces. The toppling failure mode has been reported in both natural and excavated rock slopes in construction works such as hydropower stations (Zhang et al. 2015; Gu and Huang 2016), highway infrastructure (Cruden and Martin 2006; Hu et al. 2020; Majdi and Amini 2011), open-pit mines, and railways (Wyllie 1980; Alejano et al. 2010; Carlà et al. 2017; Zhu et al. 2020). A topple can occur slowly or extremely rapidly, and then accelerate as the movement progresses (Cruden and VanDine 2013).

## **2.2 Toppling failure**

The toppling failure mode is distinct from the more prevalent failure types of sliding along an existing or an induced slip plane. Historically, the toppling failure mode was introduced to the rock mechanics community in the study of failures of the north face of the Vaiont slide in the Italian Alps by Müller who recommended that block rotation or toppling could have been an effective factor in that slide (Müller 1968). The simple criteria were developed based on physical and numerical modeling techniques of the toppling failure mode by Ashby (1971) and De Freitas and Watters (1973). Various field tests have demonstrated the toppling and toppling-sliding mechanisms in real cases (Ashby 1971). Ashby demonstrated the kinematics of toppling; he built the basic foundation of a limit equilibrium method of toppling by examining the influence of physical and mechanical parameters (Ashby 1971). These investigations show that toppling can develop on a surface that has dip angles that are smaller than the joint friction angle. However, an initial movement of the toe is necessary in order to provide enough space to let the rock rotate from above (Goodman 2013). De Freitas and Watters (1973) performed field studies and demonstrated that toppling failure can occur in nature. They convinced the geotechnical community that toppling is a significant and distinct mode of failure. Toppling occurs over a wide range of scales in a variety of rock types and there is no unusual geological condition linked to the development of this failure. De Freitas and Watters also noted how this failure was linked to lateral restrictions and to internal

restrictions, such as rock bridges. These local rock bridges, which exist in the path of progressing zones of tensile strain, affect the rock mass (De Freitas and Watters 1973).

Toppling failure was divided into main and secondary categories by Goodman and Bray (1976). The rock mass weight has a significant effect on instability in the main toppling regime, while in secondary toppling, it is external factors that trigger a failure (Goodman and Bray 1976). The main toppling failures are classified as flexural, blocky, and block-flexural, as illustrated in Figure 2.1. Toppling failure was defined by Hoek and Bray (1981) as the “rotation of columns or blocks of rocks about some fixed base” (Brideau and Stead 2010).

Flexural toppling normally occurs in a rock mass composed of a group of parallel, steeply dipping discontinuities that are closely spaced. These prevailing discontinuity sets behave like cantilever beams. By exceeding the maximum stress beyond a failure yield due to bending, a rock cantilever will fail and topple. If such a rock mass also has one widely spaced basal cross-joint set, then the structure cannot bear the tensile portion of the bending stress; therefore, the columns or blocks of stone overturn due to their own weight. This failure mode is recognized as block toppling. In most real-world case records, block-flexure, representing a combination of blocky and flexural toppling failure modes, is reported as the toppling failure mode. In this failure mode, both the strength of the material and the presence of widely spaced discontinuities play significant roles; thus, tensile bending stresses and overturning due to the self-weight of a rock block cause or trigger failure in this mode (De Freitas and Watters 1973; Amini et al. 2012).

Secondary toppling is divided into four types. *Slide head toppling* is possible behind a landslide, which makes a space into which the upper slabs that may topple. Similarly, *slide base toppling* can be developed when a rock mass slides and intersects multiple vertical or inclined layers that have the capability to topple. *Slide toe toppling* can be initiated when the force of the mass that slides influences the boundary of a different rock mass which has a toppling failure propensity. *Tension crack toppling* can occur after a landslide or slump, reducing the forces that prevent layers from separating and toppling (Goodman 2013).

Extensive research has been conducted into different modes of toppling failure since Goodman and Bray’s 1976 classification; for example, the works of Aydan (1992) and Adhikary (1997) developed flexural toppling through laboratory research and analytical methods (Adhikary et al. 1997). Majdi and Amini (2011, 2012) studied the mechanisms of block-flexure mode failures and systematically analyzed them (Amini et al. 2012).

The main reason for classifying toppling failures is to establish the viewpoint from which to model these failure modes. For instance, while the dimensions of blocks are not needed for the initial modeling of flexural toppling, the geometry of a single block is required for the overall geometry of blocks in block toppling (De Freitas and Watters 1973). Understanding the different types of toppling failure can help to determine the most appropriate numerical method with which to investigate the behavior of toppling on slopes.

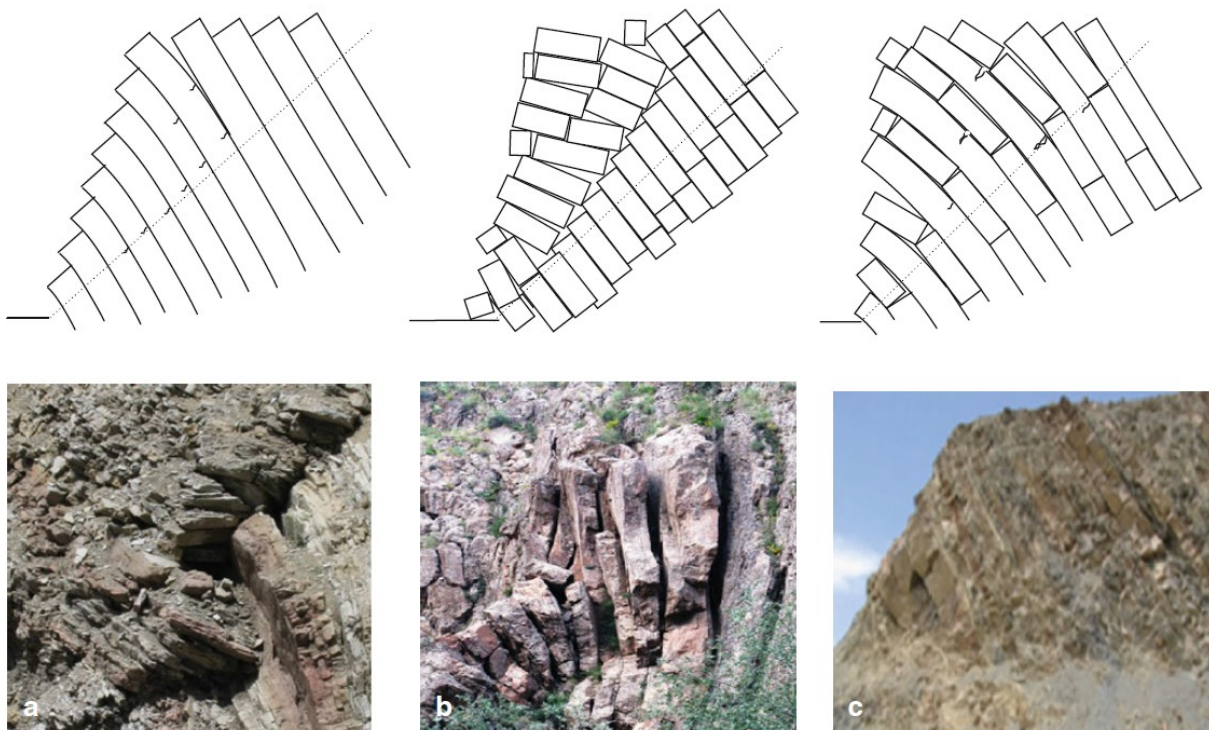


Figure 2-1: Possible main toppling failure in rock slopes. a. Flexural. b. Blocky. c. Block-flexural (Amini et al. 2012)

## 2.3 Rock slope analysis methods

Kinematic and equilibrium-based approaches are the conventional methods of analysis used in rock slope stability assessment. The kinematic method only can help to find the potential of structurally

controlled rock slope instabilities. This means that the blocks that are formed by discontinuities can slide freely due to new excavations or erosion effects. However, external forces such as water or reinforcement by means of tensioned rock bolts and other external forces cannot be considered in this method. The kinematic feasibility study was used, based on a stereographic criteria method, by Goodman and Bray (1976) to determine the preliminary investigation of the stability of rock slopes (Babiker et al. 2014). Rock slope stability was investigated using the limit equilibrium analysis method. Among the conventional methods, equilibrium methods remain the most common option for the analysis of slope instabilities. However, these methods are only relevant to slopes that are not very complex and that have a simple geometry and loading condition. Furthermore, the rigidity assumption has no effect on the appropriate results (Eberhardt 2003). Limit equilibrium methods have been used by many different individuals in the geotechnical engineering field (Babiker et al. 2014).

## **2.4 The limit equilibrium method for slope toppling instability**

Over the past few decades, many scholars have developed the analytical method from different perspectives (Amini et al. 2012; Aydan and Kawamoto 1992; Goodman and Bray 1976; Zheng et al. 2019).

As stated earlier, a rock slope can fail in several modes. Ashby (1971) proposed the following modes that lead to failure in a rock slope:

- Transitional sliding on discontinuities;
- Rotational sliding in the plane of the discontinuities;
- Toppling (rotation about pivot points); and
- Failure throughout a rock mass due to tension or compression that results in shear failure.

Ashby (1971) considered the situation shown in Figure 2-2 for describing the different conditions of a block on an incline with the dip angle  $\alpha$  and a friction coefficient  $\mu = \tan \phi$ , where  $\phi$  is the slope's friction angle.

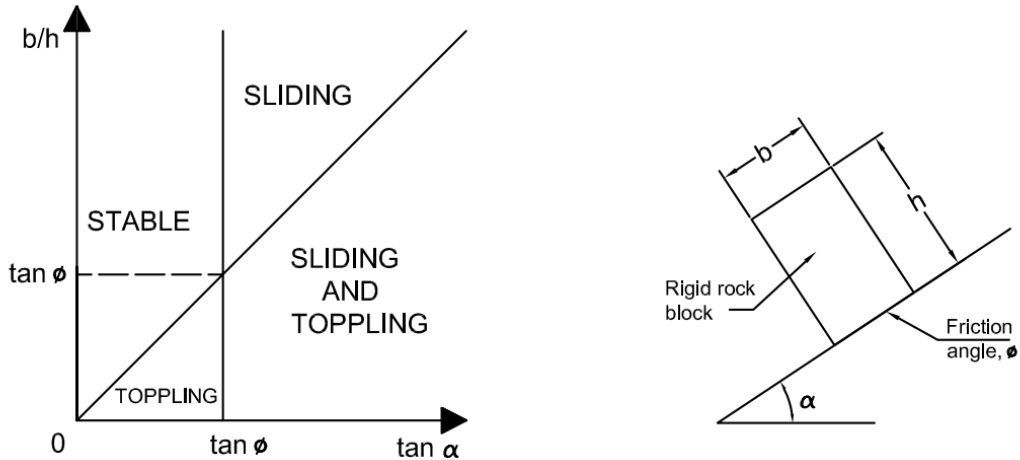


Figure 2-2: Condition for toppling and sliding for a block on an inclined plane (Sagaseta 1986)

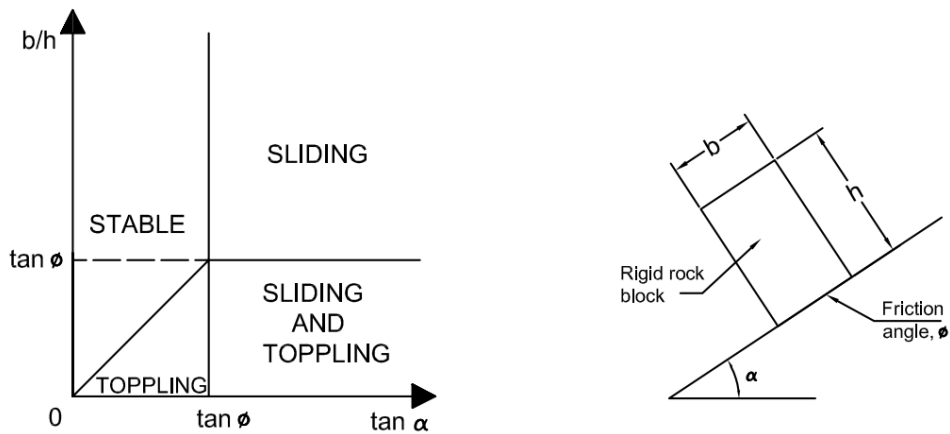


Figure 2-3: Overturning and sliding criteria for a single block on an inclined plane (Sagaseta 1986)

The conditions for the sliding and toppling criteria later were changed by Bray and Goodman (1981) to those shown in Figure 2-3. However, by considering the dynamic-equilibrium conditions, Sagaseta showed that the region of toppling was greater than the area that was proposed by Goodman and Bray (Sagaseta 1986). According to Sagaseta, Goodman and Bray's method has two sources of error which are related to the toppling condition and their consideration of a non-zero resultant force. If the weight vector falls outside the base of a block and the acting friction force at the toe is sufficiently large to deliver toe fixity, the two main necessary conditions for toppling are provided. Regarding the resultant force, when a block topples, the center of rotation is at the toe,

so some linear acceleration is applied to the center of gravity and the resultant force on the block is not zero. As a result, Sagaseta developed Figure 2-4 to correct the region of toppling failure suggested by Goodman and Bray (1981).

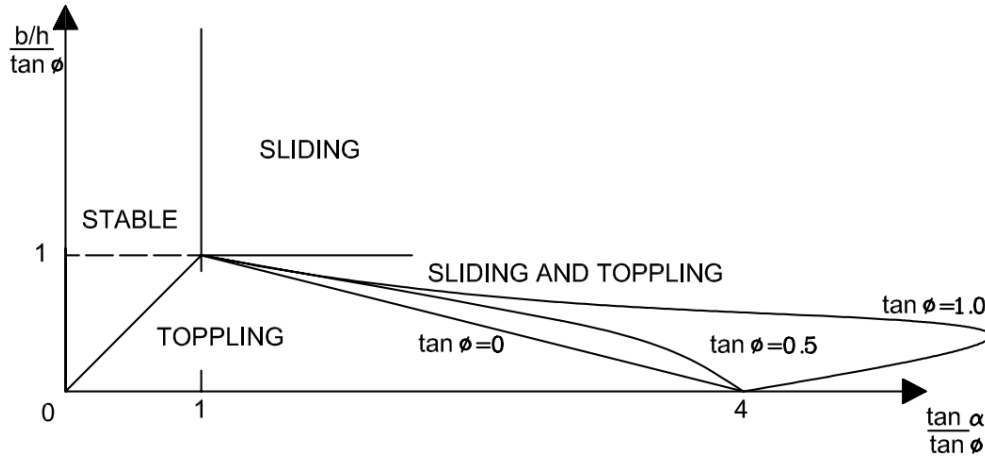


Figure 2-4: Stability criteria (Sagaseta 1986)

In a real rock slope, that has the potential of toppling, the interaction between columns and blocks is more complicated than for a single block. The interaction between blocks has more degrees of freedom. The limit equilibrium method was first applied by Goodman and Bray (1981) to investigate the potential of blocky toppling on a stepped-base slope. Different kinematic conditions were considered in their methods. For the first condition, as discussed above, toppling occurs when the center of gravity of a block lies outside its base. This situation occurs when

$$\Delta x/y < \tan \varphi_p \quad (2-1)$$

where,  $\Delta x$  and  $y$  are the width and height of the block, respectively, and  $\varphi_p$  is a dip angle of the plane, as illustrated in Figure 2-5.



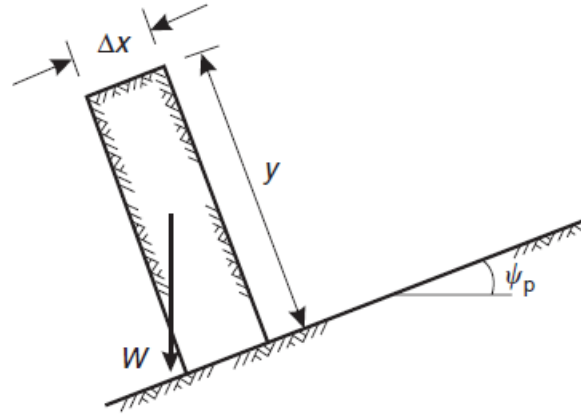


Figure 2-5: Block height/width and a plane dipping (Wyllie and Mah 2004)

The second condition is inter-layer slip. The necessity of toppling between blocks is the generation of shear displacement between the contact faces on the top and bottom faces of blocks. The following conditions are required to generate sliding between these faces. For a rock slope, the state of stress is uniaxial with  $\sigma$  and the direction is parallel to the slope face. When the layers slip, the direction of the  $\sigma$  is changed. The new angle between the normal to the layers and  $\sigma$  must be  $\phi_d$ , where  $\phi_d$  is the friction angle of the sides of the blocks.

By considering  $\phi_f$  as the dip of the slope face and  $\phi_d$  as the dip of the planes forming the sides of the blocks, the condition for having an interlayer slip, as Figure 2-6 shows, is

$$(180 - \phi_f - \phi_d) \geq (90 - \phi_d)$$

Or

$$\phi_d \geq (90 - \phi_f) + \phi_d \tag{2-2}$$

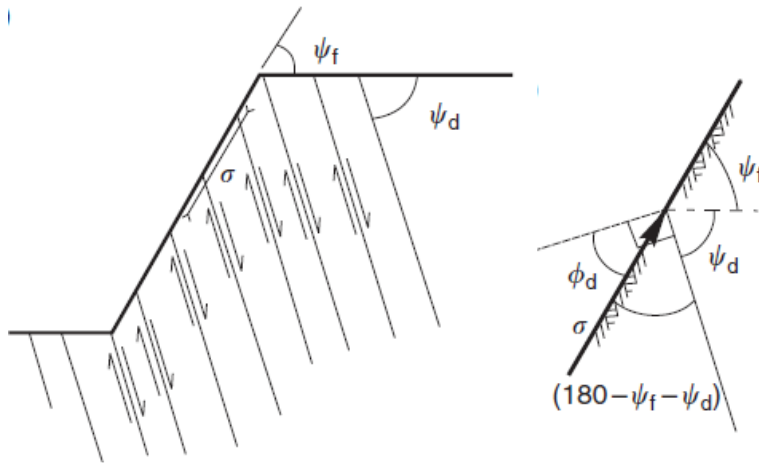


Figure 2-6: Directions of stress and slip directions in a rock slope(left), and condition for interlayer slip(right) (Wyllie and Mah 2004)

A limit equilibrium method was developed and applied by Goodman and Bray to predict blocky toppling failure in a rock slope (Goodman and Bray 1976). This stability analysis was based on the iterative process to determine if the blocks in a slope will be stable, topple or slide. The entire slope is considered unstable if the lowermost block is either sliding or toppling. Figure 2-7 shows the general model for the limit equilibrium analysis of toppling on a stepped base (Wyllie and Mah 2004). Zambak, however, demonstrated that the initiation mechanism of toppling on a stepped base slope was entirely different from the mechanism of toppling on a flat base (Zambak 1983). He proposed that the toppling analysis method could show the appropriate behavior of a slope while the physical model satisfied the boundary condition for statically indeterminate problems. In this case, as illustrated in Figure 2-8, toppling in blocks requires dilatancy  $\delta$  of the blocks along the base plane and shearing on the faces of the blocks (Zambak 1983; Wyllie and Mah 2004).

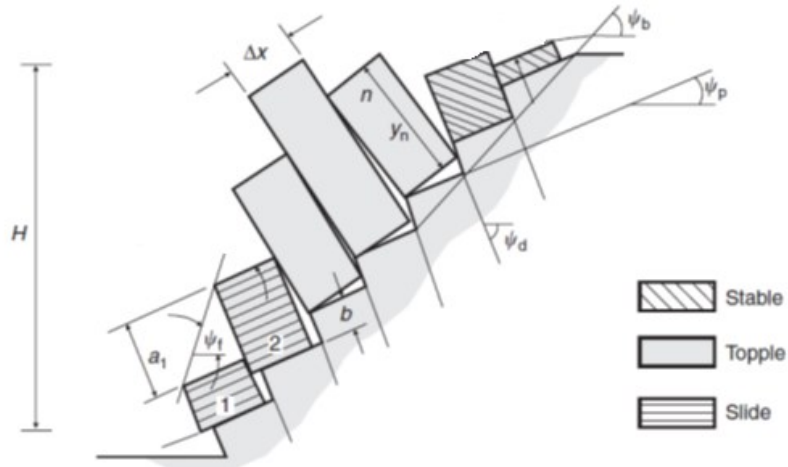


Figure 2-7: Model for limit equilibrium analysis of toppling on a stepped base (Wyllie and Mah 2004)

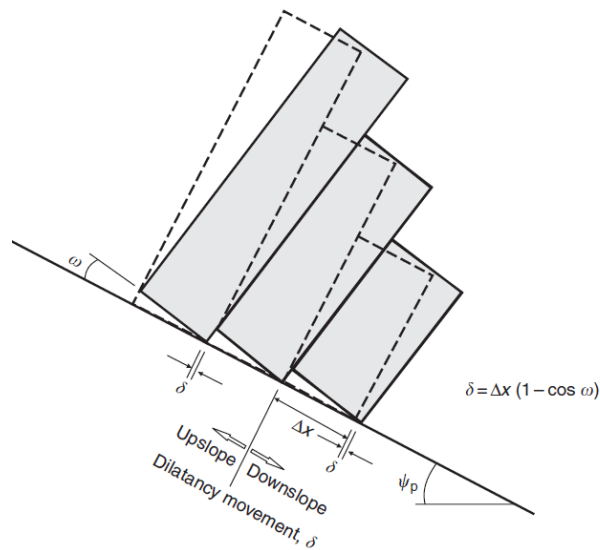


Figure 2-8: Dilatancy of toppling blocks with base plane coincident with normal to dip of blocks (Zanbak 1983; Wyllie and Mah 2004).

Aydan et al. (1989) applied dynamic equations to investigate the stability of block columns and discontinuous rock slopes. Their method was identical to Goodman and Bray's; however, they used a dynamic equilibrium equation instead of a static equilibrium equation as with Goodman and Bray. They considered sliding failure, toppling failure, and combined toppling and sliding failures. In

addition, they derived the conditions for stability and some possible forms of instability of a blocky column. The results compared well with experimental results on blocky column model slopes in the laboratory (Aydan et al. 1989).

When the characteristic dimension of a slope is sufficiently large relative to the thickness of a block, the continuum assumption can logically be used to solve toppling failure problems, rather than by considering a discrete assemblage of blocks (Bobet 1999). Bobet (1999) developed an analytical solution by considering an ordinary differential equation for rotational equilibrium. The block base and the baseline normal to the dip of the main discontinuities both play a key role when applying this method to model analysis (Bobet 1999). Later, Sagaseta et al. (2001) extended the continuum solution for the condition in which the baseline is not normal to the dip of the dominant discontinuities (Sagaseta et al. 2001). Liu et al. (2008) further improved this solution and considered transitional positions using the limit friction equilibrium condition (Liu et al. 2008a). In rock slopes, that have a potential for toppling failure, blocks have three displacement modes: (1) blocks behind the crest that are stable; (2) blocks in the middle of the slope that are prone to toppling; and (3) blocks near the slope toe that have the potential to slide (Figure 2-9) (Liu et al. 2008b).

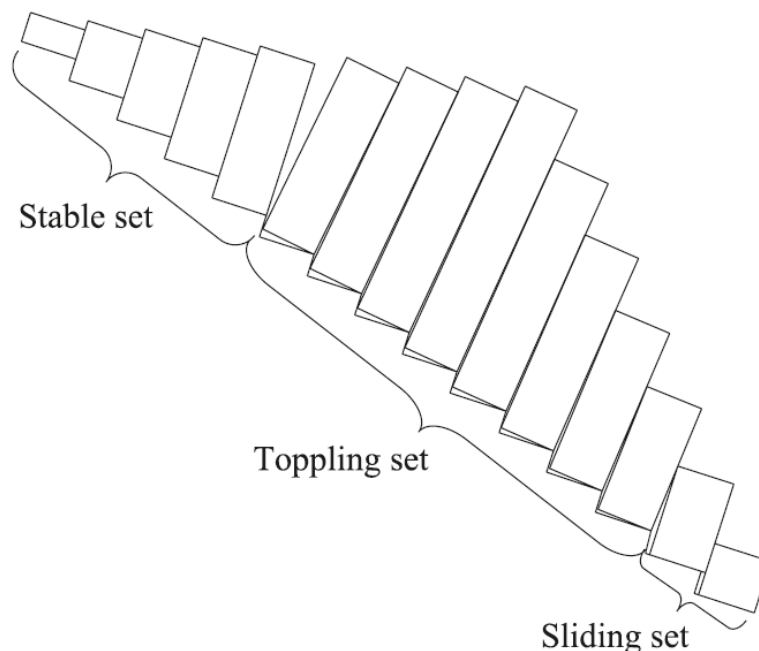


Figure 2-9: Block toppling failure mode (Liu et al. 2008b)

### 2.4.1 Flexural toppling

The method of analysis for flexural toppling, introduced by Aydan and Kawamoto, considers layers of rock that behave as cantilever beams (Aydan and Kawamoto 1992). Bending moments fracture the rock columns at locations where the tensile stress is maximum. A limit equilibrium method was proposed, employing the column theory and using the theory of elasticity. The following assumptions were considered in this method (Adhikary et al. 1997).

1. The forces, including gravity forces, are considered on each layer, which is treated as a cantilever beam, as shown in Figure 2-10. To simplify the problem, the total side force is applied at a point  $xh_j$ , where  $h_j$  is the height of the side of a layer that corresponds to the force,  $j$  is the layer number, and  $x$ , which is between (0, 1), is a factor to determine the inter-column force distribution (cf. Figure 2-11). In terms of the side force distribution coefficient, Adhikary et al. proposed  $x=0.6$ , based on laboratory centrifuge tests (Adhikary et al. 1997).
2. A limiting equilibrium's state exists simultaneously across whole layers along the future fracture, at least exactly before failure.
3. The maximum tensile stress  $\sigma_{x|b=y/2}$  exists for each layer along the future fracture plane and is equal to the tensile strength of a material  $\sigma_t$ .
4. It is assumed that the fracture plane is at an angle of  $\theta$  degrees upward from the normal dip angle of the joint (Figure 2-10). However, this angle is considered to be zero by Aydan and Kawamoto (1992). However, Adhikary et al. calibrated this angle to 10 degrees by performing and comparing centrifuge tests (Adhikary et al. 1997).

From the basic strength of materials, the axial stress  $\sigma_x$  at distance  $y$  from the centroid of a cross-section is:

$$\sigma_x = -\frac{N}{A} + \frac{M}{I}y \quad (2-3)$$

where  $N$  denotes the axial force in a column,  $M$  is the bending moment,  $A$  is the cross-sectional area and  $I$  denotes the second-moment inertia.

By substituting the applied forces shown in Figure 2-11 and by rearranging the formulation, Aydan and Kawamoto (1992) derived the following expression:

$$P_{j-1} = \frac{\max(P_{j,0}) \left( x h_j - \frac{1}{2} \mu b_j \right) + \frac{1}{2} T_j \bar{h}_j - \frac{2I_j}{b_j} \left( \sigma_{tj} + \frac{N_j}{b_j} \right)}{x h_{j-1} + \frac{1}{2} \mu b_j} \quad (2-4)$$

Where  $I_j = \frac{b^3}{12}$ ,  $W_j = \gamma b_j h_j$ ,  $N_j = W_j \sin \alpha$ ,  $T_j = W_j \cos \alpha$ ,  $h_j = 0.5 (h_j + h_{j-1})$ ,  $\mu = \tan(\varphi_j)$ ,  $\varphi_j$  is the joint friction angle,  $\alpha$  is the column inclination angle,  $b_j$  is the column thickness, and  $\gamma$  is the unit weight of the material.

The iterative process begins by calculating  $P_{j-1}$  for the uppermost block, and then progressing down to the toe of the slope. The value of  $P_{j-1}$  is reused as the  $P_j$  for the next step. In the final step, the  $P_0$  is reached for the lowest-most block. The value of  $P_0$  is an indicator of stability:

$P_0 > 0$  – *unstable*

$P_0 = 0$  – *at limit equilibrium*

$P_0 < 0$  – *stable*

Amini et al. (2009) tried to modify the analytical method for the analysis of flexural toppling failure by considering the principle of compatibility equations, given that rock layers are statically indeterminate (Amini et al. 2009).

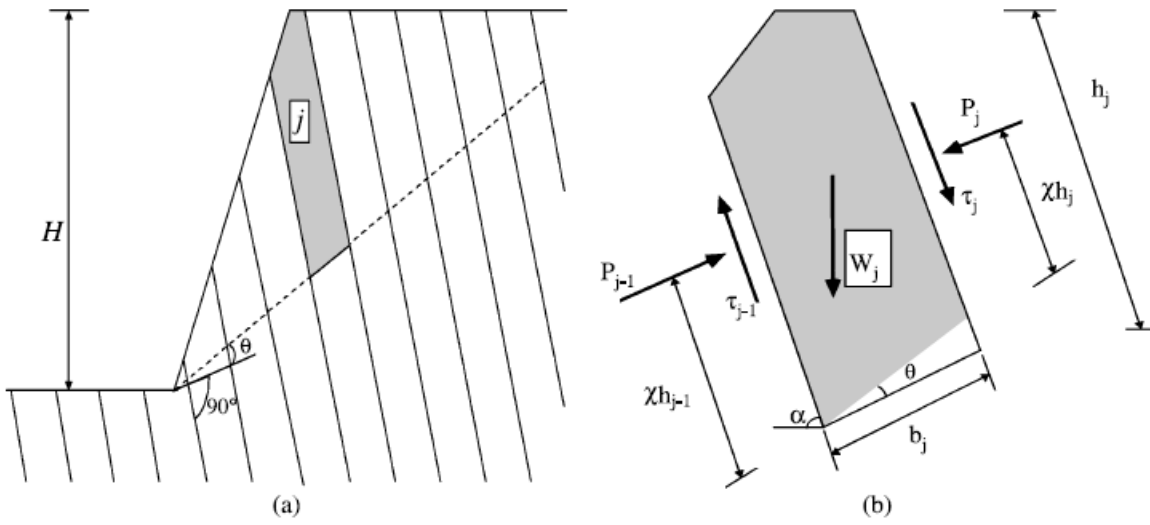


Figure 2-10: Schematic diagrams showing: a) slope geometry and b) forces acting on a single column. Here  $\tau_j$  and  $\tau_{j-1}$  represents the shear forces acting along the inter-layer boundaries (Adhikary and Dyskin 2007)

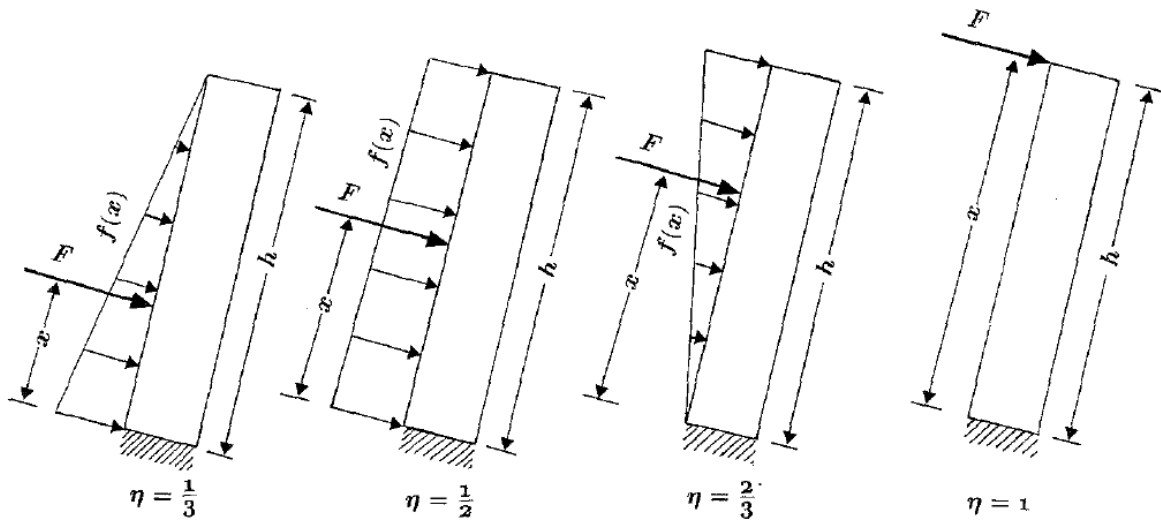


Figure 2-11: Illustration of the position of action of normal force on a column for various distributions of normal stress (Aydan and Kawamoto 1992)

## 2.4.2 Block-Flexure Toppling

The potential for block-flexure toppling instability was investigated by Amini et al. (2012). These authors proposed a method, based on the limit equilibrium analysis of toppling failure, to control the stability of slopes with a potential for block-flexural toppling instability. To simplify the real behavior of rocks, some assumptions were incorporated into this model. Firstly, that two adjacent blocks cannot have a similar failure potential (i.e. blocky failure or flexural failure only). Secondly, blocky and columnar toppling failures are similar. Thirdly, all blocks have an equivalent factor of safety against failure for the whole slope. Lastly, the total failure plane is assumed to be 10-20 degrees above the normal line of the main discontinuities. In block-flexure toppling, blocks, that are subjected to failure due to high tensile bending stresses or separation from the cross-joint surface, topple together. Block-flexural toppling involves a combination of block toppling failure, flexural toppling failure, and block sliding modes. Figure 2-12 shows a theoretical model that was applied in order to study the phenomenon. Two different cases were considered to analyze the slopes. One block, with a potential for blocky toppling, was assumed between blocks with a potential of flexural toppling failures as a first case. Another block, with a flexural toppling potential failure, was considered between two other blocks that have the potential for blocky toppling failures as a second case. The different appropriate theoretical mechanics were considered for each case to investigate and evaluate block-flexure toppling. As this step-by-step procedure was time-consuming, a FORTRAN program was used to simplify the stability analysis of rock slopes against failure. Two case studies were used to verify the program results (Amini et al. 2012).



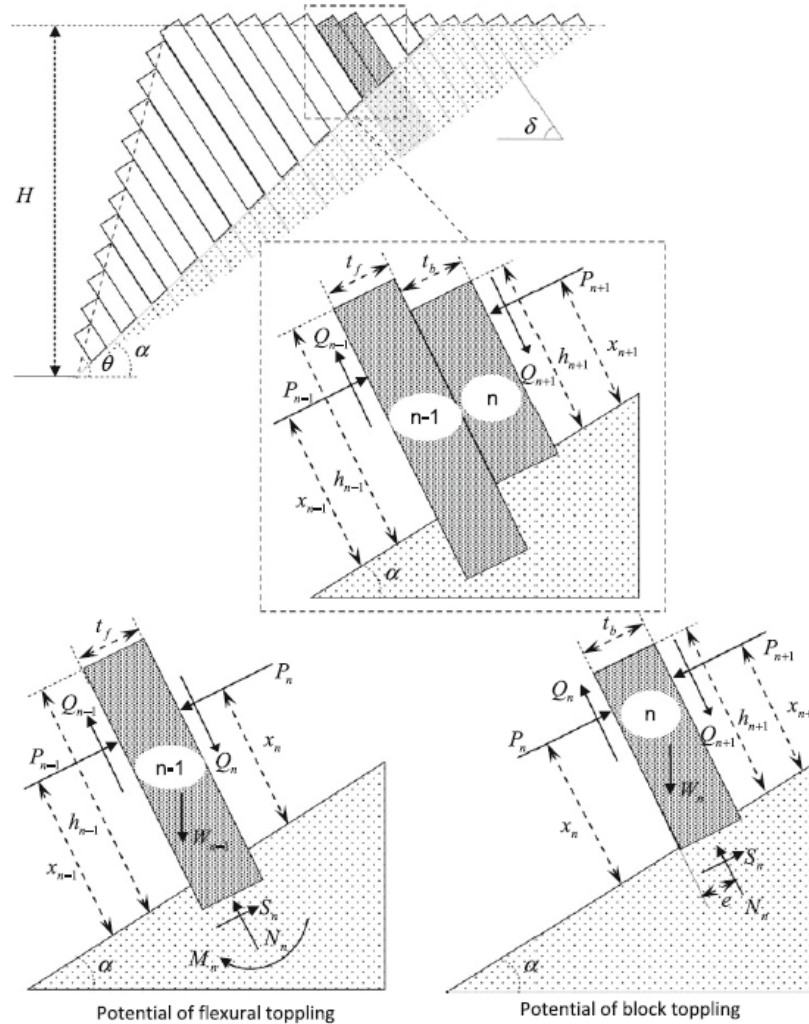


Figure 2-12: Block-flexure toppling failure mechanism (Amini et al. 2012)

## 2.5 Physical modeling to simulate toppling

Physical modeling is a crucial part of investigating geotechnical problems, especially for rock slope stabilities. On their own, field studies cannot help to investigate the underlying failure mechanism of rock slopes. In addition, aside from their considerable cost, some field studies may simply not be feasible. Hence, small-scale physical modeling is an appropriate substitute for exploring failure mechanisms.

Various physical methods can be applied to investigate rock toppling, such as *tilting table* (Ashby 1971; Lanaro et al. 1997; Amini et al. 2015), *base friction* (Hittinger 1978; Bray and Goodman 1981; Aydan and Kawamoto 1992), and *centrifuge* (Adhikary et al. 1997; Adhikary and Dyskin 2007; Li et al. 2015; Wang et al. 2022; Zhang et al. 2007).

Centrifuge modeling provides a framework in which to study the prototype behavior at a model scale and body forces control how the mechanics is being involved. The stress and strain forces in a prototype can be similar to those in a scale model by applying an acceleration factor to the scale model (Adhikary et al. 1997).

Adhikary and Dyskin (2007) investigated the magnitude of the joint friction angle to identify the mechanism of flexural toppling failure of slopes based on centrifuge tests: a limit equilibrium model and finite element model, based on Cosserat continuum theory, were then used to analyze the results. A major cause of changes in the joints' frictional strength is groundwater variations. Adhikary and Dyskin (2007) determined that the magnitude of joint friction angles played a key role in developing instantaneous or progressive flexural toppling failure: they observed that instantaneous failure occurred for joint friction angles of  $\sim 20^\circ$  and above, whereas progressive failure was observed for joint friction angles below  $20^\circ$ . In addition, the joint cohesion had no notable effect on the failure mechanisms, unless it was sufficiently low to permit sliding between layers, as sliding is a prerequisite for flexural toppling. Adhikary and Dyskin (2007) also observed that the limit equilibrium method can be used to determine the failure load under conditions with high joint friction angles. However, at smaller joint friction angles, the limit equilibrium method was incapable of calculating the correct failure load and instead consistently overestimated it. They concluded that the joint friction angle has a significant role in the mechanics of toppling failure (Adhikary and Dyskin 2007).

Zhang et al. (2007) performed a centrifuge test to validate Goodman and Bray's (1976) model for non-persistent basal planes of rock columns. Their results did not confirm the straight failure plane reported by Goodman and Bray; instead, a biplanar slip surface, i.e. a plane with a flatter inclination near the toe of the slope, and a deep-seated portion, was observed. Their findings revealed that determining the critical failure surface is essential for analyzing a toppling failure.

Chen et al. (2015) used a series of centrifuge tests to investigate toppling mechanisms and identified two failure surfaces in all tests: an upper surface called the 'linear failure surface', and a surface

defined as a 'basal plane'. Their centrifuge test results showed that the model, which incorporated a certain bending resistance, was stable compared to another model without such resistance.

Li et al. (2015) performed dynamic centrifuge tests under seismic loading to investigate the toppling failure of two physical models made of a synthetic material. One model only included intermittent rock planes, and the other one had rock planes and secondary rock joints. The results revealed that secondary rock joints inside a rock slope dramatically reduce the dynamic stability. The failure of a toppling rock slope without secondary rock joints (the first model) occurred because bending and toppling started from the slope foot and then the rear layers toppled. The second model, which consisted of secondary rock joints, failed in a different process; the failure started to form at the top rock layer due to the penetration of secondary rock joints inside the slope, and then the failure proceeded to the underlying rock layers. The angle of the final failure plane was also different than in the first model, it was much steeper in the slope with secondary rock joints, and the failure plane was formed in a noticeable step-path shape. In addition, they found that, while the failure plane surface in the slope with no secondary joints failed in shearing at the failure plane, the failure observed in the slope with secondary joints was due to breaks along secondary rock joints in tension mode at the failure plane (Li et al. 2015).

Wang et al. (2022) conducted centrifuge tests to investigate the effect of unequal strata thicknesses on flexural toppling failure. Their results showed that failure processes are divided into slope toe failure, fracture development, and slope failure. In slopes with thick layers at the slope toe, the deformation of the upper layers is affected by deformation in the lower layers (Wang et al. 2022).

## **2.6 Numerical analysis of slope toppling**

Limit equilibrium analysis is generally used to estimate slope stability in geotechnical practice (Michalowski 1995). The failure surface must be assumed in advance. The irregular discontinuities of a natural rock mass make it difficult to estimate its failure surface. Experimental tests are costly and several tests are required. Moreover, it is extremely complicated to simulate rock slopes on a real scale. Therefore, studying the fundamental process that takes place in a rock slope entails the use of numerical simulation.

It is difficult to assess the appropriate design of rock slope stability because the features and behavior of a rock mass are complex. The nature of rock mass material is heterogeneous,

anisotropic, and elasto-plastic (Harrison and Hudson 2000). Discontinuity is the main rock mass behavior, and so rock stability is mainly managed by ‘joint behavior’ rather than by the mechanical properties of intact rock. As a result, ‘joints’, or more specifically, ‘discontinuity’ or ‘fracture’ affects the stability of rock engineering structures. This nature of rock itself leads to complicated mechanical behavior that can be a challenge in classical numerical models. Numerical modeling can help to advance rock modeling investigations in ways that have not been possible by using conventional methods.

Generally, numerical models can be divided into three groups: continuum, discontinuum, and hybrid models. Key differences between the continuum and discontinuum analysis techniques rely on the conceptualization and modeling of the fractured rock mass, and the ensuing deformation. A continuum model mostly simulates material deformation, while the block-by-block movement of the system is the main characteristic of a discontinuum model. With the improvements in computing, a number of numerical methods can now be used in slope stability analysis (Jing 2003; He et al. 2013).

The many methods for numerical modeling of discontinuous rock masses can be organized into three groups: continuum, discrete element, and hybrid methods, as detailed below (Jing 2003):

- Continuum methods: Finite Element Method (FEM), Boundary Element Method (BEM), and Finite Difference Method (FDM);
- Discrete element techniques: Discrete Elements Method (DEM), Discontinuous Deformation Analysis (DDA); and
- Hybrid models: Hybrid BEM/DEM, Hybrid FEM/BEM, Hybrid FEM/DEM Hybrid FEM/DDA, and other hybrid models.

In cases where the rock mass does not experience large deformations, continuum-based approaches have proven to be successful. Nonetheless, when the geometry and strength characteristics of discontinuities control the rock mass behavior, the discontinuum model should be considered to model the interaction between individual blocks.

### 2.6.1 FEM/BEM/FDM Continuum Methods

The FEM is a numerical method that divides the problem domain into sub-domains (elements) with standard shapes (triangle, quadrilateral, tetrahedral, etc.). Elements are connected to each other at certain points called nodes. The local algebraic equations of the elements are assembled to solve the global system of algebraic equations after considering initial and boundary conditions. Additional parameters such as stresses, which are obtained after the solution of the global equation system, can be computed as well (Jing 2003).

BEMs only use discretization on the boundary of the domains. The information required for the solution domain is computed separately from the information on the boundary, based on the solution of a boundary integral equation (Jing 2003).

The FDM is a numerical approach that uses regular or irregular grids over problem domains. Partial differential equations are solved by replacing partial derivatives with differences at the grid points. The boundary and initial conditions are assigned before solving the system of equations (Jing 2003).

FEM, BEM, and FDM are the most popular numerical tools in many engineering domains. While special joint elements can be applied to model rock mass discontinuities in a discrete manner, using FEM and BEM methods with these special joint elements, many difficulties arise in describing discontinuities and managing permitted deformations. Discrete element methods (DEM), described next, use a specific type of contact to solve this problem of multiple material discontinuities.

### 2.6.2 Discrete Element Methods

The discrete (or discontinuous) modeling method (DEM) approach is one of the most well-known methods in computational mechanics, and its use has been developed in rock and soil mechanics since the 1970s. The distinct element method (DEM) was introduced by Cundall (1971) and subsequently developed by other researchers (Cundall and Hart 1992; Itasca 2004; Potyondy and Cundall 2004).

The DEM method is classified as *discontinuum analysis* technique, so this method considers material directly as an assemblage of explicitly separate blocks or particles and their interactions. The formulation of DEM relies on a dynamic or transient analysis that studies the dynamic interaction between separate blocks and studies assumptions of their kinematics and deformation

systems (Lisjak and Grasselli 2014; He et al. 2013). The large displacement along discontinuities makes the simulation of the block movements (translation and rotation) possible for the DEM (Jing 2003).

The DEM can capture a broad range of mechanical soil and rock aspects, even if only simple numerical models are applied. Unlike a continuum model, which assumes soil or rock as a continuous material and does not consider the internal relative movements and rotations, in the DEM, inter-particle and mechanical response features can be captured (O'Sullivan 2011).

Cundall and Hart (1992) consider a discrete element method to have the following properties:

- Discrete elements are allowed finite displacements and rotations as well as complete detachment; and
- During the simulation progresses, new contacts are identified and generated automatically.

The DEM method can be classified according to several criteria: the type of contact between bodies, the representation of the deformability of solid bodies, the procedure for the detection and modification of contacts, and the procedure for solving the equations of motion are the main ones (Jing and Stephansson 2007).

The DEM uses an explicit scheme to solve the equations of motion for each discrete block. The blocks can be rigid or deformable; however, the contacts between bodies are deformable. For rigid blocks, the equations of motion include only the translation of the blocks' centroids and the rigid body rotation of blocks. Nevertheless, with deformable blocks, block deformations (strains) need to be considered in the governing differential equations. The computational cost thus increases due to increasing the number of degrees of freedom in the system (O'Sullivan 2011; Cundall and Hart 1992; Cundall and Strack 1979). Two-dimensional (2D) DEMs that use arbitrary polygons were developed by Cundall (1980), Cundall and Hart (1985), and Walton (1980) (Morris et al. 2003), and three-dimensional (3D) DEMs or DEMs with rigid or deformable polyhedra were established by Cundall (1988) and Hart et al. (1988) (Morris et al. 2003). The most prevalent software based on DEMs are the universal distinct element code (UDEC) and the 3D distinct element code (3DEC) (Board 1989; Itasca 2000).

In a DEM, contact detection and contact resolution are two stages that are considered to determine the interaction between blocks. Firstly, a series of calculations are performed to find the blocks or particles that are in contact with each other. Next, separate calculations identify the force contacts between rigid or deformable blocks. The integral of the real stresses or tractions acting along a physical contact expresses the contact forces in a DEM model. A combination of springs, sliders, and dashpots act at the contact points between particles, allowing only forces to be transmitted. The resulting inter-particle forces are separated into their two orthogonal components, normal and tangential to the contact point (O’Sullivan 2011).

As explained in Chapter 3, the distinct-element method (DEM) formulation and framework are implemented in the code developed for this research.

### **2.6.2.1 Discrete Element Method (DEM) formulation**

Based on the literature review, the method selected for this research is the distinct-discrete element method (DEM) proposed by Cundall and Strack (1979), which has been widely used to simulate geotechnical and rock mechanics problems. The unique capability of this numerical method is in describing rock behavior as the mechanical behavior of assemblies of discs and spheres.

In DEM, the specification of geometry and properties of materials are not as straightforward as in continuum methods (Itasca 2004). While the generation of particles in a domain geometry is a prerequisite of a DEM simulation, there is no unique way to produce and to compact particles. Several methods have been developed to generate and compact particles for use in a DEM simulation, including geometric methods and dynamic methods; however, some of these methods are time-consuming and they affect the operation of DEM simulation (Zsaki 2009).

The physical process of compacting in a DEM method must be followed until the required porosity is reached. The initial stress is dependent upon the initial packing and the contact forces between particles, so it cannot reach the appropriate level unless the packing procedure is conducted properly (Itasca 2004).

The mechanical behavior of rocks can be simulated via the DEM. Many features of rock behavior can be reproduced using this method including fracturing, crack propagation, rock softening and dilation, post-peak softening and strength increase with confinement, anisotropic rock behavior in the damaged zone, dissipation, and Coulomb failure envelope (Potyondy and Cundall 2004;

Fakhimi and Villegas 2007). However, this method required the appropriate micro properties to result in a synthetic material with ideal macromechanical properties, such as Young's modulus, Poisson's ratio, tensile strength, and the failure envelope (Fakhimi and Villegas 2007). The correct macroproperties of the rock material identified through laboratory tests rely on calibrating microproperties in advance (Shi et al. 2019).

Several researchers have investigated the relationship between the macro and micro properties of rocks for calibrating discrete element methods. A particle-flow code (PFC2D and PFC3D) was used to establish a bonded-particle model (BPM) to simulate rocks and describe the relationships between micro and macroparameters (Hsieh et al. 2008) and (Potyondy and Cundall 2004). Benvenuti (2016) used an artificial neural network to identify discrete element parameters. Rackl et al. (2016) utilized a systematic optimization process for the overall calibrated workflow of the discrete element model with experimental data. A trial-and-error calibration method has been selected based on uniaxial compression tests (UCS) conducted in this research; however, this method is tedious and requires a rigorous calibration procedure and a process of trial and error (Shi et al. 2019)

In this method, the distinct particles that make up a model can move independently from one another, and the interaction between particles is only at the contacts and interfaces. By considering particles as rigid and contacts between particles as soft, the mechanical behavior of such a system is indicated by the movement of each particle and the forces resulting from each contact point. The fundamental relation between particle motion and forces is based on Newton's laws of motion. The complex behavior can be simulated by bonding particles to each other at the contact points. Whenever the acting force at the contact points goes beyond the bond strength, that bond is broken. In this way, tensile forces can progress between particles. As a result, cracks, which cause blocks to fragment into smaller blocks, can be modeled.

In the DEM, particle interactions are based on a dynamic process; when the internal forces are balanced, the system achieves a state of equilibrium. A time-stepping algorithm, in which the velocities and accelerations are constant within each time step, is used to represent the numerical dynamic behavior using an explicit time-difference scheme. The selected time step should be sufficiently small that disturbances cannot propagate further than immediate-neighbor particles. The calculation cycle in this method consists of the law of motion for each particle and the force-displacement law for contacts between particles. These particle contacts can be broken or reformed



as needed. These particle contacts can be broken or reformed again if necessary. The calculation cycle is repeated iteratively to simulate the behaviour of a system of particles over time. The fundamental description of the calculation cycle, presented in Figure 2-13, is as follows (PFC3D 2016):

1. Model Initialization;
2. Contact detection;
3. Contact force determination;
4. Total force update; and
5. Application of Newton's laws of motion

#### **2.6.2.2 Model initialization**

Particle radii can be distributed uniformly or randomly within a model. In addition, a clump, which is a rigid body comprised of particles, can be used to make composite particles in special cases. If the density of particles is not sufficient to achieve the behavior of a simulated solid material, the particle size can be changed to achieve the prescribed porosity.

#### **2.6.2.3 Contact detection**

Contact detection is a step to find contact pairs between particles. A contact takes place between particles, called particle-particle contacts, or between particles and boundaries, called particle-boundary contacts (Figure 2-13). Two particles are assumed to contact when they have an overlap. The existence of overlap, which determines a relative normal displacement, must be verified to detect contact pairs.

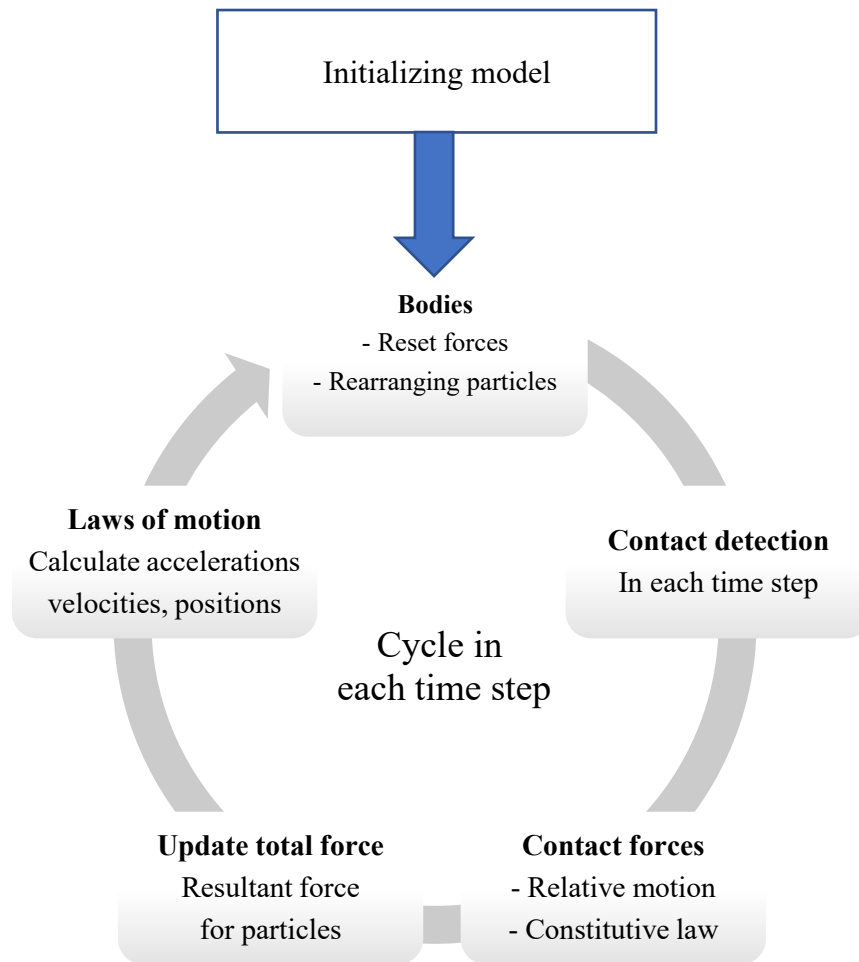


Figure 2-13: Plot illustrating the calculation cycle for the discrete element method

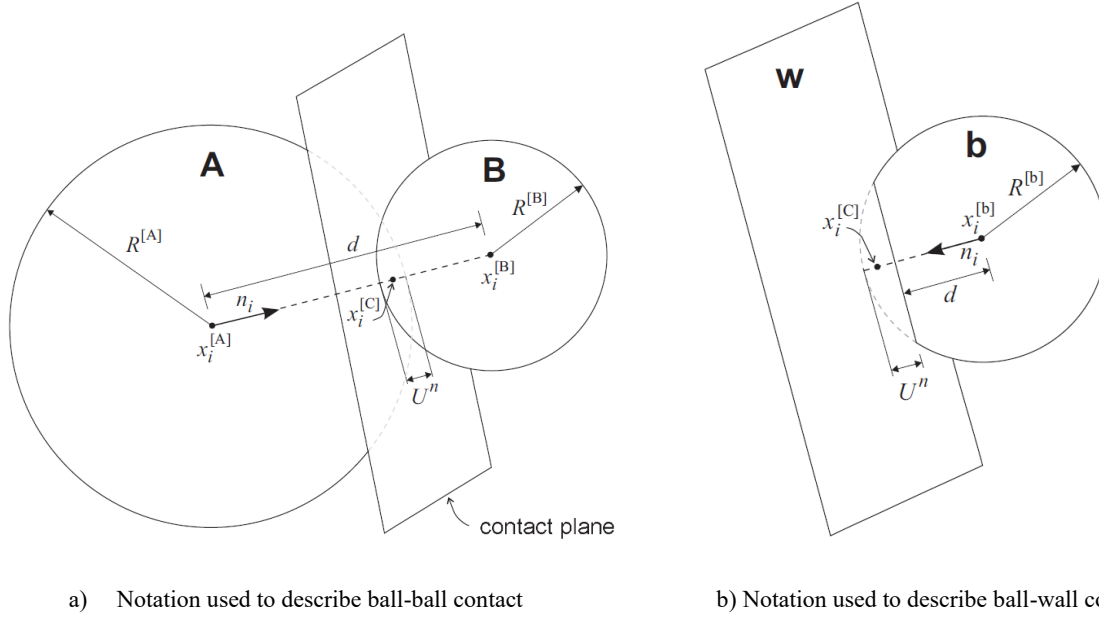


Figure 2-14: Contact notation (a): particle-particle contact, (b): particle-boundary contact (Itasca 2004).

Overlap or contact penetration,  $U^n$ , is defined by equation (2-5) (PFC3D 2016):

$$U^n = \begin{cases} R^{[A]} + R^{[B]} - d, & (\text{particle} - \text{particle}) \\ R^{[b]} - d, & (\text{boundary} - \text{particle}) \end{cases} \quad (2-5)$$

where,  $U^n$  is the magnitude of normal overlap,  $R^{[A]}$  and  $R^{[B]}$  are radii of particles A and B,  $R^{[b]}$  is the particle radius for particle-boundary contact, and  $d$  is the distance between particle centers. The location of a contact point can be determined by equation (2-6):

$$x_i^c = \begin{cases} x_i^{[A]} + (R^{[A]} - \frac{1}{2}U^n) n_i, & (\text{particle} - \text{particle}) \\ x_i^{[b]} + (R^{[b]} - \frac{1}{2}U^n) n_i, & (\text{boundary} - \text{particle}) \end{cases} \quad (2-6)$$

where  $x_c^i$  ( $i = 1, 2, 3$ ) indicates the contact point coordinate,  $x_i^A$  ( $i = 1, 2, 3$ ) indicates the coordinate of the center of particle A for a particle-particle contact,  $x_i^b$  ( $i = 1, 2, 3$ ) indicates the

coordinate of the particle center at a particle-boundary contact, and  $n_i$  is the normal unit of a contact plane.

The unit vector,  $n_i$ , for particle-particle contact is introduced by equation (2-7):

$$n_i = \frac{x_i^B - x_i^A}{d} \quad (\text{particle} - \text{particle}) \quad (2-7)$$

where  $x_i^A$  ( $i = 1, 2, 3$ ) denotes the coordinate of the center of particle A at particle-particle contact,  $x_i^B$  ( $i = 1, 2, 3$ ) denotes the coordinate of the center of particle B at particle-particle contact.

#### 2.6.2.4 Contact force determination

The contact force vector,  $F_i$ , which represents the interaction between two particles that can be decomposed into normal and shear constituents by equation (2-8) (PFC3D 2016):

$$F_i = F_i^n + F_i^s \quad (2-8)$$

where,  $F_i^n$  refers to the normal component force vector and,  $F_i^s$  refers to the shear component force vector.

Normal contact force is calculated by equation (2-9):

$$F_i^n = K^n U^n n_i \quad (2-9)$$

where,  $K^n$  is the normal contact stiffness,  $U^n$  is the normal contact penetration,  $n_i$  is the unit normal of the contact plane.

A shear contact force is calculated in an incremental manner; in each time step, the elastic shear force, which is generated due to the relative shear-displacement increment is added to the current value. Also, the motion of the contact plane is essential to be reflected in this process.

The shear contact force vector  $F_s^i$ , which is stored as a force vector in global coordinates, must be updated based on the new position of the contact plane in each new step. Therefore,  $F_s^i$  needs two

rotations. Equations (2-10) and (2-11) demonstrate the rotation of a line common to the old and new contact planes, and about the new normal direction, respectively (PFC3D 2016):

$$\{F_i^S\}_{rot.1} = F_j^S (\delta_{ij} - e_{ijk} e_{kmn} n_m^{[old]} n_n) \quad (2-10)$$

where,  $\{F_i^S\}_{rot.1}$   $i = (1, 2, 3)$  denotes an updated shear force vector in global coordinates due to rotation about a line common to the old and new contact planes,  $n_m^{old}$  represents the old unit normal to contact plane

$$\{F_i^S\}_{rot.2} = \{F_j^S\}_{rot.1} (\delta_{ij} - e_{ijk} \langle \omega_k \rangle \Delta t) \quad (2-11)$$

where,  $\{F_i^S\}_{rot.2}$   $i = (1, 2, 3)$ , denotes an updated shear force vector in global coordinates due to rotation about the new normal direction in the current step,  $\langle \omega_k \rangle$  is the average angular velocity of the two contact pairs in the new normal direction according to equations (2-12) and (2-13) (PFC3D 2016):

$$\langle \omega_k \rangle = \frac{1}{2} (\omega_j^{[\Phi^1]} + \omega_j^{[\Phi^2]}) n_j n_i \quad (2-12)$$

$$\{\Phi^1, \Phi^2\} = \begin{cases} \{A, B\}, & (particle - particle) \\ \{b, w\}, & (particle - boundary) \end{cases} \quad (2-13)$$

where  $\omega_i^{[\Phi^j]}$  is the rotational velocity of the entity  $\Phi^j$ .

The contact shear component force for each step is determined by summing the old shear force vector at the start of a time step, which was updated by considering the contact plane in the current step, with the shear elastic force-increment vector by equation (2-14) (PFC3D 2016):

$$F_i^S = \{F_i^S\}_{rot.2} + \Delta F_i^S \quad (2-14)$$

Where  $\Delta F_i^S$  is the shear elastic force-increment vector which is calculated by equation (2-15) (PFC3D 2016):

$$\Delta F_i^S = -k^S \Delta U_i^S \quad (2-15)$$

where  $k^s$  is the shear stiffness,  $\Delta U_i^s$  is the shear component of contact displacement-increment vector over a time step calculated by equation (2-16) (PFC3D 2016):

$$\Delta U_i^s = V_i^s \Delta t \quad (2-16)$$

where  $V_i^s$  denotes the shear component of contact velocity.

The contact velocity is composed of normal and shear components with respect to the contact plane. The shear component of contact velocity can be determined by (2-17) (PFC3D 2016):

$$V_i^s = V_i - V_i^n = V_i - V_j n_j n_i \quad (2-17)$$

where  $V_i^s$  and  $V_i^n$  are shear and normal components of contact velocity, respectively and  $V_i$  is contact velocity which is determined by (2-18) (PFC3D 2016):

$$\begin{aligned} V_i &= \left( \dot{x}_i^{[c]} \right)_{\Phi^2} - \left( \dot{x}_i^{[c]} \right)_{\Phi^1} \\ &= \left( \dot{x}_i^{[\Phi^2]} + e_{ijk} \omega_j^{[\Phi^2]} (x_k^{[c]} - x_k^{[\Phi^2]}) \right) - \left( \dot{x}_i^{[\Phi^1]} + e_{ijk} \omega_j^{[\Phi^1]} (x_k^{[c]} - x_k^{[\Phi^1]}) \right) \end{aligned} \quad (2-18)$$

where,  $\dot{x}_i^{[j]}$  represents the transitional velocity and  $\omega_i^{[\Phi^j]}$  is the rotational velocity of the entity  $\Phi^i$  from Eq. (3.9).

### 2.6.2.5 Total force update

The resultant force and moment on the two entities in contact are accomplished by adding the final contact force in each time step. Equation (2-19) shows these relations (PFC3D 2016):

$$\begin{aligned} F_i^{[\Phi^1]} &\leftarrow F_i^{[\Phi^1]} - F_i \\ F_i^{[\Phi^2]} &\leftarrow F_i^{[\Phi^1]} + F_i \\ M_i^{[\Phi^1]} &\leftarrow M_i^{[\Phi^1]} - e_{ijk} (x_j^{[c]} - x_j^{[\Phi^1]}) F_k \end{aligned} \quad (2-19)$$

$$M_i^{[\Phi^1]} \leftarrow M_i^{[\Phi^1]} + e_{ijk}(x_j^{[c]} - x_j^{[\Phi^1]})F_k$$

where,  $F_i^{[\Phi^j]}$  and  $M_i^{[\Phi^j]}$  denote the force and moment sums for the entity  $\Phi^j$ .

### 2.6.2.6 Application of Newton's Laws of motion

Newton's Second Law of motion states the relation between force and an object's acceleration by equation (2-20).

$$\sum F = ma \tag{2-20}$$

where  $m$  is the mass of the object (in our case, a particle);  $a$  is the acceleration of a particle; and  $\sum F$  is the resultant of forces acting on a particle. Should the inclusion of damping forces be necessary, a damping-force term is incorporated into the equations of motion.

By applying Newton's Second Law of motion, the translational and rotational accelerations for each particle at time  $t$  with respect to the Cartesian coordinate system are realized using equations (2-21) and (2-22), respectively (PFC3D 2016):

$$x_i^{(t)} = \frac{1}{\Delta t} (\dot{x}_i^{(t+\Delta t/2)} - \dot{x}_i^{(t-\Delta t/2)}) \tag{2-21}$$

$$\omega_i^{(t)} = \frac{1}{\Delta t} (\dot{\omega}_i^{(t+\Delta t/2)} - \dot{\omega}_i^{(t-\Delta t/2)}) \tag{2-22}$$

where,  $x_i^{(t)}$  ( $i = 1, 2, 3$ ) represents the translation acceleration at time  $t$ .  $\omega_i^{(t)}$  ( $i = 1, 2, 3$ ) represent the rotational acceleration at time  $t$ .

Integration of acceleration results in transitional and rotational velocity at time  $t + \Delta t/2$ , equations (2-23) and (2-24) are used (PFC3D 2016):

$$\dot{x}_i^{(t+\Delta t/2)} = \dot{x}_i^{(t-\Delta t/2)} + \left( \frac{F_i^{(t)}}{m} + g_i \right) \Delta t \tag{2-23}$$

$$\dot{\omega}_i^{(t+\Delta t/2)} = \dot{\omega}_i^{(t-\Delta t/2)} + \left( \frac{M_i^{(t)}}{I} \right) \Delta t \tag{2-24}$$

The position of the center of the particles can be calculated by the transitional velocity obtained by equation (2-25). Finally, the position of the particles is updated by equation (2-25).

$$x_i^{(t+\Delta t)} = x_i^{(t)} + \dot{x}_i^{(t+\Delta t/2)} \Delta t \quad (2-25)$$

Obtaining the demanded porosity without considering the stress level is not meaningful in the geotechnical field. Therefore, a compacting phase is necessary to produce initial stress states. The meaning of stress in a discontinuous medium is different from that in a continuum and an estimate of stress is only possible over a finite volume of space. The average stress tensor  $\bar{\sigma}_{ij}$  in volume  $V$  of material, is defined by (2-26) (Itasca 2004):

$$\bar{\sigma}_{ij}^{(p)} = -\frac{1}{V^{(p)}} \sum_{N_c} x_i^{(c)} F_j^{(c)} \quad (2-26)$$

where,  $x_i^{(c)}$  denotes the location and  $F_j^{(c)}$  denotes the force, acting at contact (c);  $N_c$  denotes the number of contacts in a measurement volume;  $V^{(p)}$  denotes the measurement volume.

$$x_i^{(c)} = x_i^{(p)} + |x_i^{(c)} - x_i^{(p)}| n_i^{(c,p)} \quad (2-27)$$

where  $x_i^{(p)}$  is the location of a particle's centroid; and  $n_i^{(c,p)}$  is the unit-normal vector directed from the particle centroid to the contact location.

### 2.6.3 Discontinuous Deformation Analysis (DDA)

The Discontinuous Deformation Analysis (DDA) method is a numerical modeling method in the family of DEM methods and uses an implicit solution method. A backward analysis to determine a DDA was presented by Shi and Goodman to back-calculate the best fit for the deformed geometry of block systems from measured displacements and strains (Shi and Goodman 1985). The DDA technique has rapidly become a numerical method for many applications and as a result, some of its limitations have been resolved, making it a much more efficient method. For instance, Hu et al. (2020) simulated the fracture propagation and rock mass deformation by considering the fluid flow within fractures (Hu et al. 2020).



The DDA method is comparable in features to the finite element method (FEM). The formulation of the DDA blocks is very close to the mesh of the FEM, but blocks are isolated and bounded by pre-existing discontinuities.

The basis of the DDA approach is a system of autonomously deformable blocks that can translate independently without interpenetration. The geometry of blocks that are used in DDA can be assumed to be any shape (convex or concave), so there is no concern about topology determination as there is with the FEM (Jing 1998).

By using the second law of thermodynamics, a mechanical system must have movements or deformations in order to reach the minimum total energy, which consists of potential and kinematic energy, for the whole system under any external and internal load conditions. Equations of motion of a system are driven by minimizing the system energy, part of the so-called energy minimization principle, as applied in FEM (Jing and Stephansson 2007). The energy minimization principle is the fundamental method to govern equations in the DDA (Wu et al. 2005).

In the DDA, a penalty-based contact system is employed to deal with contacts between blocks. This system employs an impenetrability constraint, which prevents blocks from having overlap or interpenetration with each other. When blocks are in contact, Coulomb's law controls the contact interface, and simultaneous equilibrium equations are formed and solved at each loading or time increment. Lin and Amadei applied the augmented Lagrangian method instead of the penalty method and achieved satisfactory results (Lin et al. 1996).

Al-Zahrani presented a hybrid numerical model that combined the DDA with the BEM, in which the DDA was used to numerically simulate the near field behavior and the BEM was employed to model the behavior of the far field (Al-Zahrani 2000).

#### **2.6.4 Hybrid Methods**

Rock is a natural geological material that is formed by complex processes. Rock masses have many discontinuities such as bedding planes, joints, shear zones and faults. These characteristics make each rock mass a combination of continuous and discontinuous materials.

As described before, numerical modeling methods fall into three categories: continuum, discontinuum and hybrid. The Finite Element Method (FEM) and the Finite Difference Method (FDM) are very well-developed methods to model continuum materials, while the DEM and DDA model the discontinuum behavior. The last category, hybrid numerical methods, models the

complexity of rock masses by combining continuum and discontinuum methods. The Finite-Discrete Element Method (FDEM) is a hybrid numerical simulation method that combines features of both the FEM and the DEM (Munjiza 2004). Deformability can be described based on a continuum formulation that is applied in FEM, while the interaction and motion of the particles can be described in the DEM approach, based on discontinuum formulations. Therefore, the FDEM is a suitable approach for modeling in a range of fields, especially in rock mechanics. This model can be used in discontinuous cases where the particles are deformable, and fractures and fragments can occur. The FDEM has the advantages of the FEM in defining elastic deformations, combined with the capabilities of the DEM in modeling interaction and fracturing processes. In the FDEM, each block in the body interacts with other particles based on the formula for the discrete element method. In addition, each block has its own finite element mesh to model the deformability according to continuum-based phenomena (Munjiza 2004).

## **2.7 Application of numerical modeling for rock slope stability**

Distinct element methods have been applied to study block toppling (Cundall 1971; Cundall et al. 1978). Ishida used a DEM method which is fundamentally the same as that of Cundall (1971) in a real example of block toppling (Ishida et al. 1987).

The numerical manifold method (NMM) was used to simulate toppling failure for rock slopes including rock bridges and high discontinuities. The process of toppling not only includes the opening of pre-existing joints and the sliding of existing structures, but also the shear and tensile failure of rock bridges and the failure of intact rock masses, as they all have effective roles in toppling failure mode (Zhang et al. 2010). The safety factor is also affected by both the length of existing cracks in rock columns and the joint persistence. According to the principle of fracture mechanics, the rock columns fail due to high-stress concentration at the crack tips when the length of cracks goes beyond the critical length (Majdi and Amini 2011). The deformation of rock masses and the stress introduced by this deformation affect the failure process. Therefore, numerical methods should not only consider the opening and sliding along the existing joints, which complies with Mohr–Coulomb failure criteria, but also be able to mimic the deformation and failure of the intact rock mass.

Pritchard and Savigny (1990) conducted numerical modeling of the flexural toppling of layered rock slopes by applying the distinct element method (UDEC). The aim of their simulation was to determine that the UDEC could evaluate the flexural toppling deformation and study various scales of the morphology of flexural toppling. They concluded that the distinct element method (UDEC), unlike the finite element method, can simulate flexural and blocky toppling. However, the layering in their case study was formed by continuous joints, and tensile rupture was not considered across the layers (Pritchard and Savigny 1990).

UDEC was not designed to consider isolated joints or to evaluate the propagation of a crack in intact rock (Alzo'ubi et al. 2010). Alzo'ubi et al. (2010) developed the UDEC damage model (UDEC-DM) to overcome the limitations of conventional UDEC. To create a rupture surface through the flaws in the intact rock that describes grain boundary or internal flaws, UDEC-DM produces random polygons that make a pattern that is similar to that of the flaws, generated with the help of Voronoi tessellation. The polygonal block pattern simulates shear and/or tensile fracture in blocks. By assigning cohesion, friction, and tensile strength to the boundary of these polygonal blocks, the same strength as the intact rock can be provided in the simulation.

Alzo'ubi et al. (2010) compared two centrifuge tests with the discrete element method (UDEC) with and without a damage model (UDEC-DM) in a homogenous slope with continuous joints and in a heterogeneous slope with discontinuous joints. The size of the model was selected as that of Adhikary's experiment, along with the shear strength and deformation properties as those in Adhikary's experiments. They stated that the UDEC had better results than the FEM; results for the homogenous slope show that while the conventional UDEC correctly estimated the maximum displacement, the results could not capture the behavior of the centrifuge test and the failure surface was not accurate. Moreover, displacements were underestimated, and the failure load was greater than the experimental test results. The UDEC based on a damage model had a better agreement with centrifuge test results rather than the conventional method, and it captured many aspects of the test results besides those of the peak load. Alzo'ubi et al. also stated that tensile strength is a key factor in toppling failure. This factor can change the progress of failure in the case of flexural toppling. Their investigation showed that tensile strength determines the failure load in flexural toppling, and that the friction angle of intact rock did not have an important role in the toppling failure mechanism (see Figure 2-15) (Alzo'ubi et al. 2010).

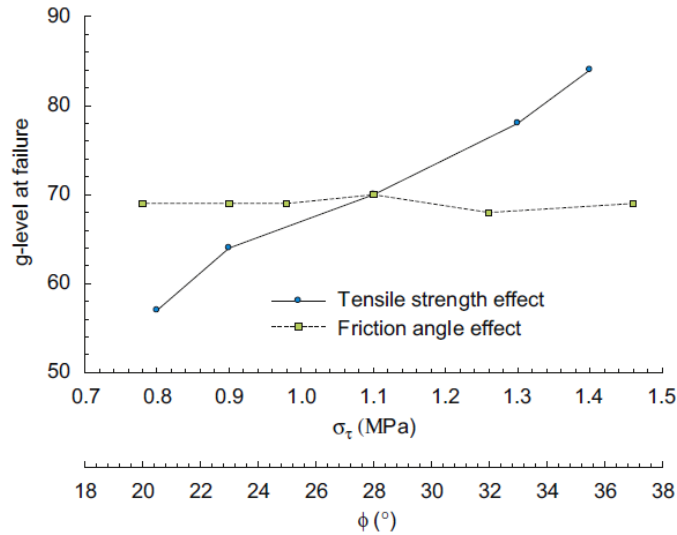


Figure 2-15: Tensile strength and friction angle effects on the failure load (Alzo'ubi et al. 2010)

Alzo'ubi et al. (2010) reported that the tensile strength controls the rupture load, and that the tensile strength has no influence on the position of a rupture surface. They considered 15 kPa for an apparent cohesion to match the numerical results with the centrifugal test results. The low confinement frictional behavior, which causes a nonlinear behavior, justified using an apparent cohesion intercept in linear Mohr-Coulomb space. The failure surface, deformation patterns, and failure load were affected by the apparent cohesion of the bedding planes.

In addition, the results of UDEC and UDEC-DM approaches for the heterogeneous slope revealed that the conventional discrete element method, UDEC, could not adequately simulate the rupture surface and the gravitational load obtained from Zhang's centrifuge test, while the UDEC-DM did accurately capture the deformation and the location of the rupture surface and the failure load, obtained according to the centrifuge test failure load. Moreover, in heterogeneous slopes, the tensile strength plays an important role in the collapse load, although no effect on the rupture surface location was found (Alzo'ubi et al. 2010).

Lian et al. (2017) applied the distinct lattice spring model (DLSM) to study toppling failure of a jointed rock slope. To consider the loading condition of a centrifuge test, the gravity increase method (GIM) was used in the DLSM. In their study, all the parameters of Adhikary and Dyskin's centrifuge test were directly applied to the model. The macroscopic joint parameters were applied directly, and the only adjustable parameter was the tensile strength of rock blocks. The limitation of this method is that a large deformation problem, associated with this type of constitutive

modeling applied, cannot be solved. Therefore, the focus of this research is on fractures of the jointed slope under small deformation (Lian et al. 2017; Zhao 2015). In addition, their results were compared with those of Alzo'ubi et al. (Lian et al. 2017). Figure 2-16 shows the comparison between the failure patterns for Lian et al.'s model and experimental results and Alzo'ubi et al.'s numerical simulation. The results show that the GIM-DLSM approximates the failure pattern of Alzo'ubi et al.'s numerical simulation. Lian et al. also claimed that the displacement at two measurement points of the model was close to the experimental test values (Lian et al. 2017). However, the g-level of failure load shows a large difference. Lian et al. (2017) studied the influence of some parameters on flexural toppling failure of a jointed rock slope. They concluded that the deformation of a jointed rock slope could be affected by both the g-level and the fracture surface. The failure pattern of the surface rupture is not sensitive to the tensional strength of rock blocks. The deformation history of measurement points can be used to calibrate the tensional strength of a jointed rock slope. In terms of joint cohesion, when the cohesion is increased, the deformation and failure angle of a jointed rock slope also increase; however, the variation of the failure angle of a jointed rock slope was too small and the deformation was different. Therefore, it was not possible to calibrate the joint cohesion by using the rupture pattern of toppling failure. In addition, joint cohesion and joint spacing have a slight influence on the flexural toppling of jointed rock slopes, whereas joint friction angle and joint angle had significant effects on their displacements and failure paths (Lian et al. 2017).

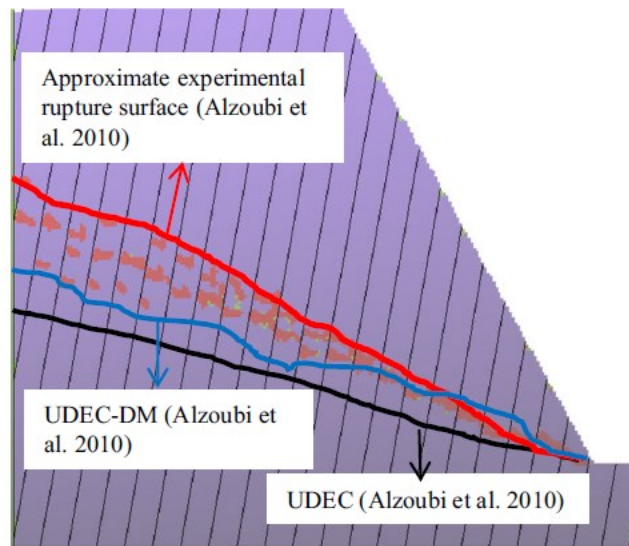


Figure 2-16: Comparison of the failure patterns predicted (Lian et al. 2017).

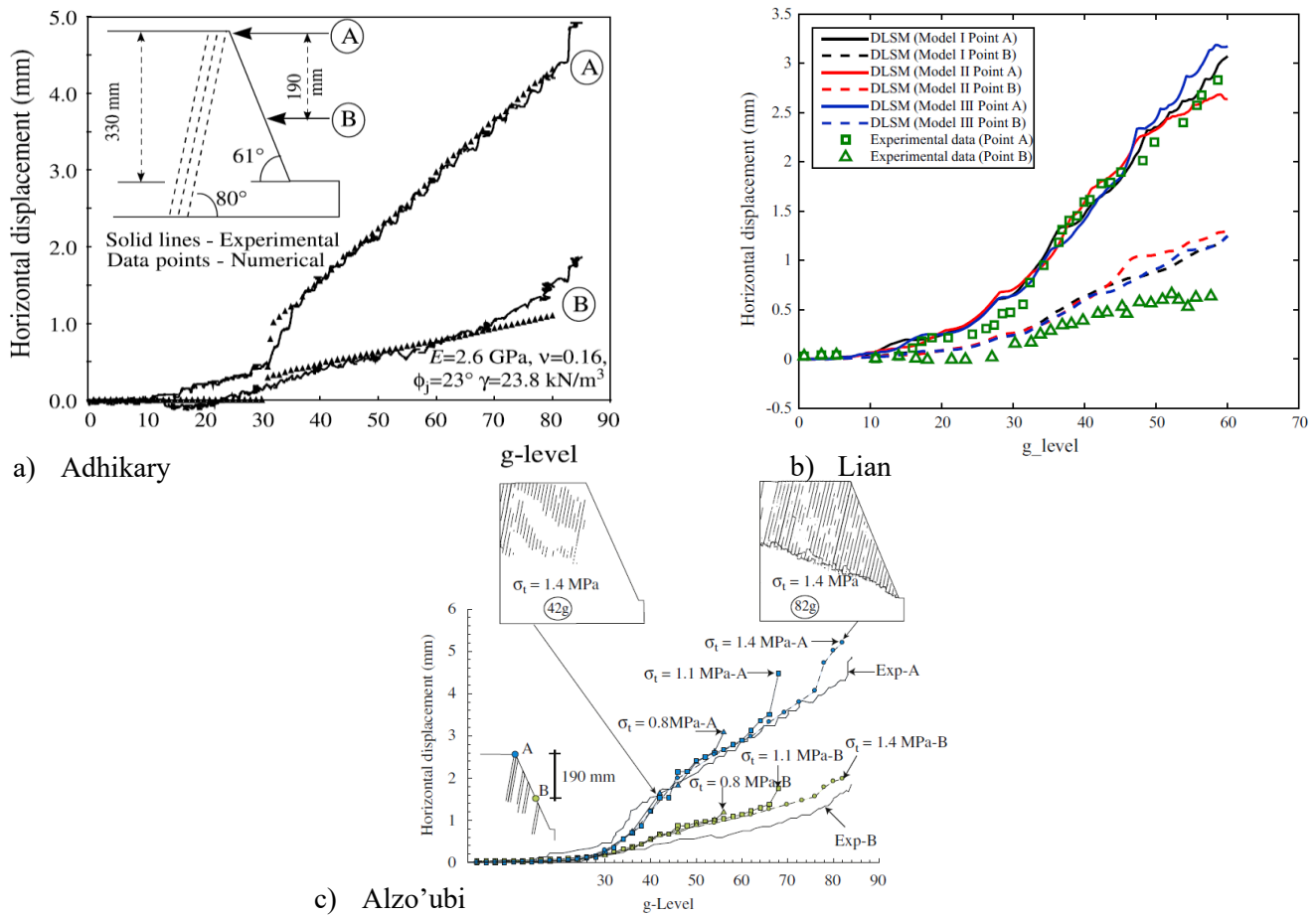


Figure 2-17: Horizontal displacements at the two monitoring points versus g-level. a) Adhikary and Dyskin's centrifuge test and FEM results; b) Lian et al.'s numerical test results; and c) Alzo'ubi et al.'s numerical test results (Adhikary and Dyskin 2007; Lian et al. 2017; Alzo'ubi et al. 2010).

A discrete numerical method, covering both the hard-particle model and the soft-particle model, was used to simulate the failure behavior of intact rock material (Meng et al. 2018). Meng et al. (2018) also used Adhikary and Dyskin's experimental centrifuge test to validate their numerical methods. The results of their numerical method were compared with the work of two other researchers, as outlined above in Figure 2-18. As illustrated in Figure 2-18(a), displacements gradually increase in the initial stage where the g-level loading is small. After reaching a particular level of gravity loading, the displacement of point A increases drastically as the bonding between joints fails and makes the layers detach (Meng et al. 2018). With this method, horizontal displacements had a good agreement with experimental results; however, joint failure occurs at an earlier stage, and the maximum g-level of load failure was different from the experimental load

failure value. Figure 2-18(b) shows a comparison of the failure patterns formed by different methods and the experimental surface failure (Meng et al. 2018).

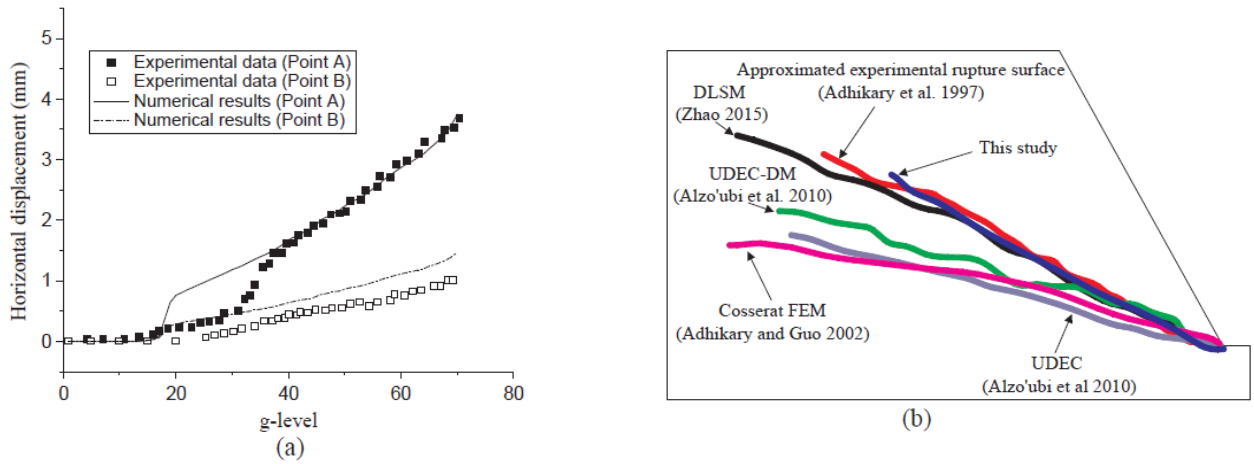


Figure 2-18: Numerical results for the jointed slope showing (a) displacements of two monitoring points, (b) the corresponding failure surface (Meng et al. 2018).

Scholtès and Donzé (2012) used a 3D discrete element method to simulate progressive failure in fractured rock mass in order to consider coupled mechanics related to deformation along existing discontinuities and brittle fracture of intact rock masses. By means of this method, both mass strength degradation and progressive failure mechanisms in rock bridges could be considered. Incorporating discrete fracture networks with discrete elements can be used to imitate intact rock fracturing and the yielding of discontinuities. This method can be used to simulate a rock slope failure involving a complex interaction between pre-existing discontinuities and the brittle fracturing of intact rock. Scholtes and Donze also tried to simulate flexural toppling in a 3D scenario, and sought to confirm their results with an essential condition, stated by Goodman and Bray, based on a simple kinematic analysis to result in a flexural toppling failure.

The following relationship, as a necessary condition to assess flexural slip, was established by Scholtes and Donze (2012):

$$\alpha > 90^\circ + \phi_j - \beta \quad (2-28)$$

where  $\alpha$  is the slope angle,  $\phi_j$  is the joint frictional angle and  $\beta$  is the foliation angle. For toppling to occur, shear displacement must happen at the face-to-face contacts on the front and back faces of the blocks. Sliding on these faces will take place if certain conditions are met. Near the slope face, the stress state must be uniaxial, with the normal stress  $\sigma$  oriented parallel to the slope face. When the layers slip past one another,  $\sigma$  needs to be inclined at an angle  $\phi_j$  relative to the normal of the layers.

Although Scholtès and Donzé's (2012) model considerably agreed with Goodman and Bray's condition, using this model needs to be assessed by further study. In addition, when the method was applied to simulate slope stability in a homogenous intact rock, the failure path could be determined without any assumptions; the induced stress imposed fractures and crack propagation inside the zone where the strength was not sufficient for loads. The extension of the failure across a rock bridge was simulated. This simulation resulted in a complicated interaction between deformation along existing discontinuities and fracture propagation inside intact rock. This simulation was only conducted only for particular joint sets and slope configurations; needless to say, it still merits a further study. Among other factors, the spatial variation of properties of rock masses and a typical distribution of discontinuities have to be sufficiently addressed.

Pinheiro et al. (2015) used UDEC to investigate failure mechanisms in large-scale mine slopes. They studied the influence of stiffness on the geomechanical behavior of discontinuities, and the effect of in situ stress on the failure mechanism. For high values of  $k$ , which represent the vertical stress to horizontal stress ratio, the displacement and separation of the column at the top, which were affected by toppling failure, were extremely large; a prediction that did not match the field observation. This large separation was due (in part) to the in situ confining stresses in the displacement values. Pinheiro et al. also considered the effect of discontinuity stiffness; and found that a flexural toppling occurred for both high and low values of stiffness. However, the failure mechanism was more sensitive to the material deformation than to the influence of discontinuity stiffness.

Dabirmanesh et al. (2024) utilized a particle-based DEM approach to investigate a comprehensive understanding of the stability of rock slopes prone to toppling failures in a real-world slope case and compare the DEM results with those from a prior finite element method (FEM) study. Both FEM and DEM approaches can effectively simulate toppling failure during the initiation and small deformation phases. Though the fundamental processes remain the same, we observed variations



in the magnitude of deformation between models. In the case of slope degradation where large deformations and block separation occur, the DEM more accurately predicts the failure mechanisms (Dabirmanesh et al. 2024)

## Chapter 3. Research methodology, model development, and approach

---

### 3.1 Summary

As stated in Chapter 1, the discontinuum-based simulation must consider the separations between blocks, the movement of blocks, large deformations, and any crack propagations due to the tensile stress having exceeded strength limits. A distinct-element method has therefore been adapted in this study to numerically simulate toppling failure. The distinct-element method (DEM) formulation and framework are discussed in Chapter 2. A Python object-oriented programming (OOP) approach, including several classes, objects, and functions was developed to implement the DEM to simulate toppling failures.

This chapter explores the algorithms used in the discrete element code.

### 3.2 General description and algorithm for model development

#### 3.2.1 The flowchart of the developed DEM code

The overall diagrammatic algorithm of the main DEM code is presented in Figure 3-1. The flowchart represents the general algorithm used in the development of the code to implement a discrete element method for simulating toppling failures.

The developed object-oriented programming (OOP) DEM code (HDPAC) consists of several classes and functions including `grain`, `boundary`, `contact_pair`, `generate_particles`, `define_joint_set_2d_s`, `set_up_bond_contact` and `plot`. The classes contain objects and methods (functions), all denoted with `CourierNew` font. A Class is a blueprint that defines logical data and function grouping, while an Object is the actual instance of the Class. An Object is a collection of data (variables) and methods (functions) that act on those data.

The `grain` Class was introduced to hold the variables described in the particles and made them available to any object.

The `boundary` determines the boundary conditions for the model.

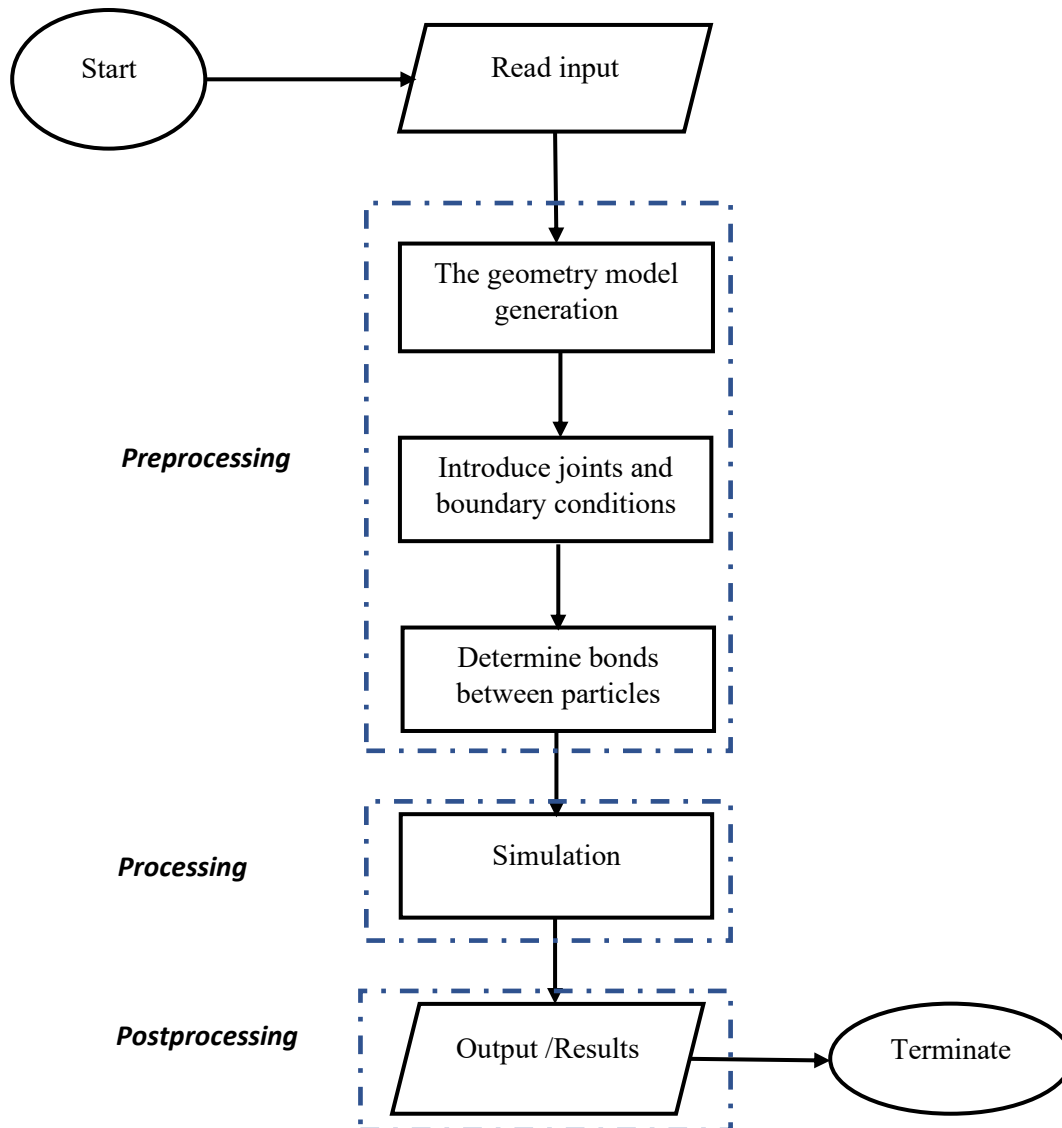


Figure 3-1: Flowchart representation of the main body of the developed HDPAC

The `contact_pair` serves to find the neighboring particles that have contact with each other.

The `generate_particles` function produces the geometry of the model.

The `define_joint_set_2d_s` function defines the pre-existing joints.

The `set_up_bond_contact` function determines the neighbor particles for a particle and assigns the parallel bond to their contact, and the `plot` function provides a plot of particles.

In the following sections, the preprocessing including the geometry model generation, defining joints and boundary conditions, determining bonds between particles, and processing including simulation will be discussed.

### 3.2.2 The geometry model generation

In a DEM, generating particles in a geometry domain is not an easy task. Particle arrangements require considerable time, and the outcome may not be appropriate, such as the need for a particular packing arrangement or the existence of some gaps in the domain. Depending on the problem, different approaches are adopted to create the geometry of the model. The geometry must present the model requirements and it needs to be simple enough to reduce the complexity and time-consuming features of the DEM.

The aim of this research is to simulate and study toppling failure; the block arrangement, dip direction and angle of the joints, and the configuration of the layers all have key roles in the initiation and progression of this failure. The geometry, therefore, is represented by a slope that has a potential for toppling, and the joints and layers must be modelled accordingly. Figure 3-2 shows the required geometry consists of different polygons, which together compose the boundary as well as the layering of rock columns with a toppling failure potential.

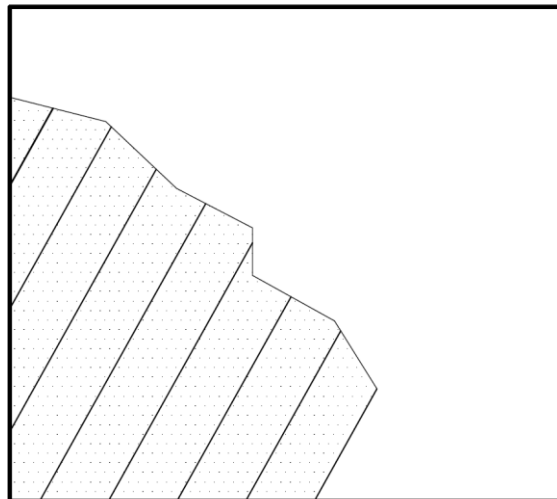


Figure 3-2: Boundaries and geometry needed for the toppling model

To generate a model, the boundary of the model and the geometry of a slope can be created by polygons made with different segments (Figure 3-3). Generating particles in one large polygon and removing contacts and bonds that are close to each joint can produce the desired model (see Figure 3-4). However, in this case, a non-straight line joint leads to a ‘rough’ joint and the results may be affected by the roughness. In another approach, the particles can be generated in polygons between parallel joints, and then a model can be produced (see Figure 3-5) by using the ‘smooth’ joints between polygons.

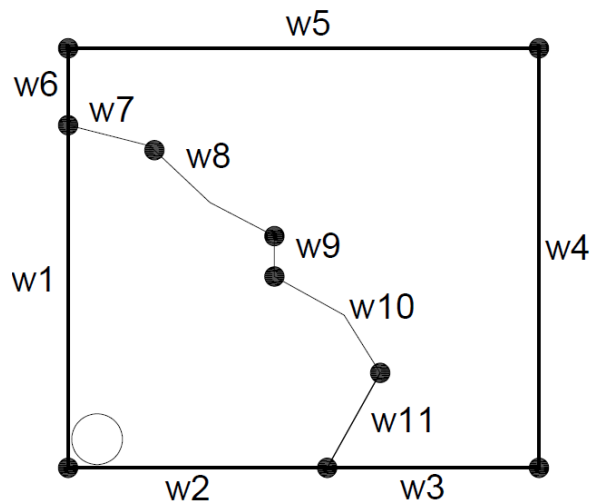


Figure 3-3: Line segments representing the model's boundary and slope geometry

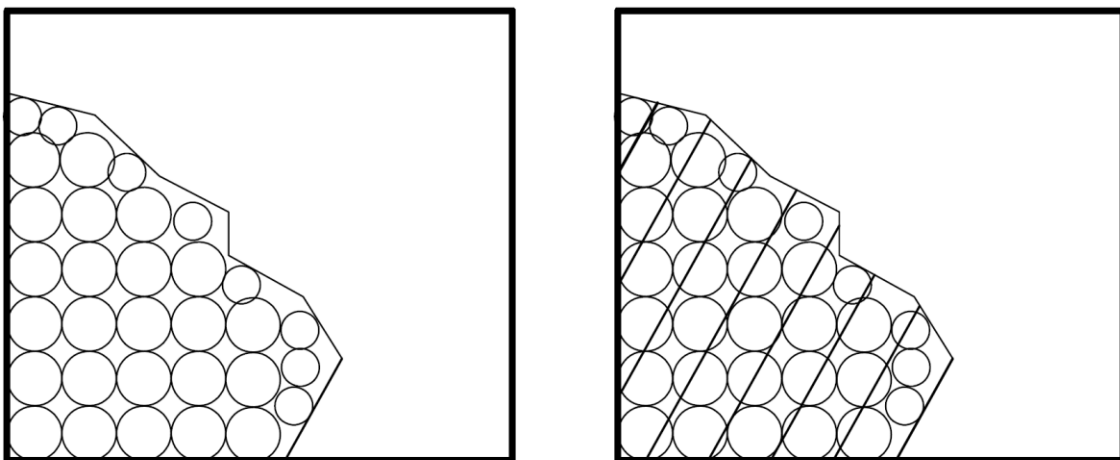


Figure 3-4: (a) Generating particles in one large polygon, (b) Removing contacts and bonds between particles where joints are needed in order to generate layers

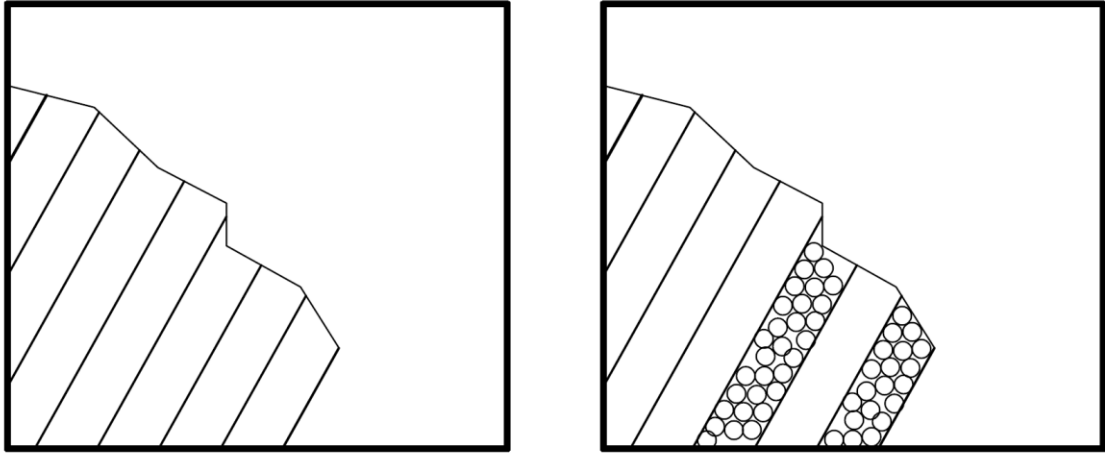


Figure 3-5: Particles generated in polygons between parallel joints

The easiest way to place particles within a specified boundary is to use small initial radii. In this way, the available void spaces are large and so the trial and error processes can be reduced in order to place subsequent particles. The radii of particles are then extended to reach the desirable void ratio. Another method is to create particles at their final radii in numbers that are high enough to achieve the preferred porosity. Therefore, in that method, large overlaps and correspondingly immense forces will occur once the simulation starts, which can lead to instability in the simulation. After filling a domain with particles, the assembly is allowed to reach equilibrium by running the simulation. Afterward, additional particles are injected into the domain to achieve the desired porosity. Figure 3-6 shows the positions of injected particles as they settle due to the gravitational load and the system reaches an equilibrium state.

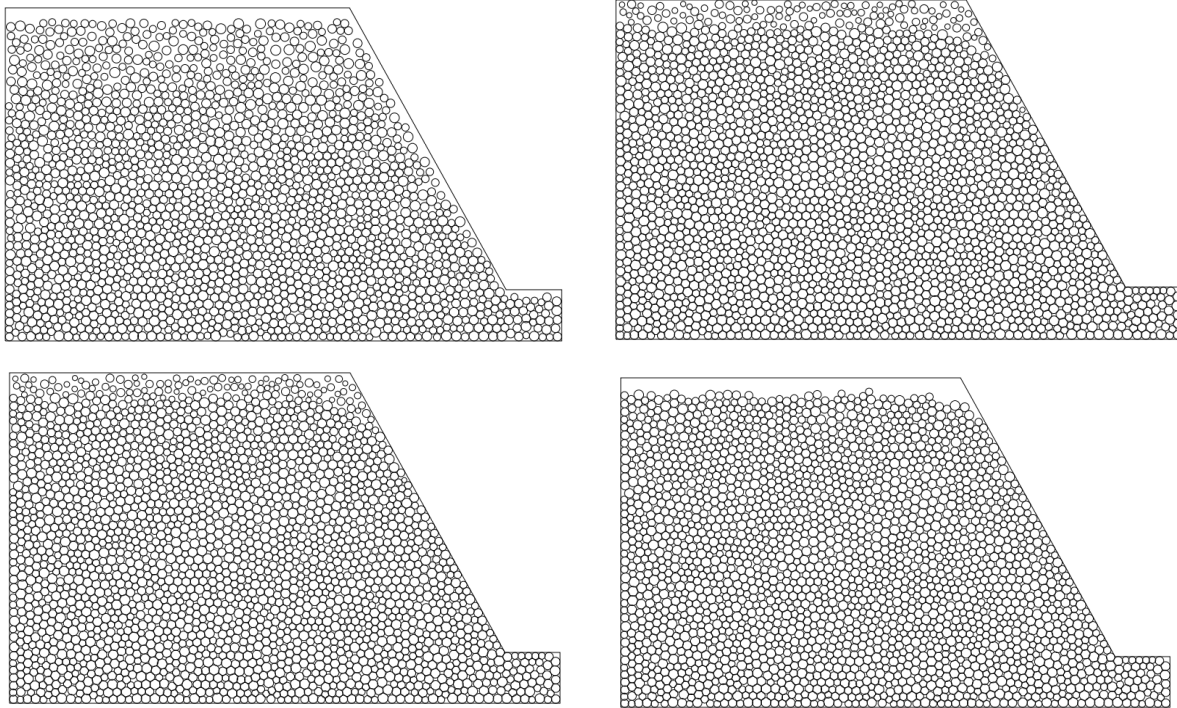
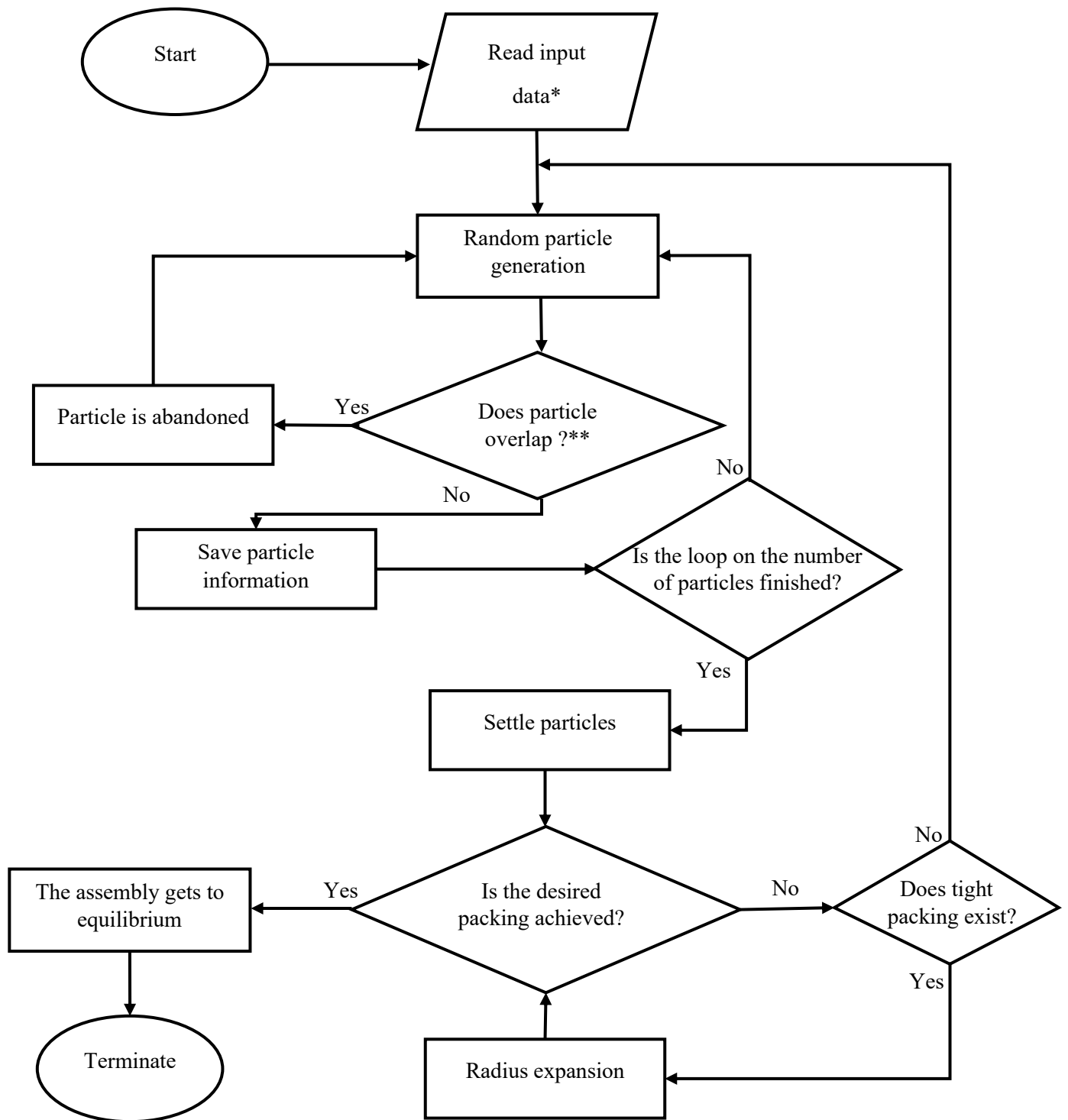


Figure 3-6: The position of the injected particles following settlement due to gravitational load

The processes of filling a domain and compacting the particles to create rock mass and of adding pre-existing joints after the initial preparation of the model require the implementation of different algorithms and coding.

Figure 3-7 illustrates the overall process of generating particles in a domain to produce a model's geometry. The polygonal domain of the geometry is divided into several segments. Each segment is defined by the coordinates of two endpoints. In the first phase, particles are generated with different radii sizes using a random sampling of a distribution function. The uniform distribution function is used to generate particle positions and particle sizes ranging from  $R_{\min}$  to  $R_{\max}$  throughout the domain of the model. However, non-overlapping between particles and between particles and segments of the domain are controlled before generating new particles so that particles can be placed without overlap. If any overlapping occurs, the generation of a new particle will be abandoned. During the next phase, gravity will settle the particles (see Figure 3-6), and the process will be repeated to fill any empty spaces in the predetermined domain. In the final phase, the particle's radii are expanded in order to fill all gaps in the domain, as well as to achieve the desired levels of packing and porosity.



\* Data including segments of the geometry domain and particle properties

\*\* Overlaps any existing particles or segments of the domain

Figure 3-7: Flowchart of the process of generating particles in a domain to produce a model's geometry



### 3.2.3 Introduction of joints and boundary conditions

The presence of pre-existing discontinuities such as joints and bedding planes is defined using a function `define_joint_set_2d_s` in HDPAC.

The `define_joint_set_2d_s` function receives the origin point as a reference point, the orientation of the set joints, and the joint spacing. As an output of the function, it returns the geometry of joints as line segments represented with two endpoints on either side of the line as start and end points. The smooth-joint contact model proposed by Cundall (2005) is then assigned to the particles that are the neighbors of the defined joints. The behavior of all contacts between particles that lie on opposite sides of the joints will be simulated, regardless of the local particle contact orientations along the interface (Ivars et al. 2008).

Similar to continuum numerical modeling, the boundaries of a DEM model must be described numerically, which means that the particles forming the boundaries of a model must be identified and have appropriate boundary conditions assigned to them. In HDPAC, at the beginning of a simulation, functions in the `boundary_2d` are called on to identify particles forming boundaries. Displacement boundary conditions can be determined by fixing or assigning a specific coordination value to selected particles. Determining the force boundary conditions is also achievable by applying a specific force to selected particles forming a boundary. This determination step requires an algorithm to select specific particles forming a boundary. Each boundary is predefined as a segment or segments. The algorithm in `boundary_2d` uses a For Loop over all particles and determines and flags particles in the neighborhood of each segment by considering the pre-defined threshold conditions. The selected particles will be classified and flagged as a specific boundary, and assigned boundary conditions will be assigned. The boundaries are defined with different segments that represent the boundaries of the model. A threshold for noting the distance from segments according to the maximum value of the radius of the largest particle is considered as a means to determine which particles will be selected to be assigned specific boundary conditions.

### **3.2.4 Determine bonds between particles**

The parallel bond presented by Potyondy and Cundall (2004) is used to bond the particles that are located in their neighbors. The `set_up_bond_contact` function determines a particle's neighboring particles and assigns the parallel bond to their contact.

Unless a smooth joint is assigned, the contact between a particle and the particles around it is a parallel bond. Essentially, when two particles have a smooth joint contact, the parallel bond between them will be removed, allowing the smooth joint contact to control the interface's behavior.

### **3.2.5 Simulation**

The flowchart in Figure 3-8 shows the overall framework of HDPAC employed as a numerical approach, including the framework's concept and how each component relates to others. During the initiation phase, the particles' properties, including coordination, radius, mass, velocity, contact forces, and all related information, are assigned. In addition to defining joint properties, particles located near the joints will be defined as well. As explained earlier, boundary conditions also apply to particles forming boundaries. Time steps should be small enough in order to provide a stable simulation, but not so small as to cause computational inefficiency. As bond contacts are assigned, the type of contact may change due to parallel bond breakage during each iteration. The contact detection and resolution must be performed in every iteration as explained in section 3.2.6. The contact acting on the particles, the resultant forces, translational and rotational accelerations, and the particles' velocity and position are updated at each iteration. The procedure is repeated until the accumulated time exceeds the pre-determined maximum time.

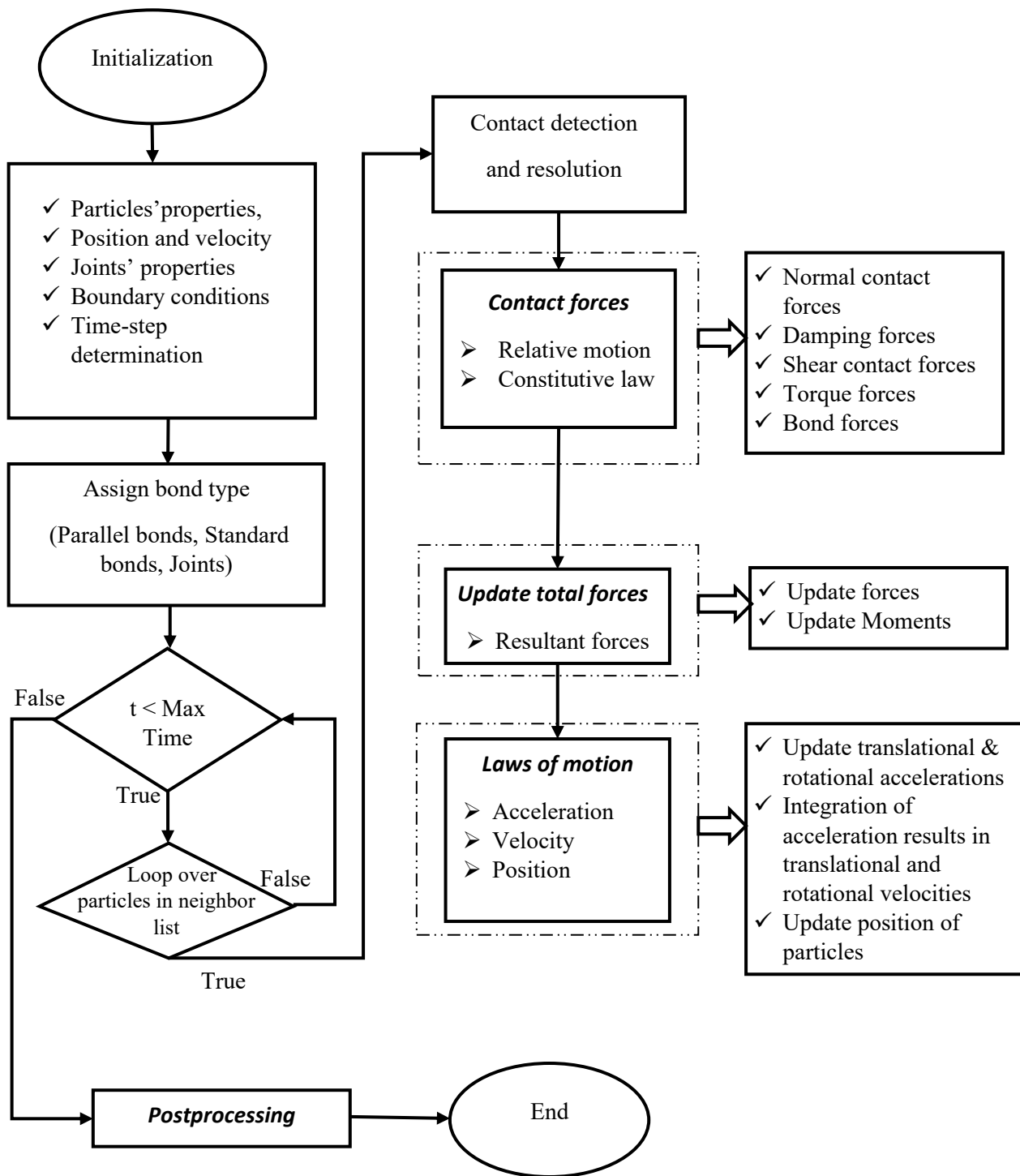


Figure 3-8: Overview of the algorithm of the numerical approach for HDPAC

Contact forces, calculating total force, and the law of motion were employed in HDPAC according to the formulation discussed in section 2.6.2.1. The contact detection and resolution are discussed in section 3.2.6.

### 3.2.6 Contact detection and contact resolution

In a DEM, the particles in contact with one another need to be determined. A calculation is then conducted to identify the actual contact forces between particles in contact with each other. These two steps are known as contact detection and contact resolution (O’Sullivan 2011).

To identify the particles that come in contact with each other, the `contact_pair` class was developed to perform contact detection and resolution in HDPAC. The contact detection process uses two nested For Loops to check every single particle against all other particles in the model at each time increment. Since the position of the particles changes during analysis, these detections must be repeated in every step. This method has an extremely high computational cost and results in a  $O(N^2)$  running time for contact detection where,  $N$  is the number of particles in the model. Thus, the simulation time will increase significantly as the number of particles increases (Zsaki 2009).

To reduce the time complexity, particles that are far from each other and not in contact must be eliminated. This will reduce the number of particles to those that are neighbors of each other, which will reduce the time complexity, as two nested For Loops just will only need to be executed repeatedly for the smallest list of the neighbors of each particle. To reduce the computational cost of searching for neighboring particles, the bucket (boxing) algorithm introduced by Mishra (2003) will be applied by calling the `parent_matrix` function in `contact_pair` class. Figure 3-9 shows a domain of a model divided into cells using grids. The application of this more general algorithm simplifies the contact detection problem (Munjiza 2004). The problem domain is subdivided into cells and each particle is mapped onto a cell as shown in Figure 3-10. Therefore, it is sufficient to check a particle against the particle located in the central cell neighboring cell as shown in Figure 3-10. The size of a single cell is chosen as equal to the diameter of the biggest particle so that the largest particle in the model can be fitted into a single cell (Munjiza 2004).

A two-dimensional array is a collection of rows and columns used to identify particles. Each particle is mapped onto a cell which is represented by array  $i, j$  where  $i$  is the number of rows, and

$j$  is the number of columns. The  $i$  and  $j$  are determined through the coordinations of the particles according to equations (3-1) and (3-2), respectively:

$$i = 1 + \text{Int} \left( \frac{x - x_{min}}{d} \right) \quad (3-1)$$

$$j = 1 + \text{Int} \left( \frac{y - y_{min}}{d} \right) \quad (3-2)$$

where  $i$  and  $j$  indicate a cell to which the particle that has the current center coordinates  $x$  and  $y$  is mapped. *Int* indicates the truncation of a real number and  $d$  is the greatest diameter of the particles in the model. For instance, particle 3 is mapped onto cell (5,6), while discrete element 6 is mapped onto cell (6,6), and so on. Thus, each particle is mapped to one and only one cell. To find the particles that may be in contact, the neighbors of the particles must be determined. As illustrated in Figure 3-10, the cell that contains each particle is called the central cell. The particles located in the central cell and in the neighboring cell will be added with a neighbor particle for each particle. Given the central cell  $(i, j)$  for a particular particle, the neighboring cells are simply:  $(i - 1, j - 1)$ ,  $(i, j - 1)$ ,  $(i + 1, j - 1)$ , and  $(i - 1, j)$ . All particles mapped onto these cells have to be added to the neighbor list of each particle. Thus, the detection of contact for a particular particle from the central cell is reduced to its neighbor list containing particles in the central cell and in the neighboring cells, minimizing the number of cells required to check neighboring particles, as shown in Figure 3-10 (Munjiza 2004). For instance, to find the neighbor of particle 3, the central cell is cell (5,6) and the neighboring cells are (4,5), (5,5), (6,5), and (4,6). Therefore, the probable neighbor list of particle 3 is an array that includes [1,2,4,5, and 7].

The contact resolution is a distinct series of accurate calculations, generally characterized by the overlap length or separation. According to the type of contact, a contact constitutive model is used to calculate the contact forces.

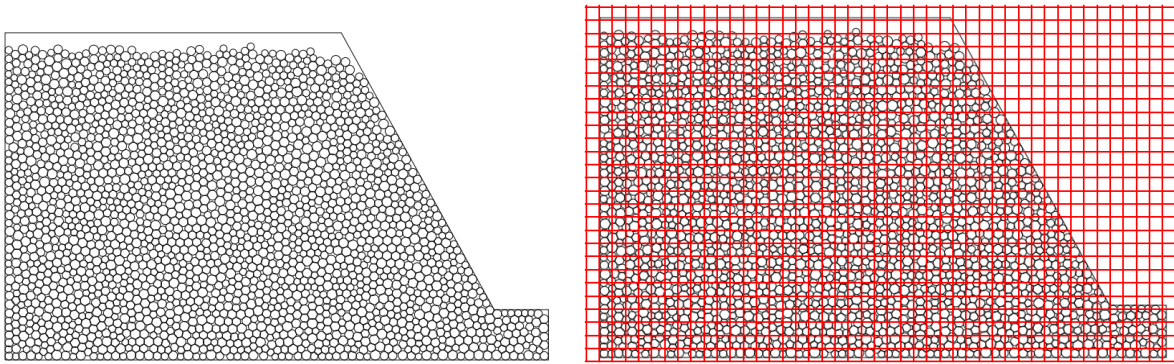


Figure 3-9: Typical subdividing of the domain of a model into cells

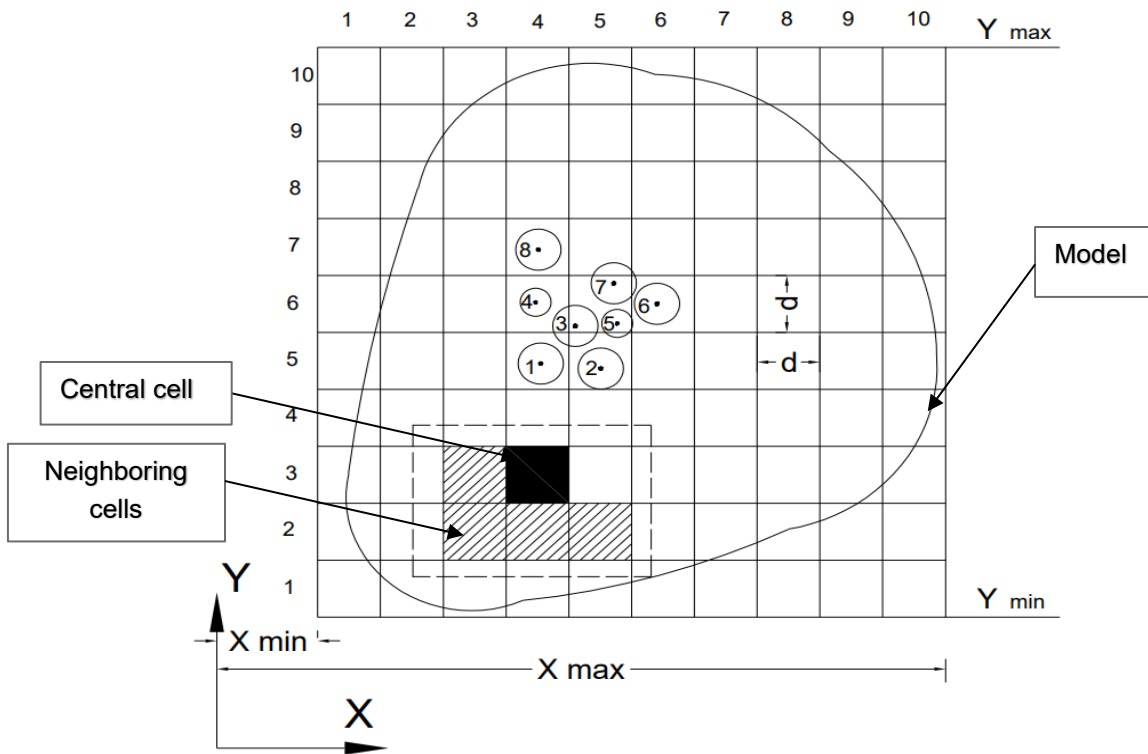


Figure 3-10: The problem domain is divided into identical square cells, each large enough to contain the largest particle, so that cell size  $d$  is equal to the diameter of the largest particle.

## Chapter 4. Validation of the DEM framework

---

The purpose of this chapter is to confirm and validate HDPAC. This includes contact detection and resolution, the laws of motion, contact force, parallel bonds, and the smooth joints required for the final simulation to study toppling failure. Several cases were conducted to numerically simulate and validate the developed HDPAC.

### 4.1 Case of a particle in free fall

The simulation of particles in free fall is used to determine the accuracy of the force-displacement law applied to each contact to update the contact force and relative motion between contacts based on the law of motion in HDPAC.

The implemented DEM method was applied to simulate a freefalling particle impacting a flat boundary (see Figure 4.1). The properties of the particle and boundary are shown in Table 4.1.

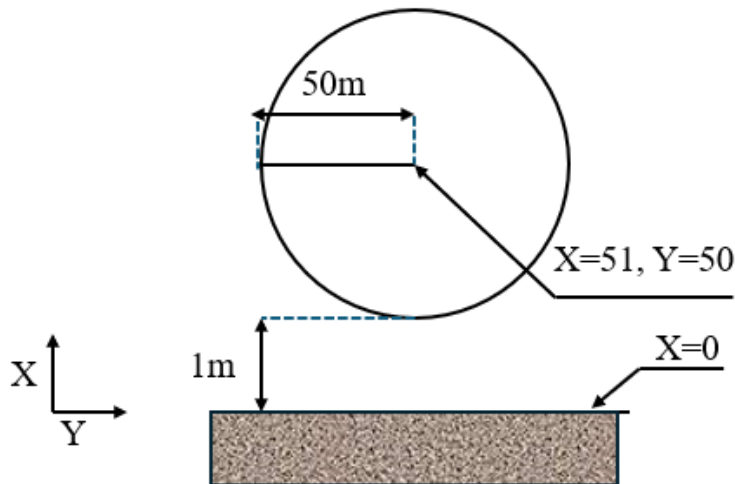


Figure 4-1: Sketch of the freefalling model

Table 4-1: Properties of the boundary and the particle

Parameters	Values (units)
Radii of the particle (disc)	50 (m)
Density of particle material	1000 (kg/m <sup>3</sup> )
kn particle	1.35×10 <sup>9</sup> (N/m)
kn boundary	1.35×10 <sup>11</sup> (N/m)
Damping	0
Initial velocity of particle in x and y direction	0 (m/s)
The position of the center of disc (particle)	(x=51 (m), y=50 (m))
Time step	0.0003 (s)
Number of steps	40000

The particle falls from 1m distance above the boundary and impacts the boundary. The center coordinate of the particle during this time is plotted, as shown in Figure 4.2. The particle bounces without any change to the amount of amplitude because the damping factor is set to zero. The velocity of the particle was plotted versus time, and the results were compared with a theoretical physics formulation and are represented in Figure 4.3.

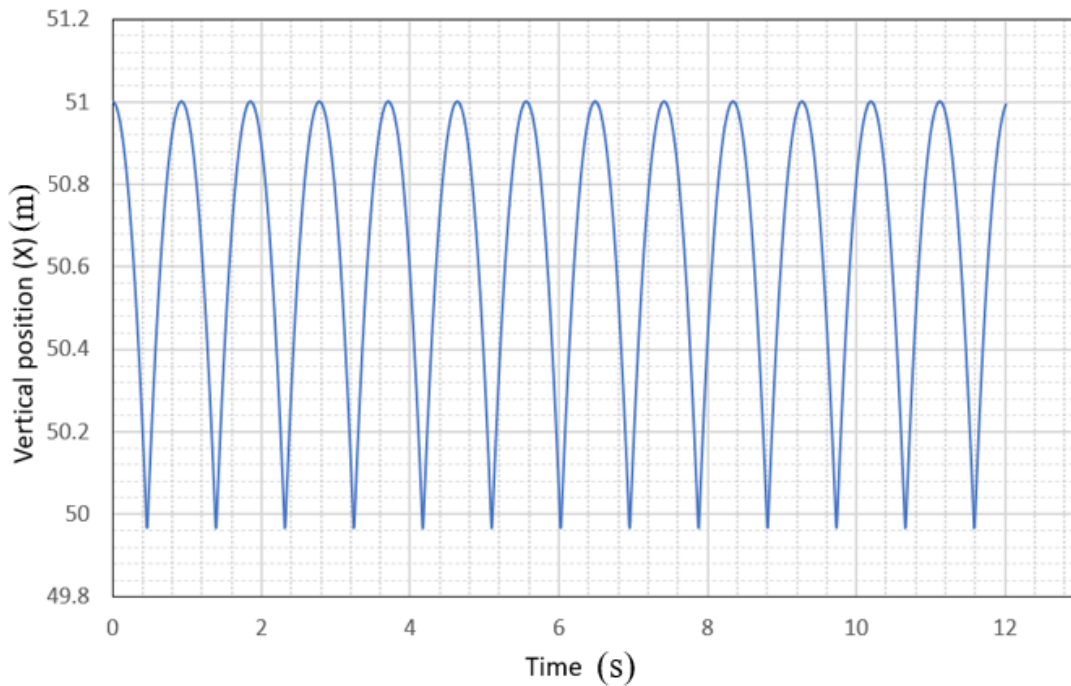


Figure 4-2: The vertical position of the particle's center during time



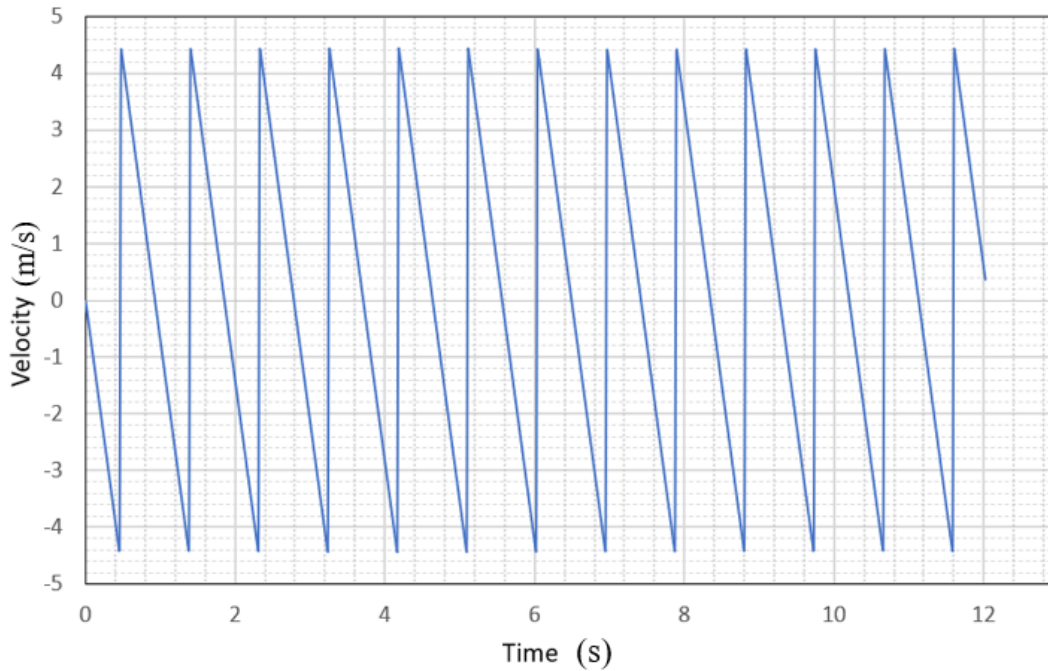


Figure 4-3: The velocity of the particle versus time

The position and velocity are compared with a kinematic physics formulation, for a particle falling under the influence of gravity, given as

$$v^2 - v_0^2 = 2ax \quad (4-1)$$

where  $v$  and  $v_0$  are the particle's final and initial velocity, respectively,  $a$  is the particle's acceleration and  $x$  is the particle's displacement.

By considering  $x = -1\text{m}$ ,  $a = -9.81 \text{ m/s}^2$ , and  $v_0 = 0 \text{ m/s}$ , the velocity when the particle hits the boundary should be

Calculated velocity using equation (4-1)	$v = 4.4294 \text{ m/s}$
HDPAC result	$v = 4.4307 \text{ m/s}$
The results difference between Formula and HDPAC	-0.03%

In addition,

$$x = \frac{1}{2} gt^2 + v_0 t \quad (4-2)$$

where  $x$  is the particle's displacement,  $g$  is the gravity acceleration,  $t$  is the time interval and  $v_0$  is the particle's initial velocity. To compare the result from HDPAC and formula according to the equation 4.2, the  $t = 0.465$  s, which is when the particle impacts on the boundary, is selected. For  $t = 0.465$  s, the results are:

Calculated displacement using equation (4-2)	$x = 49.9394$ m
HDPAC result	$x = 49.9662$ m
The results difference between Formula and Code	-0.05%

Therefore, the DEM numerical method obtains the appropriate result when simulating a free-falling particle's behaviour.

## 4.2 Case of a cantilever beam

The simulation of a cantilever beam examines how the parallel bond presented by Potyondy and Cundall (2004) works in HDPAC. The DEM method can be used to simulate every single grain of soil. However, non-convex granular material and rocks can be made up of arbitrarily connected particles using bond contact (Harmon et al. 2021). Therefore, to simulate intact rock material, the parallel bond will be used to bond the particles to make an intact rock mass material.

To test that the parallel bond is working well in HDPAC, a beam cantilever was simulated by applying the concentrated load at the tip of the beam. The deflection results of the numerical simulation were then compared with the theoretical beam theory results. It should be noted that the capability of the parallel bond will be used later to bond the particles to each other to make rock material.

A closed-form method based on the beam theory in the Cartesian coordinate system was used to determine the deflection of the cantilever (Figure 4-4). The deformation at the tip of the cantilever beam applying the concentrated load at the tip of the beam is given by McGuire et al. (1977):

$$\Delta_y = \frac{F x^2}{2EI} \left( L - \frac{x}{3} \right) + \frac{M x^2}{2EI} \quad (4-3)$$

The cantilever beam was modeled with a length,  $L$ , of 508 cm by joining 11 balls, and has a rectangular cross-section of unit thickness and height  $2R$  where  $R$  is 20.32cm, in 2D. The Young's modulus,  $E$ , is  $6.89 \times 10^4$  MPa, and the shear modulus,  $G$ , is  $2.6 \times 10^4$  MPa, which demonstrates the material properties of 2024-T3 aluminum. The concentrated vertical load,  $F$ , and bending moment,  $M$ , were applied at the tip of the cantilever beam with a fixed end. The parallel bond parameters (normal and shear stiffness) were selected so that the equivalent beam presents the equivalent elastic cylinders indicated in Table 4.2 (PFC3D 2016).

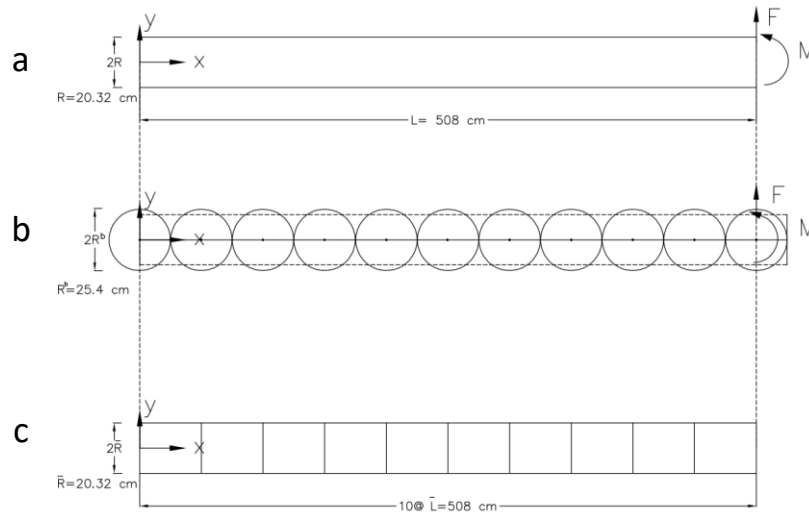


Figure 4-4: The cantilever beam model (a) Physical model, (b) DEM model, and (c) Equivalent elastic parallel bonds (PFC3D 2016)

Table 4-2: The parallel bond model properties

Parameters	Values
Normal Stiffness of ball $k_n$	$2.803 \times 10^9 \text{ N/m}$
Shear Stiffness of ball $k_s$	$2.803 \times 10^9 \text{ N/m}$
Normal Stiffness of parallel bond $\bar{k}^n$	$3.45 \times 10^9 \text{ N/m}^3$
Shear stiffness of parallel bond $\bar{k}^s$	$1.3 \times 10^9 \text{ N/m}^3$
Normal strength	$6.89 \times 10^2 \text{ GPa}$
Shear strength	$6.89 \times 10^2 \text{ GPa}$

The deformation caused by applying a concentrated load,  $F$ , of 4.44 kN, and bending moment,  $M$ , of  $11.3 \text{ kN} \times \text{m}$  at the tip of the cantilever beam was compared with the theoretical beam theory result, with the resulting deformation listed in Table 4-3. Figure 4-5 shows the graphical cantilever beam deformation pre-load and post-load application at the beam tip.

Table 4-3: The deformation of the tip of the beam by applying  $F$ (Force) and  $M$ (Moment) at the beam tip

Numerical result Vertical deformation (mm)	Analytical result Vertical deformation (mm)	Relative Error
34.715	34.727	$0.0003 < 0.1\%$

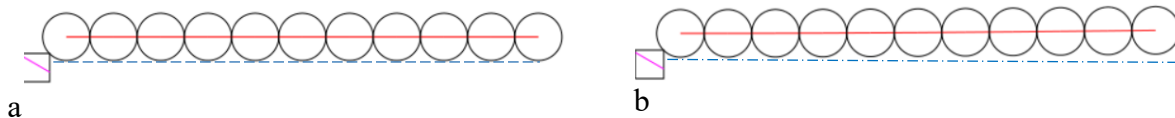


Figure 4-5: The graphical cantilever beam deformation (a) before, and (b) after applying load at its tip

### 4.3 Case of Uniaxial Compressive Strength (UCS)

Uniaxial compressive strength (UCS) is a common and essential test used to determine the mechanical properties of rocks. Discontinued modeling methods (Cundall and Strack 1979) are calibrated to find the micromechanical properties of rock by applying different tests such as UCS. The objective of this case study is to determine whether the implemented algorithm and code work correctly to simulate bonded particles which represent intact rock. The numerical UCS results show that the combination of the contact detection and resolution, normal contact, calculation of the tangential force, parallel bond model, boundary conditions, contact force, and laws of motion work accurately.

The properties of the material in continuum models can be provided by measuring directly from specific tests in the laboratory (properties such as Young's modulus, Poisson's ratio, and strength). However, determining the micro-properties used in parallel bonds in the DEM is not straightforward; a calibration process must be followed to determine the micro-properties and a

particular assembly of the arbitrary packing of particles (Potyondy and Cundall 2004). Many unknown parameters and various packing configurations must be evaluated and modified to achieve an appropriate model to demonstrate the test results; a challenging and time-consuming procedure in the DEM method. These parameters will not be used directly to simulate the slope, the final aim of HDPAC developed in this research, because the other parameters such as a joint space, orientations, and the constitutive properties of the joints will also affect the results. Therefore, slope calibration must be performed by considering the joint's properties with the micro-parameters of the rock material. Adding joints to a model will make the calibration process more complicated. In the numerical UCS test case, the calibration process is performed to determine if the parallel bond applied in HDPAC is working correctly.

An unconfined compressive strength (UCS) test was performed on a granite sample from the Underground Research Laboratory (URL) in Southeastern Manitoba (G.R.Simmons 1990). The laboratory testing of Lac du Bonnet Granite was carried out by the University of Manitoba Martin (1993) and the UCS test properties of the 62 mm diameter sample with a ratio of length over a diameter of 2.5 are summarized in Figure 4-6. The average unconfined compressive strength of this Lac du Bonnet granite was generally 200 MPa for samples collected from the near-surface (0-200 m) at the Underground Research Laboratory (Martin 1993).

The biaxial test for the Lac du Bonnet Granite was simulated numerically in PFC (Potyondy and Cundall 2004). To verify the parallel bond applied in HDPAC, a similar test on a sample with the same dimension was simulated by HDPAC. The micro-properties used in both PFC and HDPAC are summarized in Table 4-4.

Figure 4-7 shows the stress-strain response for both simulations. The graph reveals that the results of the constitutive model, built by parallel bonds, captured the biaxial results for the aforementioned sample of Lac du Bonnet Granite. These results demonstrate the parallel bonds applied in HDPAC work accurately.

The results of the PFC simulation by Potyondy and the results of HDPAC for the Lac du Bonnet Granite are presented in Table 4-5, allowing these results to be compared with the results of the experimental test at the Underground Research Laboratory. The abbreviations for the sample's properties are the elastic constants of Young's modulus ( $E$ ), and Poisson's ratio ( $\nu$ ), measured from unconfined compression tests, and the unconfined compressive strength ( $q_u$ ), all indicated in Table 4-5.

Parameter	URL
Tangent Young's modulus at 50% uniaxial compression	
Mean (GPa)	69
Stdev	$\pm 5.8$
n	81
Poisson's ratio	
Mean	0.26
Stdev	$\pm 0.04$
n	81
Uniaxial Compressive Strength (dry)	
Mean (MPa)	200
Stdev	$\pm 22$
n	81

Figure 4-6: Summary of the laboratory properties for a Luc du Bonnet granite sample obtained from Cold Spring Quarry, samples taken near the surface (0-200 m) at the Underground Research Laboratory (Modified from Martin 1993).

Table 4-4: Model microproperties for Lac du Bonnet granite

HDPAC		PFC (Potyondy and Cundall 2004)	
Grain	Cement	Grain	Cement
$\rho = 2630 \text{ kg/m}^3$	$\bar{\lambda} = 1$	$\rho = 2630 \text{ kg/m}^3$	$\bar{\lambda} = 1$
$D_{\max} / D_{\min} = 1.66$	$\bar{E}_c = 69.9 \text{ GPa}$	$D_{\max} / D_{\min} = 1.66$	$\bar{E}_c = 62 \text{ GPa}$
$E_c = 69.9 \text{ GPa}$	$\bar{k}^n / \bar{k}^s = 1.5$	Dmin varies	$\bar{k}^n / \bar{k}^s = 2.5$
$k_n / k_s = 1.5$	$\bar{\sigma} = 145 \text{ MPa}$	$E_c = 62 \text{ GPa}$	$\bar{\sigma} = \bar{\tau} = (\text{mean} \pm \text{ste. div.})$ $= 157 \pm 36 \text{ MPa}$
	$\bar{\tau} = 155 \text{ MPa}$	$k_n / k_s = 2.5$	
$\mu = 0.5$	-	$\mu = 0.5$	-

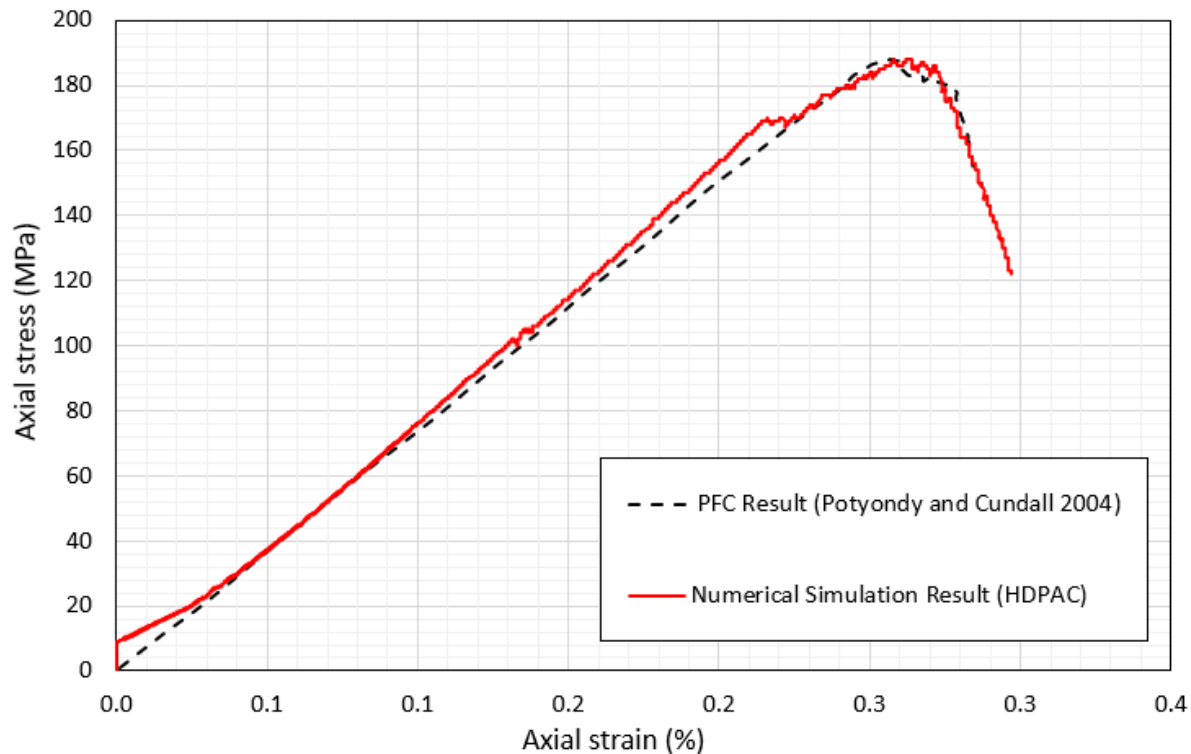


Figure 4-7: Stress-strain of a) biaxial test results of HDPAC at confinements of  $< 0.1$  MPa for a specimen granite model with  $D_{avg} = 0.745$  mm, and b) biaxial test results of the PFC2D at confinements of 0.1 MPa for a specimen granite model with  $D_{avg} = 0.72$  mm (Potyondy and Cundall 2004)

Table 4-5: The results of the numerical UCS Test of Lac du Bonnet granite, numerical results of PFC, and HDPAC

Property	Lac du Bonnet granite (Martin 1993)	PFC2D model (Potyondy and Cundall 2004)	HDPAC Result
E(GPa)	$69.9 \pm 5.8$ (n=81)	$70.9 \pm 0.9$ (n=10)	62
$\nu$	$0.26 \pm 0.04$ (n=81)	$0.237 \pm 0.011$ (n=10)	0.231
$q_u$ (MPa)	$200 \pm 22$ (n=81)	$199.1 \pm 13.0$ (n=10)	187.5

#### **4.4 Case of slip vs toppling on a surface (The necessity and application of smooth joints)**

Suppose two particles are located on two sides of the same joint, with no bond of any kind between them. The interaction between the two particles will be induced by extracting the resultant force based on standard contact interaction. The local direction of the resultant force in the contact point of two particles is the summation of their normal and shear forces. When two particles are interlocked, the change of the displacement in some conditions needs to have particles override each other (dilation) because failure inside a particle is not possible in DEM (see Figure 4-8). Such overriding of particles will affect the results and cause some problems in simulating the movement near the joints. Introducing an interface could solve the problem by allowing a correct relative displacement to be made between particles that are located on different sides of a joint. Using this interface could lead to eliminating the local particle contact orientation, thereby removing the problem. As a result, the bumpiness's effect between two surfaces will be removed especially when large particles are being used to reduce the time analysis time.

The smooth joint contact model in PFC was developed to provide an interface between particles that are separated by a joint to calculate inter-particle interaction (Pierce et al. 2007, 2009).

The smooth-joint model can simulate the joint between two particles by removing the local particle contact orientations along with the interface (PFC3D 2016).

The interface joint applied in this research is the simplest of the smooth joints proposed in PFC3D (2016).



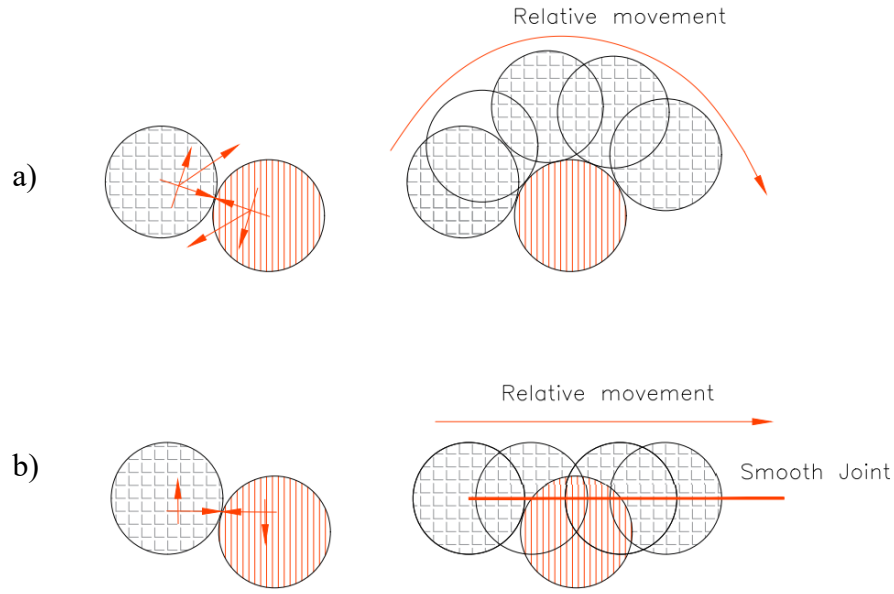


Figure 4-8: A schematic representation of the smooth joint contact on the realignment of the local particle orientation, and the interface used to adjust the roughness in the contact of the particles in joints: a) Standard contact, b) Smooth joint contact

The purpose of this section is to demonstrate how a smooth joint helps to adjust the roughness and prevent interlocking between particles located along the surface of the interface.

To present the effect of the smooth joint, we begin with a block kept on a frictionless inclined surface and which is beginning to slide due to its weight (see Figure 4-9). HDPAC was used to simulate the block and the inclined surface were made by attaching the particles. A parallel bond with very high strength is used to prevent any failure or detachment between the particles in the block and the slope (Figure 4-10).

Parallel bonds exist between the particles as indicated by the blue line connecting their centers.

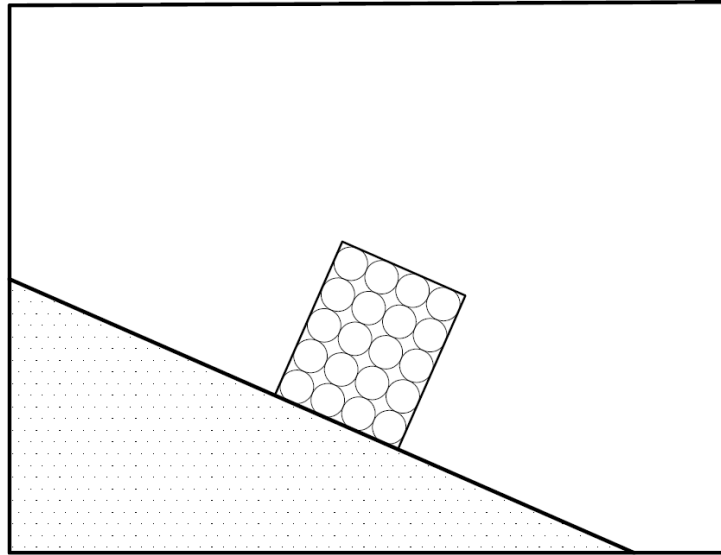


Figure 4-9: A single block on an inclined slope

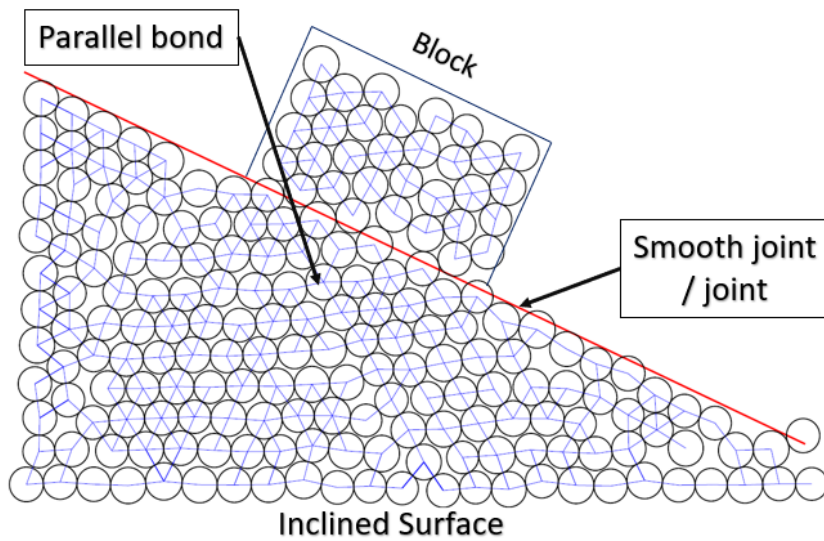


Figure 4-10: The geometry of a block on an inclined surface made by bonded particles with a parallel bond to each other in the DEM

Figure 4-11(a) shows the position of a block on an inclined surface when there is no smooth joint before gravity causes it to slide. The block slipped due to the gravitational load, and Figure 4-11 (b) shows how the interlocked forces between particles prevent the block from continued slipping,

due to the lack of a smooth joint. The particles override each other (dilation) because of the failure inside a particle. By decreasing the particles' size, the forces interlocked between particles are reduced and slip occurs. The reduction of particle size, however, results in a longer analysis when the number of particles is too large.

Figure 4-12 shows the velocity of particles at three different points in time as the block slips due to the gravitational load, with no smooth joints introduced into the model. The interlocked forces prevented the block from moving forward.

The effect of using a smooth joint is presented in Figure 4-13 (a) and (b) with the same geometry and microparameters used for the block slipping on an inclined surface. As can be seen, the smooth joint provides a smooth surface in the interface of the particles and eliminates the interlocked force, resulting in the local particles' orientation along the interface to adjust to the roughness in the contact of the particles in the joints.

Figure 4-14 shows the velocity of the particles as the block slips due to the gravitational load with a smooth joint introduced into the model.

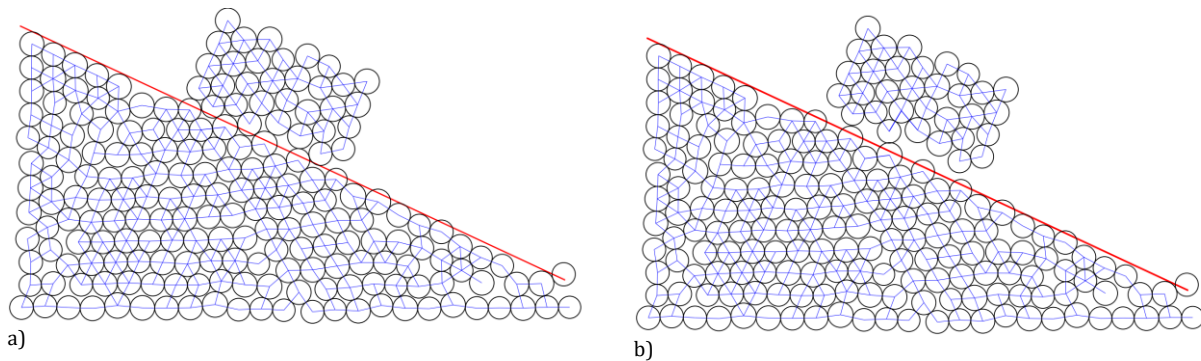


Figure 4-11: a) The block's position and state before starting to slip, b) the block's position and state after the block has slipped due to gravity.

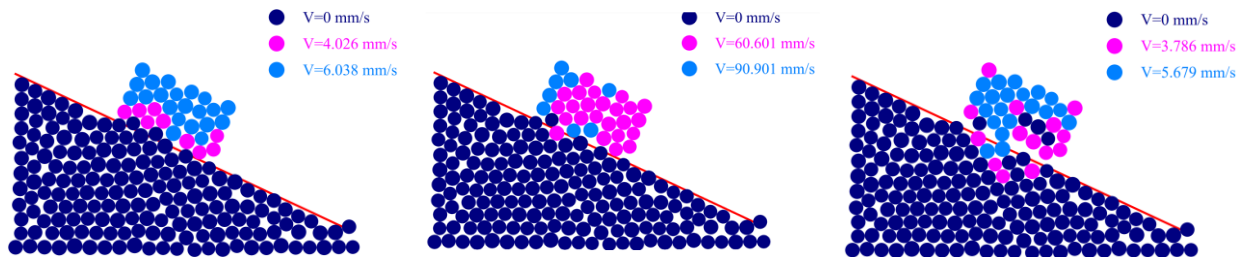


Figure 4-12: The velocity of particles when a smooth joint is not introduced into the model at three different points in time

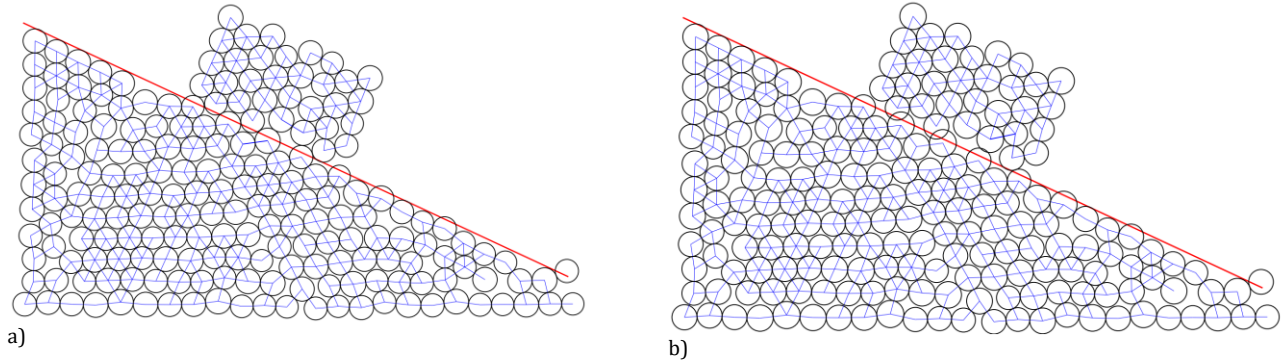


Figure 4-13: The position of the block on an inclined slope while slipping due to the gravitational load: a) during the slipping, and b) at the final step of the analysis.

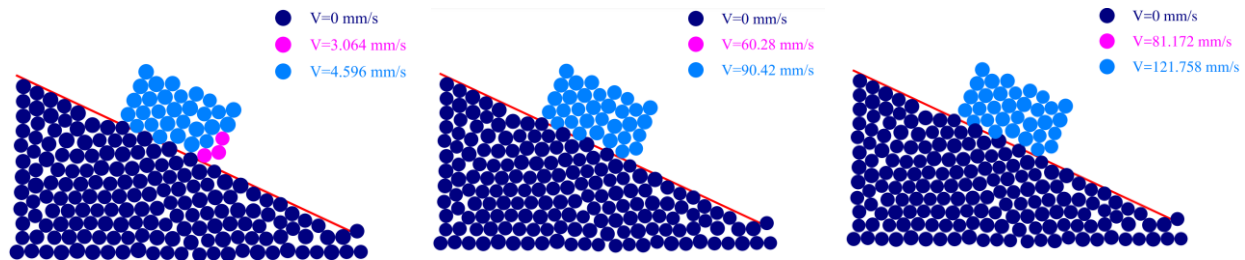


Figure 4-14: The velocity of particles when a smooth joint is introduced into the model at three different points in time

As a part of the validation, HDPAC was used to simulate the block toppling failure on an inclined surface.

For a single block laid on an inclined surface to topple, the primary kinematic condition must be that the center of gravity of the block lies outside the base, as discussed in Chapter 2. This situation occurs when

$$\Delta x/y < \tan \varphi_p \quad (4-4)$$

where,  $\Delta x$  and  $y$  are the width and height of the block, respectively, and  $\varphi_p$  is a dip angle of the plane, as illustrated in Figure 4-15. Ashby (1971) and Bray and Goodman (1981) presented the different conditions that a block can have on an incline.

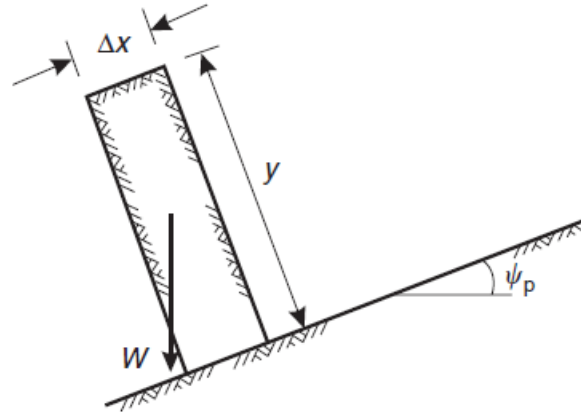


Figure 4-15: Block height/width on a plane inclined at an angle (Wyllie and Mah 2004)

Ashby (1971) described the different conditions shown in Figure 2-2 for a block laid on an inclined surface with the dip angle  $\alpha$  and a friction coefficient  $\mu = \tan \phi$ , where  $\phi$  is the slope's friction angle (Sagaseta 1986). Bray and Goodman (1981) changed the conditions for sliding and toppling criteria, as shown in Figure 2-3.

Using a modified criterion, Sagaseta showed that the toppling region was greater than the one proposed by Goodman and Bray, as illustrated in Figure 2-4 (Sagaseta 1986).

Using the DEM, a simulation was run to evaluate the smooth joint properties, and the above-mentioned criteria were used to verify the numerical results. A block, kinematically prone to toppling according to the theoretical closed-form, was placed on the slope, where both the block and slope were composed of particles (Figure 4-16). To connect the particles, parallel bonds were used, and were deemed strong enough that no bonds broke during analysis. Parallel bonds exist between the particles as indicated by the blue line connecting their centers. The blue line disappeared where the smooth joint (the red line) was introduced into the model. The smooth joint controls the interaction between the block and the inclined surface (Figure 4-16).

Table 4-6 shows the geometry of the block, the slope of the inclined surface, and the friction coefficient of the smooth joint. Table 4-6 also gives the calculation of the theoretical closed-form results based on the stability criteria discussed previously.

According to equation (4-4), the condition for toppling failure is met, so that the value of  $b/h=0.34$  is less than  $\tan \alpha=0.448$ . In addition, using the criteria in Figure 2-2 to Figure 2-4, the selected block dimensions and the slope angle of the inclined surface, combined with the friction coefficient of

the smooth joint provide toppling failure conditions for the block. The trajectory results of the DEM simulation presented in Figure 4-17 confirm the block toppling failure.

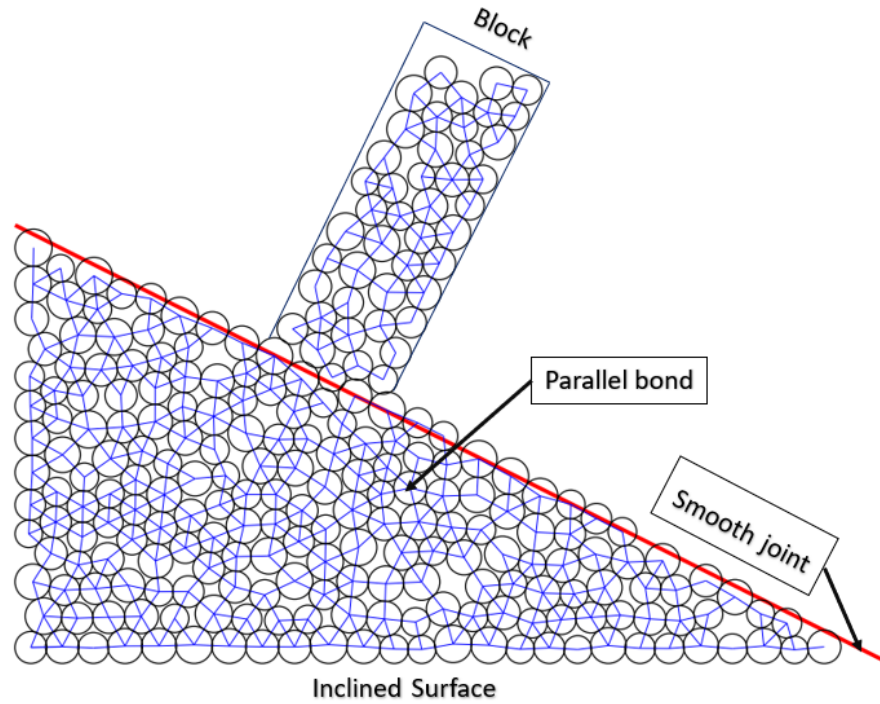


Figure 4-16: The geometry of the block and the inclined slope used in the DEM simulation

Table 4-6: Information about the block and the inclined surface

Parameter	Value
Height of the block $h$ (cm)	32
Width of the block $b$ (cm)	11
Angle of the inclined surface $\alpha$ (degree)	26
Friction angle $\phi$ (degree)	26.5
$\tan \alpha$	0.488
$\tan \phi$	0.499
$\tan \alpha / \tan \phi$	0.98
$b/h$	0.34
$b/h / \tan \phi$	0.69

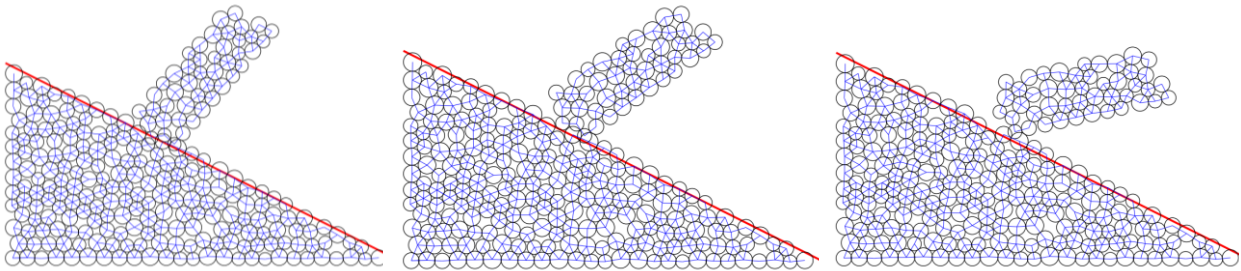


Figure 4-17: The toppling trajectory movement of the block due to its weight during a time

## 4.5 Conclusion

A numerical analysis' accuracy and credibility must be assessed through verification and validation. The validation of the developed discrete element method (DEM) was performed to demonstrate that every single component of HDPAC, including the normal force, shear force, damping force, contact detection, contact force, generation of particles, initial stress, and boundary conditions functions accurately. This detailed validation is necessary because the final developed numerical method will have different categories that together can implement the discrete element method as a tool to simulate toppling failure.

The free fall case results demonstrate that the general formulation performed correctly in the developed DEM cod. Newton's second law was therefore applied correctly to determine the motion of particles developing from the contact and body forces, as was the utilization of the force-displacement law to update the contact force due to the relative motion of the contact in HDPAC. The cantilever beam results confirmed that the parallel bond was used appropriately. The numerical UCS case simulation indicated that the combination of different components of HDPAC including contact detection and resolution, normal contact, calculation of the tangential force, parallel bond model, boundary conditions, contact force, and laws of motion work well together during the calculation cycle.

The case of a block on an inclined surface that is slipping because of its weight demonstrated the accuracy of the implementation of a smooth joint in HDPAC. Moreover, removing the interlocking between particles located along the surface of the interface when large particles are being used to reduce the analysis time showed the necessity of introducing a smooth joint. The use of larger

particles led to particles located on the opposite side of the joint to prevent the block from slipping over the surface. To remove this problem a smooth joint must be introduced to eliminate the overriding of particles because of the local particle contact orientation.

HDPAC also examined the case of a block toppling on an inclined surface and compared the result with theoretical criteria. HDPAC has been employed to simulate block instability, encompassing both toppling and sliding failure, on an inclined surface, as presented by Dabirmanesh et al. (2024). The step-by-step validation presented in this chapter shows that HDPAC can be used for simulating toppling failure. However, before starting the study of the block-flexural toppling failure in a slope, a validation of the slope with experimental results is required as well as a calibration in order to set the appropriate microparameter. The next chapter is mainly focused on the simulation of toppling failure.



## Chapter 5. Simulation of toppling failure using the Discrete Element Method

---

### 5.1 Introduction

The objective of the numerical simulation of the toppling failure using the discrete element method (DEM) (particle-based method) in this chapter is to investigate the capability of this method to simulate a toppling failure. The DEM framework is therefore used to investigate the toppling failure in rock slopes to answer the following questions:

- 1) Is the discrete element method (DEM) (particle-based method) able to simulate block-flexural toppling failure? Can the DEM capture the failure process and address the shortcomings identified in the literature, i.e., determine the toppling rupture pattern in jointed rock slopes prone to block-flexural toppling failure?
- 2) Can the DEM simulate block-flexural toppling failure in a slope with the assumptions outlined by Amini et al. (2012) as bases of the limit equilibrium method to analyze the block-flexural toppling failure as stated in Chapter 2 (including the overall surface rupture, and the consideration of two adjacent blocks with a potential of blocky toppling, and with a potential of flexural toppling failure)?
- 3) Do joint spacing, joint set configuration, and joint properties affect the assumption proposed for the theoretical method for block–flexural toppling failure?

As discussed in Chapter 2, researchers have proposed various theoretical models for analyzing the stability of toppling failure using the limit equilibrium method. These theoretical models assume an overall plane rupture surface, but there is no consensus among researchers to consider the overall surface rupture, especially for cases of block-flexural toppling failure.

An experimental tilting table test was simulated by HDPAC. The prototype of this experimental test, which consists of several blocks, assumes that the blocks' arrangement and configuration provide the potential block-flexural toppling failure condition on a tilting table can be modeled numerically by implementing DEM. The numerical results will assess the capability of the DEM particle-based approach to simulate a block-flexural toppling failure. The outcome of the calibrated model is used to investigate the theoretical assumption of the failure of block-flexure toppling proposed by Amini et al. (2012) for a slope and to enhance the assumptions used for analyzing the

stability of toppling failure. Several numerical simulations were carried out using HDPAC to investigate the effects of the joint spacing, joint set configuration, joint friction angle, and joint sets on the theoretical assumptions.

## **5.2 Numerical simulation of a rock slope with the potential of block-flexure toppling failure**

### **5.2.1 Experimental tilting test**

The experimental tilting test selected for the numerical simulation is composed of synthetic material blocks. The physical arrangement and formation of the blocks combined with their mechanical properties provide the slope with a specific potential block-flexural toppling failure. HDPAC (a discrete element-based method), after being calibrated using numerical UCS tests, is used to simulate and investigate the toppling failure based on the experimental tilting table conducted by Amini et al. (2015). A model identical to the experimental setup is produced and generated in HDPAC and numerical simulation is performed after calibrating the microparameters used. The effect of the particle size is studied in the process of calibration using the discrete element method. This section presents briefly physical results in order to compare them to numerical simulation results. The verified simulation results are used for further studies of the overall failure plane, the most important assumption in the closed-form analytical solution for the theoretical method to assess the failure of block-flexure toppling proposed by Amini et al. (2012).

The equivalent rock slope of one experimental test having the potential of toppling failure is simulated to investigate the level of similarity and accuracy of the toppling failure in the equivalent slope. The equivalent simulated slope is later used to investigate the role of joints' properties.

### **5.2.2 Physical model and laboratory test results**

The theoretical model proposed by Amini et al. (2012), as explained in Chapter 2, considered two adjusted blocks that cannot have a similar potential failure (blocky failure or flexural failure) so that they have the potential for block-flexure toppling instability. Blocky failure or flexural failure was therefore assumed for two adjacent blocks. Given that evaluating the behavior of a natural rock slope is very complicated, the blocks were arranged in a form that leads to a condition having block-flexural toppling instability in a physical model. In the ideal physical prototype, the blocks

were arranged to represent a slope with a potential block-flexural toppling failure. The slopes were composed of blocks made of a specific chemical powder mixture. The given powder consisted of a blend of chemicals and Vaseline oil in specific proportions. This mixture was thoroughly combined and then compressed, applying a consolidation pressure of 210 kPa. As a result of this pressure, the powder particles adhered tightly to each other, forming cohesive solid blocks. The blocks' mechanical properties include high densities and low tensile strength due to the powder texture; these conditions are conducive to the breakage of the blocks under their own weights at even small dimensions in a prototype of the physical model. The unit weight of the blocks was 23.4 kN/m<sup>3</sup> and their dimensions were 10×5×4.7 cm. The tensile strength was determined using a special apparatus and it was obtained at 31.37 kPa (Amini et al., 2015). The physical configuration of the test, including the configuration and alignment of the blocks, are explained later in this section for different slopes.

After the blocks were set up on the tilting table, a jack was gradually used to incline one side of the table to increase its angle. The table continued to increase its tilting angle until failure occurred. The angle at which sliding or toppling occurs and slope failure is initiated is the angle of instability (Amini et al 2015).

According to the literature review in Chapter 2, the DEM particle-based method required calibration to reach the appropriate microproperties. Therefore, a series of numerical uniaxial compressive strength (UCS) tests was conducted based on the available laboratory UCS tests. These laboratory UCS tests were performed on several 10×5×4.7 cm blocks by Amini et al. (2015).

### **5.2.3 Modeling uniaxial compressive strength (UCS)**

As mentioned above, three numerical uniaxial compressive strength (UCS) tests, for which the test results of the laboratory tests were available, were selected for the numerical simulation and to calibrate the intact material's microproperties. The uniaxial compressive strength of these blocks was reported to vary between 45 and 65 kPa, but the average value is nearly 56.7 kPa (Amini et al., 2015). For each numerical UCS test, the microparameters in the models were manipulated, as explained in the calibration procedure, to achieve similar stress-strain laboratory test results. Blocks with dimensions of 10×5×4.7 cm were used in the numerical UCS simulations to match the blocks used in the laboratory UCS tests by Amini et al. (2015). Note that according to ASTM D7012, the

samples used for UCS tests must have specific specimen dimensions, i.e., a minimum diameter of 47 mm, a length-to-diameter (L/D) ratio of 2.0 – 2.5, and the samples must have a cylindrical shape (ASTM D7012 2014). While the samples used in the laboratory tests met the minimum dimensions and L/D ratio criteria, the sample shapes were non-cylindrical. Only a limited amount of data is currently available for the UCS of non-cylindrical shapes (Al-Rkaby and Alafandi 2015).

The specimen used in the DEM method was created from randomly generated particles with radii less than the target radius, and with a range between  $R_{\min}$  (1 mm) to  $R_{\max}$  (2.5 mm); these particles were used to fill a rectangular boundary with a width of 4.7 cm and a length of 10 cm such that they do not overlap one another or the domain boundaries. Earlier investigations demonstrate that  $R_{\max}/R_{\min}$  ratio typically ranges between 1.32–3.00 (Huang 1999; Potyondy and Cundall 2004; Yang et al. 2006; Koyama and Jing 2007).

The particles were then allowed to settle under their own weight. In the next step, new particles were generated similar to the previous step; this procedure was repeated until the entire domain was filled. In the final stage, the radii of the particles were increased to achieve a dense and compacted specimen. An appropriate overlap between particles was achieved through a series of trial-and-error procedures to generate a reasonably tight initial packing and dense specimen, in addition to suitable locked-in forces developed between particles. In this procedure, the radii of the particles had to be increased before adding the parallel bonds to obtain the stress–strain result of the laboratory test in the numerical simulation. The final overall porosity in the model was 0.12.

Multiple trial-and-error iterations were conducted until the laboratory stress–strain curve was reproduced in the numerical simulation. The parameters for packing particles with radii between  $R_{\min}$  of 1mm and  $R_{\max}$  of 2.5 mm were found via a calibration process.

After the parallel bonds were configured, the boundaries of the specimen were removed and allowed to relax to reach an equilibrium state. Once this equilibrium state was reached, axial strain was applied in the loading phase. Note that, given that the DEM is a dynamic model, the velocity of the top and base boundaries must be sufficiently small to maintain an appropriate axial strain rate to produce a quasi-static loading response. In this study, based on the impact of platen speed, the loading rate  $V$  was set to a low value (0.01 m/s) for the top and bottom boundaries in the numerical UCS tests, because high velocities will lead to inaccurate results. The typical model geometry for the numerical UCS tests is presented in Figure 5-1.

Three UCS tests with different parameters were evaluated in the 2D numerical simulations. The calibrated parameters used in the numerical simulations of these UCS tests are summarized in Table 5-1. These parameters were derived via a calibration process that can match the target macromechanical properties of the intact blocks made of a specific chemical powder mixture.

To date, a variety of studies have presented recommendations to configure numerical simulations' microparameters to encapsulate macroscale material behaviour; several recommendations presented by Potyondy and Cundall (2004), Fakhimi and Villegas (2007), Zhou et al. (2018), and Shi et al. (2019) were considered for the calibration procedure in this study.

The calibration procedure is briefly summarized as follows:

- 1) Both the tensile and shear micro-failure values of the parallel bonds are set to similar, sufficiently high values to prevent any type of failure. The elastic parameters are matched by modifying the stiffness micro-parameter to obtain a behavior similar to that of the elastic UCS tests in the numerical modeling and laboratory test results.
- 2) The UCS is matched by changing the micro-failure parameters of the parallel bonds including the cohesion and internal friction angles of the bonds, and the tensile strength.

The stress-strain curves and typically observed failure modes in UCS tests obtained from the numerical simulations and laboratory test results are shown in Figure 5-2, which illustrates the desired agreement between numerical and experimental results. The results indicate that the slope of the curves conforms to the linear elastic state (Young's modulus), which is consistent with the laboratory results for the three tests. In both numerical test 3 and laboratory test 3, a perfect match in peak strength is observed. However, the numerical UCS test results show slightly higher compressive strength values for tests 1 and 2 than the corresponding laboratory UCS test results. In general, the results indicate that the slope of the curves (Young's modulus) and maximum strength (compressive strength) values of the laboratory tests and those of the numerically modelled tests are very similar.

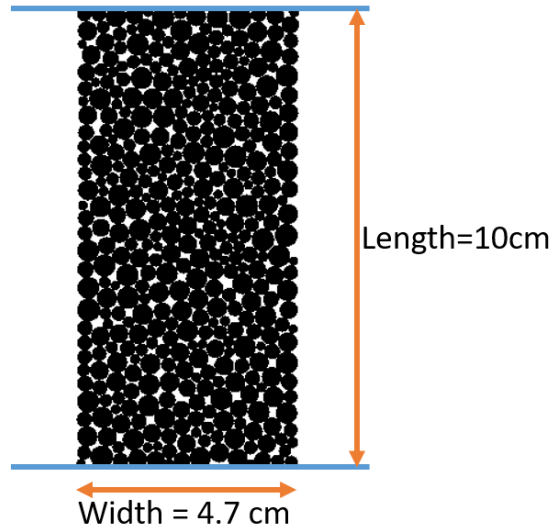


Figure 5-1: Typical model geometry for numerical UCS test

Table 5-1: Microparameters values used in the numerical simulation of three numerical UCS tests

Parameter	Test 1	Test 2	Test 3
Minimum particle radius $R_{\min}$ (mm)	1	1	1
Maximum particle radius $R_{\max}$ (mm)	2.5	2.5	2.5
Particle density $\rho$ (kg/m <sup>3</sup> )	2880	2880	2880
Young's modulus of particles $E_c$ (MPa)	12.05	7.05	13.05
Normal-to-shear stiffness ratio of particle ( $k_n/k_s$ )	1.3	1.8	1.3
Particle friction coefficient $\mu$	0.45	0.45	0.45
Young's modulus of parallel bonds $\bar{E}_c$ (MPa)	12	7.0	13
Normal-to-shear stiffness ratio of parallel bonds ( $\bar{k}^n/\bar{k}^s$ )	1.8	1.8	1.8
Parallel bond tensile strength (kPa)	19.7	13.5	19.7
Parallel bond cohesion (kPa)	25	29	25
Parallel bond friction angle (degrees)	10	15	15
Parallel bond normal critical damping ratio $\bar{\beta}_n$	0.2	0.2	0.2
Normal critical damping ratio $\beta_n$	0.13	0.13	0.13
Width of the specimen (cm)	4.7	4.7	4.7
Length of the specimen (cm)	10	10	10

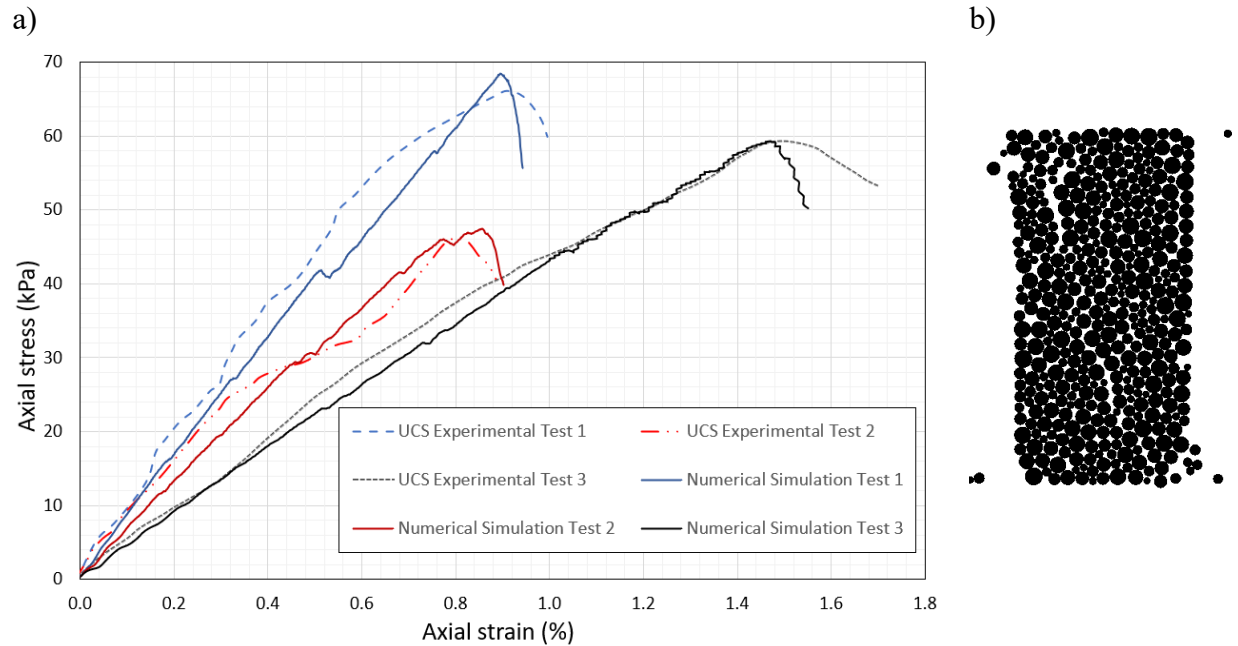


Figure 5-2: (a) Stress-strain curves for three experimental UCS tests conducted by Amini et al. (2015) and the corresponding numerical simulations of UCS tests in HDPAC, and (b) the typical example observed failure mode for numerical UCS tests

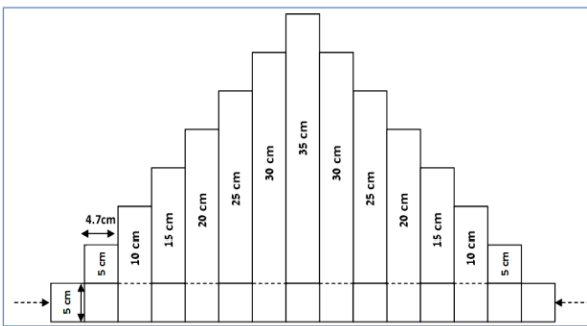
## 5.2.4 Numerical modeling of the slope

This section focuses on a numerical simulation of an experimental laboratory slope with joints dipping into the slopes, as originally performed by Amini et al. (2015). The following section introduces experimental test models that will be used in numerical simulations. The geometry of the slopes and the block's configuration provide the potential for block-flexural toppling failure. The experimental test results will be used to calibrate and validate the numerical simulation attempted in a discrete element frame using HDPAC to numerically simulate an identical model. Two physical models with different configurations were selected to verify the numerical method. A series of numerical UCS tests were conducted using HDPAC in advance to reduce the range of the microparameter describing the behavior of the artificial material of the blocks composing the slope models. The microparameters obtained from numerical UCS tests were used as the initiation parameters to calibrate the tilting table experiments for slopes composed of blocks made of artificial material.

### 5.2.4.1 Model geometry

Two of the tilting laboratory tests carried out by Amini et al. (2015) were selected for numerical simulation. A model (hereafter called the ideal arrangement) was developed with two adjacent blocks; in this model, one block has the potential for blocky failure because of the freedom at its end, while the adjacent block can withstand tensile stress because it has the potential for flexural failure due to the fixing block at its pivot point. Another model (hereafter called the randomly arranged blocks model) was set up containing randomly arranged blocks (Amini et al. 2015). Sketches of the geometry and size of blocks used in the physical tests for both models are shown in Figure 5-3 and Figure 5-4. The thickness and width values of all the blocks are 4.7 and 5 cm, respectively.

a)



b)

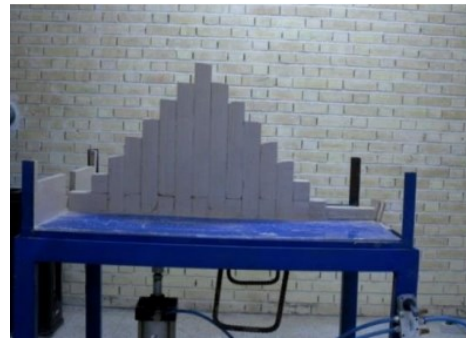
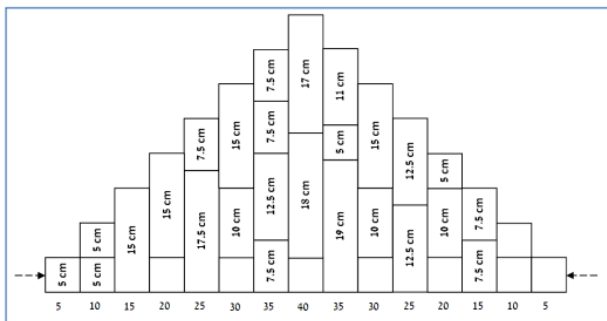


Figure 5-3: (a) A sketch of the model geometry, and (b) the physical model with the ideal arrangement of blocks (Amini et al. 2015)

a)



b)



Figure 5-4: (a) A sketch of the geometry, and (b) the physical model for the randomly arranged blocks (Amini et al. 2015)



The geometry of the models in the numerical simulation was created by generating particles in the polygons which represent the blocks' boundaries. A set of randomly distributed 6270 particles was packed into the corresponding closed boundary made with different segments to form blocks; the radius of the particles ranged from 1 mm to 4 mm and the calculated porosity was 0.12. Particles were generated in each boundary of the blocks in different stages and allowed to settle under their own weights. Next, the radii of the particles were increased to fill the gaps at the tops of the boundaries in all the domains. The models were then set to be in static states to reach their equilibrium states before the particles were bonded together. In the next phase, the particles were bonded together using parallel bonds while the blocks' boundaries were removed to allow the bonded particles to reach their equilibrium states. In the final step, the failure states in the slopes were caused by increasing the angle of the tilting table.

The geometry of the models constructed in HDPAC was formed by blocks, as shown in Figure 5-5 and Figure 5-6, which show the ideal arrangement and randomly arranged blocks, respectively. The blue lines passing through the particles' centers indicate the presence of parallel bonds between particles. The parallel bonds were removed where joints were introduced, with the base joint set indicated by red lines. Introducing a joint in the model will remove the existing parallel bond between the particles that are on opposite sides of the joint to disconnect the continuities of the block in this zone; thus the block, that is divided into two parts can no longer resist bending. This situation sets the condition for potential block failure for that block around its base joint. However, a continuum block can bear the bending force and provide flexural failure. The combination of these two modes provides block-flexural failure potential for the slope.

The particles were bonded together using parallel bonds to represent the blocks. The smooth joints represent the joints between blocks to simulate the interactions between blocks. The reason for using smooth joints is to ensure that the surface around the blocks is smooth to avoid adjacent particles of different blocks interlocking with each other due to the existence of wavy or bumpy surfaces between the block boundaries.

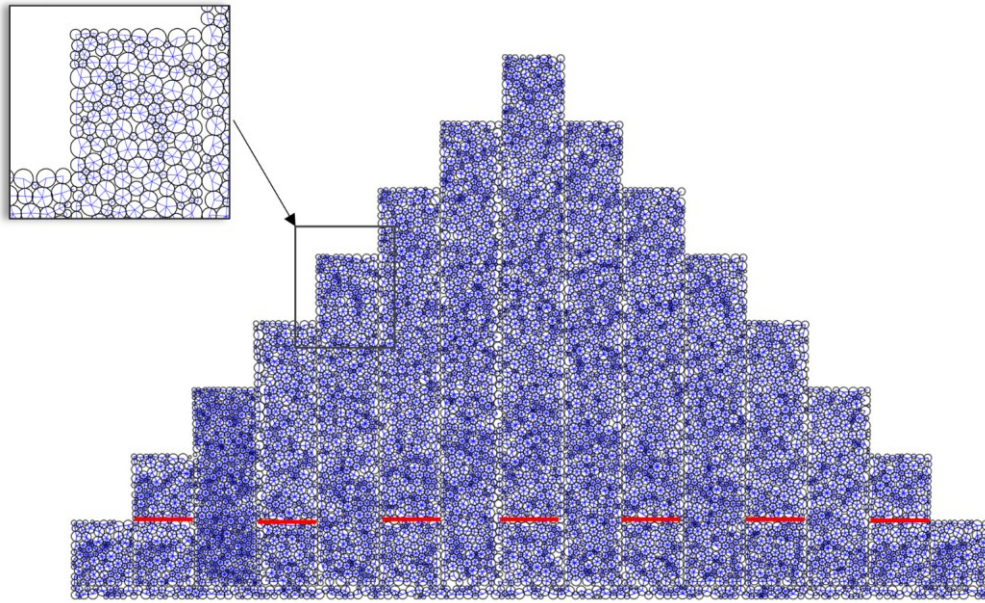


Figure 5-5: The developed slope geometry in the DEM for the ideal arrangement of blocks

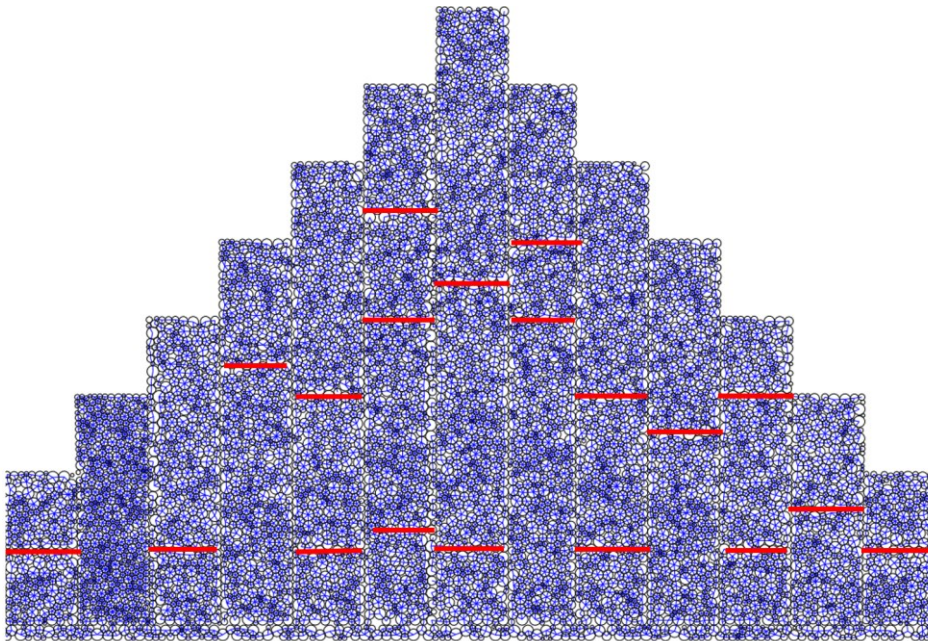


Figure 5-6: The developed slope geometry in the DEM with randomly arranged blocks

#### 5.2.4.2 Modeling methodology

##### *Calibration of the model*

Choosing the correct microparameters is the greatest challenge in DEM simulations, as these microparameters cannot be directly measured in conventional laboratory tests. Therefore, parameter calibration is the essential part of the simulation process in the DEM to ensure that the microparameters effectively represent the rock's macromechanical properties. A trial-and-error method is always used for this calibration process. Generally, numerical UCS tests are conducted to limit the parameter ranges. At the start of each simulation, the numerical UCS test results were used to determine the initial microparameters for the models. A trial-and-error methodology was then used to calibrate the numerical model results with the experimental test results. As a starting point, the microparameters obtained from numerical UCS tests were used as input data with the joint properties for the numerical simulations in this study. However, a significant discrepancy was found between the results of the numerical simulation and the experimental test results. This discrepancy occurred because the numerical UCS tests represent the intact material's behavior without considering the effects of joint spacing and joint properties during crack initiation or the failure progression due to loading, as the rock mass containing discontinuities was not considered in the numerical UCS tests. However, for simulation of the rock slope, which contains joints, a combination of the intact material's behavior, the joint configuration, joint spacing, the particle size, and the amount of interlock stress among the particles plays a pivotal role in determining the microparameters. Therefore, a calibration procedure for the slope must be conducted to fully capture the results of the experimental results test.

After the parameters were re-calibrated, ideal and randomly arranged configurations with a porosity of 0.12 and particle size distributed randomly between 1 and 4 mm were selected for the models. The parallel bond and joint properties were manipulated to achieve the overall failure surface obtained in the experimental results.

Table 5-2 shows the microparameter values determined for both the ideally arranged block configuration ("ideal model") and randomly arranged block configuration ("random model") in the numerical simulations following the completion of the calibration procedure.

The joints between blocks were simulated using the smooth joint model proposed by Pierce et al. (2007, 2009). As stated in Chapter 4, the smooth joint model provides a planar surface interface

between particles irrespective of the local particles' contact orientations along the plane contact surface (Pierce et al. 2007, 2009). The calibrated microparameters for the smooth joints used in the models are summarized in Table 5-3.

Table 5-2: The calibrated microparameters used in the numerical models

<b>Parameter</b>	<b>Ideal model</b>	<b>Random model</b>
Minimum particle radius $R_{\min}$ (mm)	1	1
Maximum particle radius $R_{\max}$ (mm)	4	4
Particle density $\rho$ ( $\text{kg}/\text{m}^3$ )	2900	2900
Young's modulus of particles $E_c$ (MPa)	15.05	15.9
Normal-to-shear stiffness ratio of particles ( $k_n/k_s$ )	1.3	1.8
Particle friction coefficient $\mu$	0.45	0.45
Young's modulus of parallel bonds $\bar{E}_c$ (MPa)	15.9	15.9
Normal-to-shear stiffness ratio of parallel bonds ( $\bar{k}^n/\bar{k}_s$ )	1.8	1.8
Parallel bond tensile strength (kPa)	209	159
Parallel bond cohesion (kPa)	50	50
Parallel bond friction angle (degree)	15	15
Parallel bond normal critical damping ratio $\bar{\beta}_n$	0.2	0.2
Normal critical damping ratio $\beta_n$	0.13	0.13
Height of the slope H (cm)	47.39	47
Bond gap (mm)	1.05	1.05

Table 5-3: Calibrated microparameters for smooth joints used in the models

<b>Parameter</b>	<b>Ideal model</b>	<b>Random model</b>
Normal stiffness of base joint per unit area, ( $k_{nj}$ )( $\text{N}/\text{m}^3$ )	$12 \times 10^{10}$	$12 \times 10^{10}$
Shear stiffness of base joint per unit area, ( $k_{sj}$ )( $\text{N}/\text{m}^3$ )	$12 \times 10^{10}$	$12 \times 10^{10}$
Joint friction coefficient of the base	0.23	0.2
Normal stiffness of joint per unit area, ( $k_{nj}$ )( $\text{N}/\text{m}^3$ )	$12 \times 10^{11}$	$12 \times 10^{11}$
Shear stiffness of joint per unit area, ( $k_{sj}$ )( $\text{N}/\text{m}^3$ )	$12 \times 10^{11}$	$12 \times 10^{11}$
Joint friction coefficient	0.17	0.15
Joint gap distance (mm)	0.1	0.1

### ***Gravitational forces and boundary conditions***

In situ stress was directly applied to the models by considering a gravity load. The maximum vertical stress was expected to develop at the base of the model which has the highest overlying. To compensate for the effects of porosity on gravitational loading, a higher density was required.

The boundary conditions in the model were the values of the field variables (i.e., force and displacement) prescribed to the boundaries. As explained in section 3.2.3 of Chapter 3, the boundary conditions were assigned to the particles located within a distance equal to the maximum particle radius from the boundaries. In this series of models, the bottom boundary of all the models was prevented from moving laterally and vertically, and displacements in both the X and Y directions were fixed. Tilting of the models was performed by changing the gravitational direction, while the model itself was not rotated (see Figure 5-7 ). Accordingly, the model experienced the equivalent force to a situation in which the tilting table was tilted to an angle  $\alpha$ .

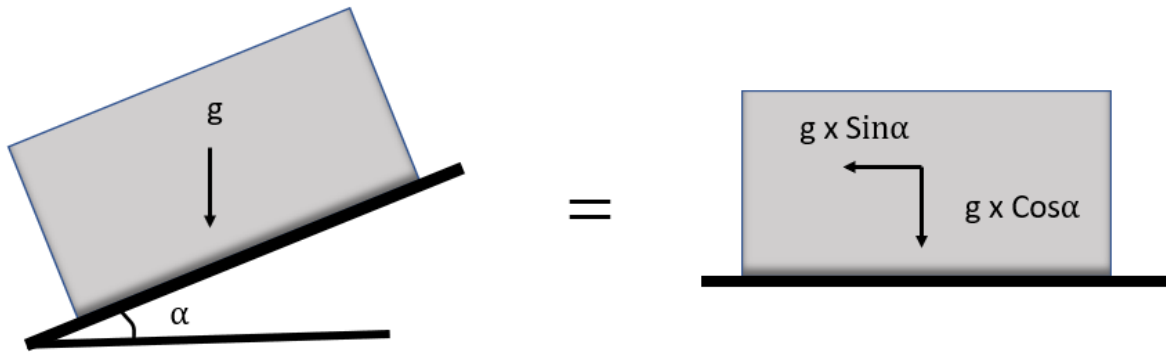


Figure 5-7: The decomposition of the gravitational force represents a tilting angle

### 5.2.4.3 Modeling results

The preliminary microparameters of the intact material were adopted for numerical simulations based on the parameters from the numerical UCS tests. As noted above, the smooth joint contact model was introduced to define the joints; however, this model requires some microparameters, the calibration of which is complicated. A trial-and-error method was used to calibrate the microparameters of this model to match the numerical simulation results with those obtained from laboratory tests, including the overall failure surface and block movements. To accomplish this, the inclination angle was increased, and the overall failure surface and block movement were monitored. The results showed that the overall failure surface differed from the experimental test results when using the intact material's microparameters determined from the numerical UCS tests. The joints defined between the blocks and the different interlocking forces between particles in the blocks meant that the microparameters of the numerical UCS tests were not directly applicable to the tilting table simulation and instead required calibration. Therefore, the microparameters of the

intact material and the microparameters of the joints were changed while the inclination of the tilting table was increased to match the failure angle of the physical tests. The overall fracture surface in the models was tracked to ensure correspondence between the model results and physical laboratory test results. This procedure was repeated until the physical results were matched by the numerical simulation. The numerical and physical test results for the tilting table test for the ideal model and random model are presented in Table 5-4. The angle of the overall failure surface and the arrangement of the blocks following the toppling failure for the ideal arrangement are illustrated in Figure 5-8. For comparison, an image showing the corresponding physical test result is presented in Figure 5-9.

In the numerical simulations, the angle between the overall failure surface and the line normal to the discontinuities is around 15° in the ideal model. An equivalent angle of 15° was reported in the corresponding physical model. The angle at which failure occurred and block sliding or toppling took place in the numerical simulation was also the same as that of the physical model (35). As the failure surface in the numerical simulation is not as smooth as that of the physical model, a stepped surface can be observed at some locations. To achieve smoother surfaces, 13561 smaller particles were used with similar properties and porosities but radii between 1 and 2.5 mm. Figure 5-10 presents the overall failure surface for the finer particles, which also occurs at 15°. Noted that the overall surface failure angle represents the angle between the overall failure surface and the line normal to the discontinuities or the dip of the main joint sets into the slope.

Table 5-4: The numerical and physical test results of the tilting table tests

Case	Angle of the tilting table at failure point $\theta^\circ$		Overall surface failure angle $\varphi^\circ$	
	Physical model	Numerical model	Physical model	Numerical model
Ideal	35	35	15	15
Random arrangement	19	19	14*	14

\* The overall surface was chosen as the lowest plane of failure at the bottom of the blocks, as shown in Figure 5-12. This angle corresponded to the experimental results.

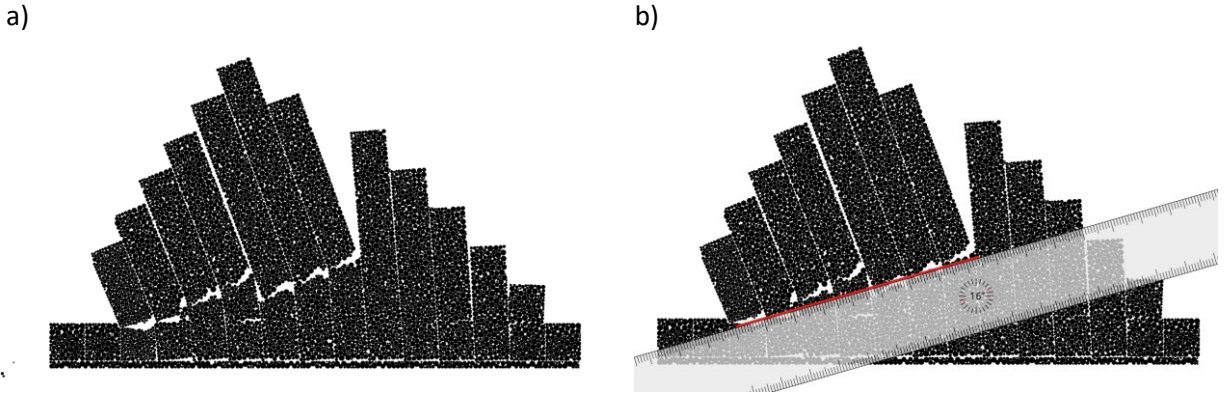


Figure 5-8: (a) Overall failure surface for the ideally arranged blocks model in the numerical simulation, and (b) the overall failure surface angle ( $15^\circ$ )

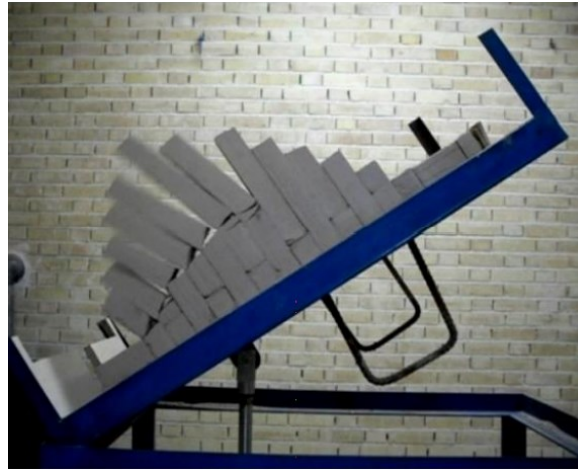


Figure 5-9: Overall failure surface for the ideally arranged blocks model in the physical laboratory tilting table test (Amini et al. 2015)

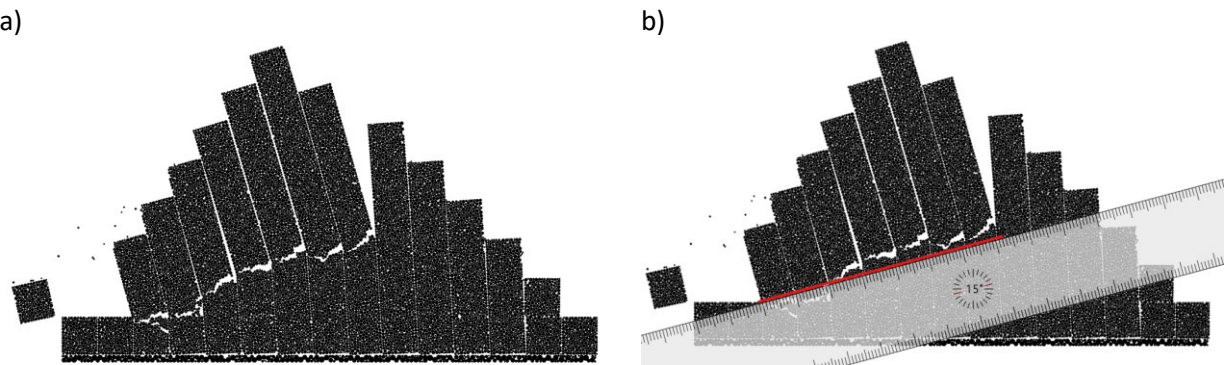


Figure 5-10: (a) Overall failure surface for the ideally arranged blocks model in the numerical simulation for finer particle sizes ( $R$  between 1 and 2.5 mm), and (b) the overall failure surface angle ( $15^\circ$ )

Figure 5-11 shows the angle of the overall failure surface and the arrangement of the blocks following toppling failure in the random model. The physical test results for the randomly arranged blocks are shown in Figure 5-12. Based on the physical test conditions at the onset of failure, the tilting angle was set at  $19^\circ$ . In the randomly arranged block configuration, two failure surfaces were observed; one occurred at the pivot of the slope and extended into the slope at a lower angle ( $14^\circ$ ), while another with a steeper angle ( $24^\circ$ ) occurred at the top of the slope. Noted that block-flexural toppling failure can occur in a slope with two different cross-joint sets; thus it is not a valid assumption to assume only a single failure surface in limit equilibrium methods. This hypothesis will be examined later next section by studying a slope with different joint sets crossing a joint set dipped to the slope.

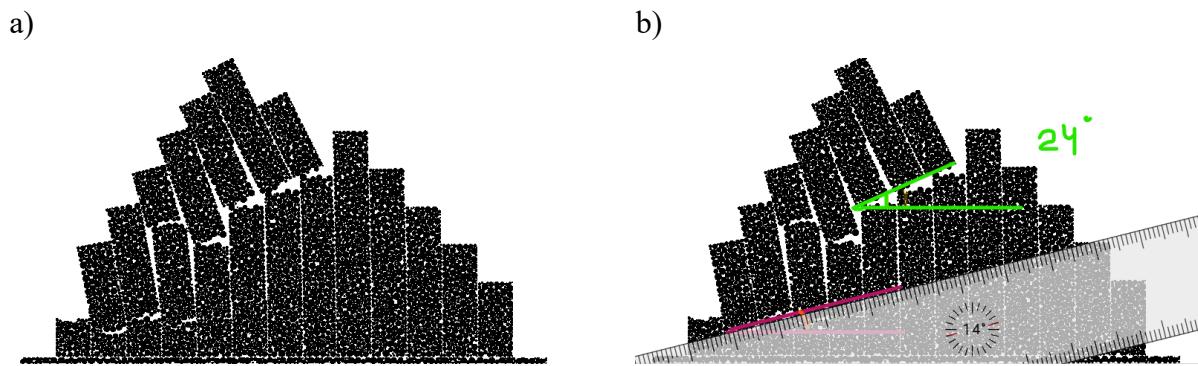


Figure 5-11: (a) Overall failure surface for the randomly arranged blocks model in the numerical simulation, and (b) The angles of the overall failure surfaces ( $14^\circ$  and  $24^\circ$ )

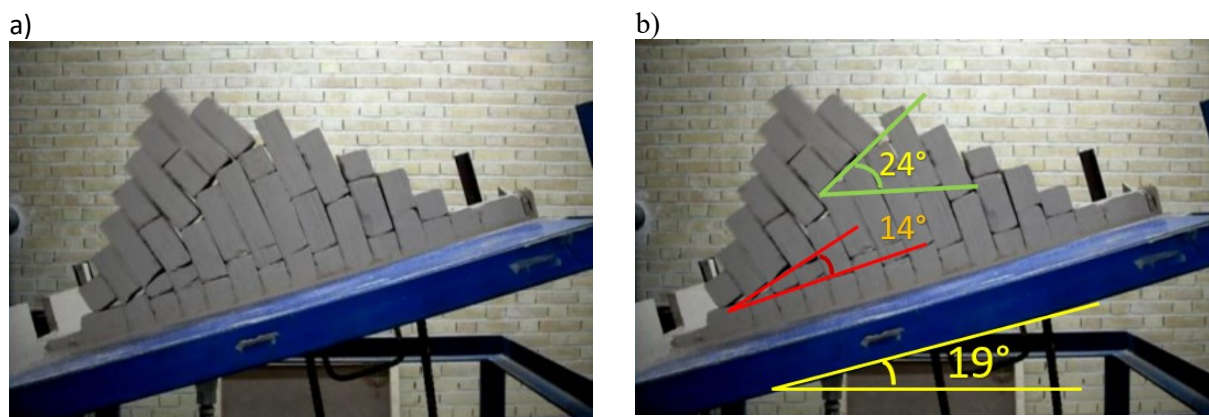


Figure 5-12: (a) Overall failure surface for the randomly arranged blocks model in the physical laboratory tilting table test, and (b) The angles of the overall failure surfaces ( $14^\circ$  and  $24^\circ$ ) (Amini et al. 2015)



#### 5.2.4.4 Conclusion

The discrete element modeling (DEM) approach was used to simulate the toppling failure. The DEM was used to simulate two cases with different block configurations with block-flexure toppling failure potentials. The numerical simulations revealed the total failure surface at which the tensile stress or shear stress of the parallel bonds exceeds a given strength limit and the parallel bond breaks between bonded particles. The overall failure surfaces corresponded to those of the experimental tilting test with values of  $15^\circ$  and  $14^\circ$  for the ideal and randomly arranged block models, respectively. In addition, the numerical simulation captured all the stable blocks, i.e., those without any movement, and distinguished between the stable zone and the zone that moved due to the toppling. In both cases, the DEM captured the overall failure surface by capturing the required failure tilting angle determined in the experimental tests. The results show that the calibrated DEM can successfully simulate toppling failure of blocks with the potential for block-flexural toppling failure.

In the ideal model, the rupture surface shape differs slightly from the simulation results and experimental tests. This aspect can be affected by the particle size, stress level, and microparameters adopted for constructing the blocks. Selecting finer particles (i.e., those with smaller radii) provides a smoother rupture surface and removes the stepwise non-uniform failure rupture surface. Therefore, while calibrating the microparameters, the particle size should be optimized to achieve the best compromise between accurate results and the time-to-solution values for the numerical simulation. The simulation results demonstrated that blocks should have a width of at least 19 times the maximum particle size. In the model of a slope with different cross-joint sets crossing a joint set dipped parallel to the slope, two failure surfaces were observed. This means that the assumption of considering only a single overall failure surface in theoretical methods to assess block-flexural toppling failure proposed by Amini et al. (2012) must be investigated.

During the calibration of the numerical simulations of the ideal and random models, it was concluded that the microparameters of the material obtained from the numerical UCS test cannot be directly used in the numerical simulation of slopes composed of blocks; instead, these parameter values can only be used as a guide to limit the microparameters value ranges. The calibration process must be performed during the validation of the numerical simulation results by changing the microparameters of both the intact material and the joints.

The results from the random model, in which the joints are distributed randomly in the model, highlight that considering a single overall failure surface is not necessarily a valid assumption in theoretical models of block-flexural toppling failure. The effect of the joint configuration in slopes is studied in the next sub-section.

### **5.3 Numerical Simulation of the Equivalent Slope**

The objective of this section is to study the main assumption used in the limit equilibrium method outlined by Amini et al. (2012) to analyze block-flexural toppling failure. As with all analytical solutions, this limit equilibrium method has some assumptions. The total failure plane, as in most equilibrium methods designed to investigate toppling failure, is assumed to be 10 - 20 degrees above the normal line of the main discontinuities. The joint spacing and joint configuration effects on the overall failure plan were not studied. The effect of the joint spacing and joint configuration can change the assumption of considering a single-failure plane for block-flexural toppling failure in the limit equilibrium method analysis. An experimental evaluation of this issue has not been done, and it would be very costly to perform experimentally. This section numerically investigates a slope with a potential block-flexural toppling failure using the DEM. Since this simulation aims to investigate the overall failure surfaces, the main assumption of the limit equilibrium analysis, the geometry of the slope, and the configuration of the joint sets must satisfy the assumptions outlined by Amini et al. (2012) to analyze the block-flexural toppling failure.

To obtain reasonable results and simplify the complicated DEM calibration process, we used a slope equivalent to that of the ideal physical model that was previously successfully simulated with the DEM in the previous subsection (section 5.2.4). An analysis of the DEM model was conducted, and the results were compared to the experimental results to determine if the DEM can adequately simulate toppling failure. The validated slope is then later used to investigate the effects of joint spacing and joint configuration to provide insights into the influence of joint sets configuration on the assumptions used in limit equilibrium methods.

### 5.3.1 The geometry of the equivalent slope

A theoretical model based on a limit equilibrium analysis assumes that adjusted blocks cannot have a similar failure potential in a slope with the potential of block-flexure toppling failure (Amini et al. 2012). One of the major assumptions related to the limit equilibrium analysis of toppling failures is determining the inclination of the total failure plane (Amini et al. 2012). Figure 5-13 presents the geometry of a slope proposed by Amini et al. (2012) to analyze block-flexural toppling failure. More detail has been presented in the literature review in Chapter 2.

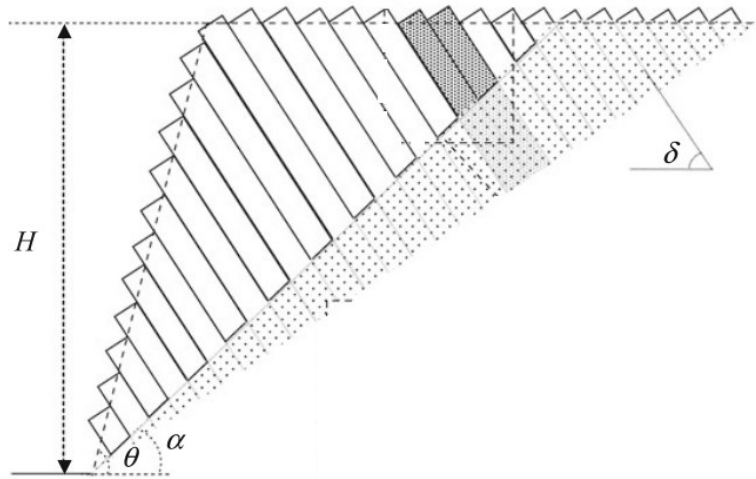


Figure 5-13: The model geometry proposed for a rock slope with the potential for block-flexure toppling failure (Amini et al. 2012)

The calibrated numerical simulation of the ideal block arrangement was used to simulate a slope representing the theoretical model proposed by Amini et al. (2012). The equivalent geometry was created using the ideal block arrangement described above. Both the configuration and the dimensions of the blocks remain the same as those used in the experimental test (see Figure 5-14). The target equivalent slope used for the theoretical model is illustrated in Figure 5-15 (Amini et al. 2009, 2015). The parameters shown in Figure 5-15 are the angle between the rock mass stratification and the horizontal ( $\delta$ ), the angle between the total failure plane and the line normal to the discontinuities ( $\varphi$ ), the angle between the horizontal and the face slope ( $\theta$ ), the angle of the upper surface of the rock slope relative to the horizontal ( $\beta$ ), and the slope height ( $H$ ).

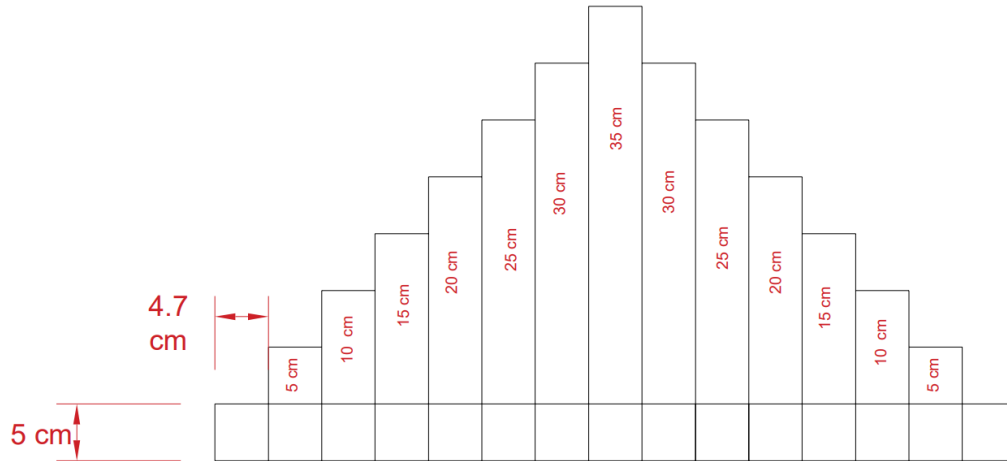


Figure 5-14: Block configuration used for ideal arrangement experimental test (modified from Amini et al. 2012)

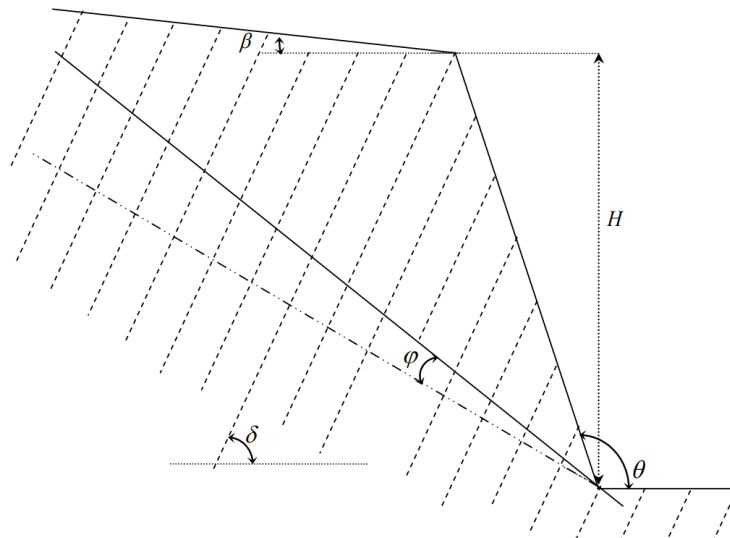


Figure 5-15: Schematic illustration of a rock slope with the potential for toppling failure (Amini et al. 2015)

To numerically simulate the geometry of the rock slope model with the potential for block-flexural toppling, the ideal arrangement block model was rotated  $35^\circ$ , equivalent to the angle at which failure begins in this model. Figure 5-16 illustrates the rotated ideal arrangement of blocks. Therefore, all parameters presenting the geometry of the slope, as described earlier, can be directly represented in this model, except for the angle between the total failure plane and the line normal

to the discontinuities ( $\phi$ ). The final equivalent geometry used in the numerical simulation for the equivalent slope is shown in Figure 5-17. To ensure that this slope correctly represented the behaviour of the ideal arrangement, the microparameters were calibrated to ensure a  $\phi$  value of  $15^\circ$ . To represent the geometry of the slope, particles were generated between the model's boundaries presenting the slope domain's geometry. Using the smooth joint contact model, joints were introduced to break the bonds between particles located on opposite sides of the joints to delineate the blocks.

The final slope model consists of a slope where  $H=0.475$  m and  $\theta=98^\circ$ . A set of randomly distributed 19,450 particles was packed into the corresponding closed geometry to represent the slope; these particles had a uniform size distribution, a ratio between the maximum and the minimum radius  $R_{\max}/R_{\min}$  equal to 2.33, and a final porosity of  $n \approx 0.12$ . The angle between the rock mass stratification and the horizontal line ( $\delta$ ) was  $55^\circ$ , and the angle between the upper surface of the rock slope and the horizontal line ( $\beta$ ) was  $8^\circ$  in this model configuration.

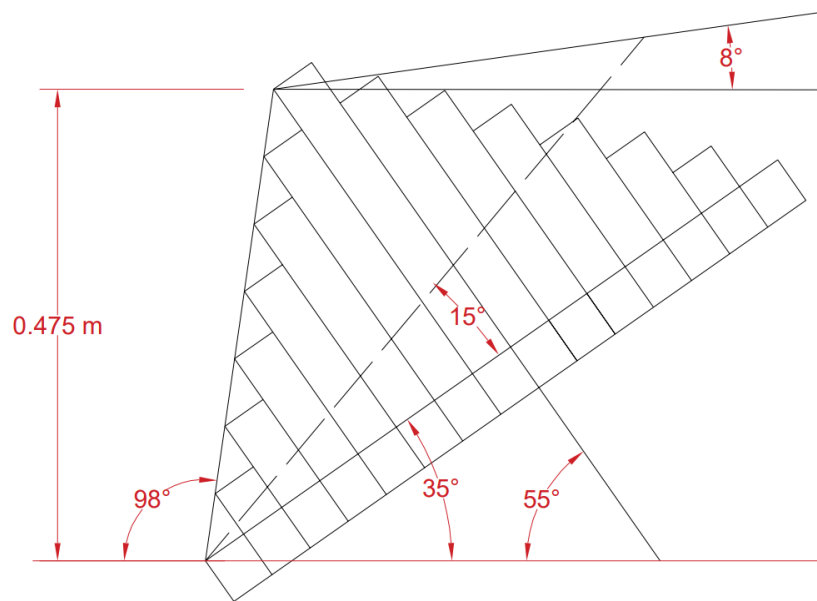


Figure 5-16: The rotated blocks of the ideal arrangement experimental model

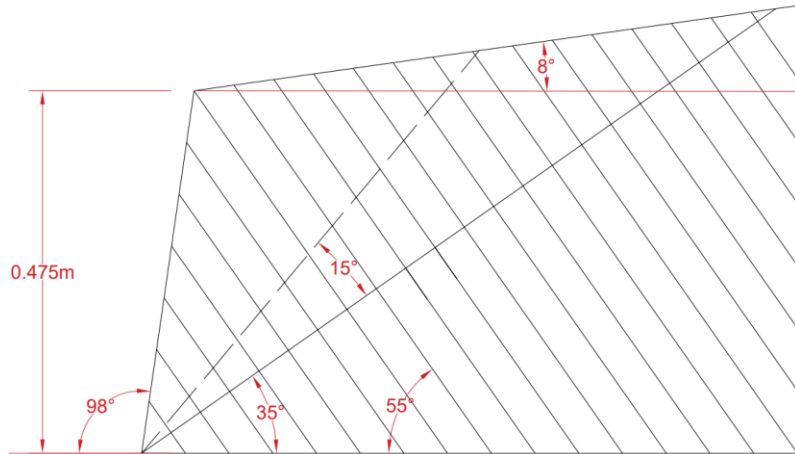


Figure 5-17: The equivalent geometry used to represent the rotated ideal experimental model in the numerical simulation

### 5.3.2 The numerical simulation

The model geometry, including the configuration of the joint set used in the numerical simulation of the equivalent slope, is presented in Figure 5-18. As described earlier, the ideal physical experimental model was rotated to  $35^\circ$ , at which angle the model began to topple; thus, the slope geometry and joint set configuration provide the necessary conditions for toppling failure. In this model, there are two adjacent blocks with different failure potentials: one with block failure potential and the other with flexural failure potential due to its lack of joint base. Therefore, this arrangement of the two adjacent blocks provides block-flexural toppling failure potential for the equivalent slope. To create the slope model in the DEM, particles were generated in a domain that represents the slope's boundary. The boundary of the slope was created using wall segments with a normal stiffness value 10 times greater than that of the particles. This stiffness value was chosen to prevent the particles from escaping the specified domain representing the slope geometry. The model was then run until it reached an equilibrium state. In the next step, the wall boundaries were removed, and the particles were bonded together using parallel bonds. The particle boundary condition was adopted on the right side of the model by fixing the horizontal displacement and on the base by fixing the horizontal and vertical displacements. Sufficient time steps were run so that the model once again reached an equilibrium state. In the final step, the pre-existing discontinuities (i.e., joints) were explicitly assigned in the model using smooth joint contacts. Accordingly, the interaction forces between particles located on either side of a discontinuity can be identified and

reoriented depending on the normal and tangential directions of the line, as explained in Chapter 4. The simulation was then run.

The microparameters and the joint microparameter properties used in the numerical simulation for the equivalent slope are summarized in Table 5-5 and Table 5-6, respectively. These parameters were chosen such that the angle between the total failure plane and the line normal to the discontinuities ( $\varphi$ ) and the layer movements of the layers in the numerical simulation approach the results of the ideal model in the experimental tilting test. The parameters were then calibrated to match the numerical results for the equivalent slope to those of the experimental tilting table tests.

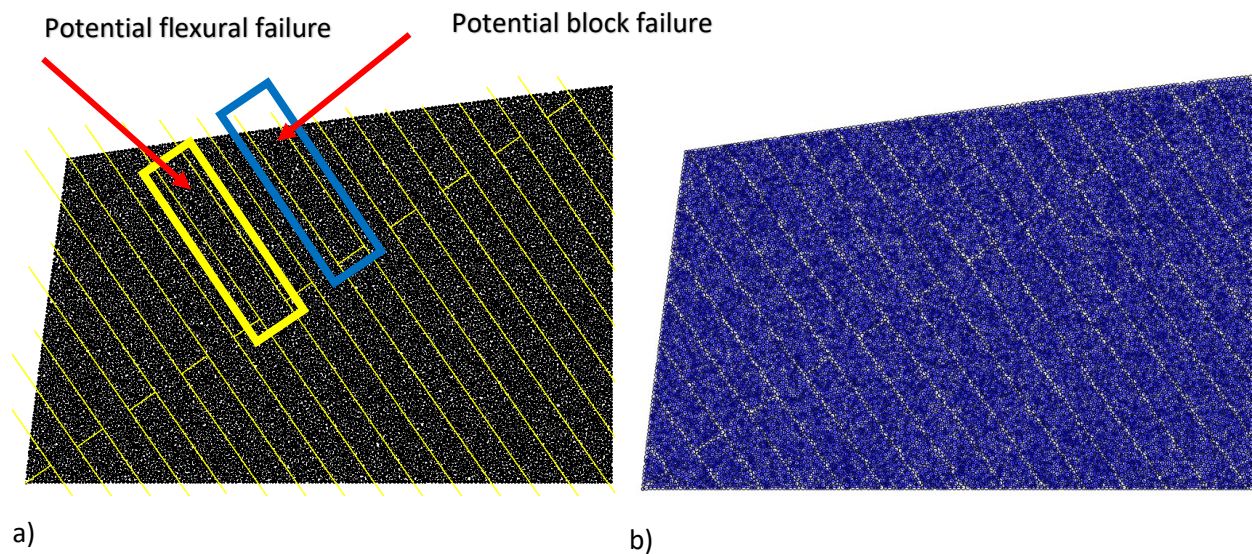


Figure 5-18: a) The geometry of the slope and joint sets used in the numerical simulation of the equivalent slope representing the ideal arrangement of blocks, and b) the corresponding slope model created with particles bonded using parallel bonds and smooth joint contacts

Table 5-5: Microparameters used in the numerical simulation of the DEM for  
The equivalent slope

<b>Parameter</b>	<b>Ideal slope</b>
Minimum particle radius $R_{\min}$ (mm)	1.5
Maximum particle radius $R_{\max}$ (mm)	3.5
Particle density $\rho$ (kg/m <sup>3</sup> )	3000
Young's modulus of particles $E_c$ (MPa)	15.05
Normal-to-shear stiffness ratio of particles ( $k_n/k_s$ )	1.4
Particle friction coefficient $\mu$	0.45
Young's modulus of parallel bond $\bar{E}_c$ (MPa)	15.9
Normal-to-shear stiffness ratio of parallel bonds ( $\bar{k}_n/\bar{k}_s$ )	1.8
Parallel bond tensile strength (kPa)	125
Parallel bond cohesion (kPa)	30.9
Parallel bond friction angle (degree)	10
Parallel bond normal critical damping ratio $\bar{\beta}_n$	0.2
Normal critical damping ratio $\beta_n$	0.13
Height of the slope H (cm)	47.5
Bond gap (mm)	1.05

Table 5-6: Microparameters for smooth joints used in numerical simulation  
in DEM for equivalent slope

<b>Parameter</b>	<b>Ideal slope</b>
Normal stiffness of the base joint per unit area, ( $k_{nj}$ )(N/m <sup>3</sup> )	$12 \times 10^{10}$
Shear stiffness of the base joint per unit area, ( $k_{sj}$ )(N/m <sup>3</sup> )	$12 \times 10^{10}$
Joint friction coefficient of the base	0.23
Normal stiffness of the joint per unit area, ( $k_{nj}$ )(N/m <sup>3</sup> )	$12 \times 10^{11}$
Shear stiffness of the joint per unit area, ( $k_{sj}$ )(N/m <sup>3</sup> )	$12 \times 10^{11}$
Joint friction coefficient	0.12
Joint gap distance (mm)	0.5

The overall failure surface, the blocks' positions, and the recognizable zones are presented in Figure 5-19. These zones are categorized as the stable zone, toppling (tensile) zone and sliding (shear) zone in a slope where block-flexural toppling failure occurs under the effect of gravity. The deformation characteristics of such a slope are complex. Shear sliding deformation at the slope toe occurs and provides movement, including separation or dilatancy sliding, along the joints. This condition then enables the blocks or columns in the middle of the slope to topple under their weight and for the upper part of the slope to move downward. The stable zone, however, remains stable



throughout the toppling failure process, but it experiences slope movement and tension crack formation is clear at the back of the stable zone. The stable zone movement induces displacements to blocks located in the toppling failure zone. Sufficient deformation in the stable zone is required to initiate the toppling failure in the toppling zone. Blocks in the toppling zone, then, topple independently under gravity loads.

The overall failure surface in the calibrated slope is  $15^\circ$  above the normal line of the main discontinuities, as numerically predicted by the DEM. In addition, the stable zone region, comprising five blocks, has complete similarity with the ideal experimental test (see Figure 5-9 and Figure 5-10). Therefore, the equivalent slope that represents the ideal block experimental model was calibrated correctly. This calibrated model will be considered as the base model for further studies of the effects of joint spacing and joint configuration and how the joint set configuration influences the assumptions used in limit equilibrium methods.

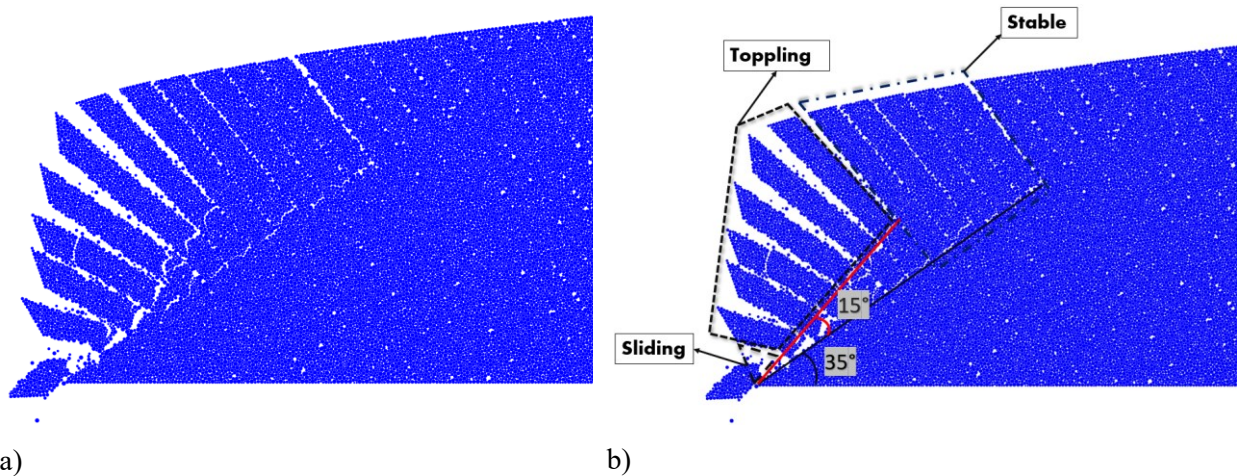


Figure 5-19: The DEM results: a) the overall post-failure surface and movements of the columns, and b) the angle of the overall failure surface with respect to the normal line of main discontinuities, and the stable, toppling, and sliding zones within the block-flexural toppling failure zone

To study the initiation and development of toppling failures of slopes subjected to block-flexural toppling, measurement points were assigned to the slope to record and monitor relevant information, as shown in Figure 5-20. Y indicates the vertical displacement in the y-direction, X indicates the horizontal displacement in the x-direction. The direction of the displacement over time ( $dY/dX$ ) indicates the ratio of the vertical displacement to the horizontal displacement. In this context, the values of X, Y,  $dY/dX$ , and the total displacement were plotted over time and Y was also plotted

directly against X. These parameters were measured at points including the middle face of the slope (point D), the crest of the slope (G), points at the top of the slope around the boundary between the toppling zone and stable zone (H, I), and points around the end of the stable zone (M, N, and O). These measurements for the calibrated model (hereafter called the base model) are presented in Figure 5-20. Labels identifying the columns formed by the joint sets are defined for ease of interpretation. The monitoring points are presented in terms of a letter indicating the slope point where the data are monitored and a number indicating the column formed by the joint sets; for example, G – 7 presents point G on the surface slope belonging to column 7 in Figure 5-20.

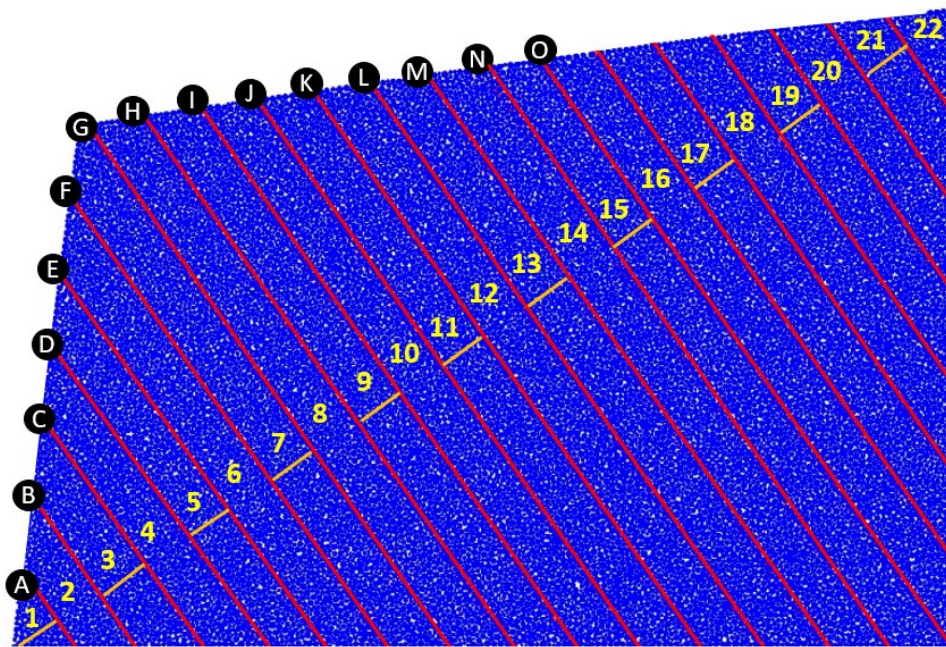


Figure 5-20: Measurement point labels and the label number of columns formed by joint sets

The monitored horizontal and vertical displacements (Figure 5-21 (a) – (f), respectively) demonstrate that the whole slope underwent movement up to column O-15; however, the movements of columns toward the back of the slope (from columns 14 to 15) show a marked decrease in displacement between point M-13 and point N-14, with much less change recorded between N-14 and O-15. In the stable zone located between columns 9 to 13 (presented in Figure 5-19 (b)), the horizontal and vertical displacements I-9 and M-13 show a significant difference:

while they are both still in the stable zone, the movement of the columns decreases upslope. In addition, the separation between the columns also decreases in this direction. Figure 5-21 (c) shows the displacement direction of the monitoring points in terms of  $dY/dX$ . The horizontal red dashed line indicates the value of  $\tan(90-\delta)$ , which is used to determine the displacement direction. When  $dY/dX$  is less than 0.7, the displacement direction angle with respect to the horizontal line is less than the angle normal to the joints with respect to the horizontal line. When the  $dY/dX$  values versus time plot in a horizontal line, the sense of displacement of the monitoring point does not change. The displacement directions of points O-15, N-14, and points in the stable zone (I-9 and M-13) remain largely stable after the initial displacement. In addition, the displacements of these points do not increase after 0.13 s, as shown in Figure 5-21 (d) and (e). In contrast, the measuring points H-8, G-7, and D-4, which are in the toppling zone, exhibit continuous displacement and the direction of their displacements changes over time. Figure 5-21 (c) shows that the direction angles for the H-8 and G-7 measuring points exceed the normal to the joints.

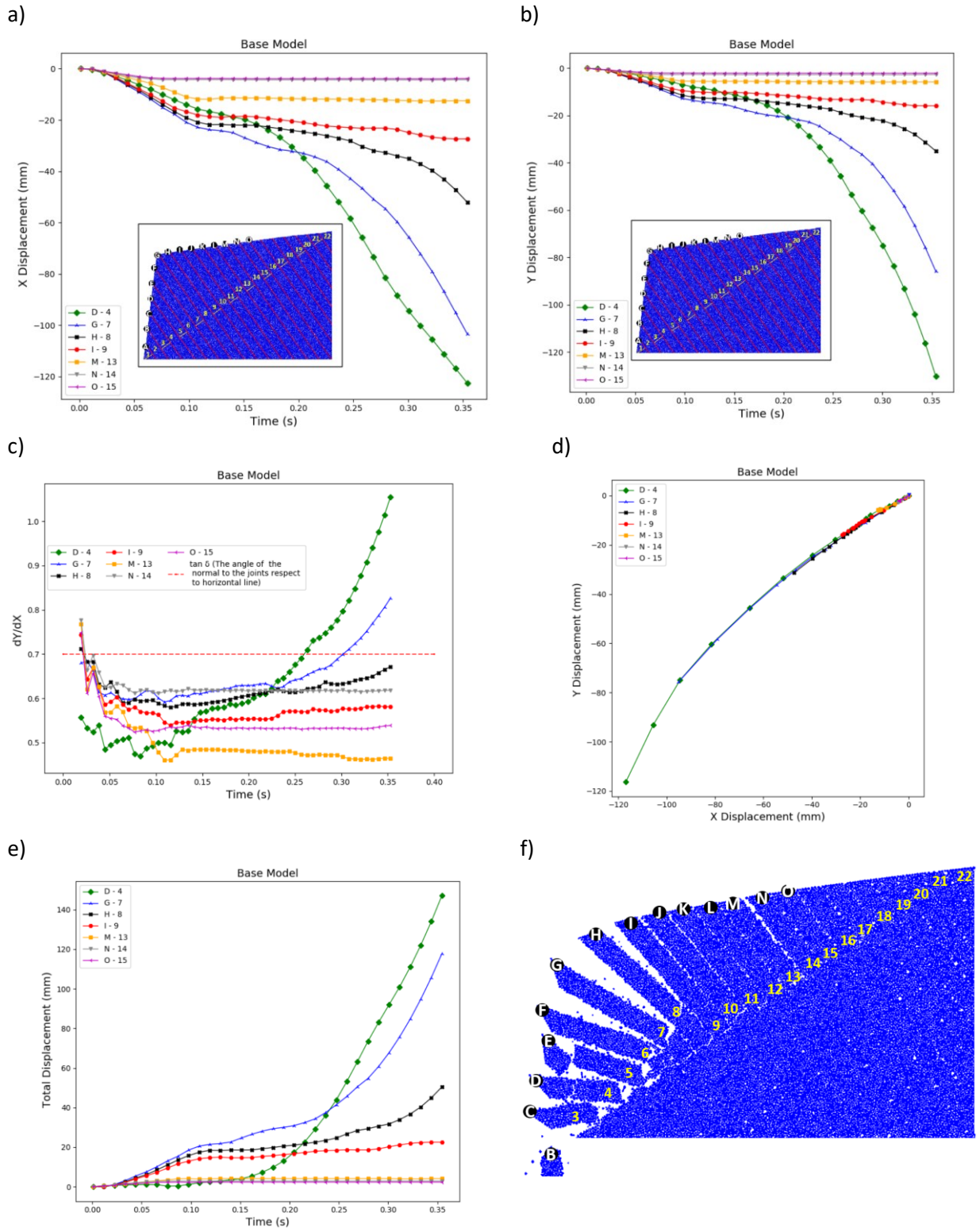


Figure 5-21: Data measurements recorded at monitoring points on the slope surface in the base model. (a) Horizontal displacement (X), (b) vertical displacement (Y), (c) vertical displacement over horizontal displacement ( $dY/dX$ ) over time, (d) vertical displacement (Y) versus horizontal (X) displacement, (e) total displacement, and (f) the position of the columns at the end of the simulation

### 5.3.3 The effects of joint on a block – flexural toppling failure

The limit equilibrium-based method used to analyze the block-flexural toppling failure proposed by Amini et al. (2012) considered a main joint set (i.e., a group of joints with the same dip and strike angle and identical joint spacing) dipping into a slope (see Figure 5-22). In addition, the base joint set was assumed to cross every other column of rock between the main joints. The objective of this section is to investigate the effect of the joint spacing, the configuration of the base joints, and the joint friction on the block-flexural toppling failure, in addition to assessing the overall failure rupture surface on slopes with the potential for block-flexural toppling failure.

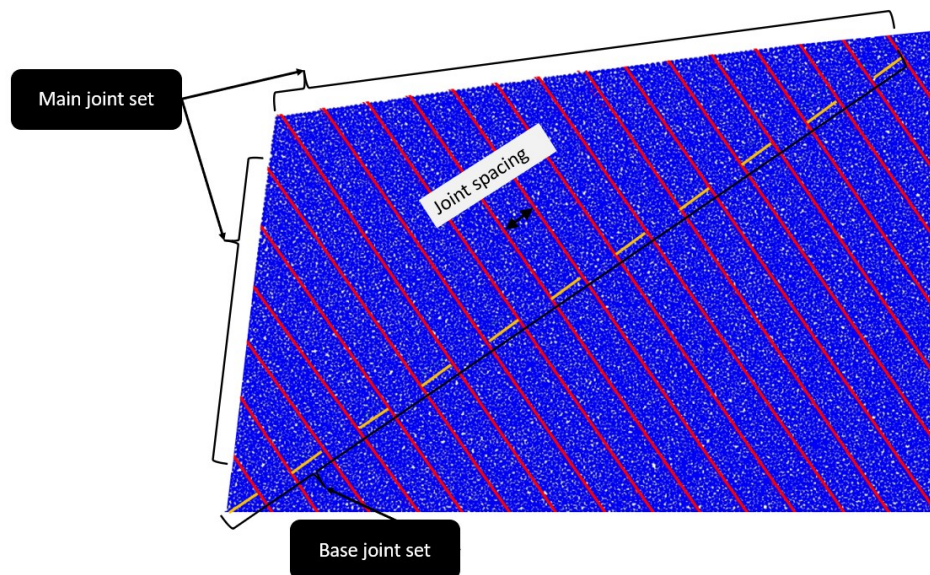


Figure 5-22: Illustration of the main joint set, base joint set, and joint spacing

#### 5.3.3.1 Influence of persistence and spacing of discontinuities

The influence of the spacing and persistence of the discontinuities or joints are investigated in this section.

In the assumptions of the limit equilibrium method outlined by Amini et al. (2012) to analyze the block-flexural toppling failure, two adjacent blocks cannot have the same potential failure (blocky failure or flexural failure); therefore, each adjacent block has the potential for a blocky or flexural toppling failure. Hence, the base joint set was assumed to cross every other main joint set that dips

into the slope (see Figure 5-23). The assumption outlined by Amini et al. (2012) in the limit equilibrium method considers the average spacing of the joint set and one specific persistence of the base cross-joint set. Kim et al. (2006) presented that since discontinuities can dominate the mechanical behavior of a jointed rock mass, certain assumptions cause inevitable errors in rock mass characterization. Joints are usually considered fully persistent for the stability analysis of tunnels or slopes; a simplification that causes overestimation of the size of the joints and thus leads to increasing the project costs. In contrast, accurately estimating the persistence of joints results in economical designs. Therefore, to achieve more accurate results, discontinuities should be measured in detail as part of the geological mapping of rock exposures.

Joint persistence can also affect the behaviour of block-flexural toppling failure mechanisms. Therefore, this section investigates the effect of the persistence of the joint base and the main joint spacing on the overall failure surface and the toppling and stable zones in slopes prone to block-flexural toppling failure.

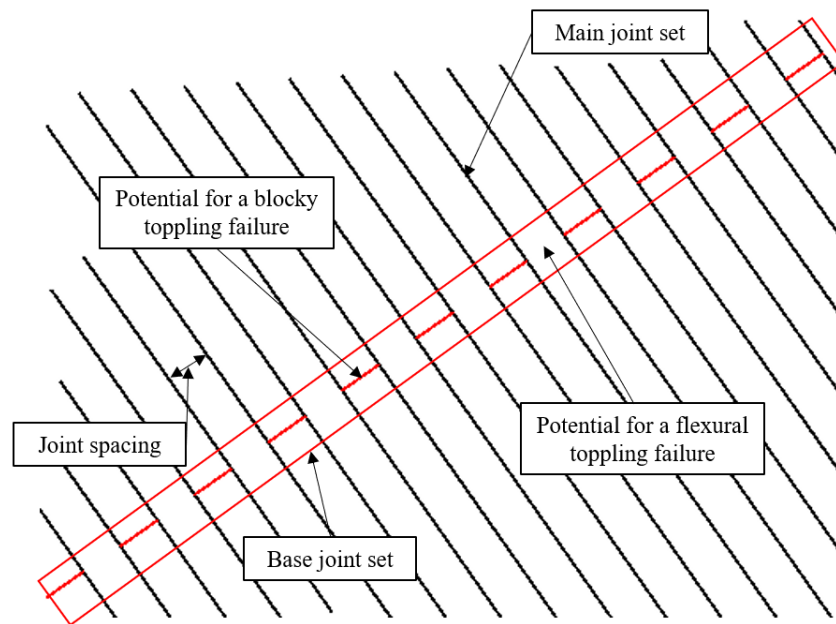


Figure 5-23: The assumptions used in the limit equilibrium method to analyze block-flexural toppling failure by Amini et al. (2012)

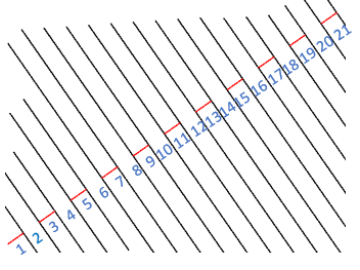
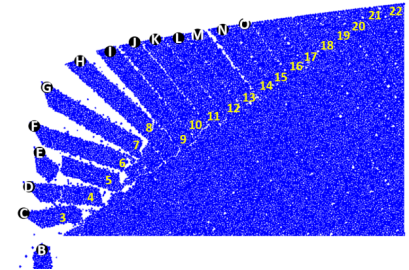
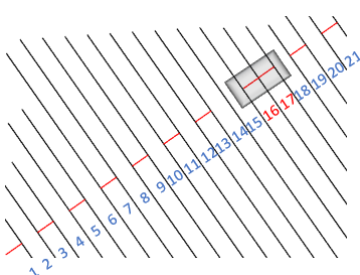
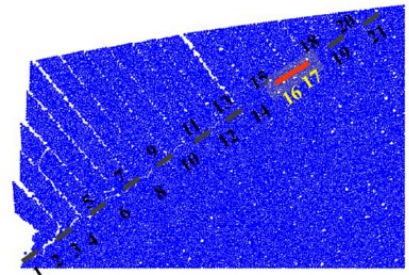
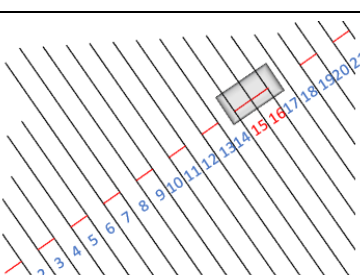
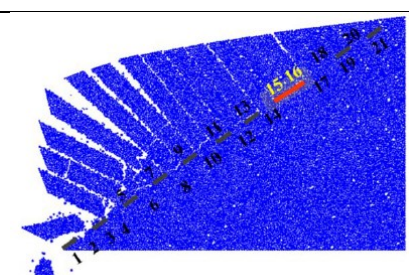
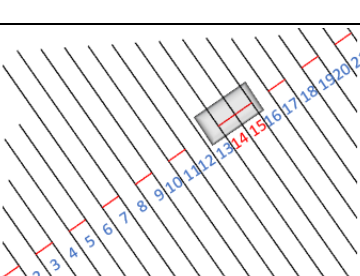
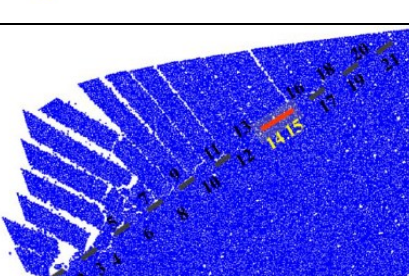
### 5.3.3.2 Influence of joint base configuration (the joint set persistence)

#### *Influence of two merged joints of the base joint set*

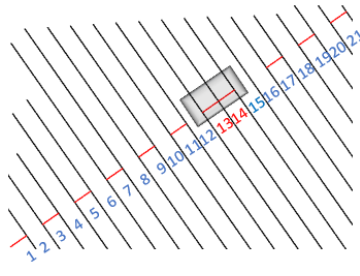
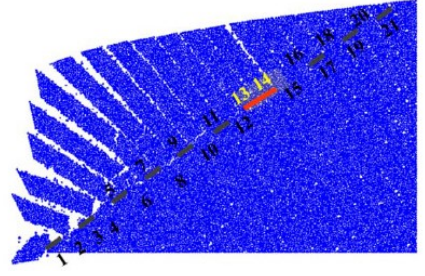
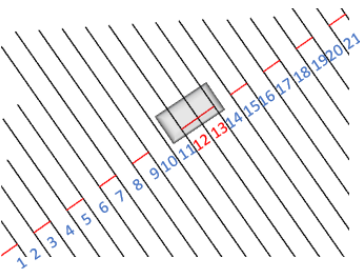
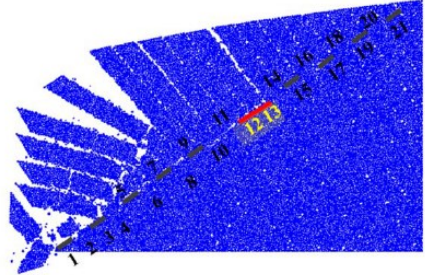
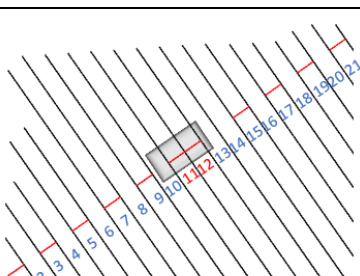
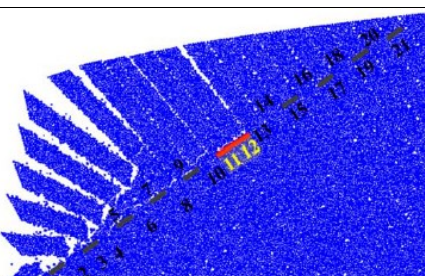
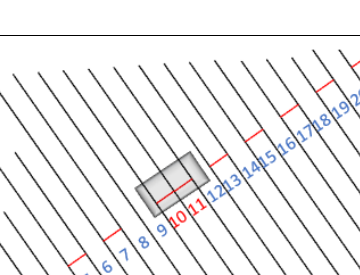
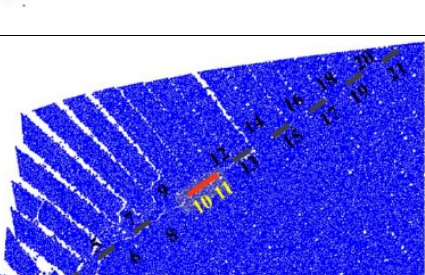
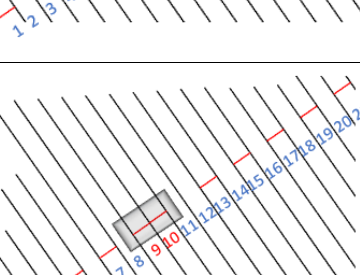
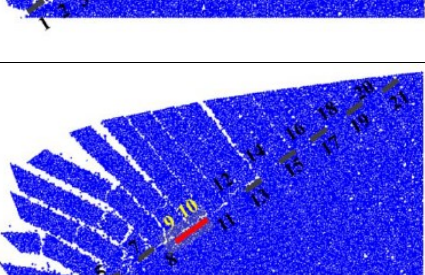
The model with identical joint sets presented in Figure 5-23 was chosen as the base model for this analysis. Note that the calibration and validation of this model were presented in detail in section 5.3.2. This model includes assumptions that lead to block-flexural toppling failure potential. The base joint set persistence is such that the base joint set crosses every other main joint set that dips into the slope.

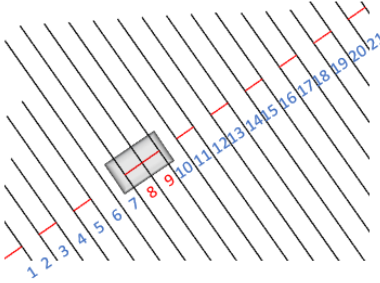
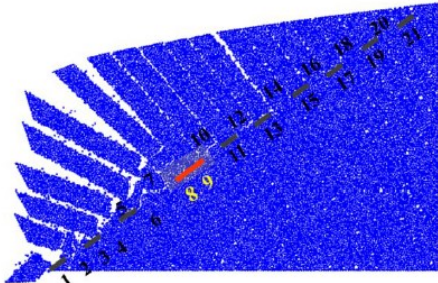
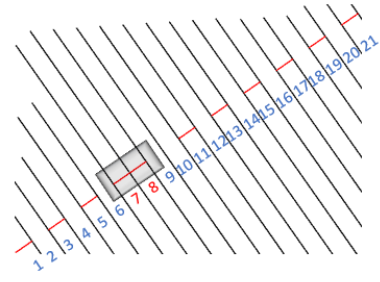
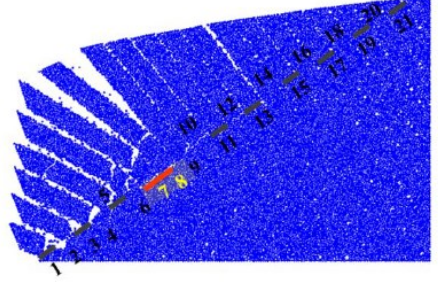
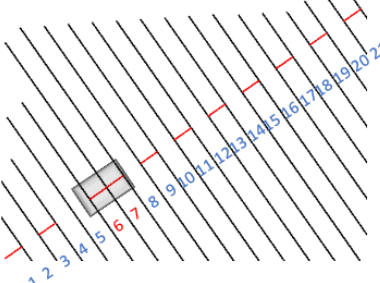
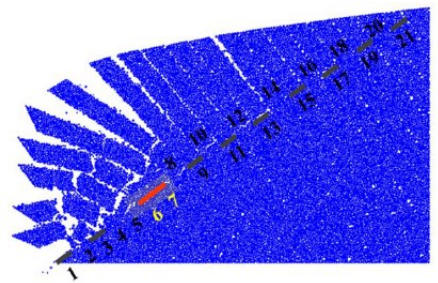
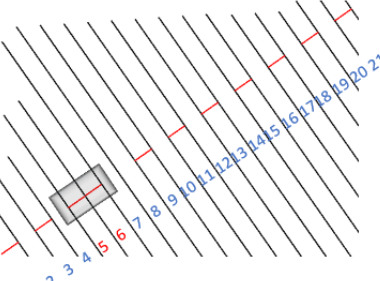
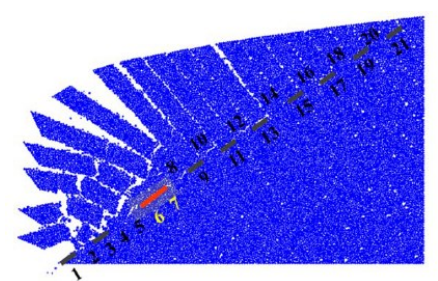
In practice, the true characteristics of joint surfaces are not accurately known, and measuring rock bridges (or the persistence of joints) is challenging in the field (Elmo et al. 2022). Therefore, 16 cases were analyzed to determine whether the persistence of the joint base had any effect on the toppling failure mechanism. In each model, a different pair of adjacent base joints was merged into a single joint, while the positions of the other base joints were maintained to provide block-flexural toppling failure potential. Table 5-7 presents the joint configurations for case studies I to XVI. In case I, the merged joint was located toward the top of the slope between columns 17 and 16. With increasing model numbers, the position of the merged joints moved toward the slope's toe, with the merged joint located between columns 2 and 1 in case XVI. Table 5-7 shows the columns' positions and the total failure surface at the end of the simulation for all the simulated cases. In each case, the blocks where the merged joint is located are indicated in the format (N2-N1) in the first column of Table 5-7. N2 and N1 indicate the column numbers corresponding to the merged joints. Table 5-7 also includes the base model to allow a comparison between this configuration and the other cases.

Table 5-7: Joint set configuration, and the position of the blocks and total failure plane for different joint configurations

Case/ (Block number)	D/H	Joint set configuration	$\phi^\circ$	The position of the columns and the total failure plane
Base model	-		15	
I (17-16)	1.31		-	
II (16-15)	1.22		15	
III (15-14)	1.14		24	



Case/ (Block number)	D/H	Joint set configuration	$\phi^\circ$	The position of the columns and the total failure plane
IV (14-13)	1.07		20	
V (13-12)	0.99		17	
VI (12-11)	0.88		17	
VII (11-10)	0.82		12	
VIII (10-9)	0.74		12	

Case/ (Block number)	D/H	Joint set configuration	$\phi^\circ$	The position of the columns and the total failure plane
IX (9-8)	0.65		12	
X (8-7)	0.57		14	
XI (7-6)	0.48		15	
XII (6-5)	0.4		13	

Case/ (Block number)	D/H	Joint set configuration	$\phi^\circ$	The position of the columns and the total failure plane
X III (5-4)	0.32		18	
X IV (4-3)	0.23		14	
X V (3-2)	0.15		27	
X VI (2-1)	0.08		27	

Figure 5-25 shows the simulation results for the 16 cases, including the base model, with HDPAC. D is the horizontal distance from the center of the merged joints to the toe of the slope and H is the slope height (see Figure 5-24(a)).  $\phi$  is the angle between the total failure plane and the line normal to the discontinuities, T is the horizontal distance between the top of the stable zone and the slope

toe, and  $S$  is the horizontal distance between the top part of the slope without any movement, marked by the red dashed line in Figure 5-24(b) and the slope toe. Lines 1 and 2 in Figure 5-25 illustrate the  $S/H$  and  $T/H$  values, respectively, for the base model on the  $X$ -axis ( $D/H$ ).

The top end of the part of the slope that has no movement can be obtained in all cases from the  $S/H$  value. In general, the  $S/H$  value is 0.8, which is very close to the value of 0.79 observed in the base model. This similarity means that the top part of the slope with no movement is identical to that of the base model, while the merged jointed positions ( $D/H$ ) vary from 0 to 0.79 (Line 1) which is the base model's  $S/H$  value. However, in case VI, the  $S/H$  value drops to 0.67, which indicates that the part of the slope with no movement is extended and approaches the slope face, and then moves further from the slope face when the position of the merged joint  $D$  is located further from the slope toe. The highest value of 1.14 is observed for case II. In case I (the stable case in which no toppling failure occurred), the  $S/H$  value was 0.79, very close to the value for the base model. These results indicate that the part of the slope in which no movement occurs is not affected when the merged joint position is located at a distance less than the  $S/H$  value of the base model. However, when the position of the merged joint is further from the slope face and passes the zone with no movement of the base slope (i.e., cases II to VI), movement will occur in the previously non-moving portion of the slope. In addition, case I demonstrates that locating the merged joint such that  $S/H$  is 0.8 provides a stable condition for the slope that failed in the base model; in this case, the non-moving part of the slope changes to become close to the slope face, approaching that of the base model. Since the two columns (14 and 15) after joint merging provide adequate strength, stable conditions are observed in the slope that was formerly toppled in the base model.

The  $T/H$  values for all cases show that the top corner of the stable zone, which is close to the slope face, varies between values of 0.15 and 0.32. The results indicate that when  $D/H$  is less than the  $T/H$  value of the base model (0.2), the position of the merged joint does not influence the stable zone. However, when the merged joint is located further from the slope face and the  $D/H$  value increases, the  $T/H$  values fluctuate between 0.15 to 0.32. For cases IV to VI, the  $T/H$  values are very similar to those of the base model.

Table 5-7 and Figure 5-25 show that the angle between the total failure plane and the line normal to the discontinuities ( $\phi$ ) varies between  $13^\circ$  and  $27^\circ$  for all cases. The effect of the merged joints on the  $\phi$  value is clear: the  $\phi$  value changes significantly when the merged joint occurs near the slope toe or in the zone with no movement. In either of these scenarios, columns 1 and 2 of the

slope toe slip and thus cannot bear any bending forces. Therefore, the lack of contributions from the shear and bending strengths of these columns at the slope toe significantly affects the  $\phi$  value for cases XV and XVI. The results also reveal that a single failure plane evolves into two failure planes in cases III, VIII, XV, and XVI.

In conclusion, measuring accurate joint persistence in the field and in real rock slopes is very complicated. The assumptions used in the limit equilibrium method for the analysis of block-flexural toppling failure have been over-simplified. Therefore, the possibility of a merged joint and its impact on the assumptions used to define the plane surface in limit equilibrium methods should be considered. This numerical study was conducted to investigate the effect of merging on the adjacent joint base in the analysis of block-flexural toppling failure.

The assumed angle between the total failure plane and the line normal to the discontinuities ( $\phi$ ) in the limit equilibrium analysis proposed by Amini et al. (2012) is based on the centrifuge physical modelling of Adhikary et al. (1997) and physical model tests by Aydan and Amini (2009) and takes values in the range 0–15°. The physical model tests were mostly performed for flexural toppling failure. However, the calibrated DEM numerical simulations indicate that the value of  $\phi$  is 15° for slopes with block-flexural toppling failure, consistent with the physical test results.

The presence of a persistent cross-base joint changed the  $\phi$  value. With various cross-base joint configurations and merged joints,  $\phi$  varied between 13–27° and, in some cases, a single failure plane changed to two failure planes. In addition, while these changes did not affect the toppling failure zone in the simulations, the stable zone and no-movement zone of the slope were affected. Identifying the stable zone and the no-movement zone of the slope provides useful information for slope stability analyses and tunnelling projects.

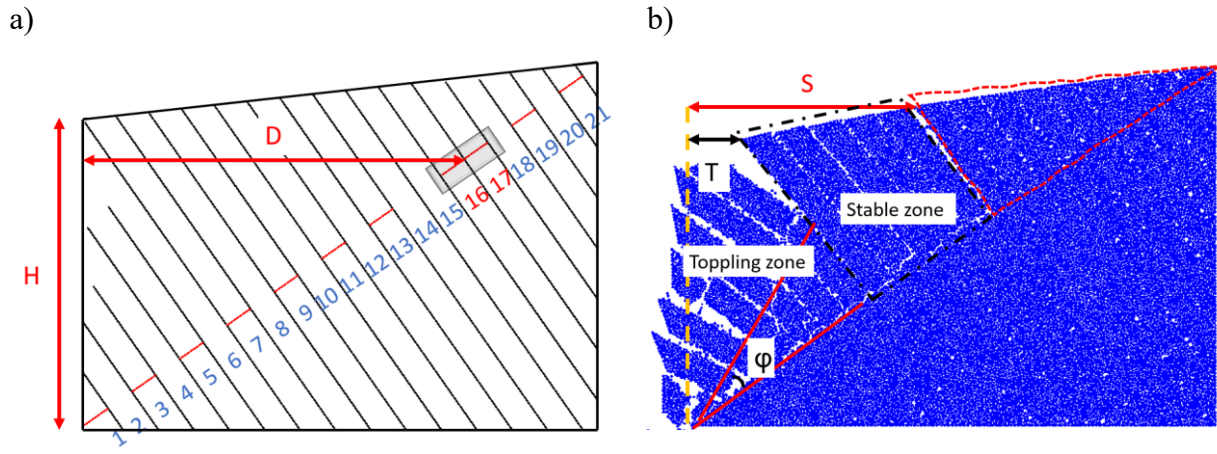


Figure 5-24: Definition of the parameters used in Figure 5-25

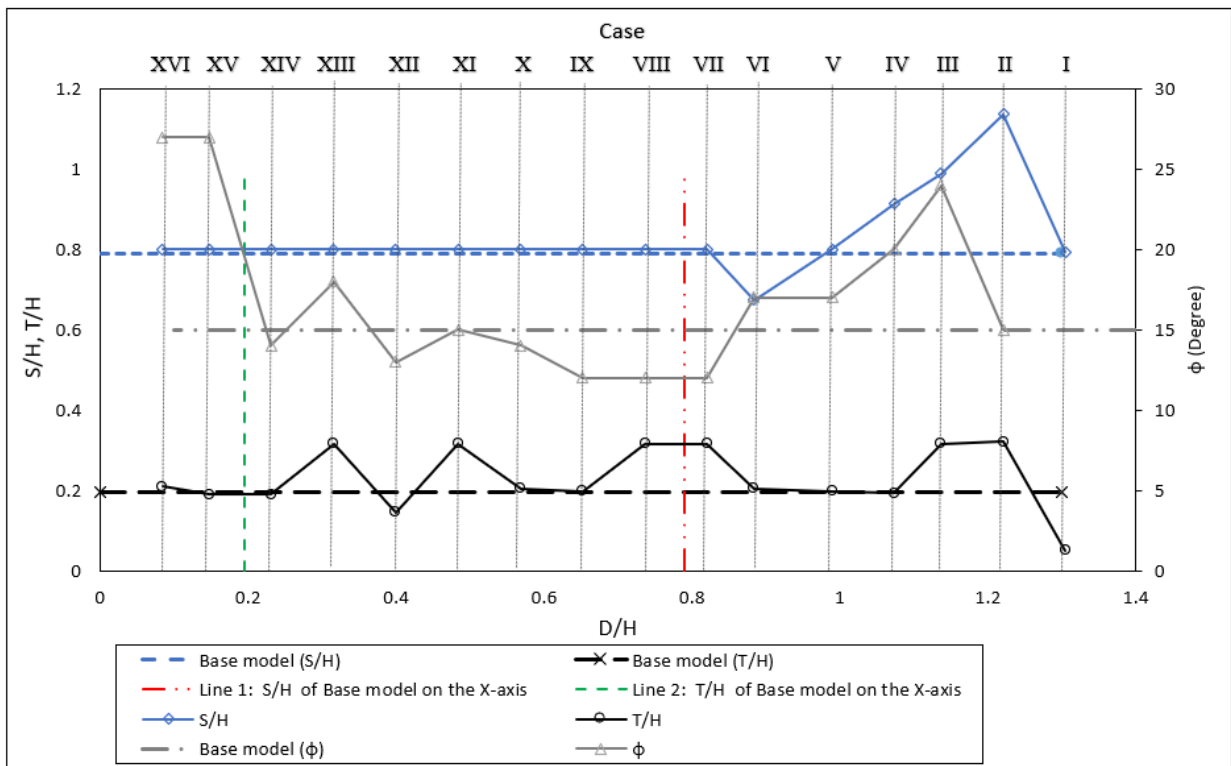


Figure 5-25: Plot illustrating the normalized horizontal distance between the top of the stable zone and the slope toe (T/H), the normalized horizontal distance between the top of part of the slope without any movements and the slope toe (S/H), and the angle between the total failure plane and the line normal to the discontinuities versus the normalized horizontal distance from the center of the merged joints to the slope toe (D/H) for cases I to XVI

### ***Influence of the joint base configuration***

To better understand the effect of the base joint set, five cases were simulated with different joint base configurations, and their results were compared with the results of the pre-calibrated model (the base model) results. The base model was used for every case, and only the base joint configuration was altered. These configurations are illustrated in Table 5-8, which also presents the S/H, T/H and  $\phi$  values (defined earlier) and the total failure plane for each numerical simulation scenario.

Block toppling occurs when a single continuous base joint set is defined in a model; therefore, in case I, the base model was modified only by introducing a single continuous joint base with the same micromechanical properties used in the base model, as illustrated in Table 5-8.

Flexural toppling occurs in a slope when no base joint set is defined in the model and continuous columns are separated by steeply dipping discontinuities; therefore, cases II and III were modeled without defining a joint base. Case III has a joint base in the sliding zone crossing columns 1 to 3 at the slope toe to provide the required deformation in the slope to fail (Table 5-8).

To consider the persistence of the base joint set, every two separated base joints in the base model were combined to make a single longer joint crossing two columns in case IV (Table 5-8).

Case V has a second cross-joint set added to the base model at a distance of 0.13 m from the initial joint cross-joint set. 0.135 m is the approximate distance between the 3 columns. Note that the assumptions used in the limit equilibrium method for block-flexural toppling failure are (1) either one block with the potential for blocky toppling failure situated between two blocks with flexural toppling failure potential or (2) one block with the potential for flexural toppling failure situated between two blocks with blocky toppling failure potential (Amini et al. 2012); therefore, three columns are involved in each case.

Table 5-8 presents the S/H, T/H and  $\phi$  values (defined earlier in section 5.3.3.2) and the total failure plan for the numerical simulation of each case.

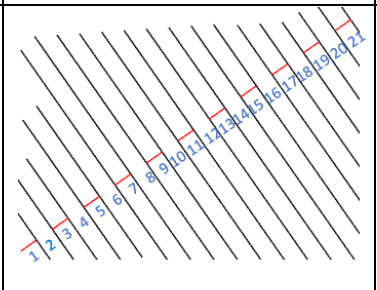
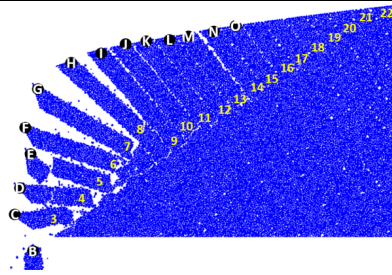
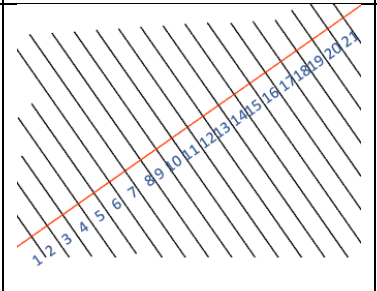
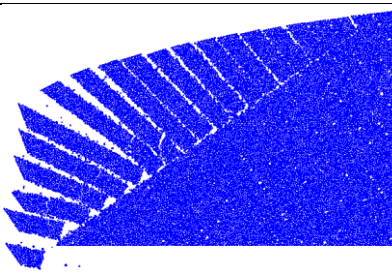
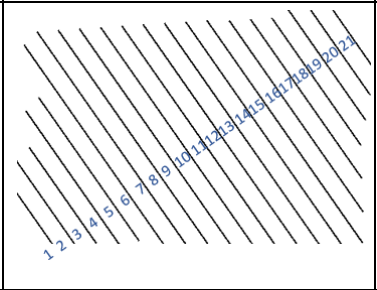
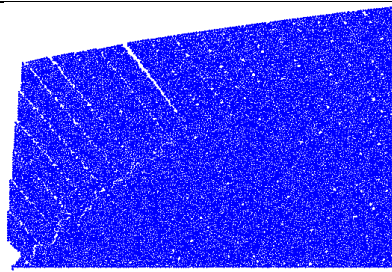
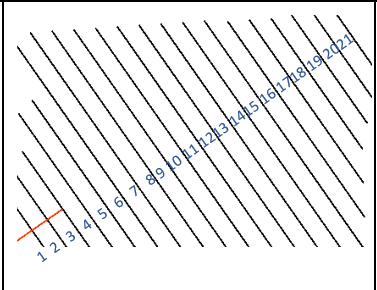
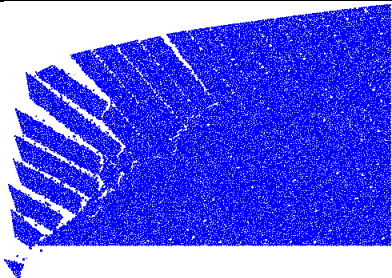
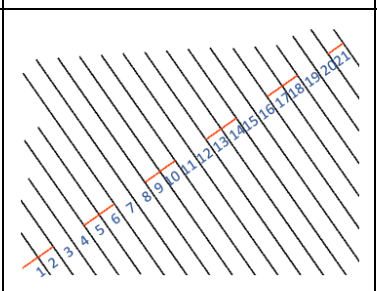
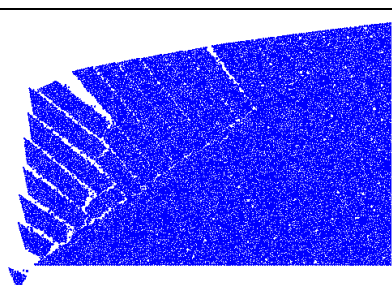
Case I shows that the no-movement zone upstream of the slope and the stable zone move, and that both get distance from the toe of the slope. The value of the overall plane surface angle ( $\phi$ ) is changed and reduced to zero when it is compared to the base model. The stable zone of the slope in general is reduced.

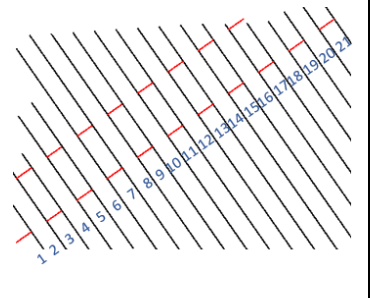
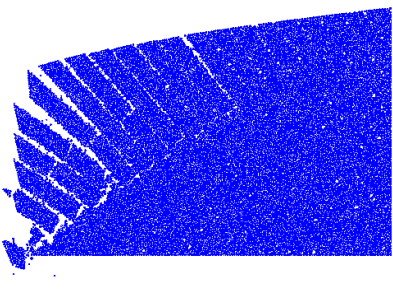
Case II is stable and no toppling failure was observed in the numerical simulation. The part upstream of the slope with no movement approaches the toe of the slope. However, to provide the initial sliding at the toe of the slope, case III was defined. The no-movement part of the slope and the stable zone location are close to those of the base model, but the overall failure plane surface angle ( $\phi$ ) was smaller, reduced from  $15^\circ$  to  $12^\circ$ . As all the base model micro parameters are used in this case, it seems that increasing the strength of the material is required to impose the flexural toppling failure behavior in the slope.

Case IV (in which every two joints of the joint base set are combined) and case V (two different base joint sets) both showed similar characteristics in the no-movement zone and the stable part of the slope; however, the overall plane failure angles ( $\phi$ ) for cases IV and V are steeper than that of the base model at  $26^\circ$  and  $31^\circ$ , respectively. In addition, the overall plane surfaces were not singular in both cases. Although case IV and the base model have a similar discontinuity persistence ratio (PR), their overall plane failure angles ( $\phi$ ) are different, and only the no-movement zone of the slope is similar in both cases.



Table 5-8: Joint set configuration, and the position of the blocks and total failure plane for different joint configurations

Case	Joint sets configuration	S/H	T/H	$\varphi^\circ$	The position of the columns and the total failure plane
Base model		0.79	0.2	15	
I Block failure		1.58	1.24	0	
II Flexural failure		0.57	0	0	
III Flexural failure with base joint		0.7	0.19	12	
IV Combined every two joints of the joint base set		0.93	0.2	26	

Case	Joint sets configuration	S/H	T/H	$\varphi^\circ$	The position of the columns and the total failure plane
V Two different base joint sets		0.8	0.2- 0.3	31	

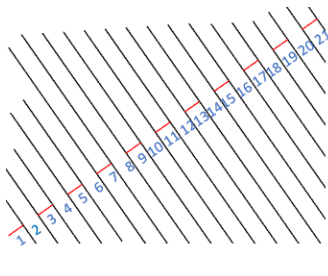
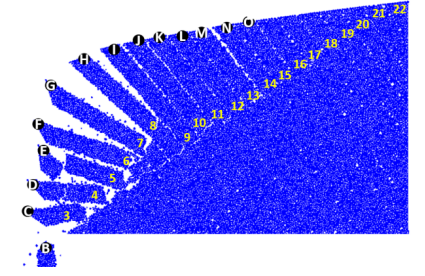
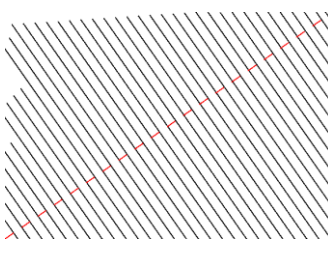
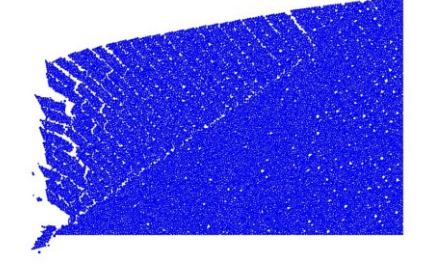
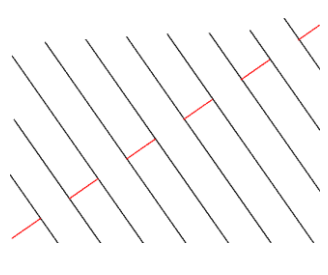
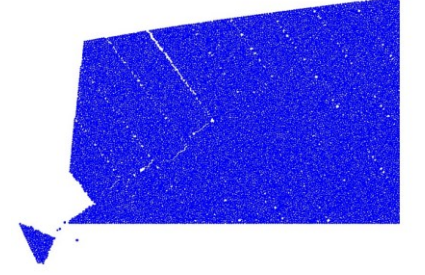
### *Influence of rock joint spacing*

In this section, the effects of joint spacing on slopes with block-flexural toppling failure are investigated. This analysis uses the initial geometry and microparameters of the base model. Analyses were performed for two different cases: small spacing (I) and wide spacing (II). Joint spacings half (2.35 cm) and double (9.4 cm) that of the base model were considered in cases I and II, respectively.

The S/H, T/H and  $\varphi$  values (defined earlier in section 5.3.3.2) and the total failure plane or the rupture surface patterns for these two cases and the base model are shown in Table 5-9. The results indicate that the stable zone, the part of the slope without movement and the overall failure plane all changed. Case II was stabilized; the no-movement zone approached the slope face and no rupture surface was observed. The strength of the column at the bottom of the slope close to the toe provides adequate resistance and thus the slope does not fail.

Case I exhibits significant changes in the stable zone, and the boundary of the no-movement zone shifted toward the back of the slope. In addition, the angle of the overall failure surface changed markedly, becoming a steep slope, with an increase in the angle of the overall failure surface from  $15^\circ$  to  $26^\circ$ . In addition, the results indicate that the columns failed because the decrease in their thickness reduced the bending and shear capacity of the blocks. Accordingly, several stepped failure planes or rupture surfaces can be observed, and the single rupture surface of the base model changes to multi-plane failure. Overall, these results indicate that the joint spacing of the main joint set has a marked impact on the overall failure plane and stability of slopes with the potential for block-flexural toppling failure.

Table 5-9: Joint spacing configuration for the main joint set, and the position of the blocks and total failure plane for two different joint configurations

Case	Joint sets configuration	Spacing thickness (m)	S/H	T/H	$\varphi^\circ$	The position of the columns and total failure plane
Base model		0.047	0.79	0.2	15	
I Small spacing		0.0235	1.15	0.3	26	
II Wide spacing		0.094	0.57	0	0	

### 5.3.3.3 Effect of joint friction

The process of weathering involves both physical and chemical changes that act continuously to reduce the shear strength of rock masses by reducing the strength of the intact rock and the shear strength of discontinuities. Wyllie and Mah (2004) presented that the walls of discontinuities are also influenced by the rock strength: a reduction in the strength will influence the surface roughness. Under high stresses, the asperities will be sheared off, decreasing the roughness component of the

friction angle of the wall discontinuities. Note that the friction angle of a rough surface is determined by the friction of the rock material and the interlocking of irregularities (asperities) on the surface. The shear strength of discontinuities is also affected by the thickness and properties of filling material or by the lack of material in discontinuities. Zhang (2016) stated that weathering can also affect the filling material and reduce its roughness and irregularity, thus contributing to changes in its shear strength. Given these processes in real-world rock masses, the effects of discontinuity strength on block-flexural toppling failure must be investigated.

Analyses were conducted to investigate the effect of the friction angle of the main columnar joint set on the failure surface pattern and the progression of block-flexural failure. The initially calibrated model (the base model) with similar microparameters was used in this study, with only the friction angle of the main joint set ( $J\phi$ ) changed. For the main joints, several numerical simulations were performed by changing the friction angle ( $J\phi$ ) from 0–31° while all other rock and joint microparameters were treated as constants, as presented in Table 5-5 and Table 5-6, respectively. The friction angles ( $J\phi$ ) and the friction coefficients (Fric) used for the main columnar joint sets are listed in Table 5-10.

Table 5-10: Joint friction angle values of the main columnar joint set used in the studied models

Case	Joint Friction angle ° ( $J\phi$ )	Friction coefficient (Fric)
1(base model)	6.8	0.12
2	0	0
3	10	0.176
4	14.6	0.26
5	19.8	0.36
6	24.7	0.46
7	29.25	0.56
8	30.11	0.58
9	31	0.6

Table 5-11 shows the total failure plane and deformation patterns of the slope, in addition to coloured contour shading of the total velocity (V) for different joint friction. For each case, the friction coefficient used in the main joint set for the numerical simulation is also presented. Measurement points C-3, G-7 and M-13, located near the toe on the face of the slope, at the crest, and upslope (approximately at the end of the stable zone on the slope’s surface), respectively, were selected to record the total, horizontal and vertical displacements. The measuring points are labelled in X-Z format, where X indicates the measuring point label and Z indicates the column

number of the slope (see Figure 5-26 (d)). A model with a  $6.8^\circ$  friction angle (friction coefficient of 0.12), calibrated earlier, was considered as the base case. The total, horizontal and vertical displacements for the measuring points are shown in Figure 5-26 to Figure 5-28, respectively, for cases 1 to 9.

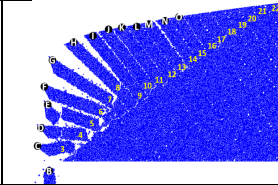
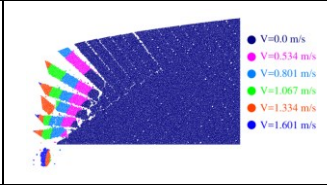
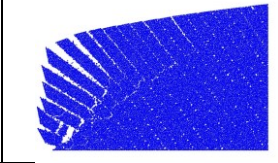
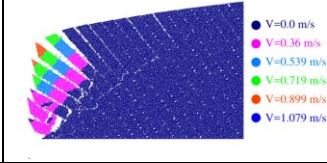
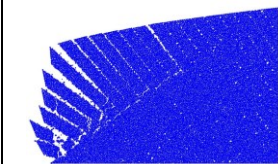
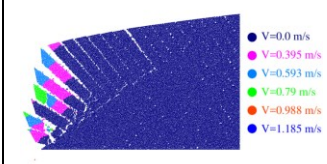
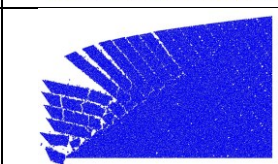
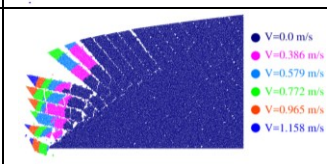
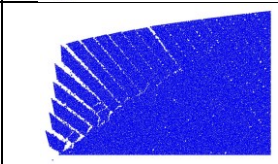
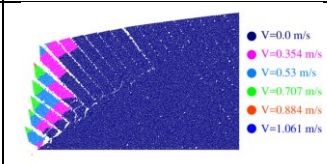
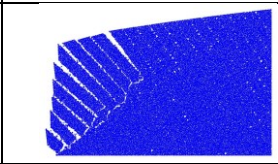
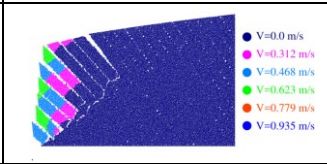
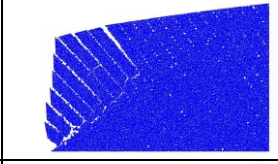
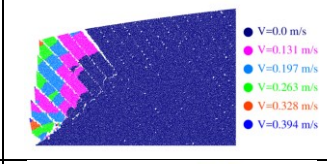
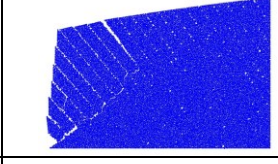
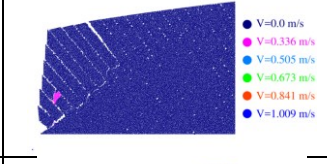
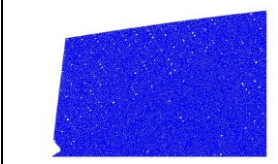
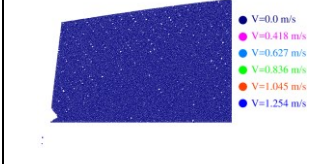
We present Figure 5-29 to better visualize the influence of  $J\phi$  on the stable zone of the slope, on the boundary of the slope with no movement and on  $\phi$ . All parameters used in this figure are described in section 5.3.3.2. The numerical simulation results demonstrate that case 9 ( $J\phi=31^\circ$ ) is the most stable slope with no failure surface observed in the model; note that this case is not presented in Figure 5-29.

In general, as the joint friction angle ( $J\phi$ ) of the main joint set was decreased from  $16^\circ$  to  $7^\circ$ , the  $\phi$  value shows a decreasing trend, with the main fracture path oriented at angles of  $16^\circ$  to  $7^\circ$  above the normal to the main joint dip angle Figure 5-29. The overall failure plane is a single surface in scenarios with high joint friction angles; however, two failure plane surfaces are observed in cases 1 to 5 (Table 5-11).

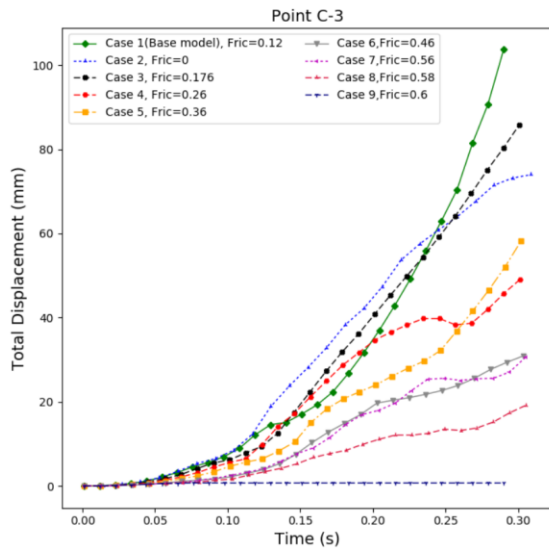
As shown in Figure 5-29, the plane failure length in cases 6 to 8 is shorter than that of the other cases, the toppling zone and stable zone are in the same area and the values of  $S/H=T/H$  are equal to 0.44. In these three cases, the no-movement zone of the slope is close to the toe, whereas in case 2, in which there is no friction in the main joint set, this zone is at the greatest distance from the toe ( $S/H=1$ ). The no-movement zones of the slopes in cases 3, 4 and 5 are similar to that of the base model; in these cases, the  $S/H$  value is 0.8. The beginning of the toppling zone in case 2 and in cases 6 to 8 all occur in the same location, i.e.,  $T/H$  is 0.4.

In general, changing the friction angle of the main joint set from  $10^\circ$  to  $20^\circ$  (cases 3 to 5) has relatively little influence on the configuration of the different zones of the slope (stable zone, toppling zone and no-movement part of the slope) relative to the base model. However, for these cases, the total vertical and horizontal displacements of measuring point M-13 exhibit marked differences during the analysis time but converged at the end of the analysis. The displacements of measuring points M-13 and G-7 (at the crest) show similar trends in cases 6 to 8. However, the crest of the slope (V) shows significant deformation compared to the stable zone.

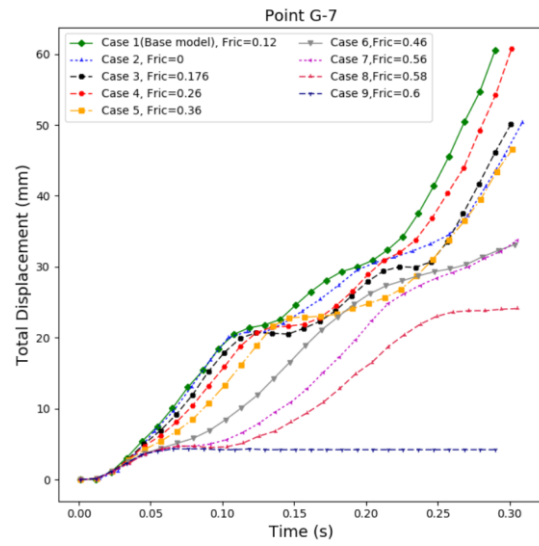
Table 5-11: Total failure plane and deformation patterns of the slope for nine different joint friction angles of the main columnar joints

Case	Friction Coefficient	Total failure plane /deformation pattern	Total Velocity (v)
1 (Base model)	Fric=0.12		
2	Fric=0		
3	Fric=0.176		
4	Fric=0.26		
5	Fric=0.36		
6	Fric=0.46		
7	Fric=0.56		
8	Fric=0.58		
9	Fric=0.6		

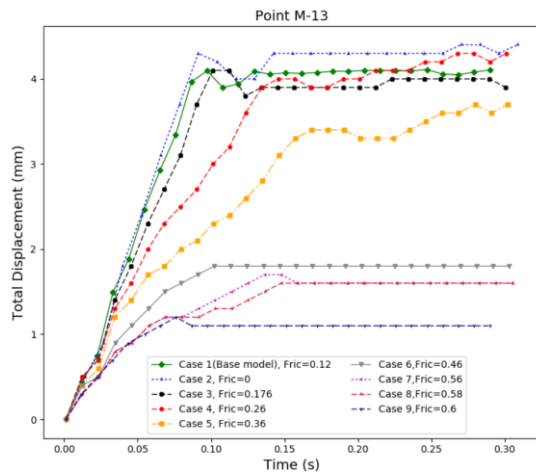
a)



b)



c)



d)

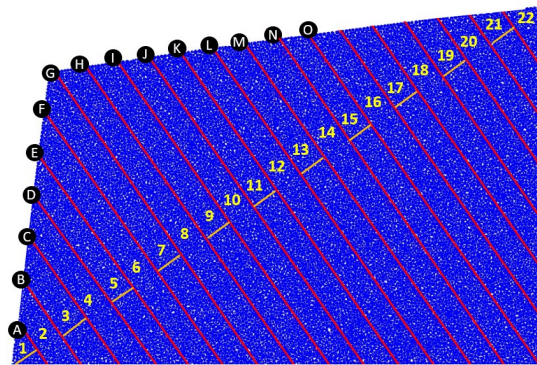


Figure 5-26: Plot illustrating the total displacement over time at three monitoring points on the slope surface for different friction angles of the main joint set: (a) point C-3, (b) point G-7, (c) point M-13, and (d) overall model configuration showing measurement point labels

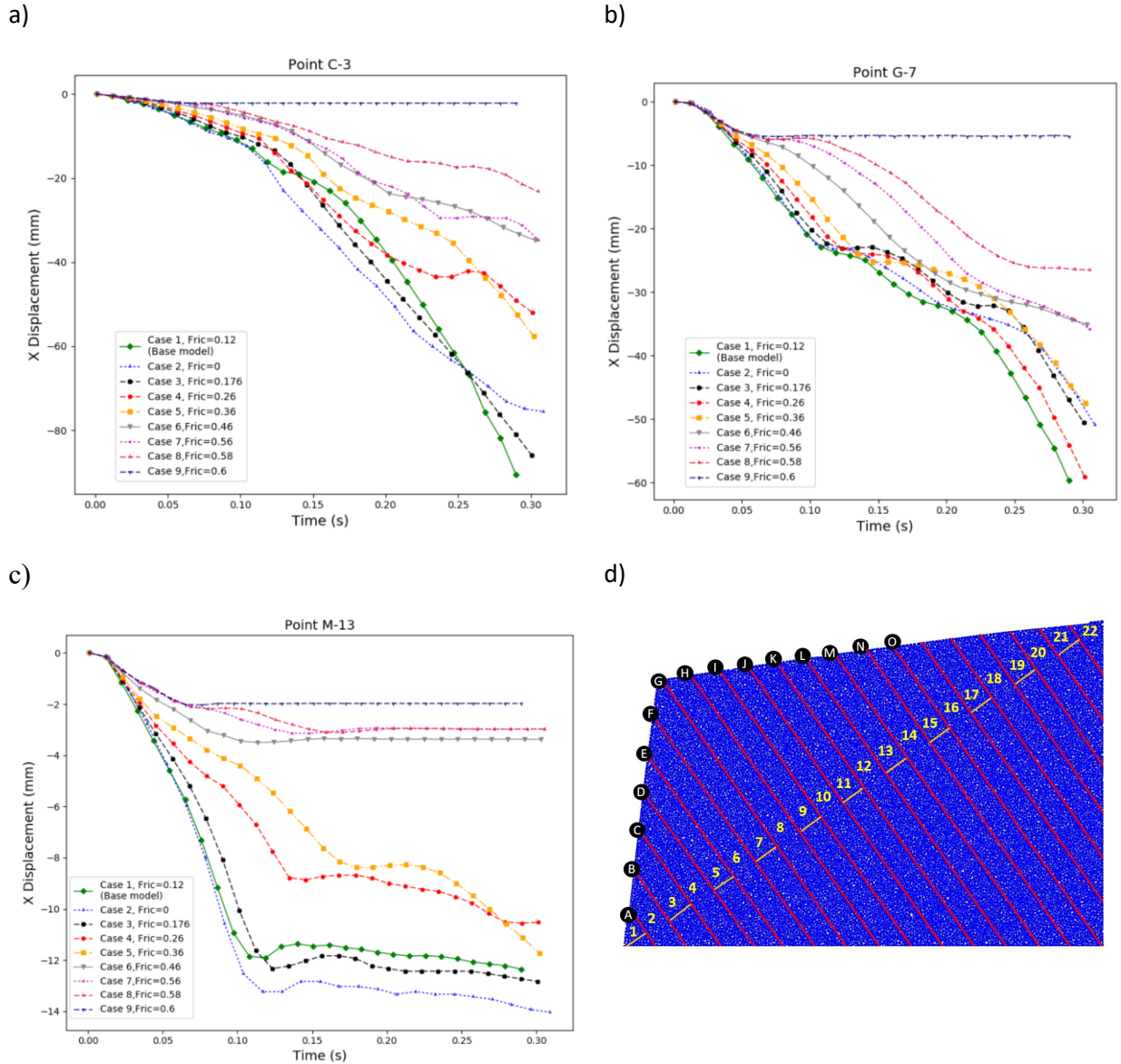


Figure 5-27: Plots illustrating the horizontal (X) displacement over time at three monitoring points on the slope surface for different friction angles of the main joint set: (a) point C-3, (b) point G-7 and (c) point M-13. (d) overall model configuration showing measurement point labels



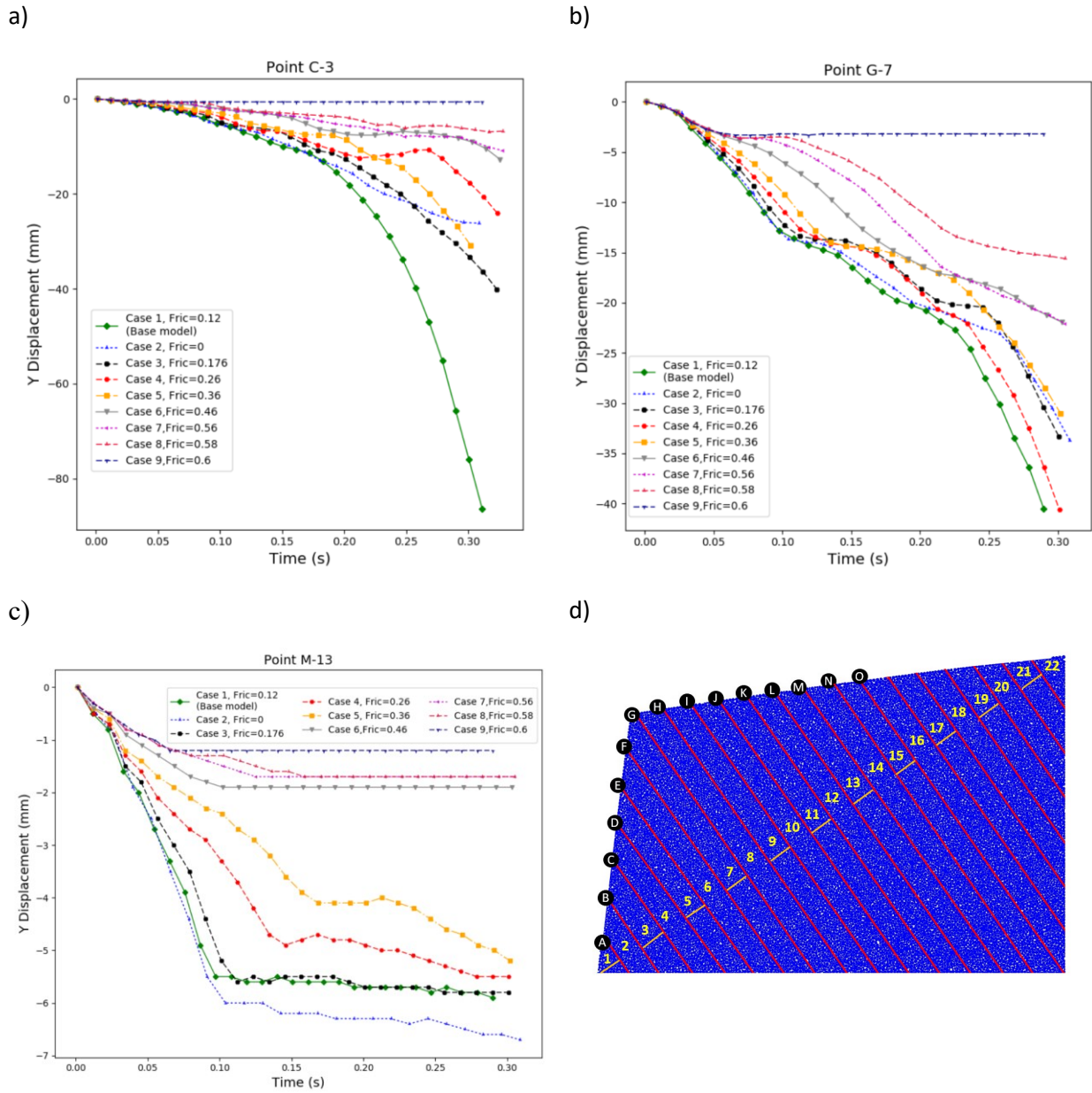


Figure 5-28: Plots illustrating the vertical (Y) displacement over time at three monitoring points on the slope surface for different friction angles of the main joint set: (a) point C-3, (b) point G-7 and (c) point M-13. (d) overall model configuration showing measurement point labels

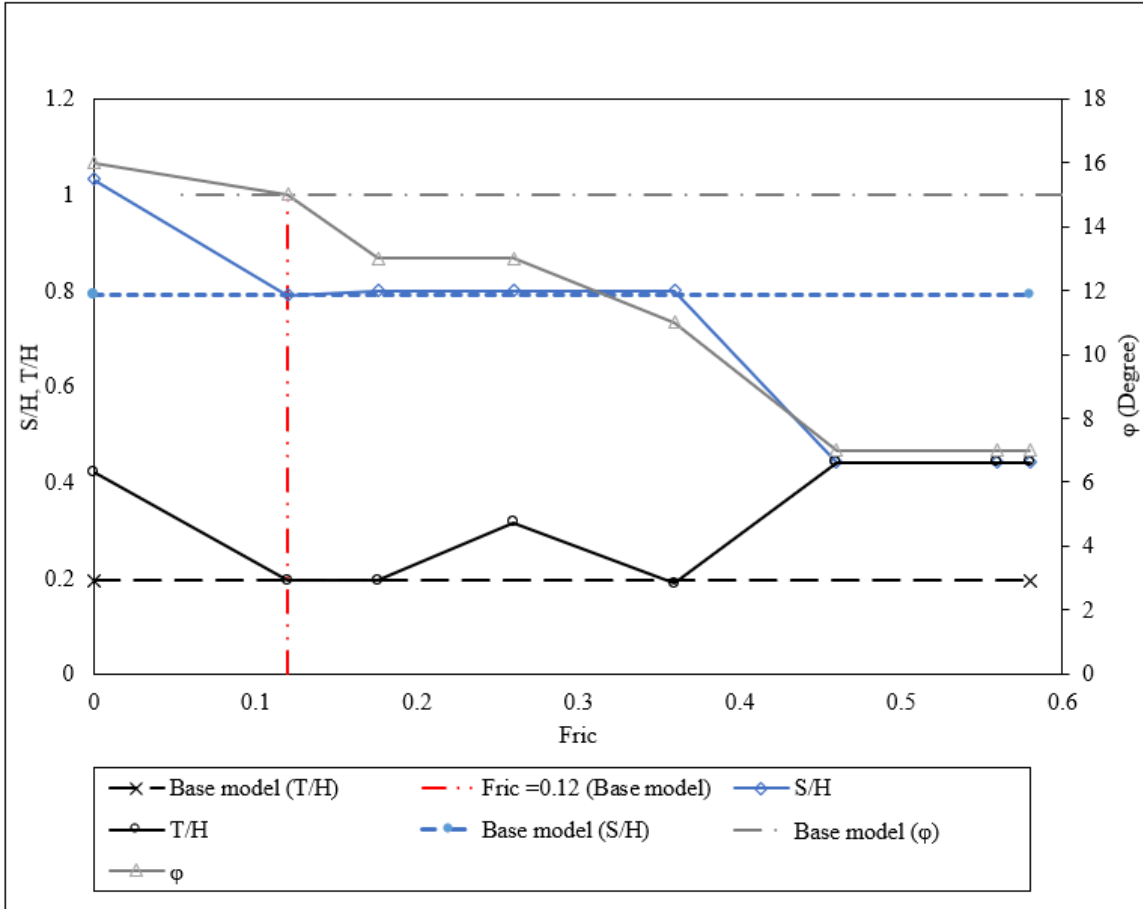


Figure 5-29: Plot illustrating normalized the horizontal distance between the top of the stable zone and the slope toe (T/H), the normalized horizontal distance between the top of part of the slope without any movements and the slope toe (S/H), and the angle between the total failure plane and the line of normal to discontinuities versus the main joint set friction coefficient (Fric)

### 5.3.3.4 Discussion

#### DEM results of the slope with a potential of block-flexural toppling failure

A slope with block-flexural toppling failure was simulated using the DEM based on the rotation of the ideal physical experimental model. The overall failure surface in the calibrated slope was  $15^\circ$  above the line normal to the main discontinuities, and recognizable zones, including stable, toppling (tensile), and sliding (shear) zones, were successfully predicted in the numerical simulation of the calibrated slope model.

Moving upward from the face of the slope to the back of the slope, the observed deformation in the slope's stable zone decreased. Negligible deformation was observed in columns 14 to 22 of the simulated slope; the equivalent columns did not exist in the corresponding physical experimental model, indicating that the presence of these columns did not affect the block toppling failure processes within the simulated slope. In the stable zone, the deformation direction at the top of the zone remained constant throughout the toppling failure process. In contrast, the displacement directions of the columns located in the toppling zone changed because, in addition to translation, these columns were rotated from their base points. The identified stable zone should be considered in construction work on failure-prone slopes to minimize the risk of toppling failures.

The assumed angle between the total failure plane and the line normal to the discontinuities ( $\phi$ ) in the limit equilibrium analysis proposed by Amini et al. (2012) is based on the centrifuge physical modelling of Adhikary et al. (1997) and physical model tests by Aydan and Amini (2009), and its values are typically in the range 10–20°. The physical model tests from these two studies were mostly performed for flexural toppling failure; however, the calibrated DEM numerical simulations indicate a  $\phi$  value of 15° for slopes experiencing block-flexural toppling failure, consistent with the physical test results. With reference to An et al. (2022), when using an analytical model to analyze slope stability, a suitable dip angle must be chosen for the potential failure surface to reach the appropriate safety factors. Therefore, this finding assists with selecting potential failure surfaces in analytical models of toppling failure that require these surfaces to be selected in advance.

The presence of a persistent cross-base joint changed the  $\phi$  value. In the various studied cross-base joint and merged joint configurations,  $\phi$  varied between 13–27° and, in some cases, a single failure plane changed to two failure planes. The formation of multi-planar failure surfaces in flexural toppling failure was also reported by Zheng et al. (2018) and in block-flexural toppling failure by Zhang et al. (2022). Furthermore, the DEM numerical simulations indicate that while these changes in joint configuration did not impact the extent of the toppling failure zone, the stable zone and no-movement zone of the slope were affected.

A configuration was also investigated with different base joints in which the pairs of base joints in the base model were each combined to make a single, longer joint spanning two columns. In this model, the no-movement zone of the slope and the stable zone were affected, with a decrease observed in the size of the slope's stable zone. The value of the overall plane surface angle ( $\phi$ ) was reduced to zero in this configuration.

Adding a joint base set parallel to the existing joint base was also investigated. The results of this configuration showed that the no-movement zone and the stable zone were similar to those of the base model; no overall single failure surface plane was observed in this configuration.

Combining every two joints from the base model and adding a joint base set parallel to the existing joint base both showed comparable characteristics in terms of the no-movement zone and the stable part of the slope, but the overall plane failure angles ( $\phi$ ) for both cases are steeper than the base model at  $26^\circ$  and  $31^\circ$ , respectively. In addition, single overall failure surfaces were not observed in either case.

The joint spacing thickness influenced the stable zone, the no-movement zone, and the overall plane failure in slopes with block-flexural toppling failure. Increased joint spacing led to the formation of a strong column with higher shear and bending strength at the slope's toe, inhibiting toppling failure by preventing the initial movement required to initiate the failure.

The study of the effect of the main columnar joint set's friction angle on the failure surface pattern and the progression of block-flexural failure showed that slope deformation decreased with increasing joint friction angle ( $J\phi$ ) values.

Overall, this study demonstrates that a particle-based DEM can be successfully applied to simulate block-flexural toppling failure. Good agreement was found between the simulation results and experimental model results obtained in the laboratory. Although DEM calibration is time-consuming, the final calibrated model can be used for parametric studies of different joint set configurations. Compared to laboratory-based tests, parametric studies with calibrated numerical models are convenient and allow multiple different cases to be easily investigated. In addition, the numerical model can be potentially extended to explore other scenarios, including real-world cases of block-flexural toppling failure. This study also yields new insights into how joint configurations relate to failure surfaces and deformation patterns in slopes that are prone to block-flexural toppling.

### 5.3.3.5 Conclusions

In this study, we used a particle-based DEM approach to simulate block-flexural toppling failure. The study's key conclusions are as follows:

1. A particle-based DEM approach was successfully used to simulate block-flexural toppling failure, and the calibrated results were validated by simulating physical laboratory models from previous studies.
2. Although the numerical UCS test can limit the microparameter ranges used in the DEM, the numerical UCS test itself cannot directly calibrate the required microparameters when simulating slopes with joint sets. The particle size and microparameters of smooth joints have deterministic effects on the calibration process. The simulation accuracy of a slope with block-flexural toppling failure was significantly affected by the ratio of the maximum particle size to the minimum sub-domain size, which is represented by the joint spacing or block width.
3. Compared to the base model, the addition of an additional base joint set changed the angle between the total failure plane and the line normal to the discontinuities ( $\phi$ ) to higher values; however, the no-movement and stable parts of the slope were not significantly affected by this change.
4. The joint spacing thickness influenced the extent of the slope zones and the overall plane failure in a slope with block-flexural toppling failure. Differences in joint spacing thickness significantly changed the slope stability and value of  $\phi$ . Thus, an accurate assumption of joint spacing is essential when using theoretical methods to analyze block-flexural toppling failure. The critical case must be investigated based on the minimum joint spacing in a slope with block-flexural toppling failure.
5. The joint friction angle can be changed by stabilization or weathering of the slope. The results show that the location and shape of the overall failure surface were influenced by changing the value of the main joint friction angle. Incorrect assumptions of joint friction values in the limit equilibrium method can lead to inaccurate predictions. A stabilization method, such as reinforcement supports, can increase the main joint friction angle and help to stabilize slopes and reduce deformation. As shown by the parametric studies, increasing the main joint friction can extend the slope's stable and no-movement zones.

6. The persistence of the cross-base joints was investigated to examine the assumptions used in the limit equilibrium method of block-flexural toppling failure by assigning different failure modes (potential for blocky failure and potential for flexural failure) to adjacent blocks. The results indicate that assuming a single total failure plane 10–20° above the line normal to the main discontinuities may not always be a reliable assumption in theoretical models; this angle ( $\phi$ ) can vary between 13–27° and a single failure plane can change into two failure planes. Therefore, the potentially oversimplified assumptions used in theoretical models must be evaluated carefully. In addition, different discontinuity persistence configurations can influence the slope's stable and no-movement zones: identifying the extent of these zones can provide important information for slope stability analyses and tunnelling projects.

## 5.4 Application of the DEM particle-based method to real-world case

### 5.4.1 Case 1: A selected section of the Ihlara Valley (Cappadocia, Turkey)

#### 5.4.1.1 Study area

In this section, the developed DEM code (HDPAC) is utilized to simulate a real case to study the toppling failure. The study area is a slope section in the Ihlara Valley (Cappadocia, Turkey) located approximately 35 km southeast of Aksaray City. At this site, due to water and wind erosion and drainage, progressive failure of rock slope, especially toppling failure, has been observed within a hard ignimbrite rock layer. This layer (the Kizilkaya ignimbrite) was reported as a blocky columnar structure by Sari (2021). Figure 5-30 illustrates the view of the valley and a fallen block.



Figure 5-30 : (a) view of the Ihlara Valley, (b) the fallen block, and (c) geological structure of Kizilkaya (Sari 2021)

#### 5.4.1.2 Site Stratigraphy and rock properties and Failure Mechanism in the Valley

The stratigraphy of the area is mostly composed of Tertiary–Quaternary volcanic units, including the pyroclastic rocks of the Selime tuff, Kizilkaya ignimbrite, and Hasandagi ashes (Sari 2021). A cross-section illustrating the stratigraphy of the valley is shown in Figure 5-31.

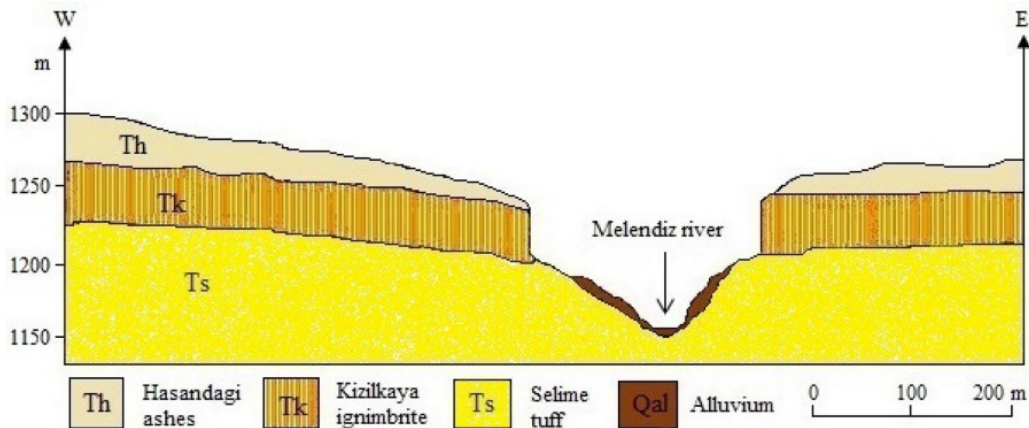


Figure 5-31: East- Weast cross-section of the stratigraphy of Ihlara Valley (Sari 2021)

Le Pennec et al. (1994) reported that the thickness of the Kizilkaya ignimbrite varies between 4 and 60 m, with an average of 25 m. The Kizilkaya ignimbrite is underlain by the soft Selime tuff. Sari (2021) noted that several factors including undercutting, basal weathering, and erosion caused by wind and water led to the secondary toppling failure mechanism in the valley. Sari (2009), performed a joint analysis on the Kizilkaya ignimbrite outcrop forming the valley cliffs based on field studies and described the area's joint configuration. Based on this information, Sari (2021) later schematically illustrated the secondary toppling failure in this area to characterize the failure process, as shown in Figure 5-32. Figure 5-32 (a) represents the original condition of the site, including the rock structure's original pre-failure geological configuration in the valley cliffs. The geological conditions as influenced by weathering and erosion are shown in Figure 5-32 (b) and (c), respectively. During the final phase, toppling failure occurs as a result of the separated block sliding on the weakened underlying tuff and overturning due to its own weight as its centre of gravity falls outside its base of support.



In the Kizilkaya ignimbrite, the average joint set is spacing 3.5 m, and the joints are vertically pervasive through the layer; thus, their height is based on the Kizilkaya ignimbrite's average valley thickness of 25 m. The weakened zone in the tuff layer extends to around halfway across the basal width of the second block in the slope (Sari 2021).

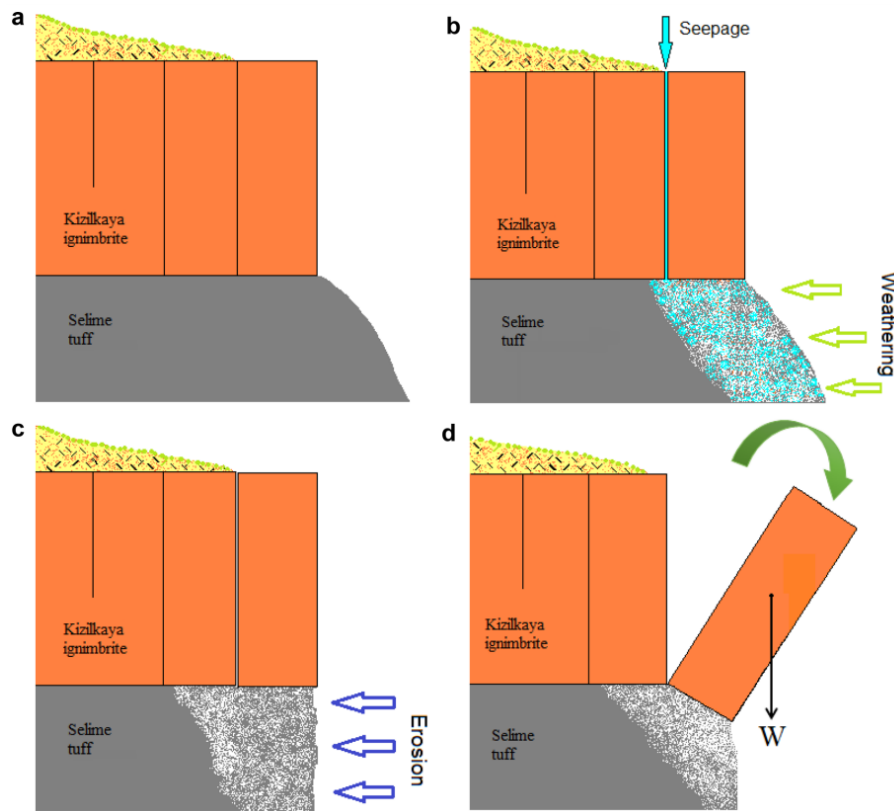


Figure 5-32: A simplified model proposed by Sari (2009) for the toppling failure mechanism in the Ihlara Valley; (a) the condition of the original slope, (b) weathering at basal Selime tuff, (c) erosion in the toe due to the basal weathering, (d) toppling of the block (Sari 2021)

The material and joint properties of the rock masses forming the valley strata were reported by Sari (2021) based on in situ measurements, laboratory analyses, and the values described in the literature, were used as the basis of the present study. The strength and stiffness parameters of each rock layer are presented in

Figure 5-33. Note that these macroparameters cannot be directly used as input parameters for the DEM model. Therefore, a series of calibration processes was conducted based on a numerical simulation of the unconfined compressive strength (UCS) to obtain suitable equivalent input microparameters to model the slope.

Parameter	Hasandagi ashes	Kizilkaya ignimbrite	Selime tuff	Weathered tuff	Joint Set1	Joint Set 2
Dry unit weight ( $\gamma_d$ ) (kN/m <sup>3</sup> )	16.2	19.6	17.5	15	-	-
Uniaxial compressive strength (UCS) (MPa)	5.5	46.06	6.68	2.82	-	-
Young's elastic modulus ( $E_t$ ) (GPa)	3.5	12.64	6.25	2.78	-	-
Cohesion (c) (MPa)	-	-	-	-	0.025	0.05
Friction angle ( $\phi$ ) (°)	-	-	-	-	33	35

Figure 5-33: Rock material and rock mass parameters for the study area (modified Sari 2021)

#### 5.4.1.3 DEM Modeling

A DEM was employed to perform a two-dimensional (2-D) numerical simulation of the Ihlara Valley with a height of approximately 40 m and a width of approximately 38 m (Figure 5-34). The model geometry was built according to the stratigraphy and joint set configuration described above in Section 3.1. The three layers of the Hasandagi ash, Kizilkaya ignimbrite, and Selime tuff were considered in the model, and the Kizilkaya ignimbrite's average valley thickness of 25 m was used. The spacing between the sub-vertical orthogonal joints (i.e. the width of the columns in the model) was set to 3.5 m, equivalent to the reported average spacing of the joint set in the study area. A set of 9,440 randomly distributed particles was packed into the corresponding closed boundary made with different segments to represent the overall geometry of the valley slope; these particles had a uniform size distribution, a maximum to minimum radius ratio ( $R_{max}/R_{min}$ ) equal to 1.66, and a final porosity of  $n \approx 0.15$  (See Figure 5-34 ). The boundary of the model was created using wall segments with a normal stiffness value 10 times greater than that of the particles. This stiffness value was chosen to prevent the particles from escaping the domain representing the slope geometry. The joints were not introduced during this stage, and the particles were allowed to reach

equilibrium. In the next step, the pre-existing discontinuities (i.e. joints) were explicitly assigned in the model using smooth-joint contacts. These contacts were introduced to break the bonds between particles located on opposite sides of the joints to delineate the columns. To represent the structural discontinuities observed in the Kizilkaya ignimbrite, two joint sets were introduced: Joint Set 1, which is defined as the bedding planes between the tuff and ignimbrite, and Joint Set 2, which contains in-plane finite-length uniformly distributed vertical joints. The model was then run until it reached an equilibrium state. In the next step, the wall boundaries were removed, and the particles were bonded together using parallel bonds. The particle boundary conditions were applied by fixing the horizontal displacement on the left side of the model and by fixing the horizontal and vertical displacements on the bottom side. The top and right boundaries, representing the topography of the model, were unconstrained. A gravity-induced in situ stress was applied to the model. Sufficient time steps were run to allow the model to once again reach an equilibrium state. The maximum vertical stress was expected to develop at the base of the model, which experiences the highest overlying load. It became imperative to use a higher-density material to mitigate the effects of porosity on gravitational loading. The model geometry, including the configuration of the joint set used in the numerical simulation of the equivalent slope, is shown in Figure 5-35.

To determine the microparameter properties of each rock layer, several DEM-based numerical simulations of UCS tests were conducted. Multiple trial-and-error iterations were conducted to reach the equivalents of the UCS and Young's elastic modulus values reported in

Figure 5-33. During UCS tests, the velocity of the top and base boundaries was set to a low value (0.01 m/s), which was sufficiently small to maintain an appropriate axial strain rate and produce a quasi-static loading response, as reported by Hanley et al. (2012). The numerical results of the UCS tests are presented in Figure 5-36.

The microparameters for the rock masses and smooth-joint microparameter properties used in the numerical simulation are summarized in Table 5-12 and Table 5-13, respectively.

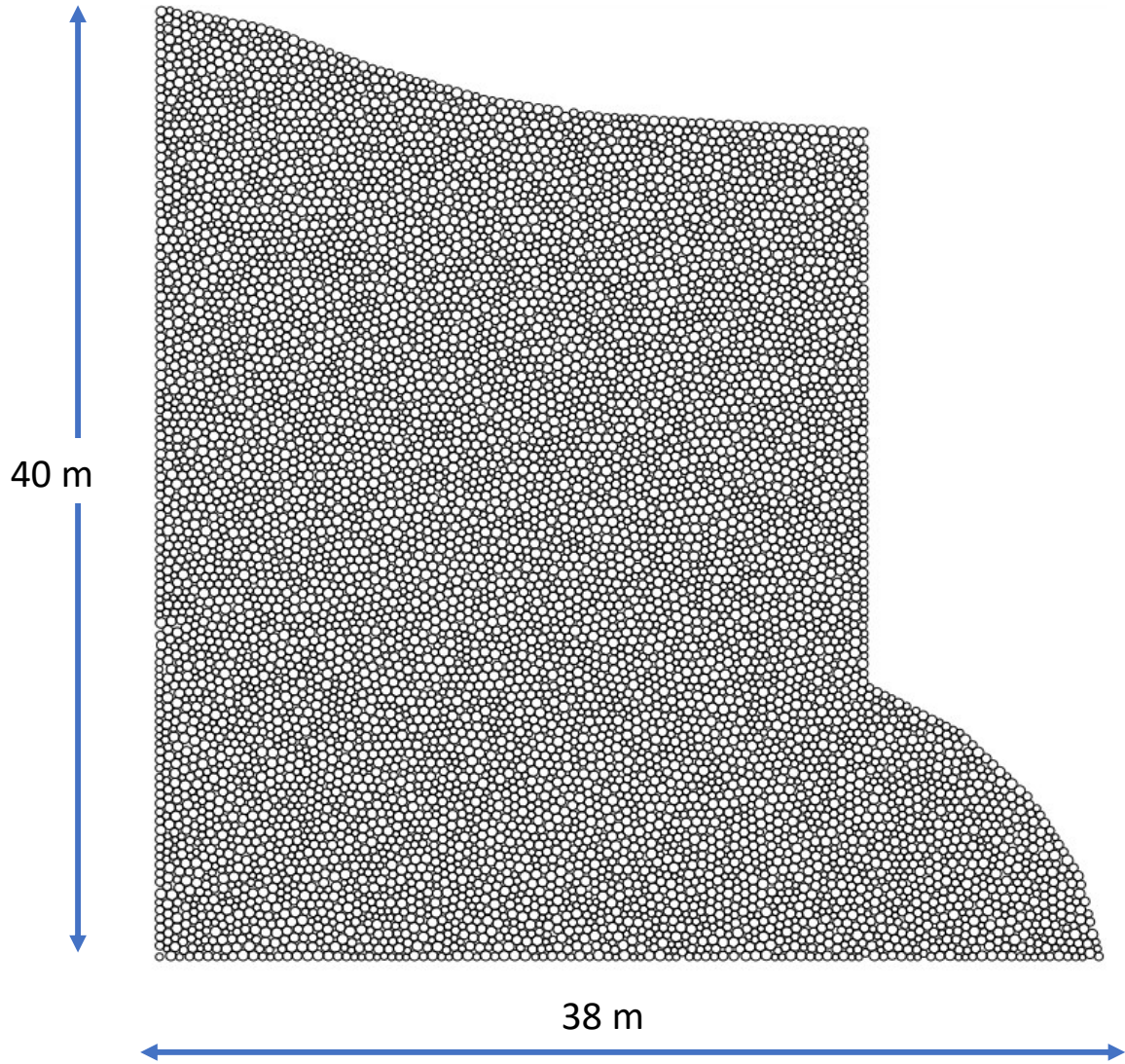


Figure 5-34: General assembly of the DEM model

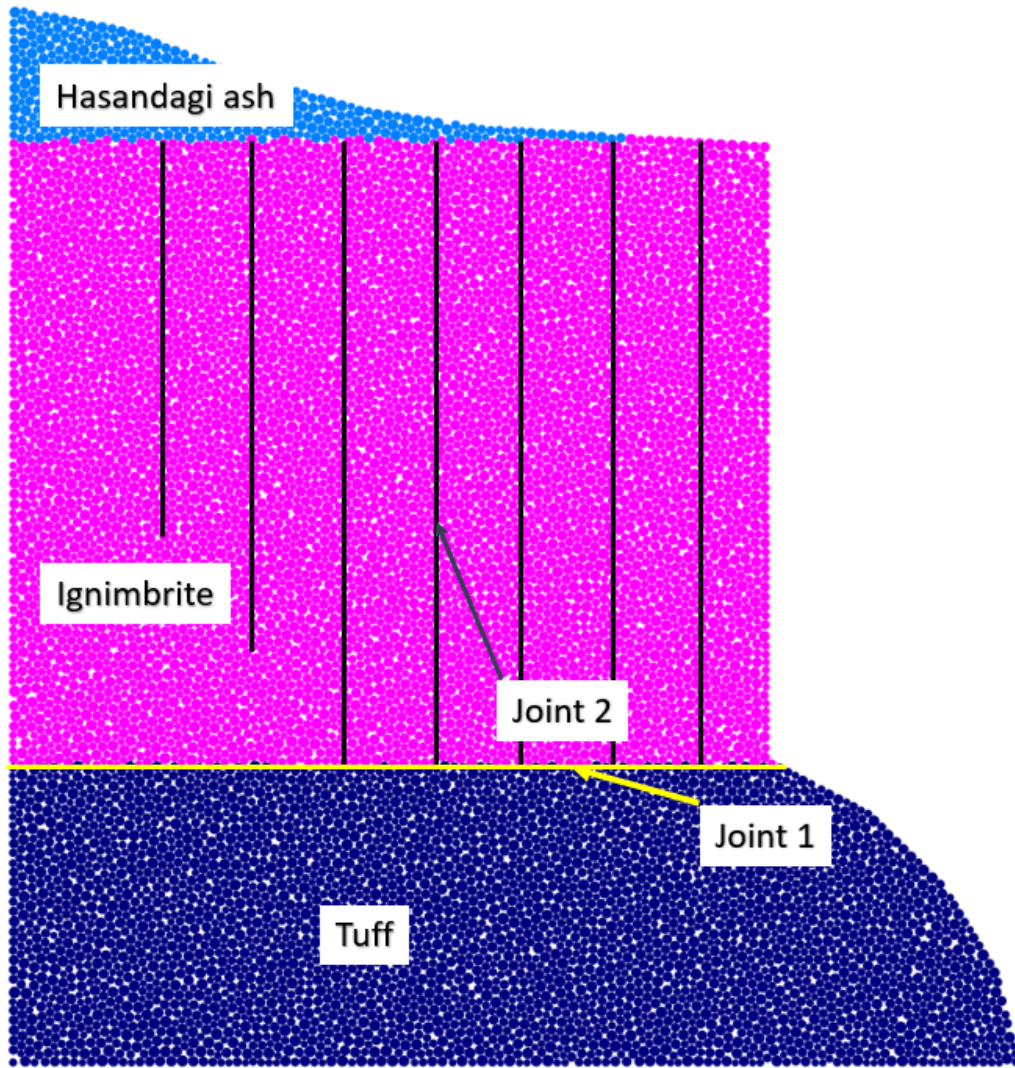


Figure 5-35: The geometry of the slope and joint sets used in the numerical simulation

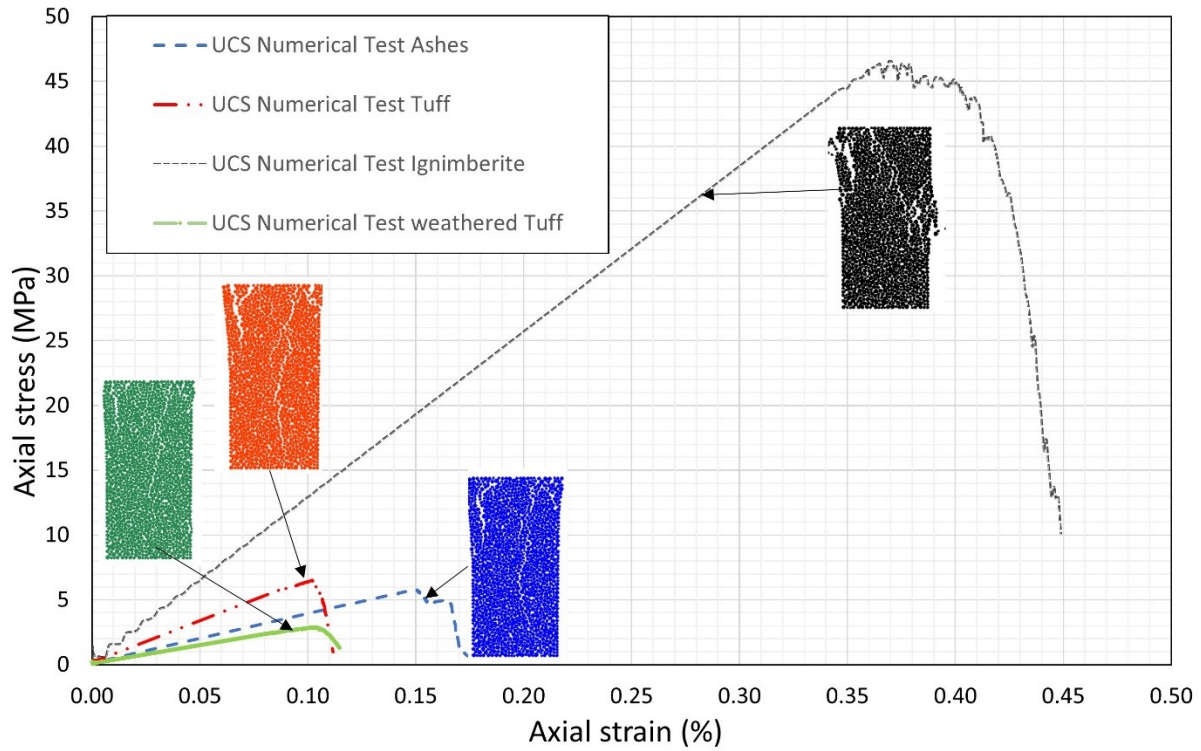


Figure 5-36: Numerical UCS test results used to calibrate the microparameters of the rock layers

Table 5-12: The calibrated microparameters used in the numerical models

Parameter	Hasandagi ashes	Kizilkaya ignimbrite	Selime tuff	Weathered tuff
Minimum particle radius $R_{\min}$ (m)	0.15	0.15	0.15	0.15
Maximum particle radius $R_{\max}$ (m)	0.25	0.25	0.25	0.25
Particle density $\rho$ ( $\text{kg}/\text{m}^3$ )	1,820	2,160	1,950	1,700
Young's modulus of particles $E_c$ (GPa)	0.6	5.28	1	0.33
Normal-to-shear stiffness ratio of particles ( $k_n/k_s$ )	1	1.2	1.2	1.2
Particle friction coefficient $\mu$	0.36	0.45	0.3	0.3
Young's modulus of parallel bonds $\bar{E}_c$ (GPa)	0.6	5.28	1	0.33
Normal-to-shear stiffness ratio of parallel bonds ( $\bar{k}^n/\bar{k}^s$ )	1.1	1.3	1.1	1.1
Parallel bond tensile strength (MPa)	17.6	45	23.5	3.75
Parallel bond cohesion (MPa)	17.6	37	17.6	2.44
Parallel bond friction angle (degrees)	20	25	16	14
Parallel bond normal critical damping ratio $\bar{\beta}_n$	0.2	0.2	0.2	0.2
Normal critical damping ratio $\beta_n$	0.25	0.25	0.25	0.25
Bond gap $G$ (m)	0.025	0.025	0.025	0.025

Table 5-13: Calibrated microparameters for smooth joints used in the models

Parameter	Joint set 1	Joint set 2
Normal stiffness of joint per unit area, ( $k_{nj}$ )(N/m <sup>3</sup> )	12x10 <sup>8</sup>	12x10 <sup>8</sup>
Shear stiffness of joint per unit area, ( $k_{sj}$ )(N/m <sup>3</sup> )	12x10 <sup>6</sup>	12x10 <sup>6</sup>
Joint friction coefficient of the base	0.53	0.55
Joint gap distance (mm)	0.1	0.1

#### 5.4.1.4 Results and Discussion

Two cases representing the degradation and erosion of the slope were simulated. The effects of degradation were implemented in the numerical simulation by reduced strength and stiffness values of the microparameters in the weathered tuff layer (see Table 5-12). The weathered zone extends to approximately halfway across the width of the second block's base, as shown in Figure 5-37 (a). To consider the effects of erosion on the toe of the slope, a second case was modelled in which the weathered tuff zone at the slope's toe was removed to investigate resulting changes in slope failure (see Figure 5-37 (b)). Therefore, a differential settlement at the base of each rock column due to non-equal stress redistribution after basal weathering can be investigated using this configuration.

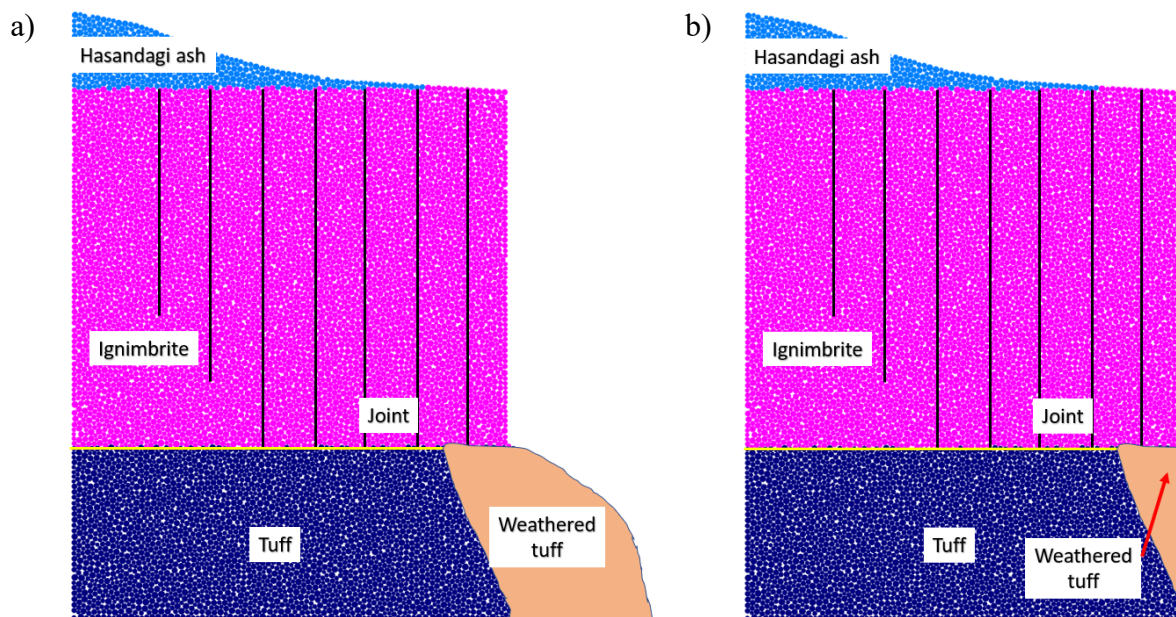


Figure 5-37: DEM model configurations simulating the toppling failure in the Ihlara Valley: a) degradation of the underlying soft tuff layer due to water infiltration and weathering, and b) removal of the slope toe due to erosion of the weathered tuff zone

Figure 5-38 (a) shows the modelled failure of the slope due to degradation of the tuff layer. In this model, bond breakage is associated with a decrease in the strength of the parallel bonds, leading to changes in particle interactions and material behaviour. Toppling failure of the first column at the front of the slope was observed. Figure 5-38 (b) illustrates the progressive failure of the slope due to the large deformation of the first column, which is effectively captured by the DEM. The movement of the first column removed lateral support for the second column and led to the movement of the other columns; however, in this case, the movement did not cause the second column to topple. Sari (2021) simulated this case using the FEM approach and similar behaviour was observed in their model, as illustrated in Figure 5-39 (a). The deformation values of the FEM and DEM models are presented in Figure 5-39 (a) and (b), respectively. The accumulated total displacements in the FEM are documented immediately preceding the slope failure, whereas the DEM results represent the total cumulative displacement throughout the study period. Consequently, the deformation values observed in the FEM findings are comparatively smaller than those evident in the DEM outcomes. The primary cause of failure, attributed to differential settlement following basal weathering, was the rotation of the unrestrained blocks located in the upper section of the slope.

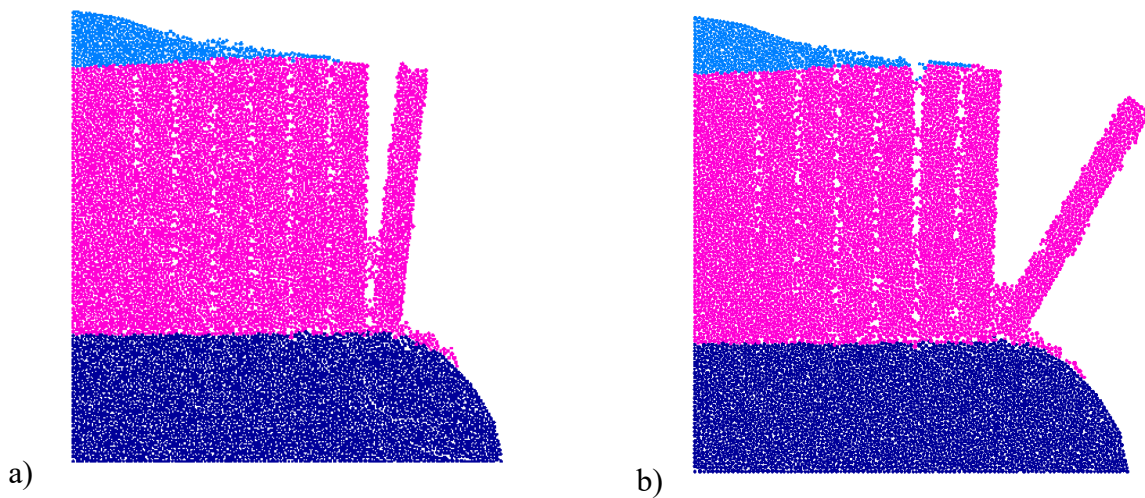


Figure 5-38: The toppling failure process in the slope: a) The toppling failure in the first column of rock and, b) the movements of the other rock column progressing the toppling of the first rock column and overall post-failure



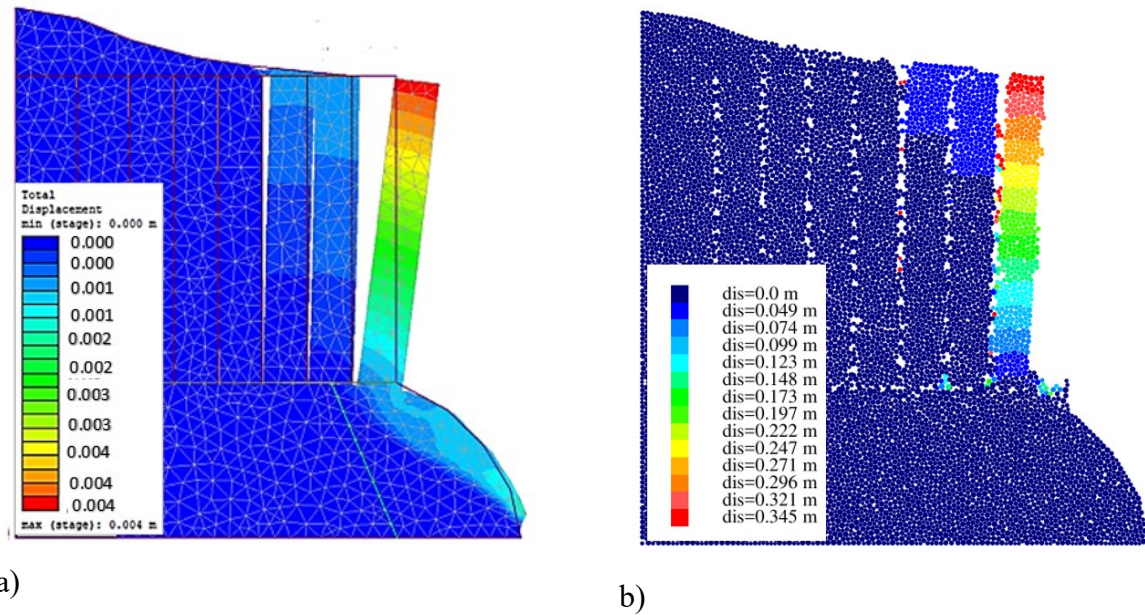


Figure 5-39: The slope failure and total displacement in the slope modelled using a) FEM for a similar slope to case 1 (Sari 2021) and b) DEM for case 1 (this study)

The deformation results of the slope for case 2 modelled using the DEM are illustrated in Figure 5-40. The eroded zone was removed from the slope toe in this simulation to investigate differences in failure behaviour in the slope. Several images of the slope's deformation overtime during the simulation are presented in Figure 5-40. An identical case simulated using the FEM approach by Sari is also presented in Figure 5-41 (a). The deformation values of the slope as calculated using the FEM and DEM models are illustrated in Figure 5-41 (a) and (b), respectively. The observed failure in the slope in case 2 shows that toppling failure occurred due to erosion of the toe of the slope. Removing the eroded zone in the model caused the release of the lateral stress that supported the tuff layer immediately underlying the first column of the ignimbrite layer. This caused breakage of the bonds in the weathered zone as illustrated in Figure 5-41, which destabilized the first overlying rock column and made it prone to toppling. The rotation of the first column contributes to the destabilization of the second and third columns, causing them to also topple. Specifically, the lateral support of the second column is removed, and the movement first column triggers the toppling of the second column. However, the FEM results exhibit different modes of failure, with backward tilting of the detached blocks over a plane of weakness in the basal tuff layer (see Figure

5-40). In this scenario, the DEM approach is advantageous as it can capture large deformations and consider the separations and movements of blocks, in addition to crack propagation throughout rock masses, thus allowing accurate simulation of rock slope failure when large deformations occur. The FEM model did not account for the crack propagation within the underlying rock mass resulting from bond breakage; consequently, the interactions between the rock fragments and the effects of large deformations were disregarded in the FEM modelling process.

Following a series of trial-and-error attempts, a back analysis was conducted to achieve back-tilting failure of the first rock column as observed in the FEM analysis results. Under these conditions, the parallel bond tensile and cohesive strength values for the weathered tuff were determined to be 2.95 MPa and 1.92 MPa, respectively. The reduction in the tensile strength and bond cohesion of the parallel bond were considered in the simulation of the weathered tuff layer. These parameter values were divided by a safety factor of 1.27. The slope failure in this configuration is shown in Figure 5-42. The deformation of the first block is similar to the FEM results; however, as the simulation progressed, the failure extended beyond the initial column and affected the columns located at the back of the model, and ultimately, the slope experienced toppling failure. Unlike the DEM, the FEM simulation was unable to capture this progressive failure.

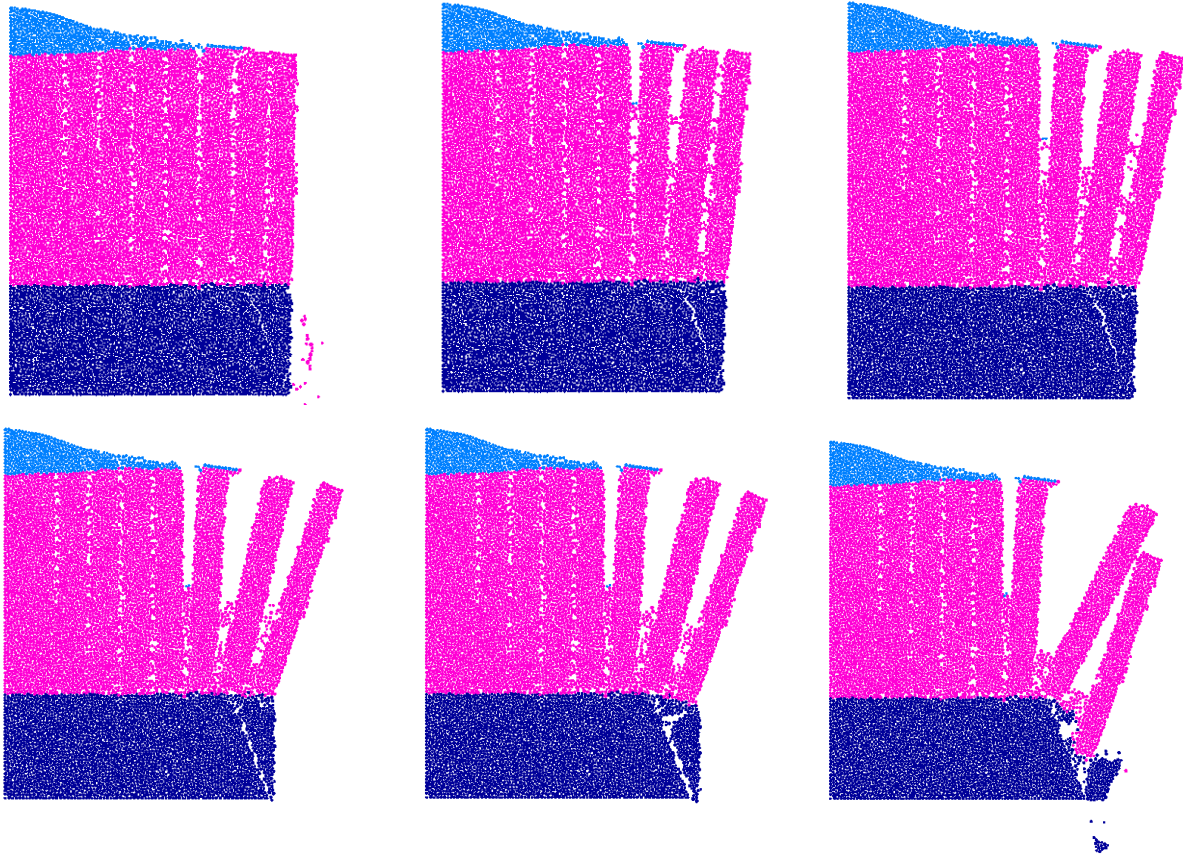


Figure 5-40: The progress slope failure in Case 2 while the erosion occurred at the toe of the slope, the mode of the failure is classified as the toppling failure.

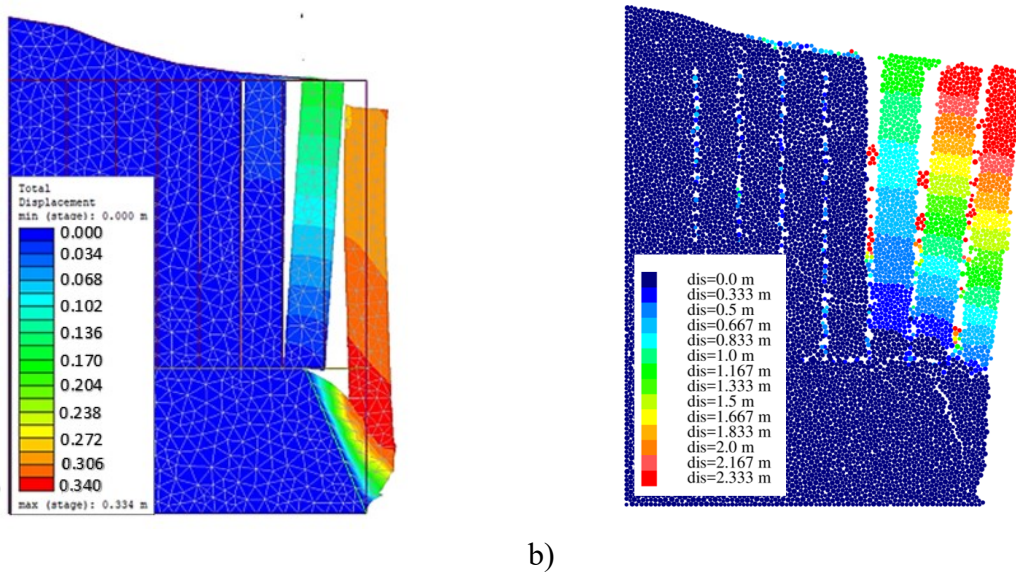


Figure 5-41: The slope failure and total displacement in the slope using (a) a FEM model for a similar slope to case 2 (Sari 2021) and (b) a DEM model for case 2

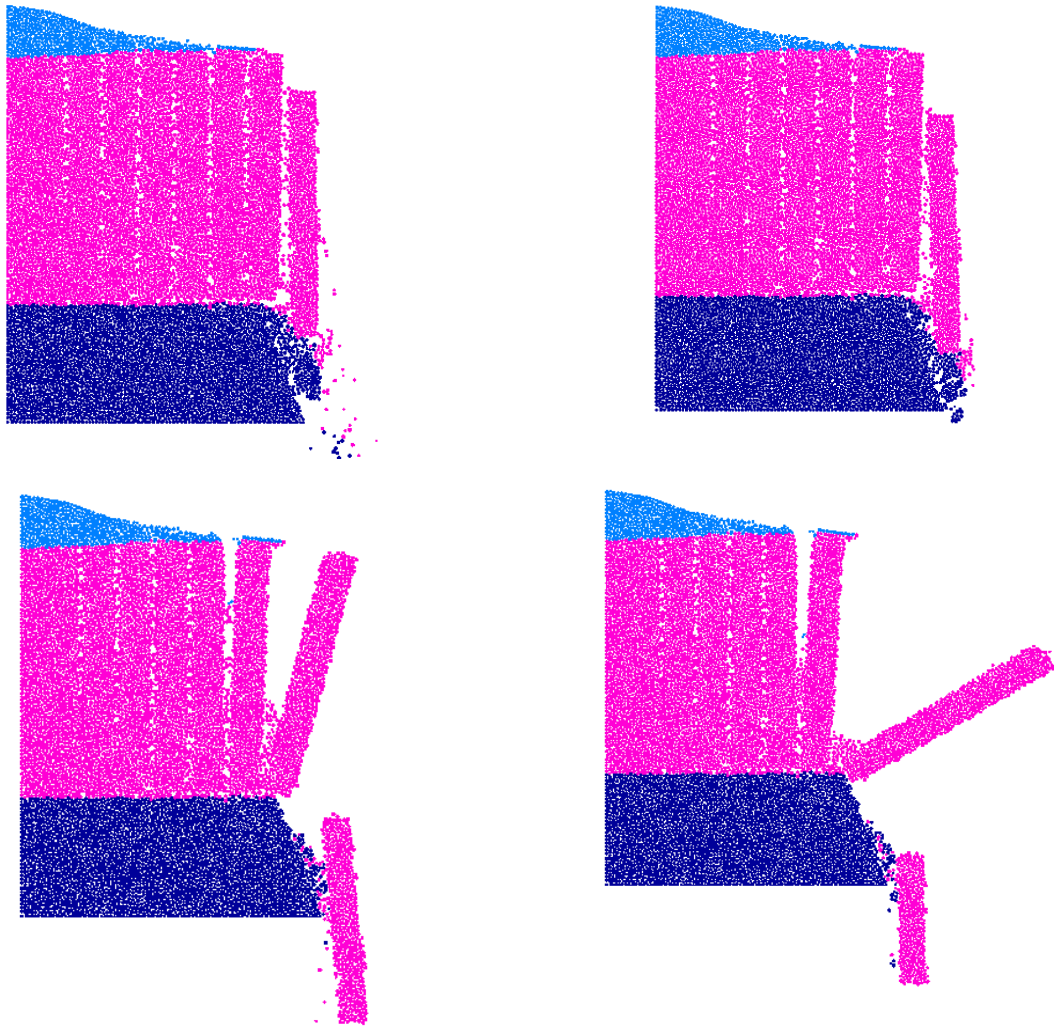


Figure 5-42: Mode and progress of the slope failure for case 2 considering the reduction in tensile strength and bond cohesion of the parallel bonds in the weathered tuff

#### 5.4.1.5 Discussions and conclusions

In this study, a DEM was applied to simulate a slope prone to toppling failure under different configurations, including an analysis of the effect of weathering and erosion in the basal slope. The results demonstrate that when the deformation is not extensive and separation between blocks is unlikely, the FEM and DEM model results are broadly consistent. In this case, the primary observed

failure mechanism was toppling and deformation of the first column of the ignimbrite layer (see Figure 5-39).

In situations where large deformations and block separation occur, the DEM can provide a more accurate prediction of the failure mechanisms, as depicted in Figure 5.41 (b). The DEM analysis revealed that erosion at the toe of the slope resulted in the failure of three columns of rock within the studied slope. Conversely, the FEM analysis indicated the failure of only two blocks (see Figure 5.41 (a)). The maximum displacement observed in the slope using the FEM is 0.35 m at the base of the first rock column; however, at the top of the first rock column in the DEM model, the maximum displacement is 2.5 m, confirming the occurrence of toppling failure in this case.

The DEM approach has several advantages that make it a valuable tool for simulating rock slope failure in scenarios where large deformation may occur. One advantage is its ability to accurately capture the large deformations that can occur in rock masses, as illustrated in Figure 5.41. Another advantage is its ability to account for the effect of the movement of the blocks due to bond breakage caused by the tensile strength of the bonds being exceeded. Therefore, the interaction of the separated block with other parts of the rock mass will be considered, as shown in Figure 5-42. In addition, the DEM method can simulate the movement and separation of individual blocks, as well as the propagation of cracks throughout the rock mass. These aspects make the DEM approach an effective tool for predicting the behaviour of rock slopes and assessing the potential for failure under a wide range of conditions.

## 5.4.2 Case 2: The Rock Slope Facing Galandrood Mine

### 5.4.2.1 Study area

The rock slope facing Galandrood Mine has been located 23 km from the Caspian Sea coastal road in the north of Iran (Amini et al. 2009). The case has been analyzed using the theoretical method proposed by Amini et al. (2012) and the results were compared with the in situ observations. The photograph in Figure 5-43 indicates that there is a clear case of local instability in Zone II of the rock slope. However, the rock mass as a whole has remained stable (Amini et al. 2012). This instability arises from the intersection of the primary joint set that dips into the slope and another joint that crosses the main joint set within Zone II of the rock slope.

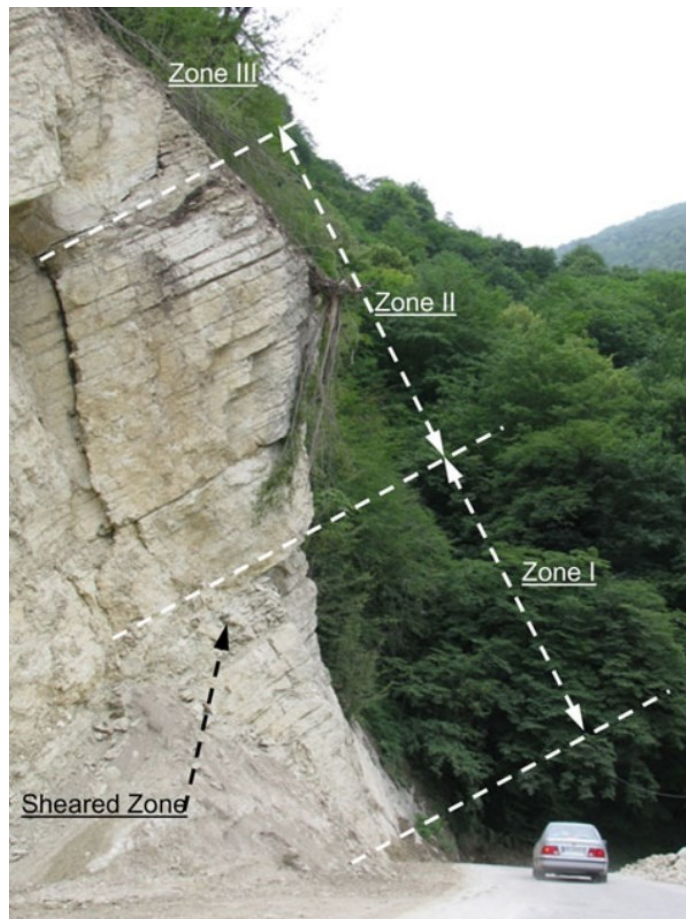


Figure 5-43: Rock slope facing Galandrood mine (Amini et al. 2012)

The joint analysis of the rock mass discontinuities and kinematic analyses of this slope presented that the dominating failure in this slope is flexural toppling, though there are a few cross-joints in the rock mass too. These joints have crossed the rock bedding planes in such a way that some rock columns exhibit the potential for blocky toppling failure. The stability of this slope against pure flexural toppling failure and block-flexure toppling failure using the analytical method proposed by Amini et al. (2009, 2012) was investigated by Amini; the results demonstrated that the overall factor of safety of this slope against flexural toppling failure and total block-flexure toppling failure was stable (Amini et al., 2009; Amini et al. 2012). The slope properties and the results of the analytical method conducted by Amini et al. (2012) are illustrated in Figure 5-44.

```

Computer program title: "BFTOP"
Coded by: MEHDI AMINI
Purpose: Analysis of rock slopes against block-flexure toppling failure
+++++
Input section
+++++
Project name:GALANDROOD      Date:12/07/2011      Analyzed by:M.AMINI
Geometrical and geomechanical parameters of the slope and the rock mass
-----
Inclination of the face slope:      81.00 Degree
Inclination of the layers:          39.00 Degree
Inclination of the total failure plane: 58.00 Degree
Inclination of the slope top surface: 32.00 Degree
Height of the slope:                16.50 m
Average thickness of the layers:     0.30 m
Friction angle at the column-column contacts: 26.00 Degree
Friction angle at the base-column contacts: 26.00 Degree
Cohesive strength of the base-column contacts: 0.01 MPa
Friction angle at the intact rock column: 45.00 Degree
Cohesive strength of the intact rock column: 1.11 MPa
Unit weight of the rock columns:     27.00 KN/m^3
Tensile strength of the rock columns: 5.00 MPa
.....
+++++
Output section
+++++
Stability assessment of the rock slope
-----
1.P0= -0.112 KN, hence the slope is STABLE against block-flexure toppling failure
2.SAFETY FACTOR of the slope against block-flexure toppling failure is: 1.3802

```

Figure 5-44: Stability analysis results of the Galandrood mine slope (Amini et al. 2012)

#### 5.4.2.2 Numerical simulation

The Discrete Element Method (DEM) was employed to conduct a rigorous numerical simulation of the above-mentioned slope measuring approximately 16.5 meters in height. The objective of this simulation is to numerically investigate the stability of the slope. To investigate the potential toppling failure in the slope, the strength properties of the rock mass were reduced by a safety factor since the slope is currently stable in the field.

The model geometry has been constructed based on the available information, which has been succinctly summarized in Figure 5-44. For a visual representation of the simulation's geometry, refer to Figure 5-45, where the sketch is presented. The joint spacing is set to 0.3 m which is equal to the average spacing of the joint set.

A set of randomly distributed 40951 particles was packed into the corresponding closed boundary made with different segments to form the slope; these particles had a uniform size distribution, a ratio between the maximum and the minimum radius  $R_{\max}/R_{\min}$  equal to 1.6, and a final porosity of  $n \approx 0.12$  (Figure 5-46). Given the relatively low joint spacing of  $h=0.3$  m, small particles were necessary to ensure a comprehensive filling between the joints. Consequently, the particle radius was intentionally reduced to facilitate effective filling inside joint spaces. The boundary of the model was created using wall segments with a normal stiffness value 10 times greater than that of the particles. This stiffness value was chosen to prevent the particles from escaping the specified domain representing the slope geometry. The joint was not introduced in this stage and let particles get to an equilibrated state. In the next step, the pre-existing discontinuities (i.e., joints) were explicitly assigned in the model using smooth joint contacts, joints were introduced to break the bonds between particles located on opposite sides of the joints to delineate the columns. The model geometry, including the configuration of the joint set used in the numerical simulation of the equivalent slope, is presented in Figure 5-47. The red-colored joints indicate evident local instability in the rock slope within zone II, as shown in Figure 5-43. This particular joint configuration and positioning were extracted from a scaled photograph of the slope's geometry, Figure 5-43. Smooth joints subsequently were employed to determine joint locations for integration into the numerical simulation. Nevertheless, it's essential to note that the overall rock mass remains stable (Amini et al. 2012). To establish the stability of the rock through numerical simulation, the slope was simulated without incorporating safety reduction factors into the strength parameters.



This approach aimed to directly assess the inherent stability of the slope. The primary joint set, represented in blue color, dips 39 degrees with respect to the horizontal and is oriented into the slope.

The model was then run until it reached an equilibrium state. In the next step, the wall boundaries were removed, and the particles were bonded together using parallel bonds. The particle boundary condition was adopted on the left side of the model by fixing the horizontal displacement and on the bottom side by fixing the horizontal and vertical displacements while the top and right boundary, representing the topography of the model, is set as unconstrained. A gravity-induced in situ stress was applied to the model. Sufficient time steps were run so that the model once again reached an equilibrium state.

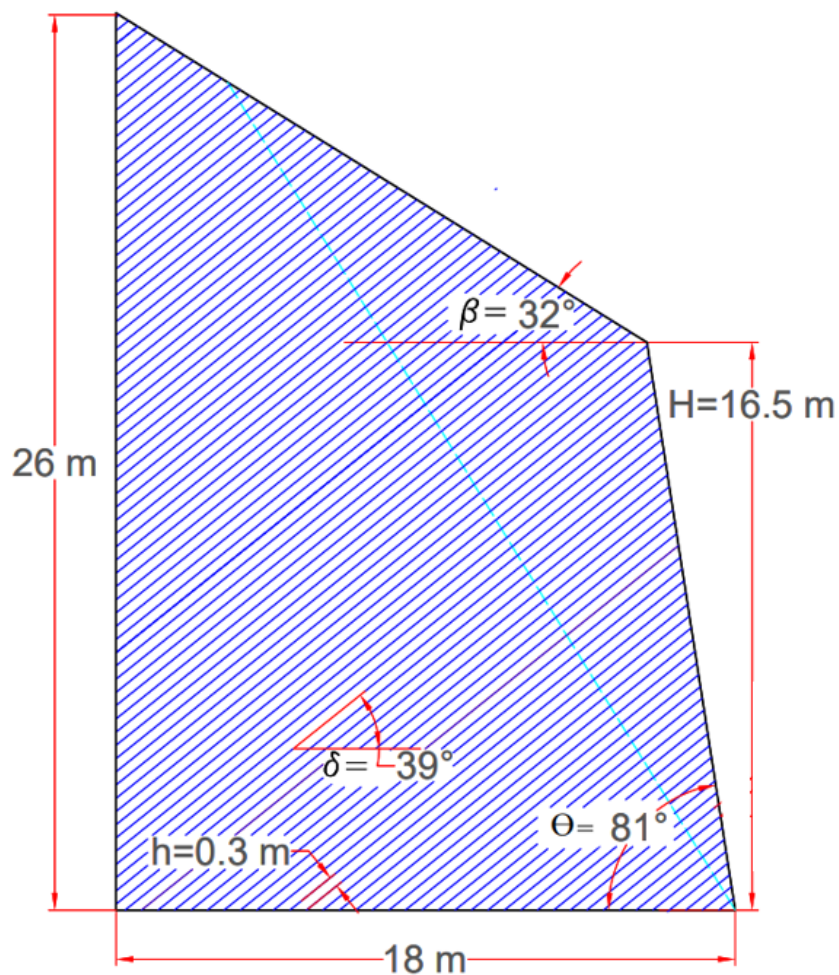


Figure 5-45: Schematic illustration of the slope

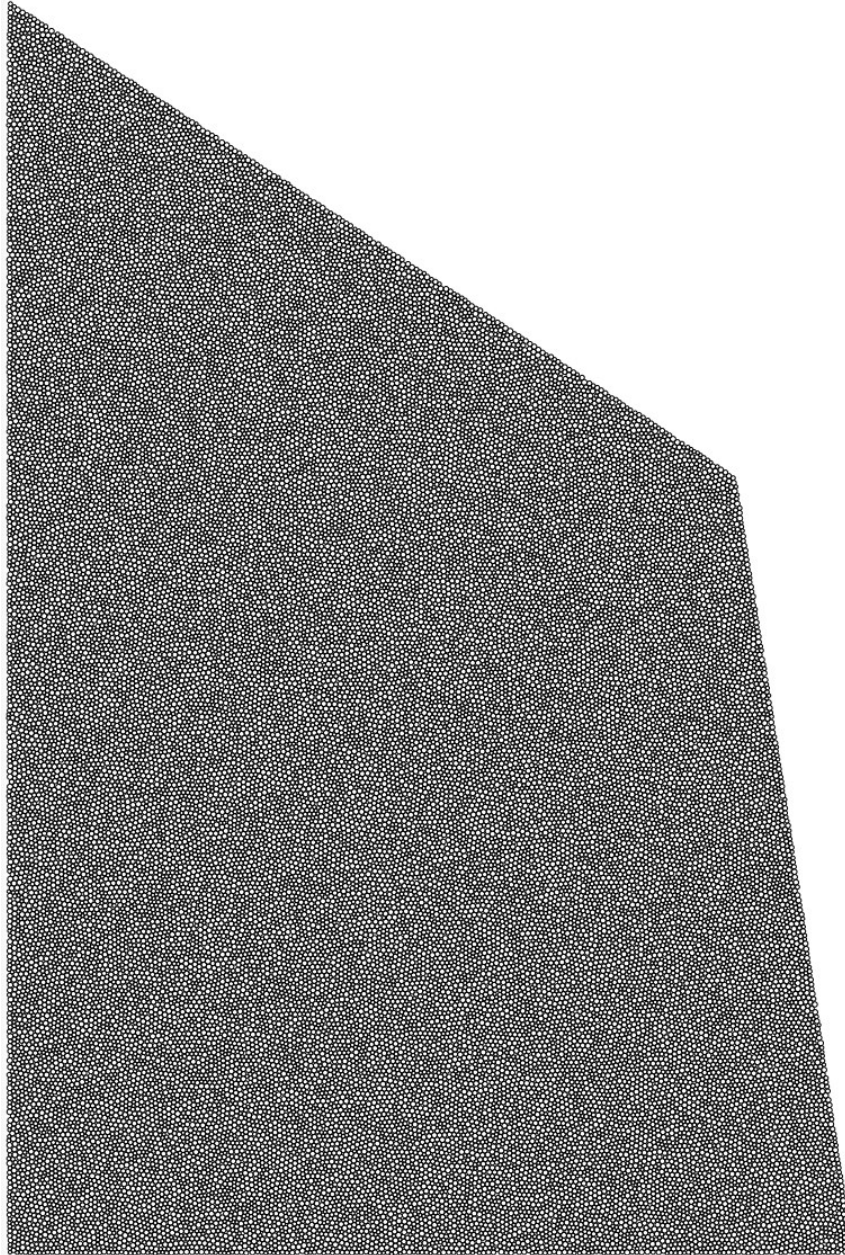


Figure 5-46: General assembly of the DEM model

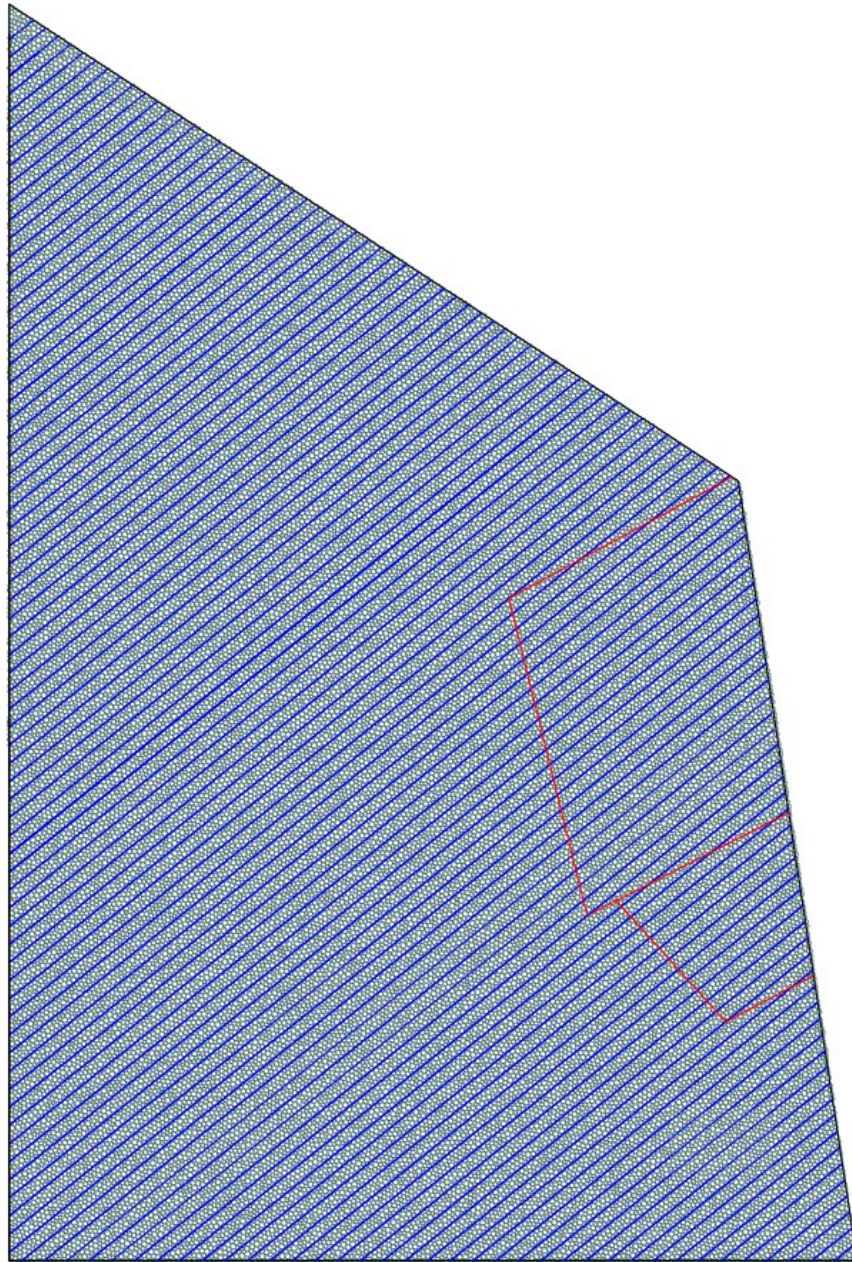


Figure 5-47: The corresponding slope model created with particles bonded using parallel bonds and smooth joint contacts

The initial microparameters properties used for intact rock and joints are summarized in Table 5-14 and Table 5-15. The slope remained stable while using these parameters. To study the potential instability in the slope, the microparameters, including parallel bond tensile strength, cohesion, and friction angle, were reduced by considering a reduction factor of 1.62 (safety factor), as summarized in Table 5-16.

Table 5-14: The calibrated microparameters used in the numerical models

<b>Parameter</b>	<b>Value</b>
Minimum particle radius $R_{\min}$ (cm)	3.75
Maximum particle radius $R_{\max}$ (cm)	6
Particle density $\rho$ (kg/m <sup>3</sup> )	3000
Young's modulus of particles $E_c$ (GPa)	6.55
Normal-to-shear stiffness ratio of particles ( $k_n/k_s$ )	1.5
Particle friction coefficient $\mu$	0.05
Young's modulus of parallel bonds $\bar{E}_c$ (GPa)	6.55
Normal-to-shear stiffness ratio of parallel bonds ( $\bar{k}^n/\bar{k}^s$ )	1.5
Parallel bond tensile strength (MPa)	149.9
Parallel bond cohesion (MPa)	114.2
Parallel bond friction angle (degree)	8.1
Parallel bond normal critical damping ratio $\bar{\beta}_n$	0.2
Normal critical damping ratio $\beta_n$	0.25
Bond gap (cm)	6

Table 5-15: Calibrated microparameters for smooth joints used in the models

<b>Joint Parameter</b>	<b>Value</b>
Normal stiffness of joint per unit area, ( $k_{nj}$ )(N/m <sup>3</sup> )	$12 \times 10^7$
Shear stiffness of joint per unit area, ( $k_{sj}$ )(N/m <sup>3</sup> )	$12 \times 10^8$
Joint friction coefficient of the base	0.5
Joint gap distance (cm)	1

Table 5-16: The parallel bond strength was reduced by a safety factor of 1.62.

<b>Parameter</b>	<b>Value</b>
Parallel bond tensile strength (MPa)	92.5
Parallel bond cohesion (MPa)	70.5
Parallel bond friction angle (degree)	5

Figure 5-48 illustrates the total displacement of the slope, which is found to be unstable against a total block-flexure toppling failure when the reduction factor is applied.

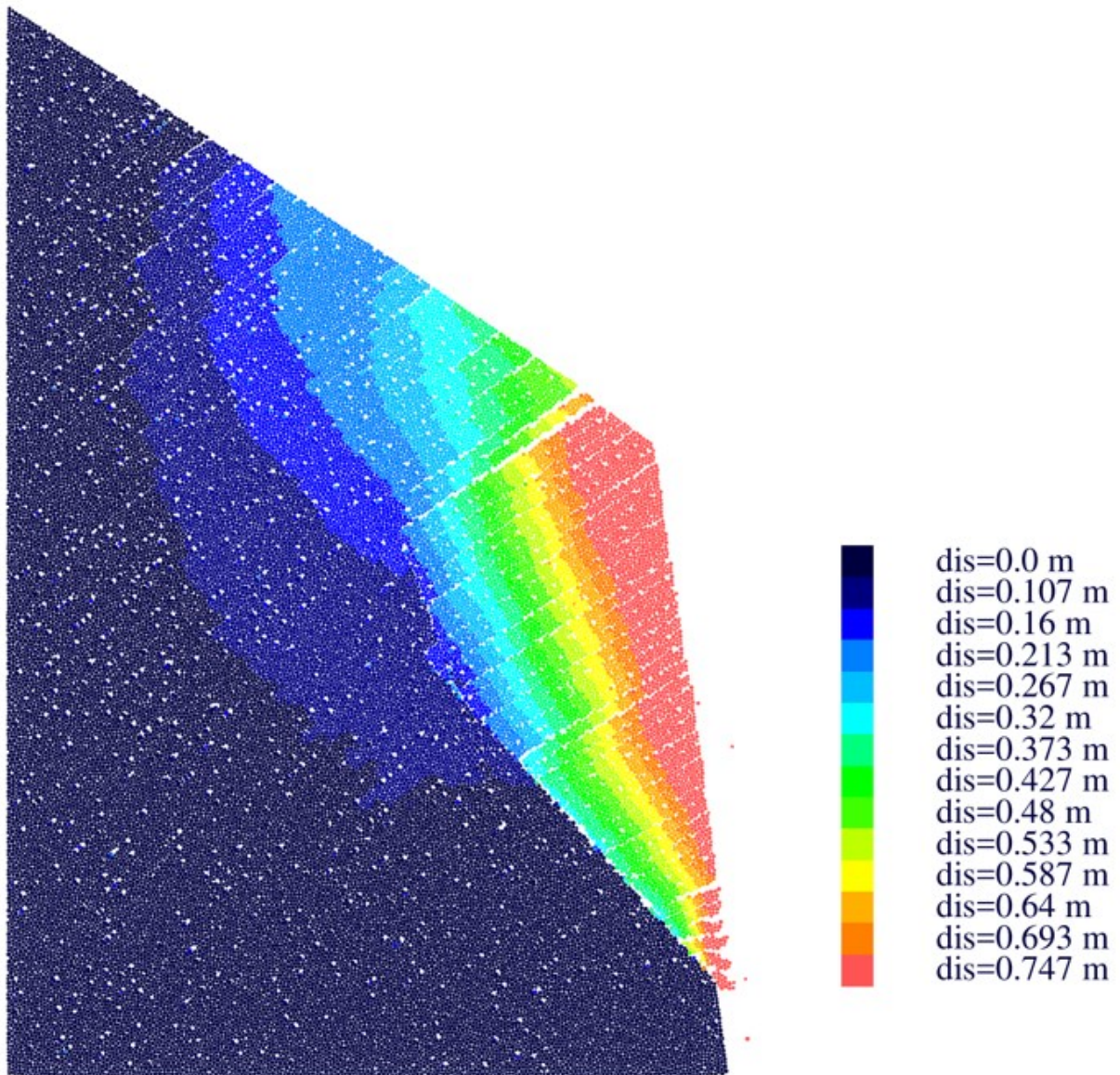


Figure 5-48: Total displacement of the slope using DEM with reduction factor applied to the strength of the parallel bonds

The DEM deformation results depict the failure surface path along pre-existing discontinuities. The failure initiation is attributed to the sliding of blocks at the toe of the slope, causing movement of the rock columns along the pre-existing surface. In zone I (see Figure 5-43), the blocks corresponding to the sheared zones underwent toppling and exhibited a downward clockwise rotation due to vertical movement from the immediate underlying rock column at the top.

The safety factor obtained for the slope using the DEM method is 1.62, which is higher than the safety factor calculated by the theoretical method (1.38).

The results yielded by the Discrete Element Method (DEM) simulation indicate a calculated safety factor for the slope of 1.62. This value surpasses the safety factor determined through the application of theoretical calculations, which amounted to 1.38. This apparent disparity between the two safety factor values can be attributed to the fundamental differences in the methodologies employed to assess slope stability.

The safety factor derived from numerical simulations using the Discrete Element Method (DEM) surpasses that obtained through theoretical analysis. The theoretical approach relies on simplified assumptions, pre-defined overall failure surfaces, and oversimplified block interactions. In contrast, the DEM method considers the actual failure surface, accounting for parallel bond breakage and block interactions, including friction and internal forces. Consequently, the DEM safety factor is higher due to its consideration of these complex interactions. On the other hand, the theoretical method's safety factor may overlook micro-level interactions and complexities within the slope, resulting in an overestimation. The disparity in safety factors arises from DEM's ability to encompass a broader range of interactions, offering a more accurate assessment of slope behavior compared to the simplified assumptions of the theoretical approach.

## Chapter 6. Conclusion and future works

---

### 6.1 Summary and conclusions

Investigating toppling failures in nature is immensely complex and often economically unfeasible. Rock layers, spanning strata, rock columns, and blocks formed by sets of discontinuities, pre-existing structures, and post-crack formations, dynamically interact to create novel geological blocks. This intricate interplay further complicates our understanding of toppling processes within rock joints. Despite extensive research and assessments dedicated to rock slope stability over the years, we still lack a comprehensive grasp of recognizing, processing, and analyzing toppling failures. To address these formidable challenges, the advanced numerical methods, Discrete Element Method particle-based (DEM), were utilized to study the toppling failure in rock jointed mass.

The purpose of this dissertation was to investigate whether the particle-based DEM can successfully simulate toppling failure in jointed rock masses. The culmination of our efforts and the insights gained from this research are outlined below:

#### **Simulation analysis:**

1. A particle-based DEM approach was successfully used to simulate block-flexural toppling failure, and the calibrated results were validated by simulating physical laboratory models from previous studies.
2. Achieving accurate numerical simulations in the DEM requires balancing computational efficiency with optimization. Utilizing smooth joints and calibrating particle size effectively enhance outcomes while minimizing computation time constraints.
3. Optimizing particle size in numerical simulations, relative to sub-domain dimensions like joint spacing, ensures smoother rupture surfaces and eliminates irregular failure patterns.
4. Calibration during microparameter adjustments is critical for balancing accuracy and solution time, with simulation findings suggesting an optimal ratio of 11 to 19 times between the smallest dimension and maximum particle size.

5. While the numerical UCS test can restrict microparameter ranges, it cannot directly calibrate them when simulating slopes with joint sets. The particle size and microparameters of smooth joints have deterministic effects on the calibration process.
6. The simulation accuracy of a slope with block-flexural toppling failure was significantly affected by the ratio of the maximum particle size to the minimum sub-domain size, which is represented by the joint spacing or block width.
7. The study explored the assumptions of the limit equilibrium method for block-flexural toppling failure, focusing on the persistence of cross-base joints. The findings suggest that:
  - Relying solely on a single total failure plane positioned 10–20° above the line normal to primary discontinuities may not consistently hold true in theoretical models.
  - The angle  $\varphi$  can vary from 13–27°, potentially leading to the transformation of one failure plane into two.
8. Different configurations of discontinuity persistence can exert influence over the stable and motionless zones within the slope. Identifying the extent of these zones provides vital insights for slope stability assessments and tunneling projects.
9. The joint spacing significantly influences the formation of slope zones and the determination of the overall failure plane in cases of block-flexural toppling failure.
10. Variations in joint spacing profoundly affect block-flexural toppling failure and require consideration of the minimum joint spacing.
11. The existence of an additional base joint set, rather than a single one, led to an increase in the angle ( $\varphi$ ) between the overall failure plane and the line perpendicular to the discontinuities, which challenges assumptions used in theoretical models.
12. Joint friction angle variations significantly influence the configuration and location of the overall failure surface.
13. Increasing the main joint friction angle expands stable and motionless zones within a slope.
14. Considering variations in joint friction angles is crucial for accurate assessments of slope stability and deformation.



## **Application of a particle-based DEM approach in real-world cases**

1. Particle-based DEM approach reveals substantial influence of large deformations and block interactions on toppling failure mechanisms and outcomes in slopes.
2. The DEM method accurately captures large deformations and block interactions in toppling failure, crucial for slopes with significant deformations resulting from pre-existing joints or deformation processes.
3. Interaction between blocks during toppling failure can change the entire process, emphasizing the importance of recognizing this aspect for appropriate support design recommendations.
4. Significant difference in safety factors between DEM and theoretical analysis, particularly in toppling failure-prone slopes
5. DEM considers actual failure surface and complex block interactions, leading to higher safety factors, while theoretical methods rely on simplified assumptions and may overestimate safety factors.
6. DEM approach is valuable for investigating rock slope behavior, particularly in the context of toppling failures, offering practical insights to enhance safety, design optimization, and resilience in geological challenges.

The time-consuming nature of the particle-based DEM, especially when dealing with a significant number of particles, presents a computational challenge. The simulation time is constrained by the available computational power, and addressing this limitation may require more advanced computational strategies, including the usage of graphics processing units (GPUs) or parallelization of multiple central processing units (CPUs), especially when applying the DEM approach to real-world cases involving high numbers of particles.

## **6.2 Recommendation for analysis and simulation toppling failure**

These recommendations aim to enhance the accuracy and reliability of both numerical simulations and analytical approaches in analyzing and simulating block-flexural toppling failure, providing valuable insights for slope stability assessments and engineering projects.

### **Numerical Simulation:**

1. Optimize particle size relative to joint spacing dimensions to ensure smoother rupture surfaces and eliminate irregular failure patterns (with simulation findings suggesting an optimal ratio of 11 to 19 times between the smallest dimension and maximum particle size).
2. Calibrate microparameters with an optimal ratio between the smallest and maximum particle size for balancing accuracy and solution time (a maximum to minimum radius ratio ( $R_{\max}/R_{\min}$ ) equal to 1.66).
3. Utilize smooth joints to adjust roughness and prevent interlocking between particles along the surface of the interface.
4. Exercise caution when using microparameters from numerical UCS tests for slope simulations with joint sets; instead, calibrate these parameters during validation by adjusting both intact material and joint microparameters.
5. In scenarios involving rock slopes with jointed rock masses demonstrating large deformations, after conducting an initial FEM-based analysis for preliminary assessment, it is recommended to employ a method that can effectively capture large deformations and interactions among distinct blocks, with a preference for DEM.

### **Analytical Approaches:**

1. Consider variability in the angle ( $\phi$ ) between the total failure plane and the line normal to discontinuities, which can range from 13–27° depending on joint persistence.
2. Consider investigating multiple potential failure surfaces, as relying solely on a single failure plane might not accurately represent the complexity of the failure mechanism, especially in jointed rock masses with varying joint persistence and configurations.
3. Assess the influence of joint persistence configurations on failure surfaces and slope stability zones, particularly in identifying stable and no-movement zones.
4. Evaluate the impact of joint spacing thickness on stable zones and overall failure planes, considering its effect on column strength at the slope's toe.
5. Investigate the effect of main joint friction angle variations on failure surface patterns and slope deformation, recognizing their role in stabilizing slopes and reducing deformation.

### **6.3 Recommendations for Future Research:**

Based on the knowledge acquired in this study, there are several domains that merit additional investigation. These suggestions aim to serve as a source of inspiration and direction for future researchers seeking to expand our understanding in this field:

1. Expand our 2D numerical simulations of slope toppling failures into three-dimensional (3D) models. This advancement represents a significant step forward, as it enables a comprehensive exploration of toppling failure phenomena, with a specific focus on their behavior in 3D contexts. The incorporation of joint sets and boundary conditions within this 3D framework is expected to provide deeper insights into the complex mechanisms governing these failures. This multidimensional approach holds the potential to contribute valuable insights that can advance our understanding and management of toppling failures in rock slopes.
2. Extend the framework and the study to analyze the dynamic responses and deformation mechanisms in the presence of seismic loading conditions, with a specific focus on block flexural toppling failure, in both 2D and 3D dimensions.
3. Extend the framework by using clumps, which are rigid collections of spherical particles, instead of using circular particles to study block flexural toppling failure in both 2D and 3D dimensions.
4. Use the framework for numerical simulations of slide-head-toppling failure, a common occurrence when a layer of soil or weak rock supports a blocky or layered rock mass. This research can yield valuable insights into comprehending the hybrid failure mode arising from the interplay between toppling failure in the upper rock layer and circular sliding in the lower soil or weak rock layer.

## References:

- Adhikary, D., and A. Dyskin. 2007. "Modelling of progressive and instantaneous failures of foliated rock slopes." *Rock Mech Rock Eng*, 40 (4): 349–362.
- Adhikary, D., A. Dyskin, R. Jewell, and D. Stewart. 1997. "A study of the mechanism of flexural toppling failure of rock slopes." *Rock Mech Rock Eng*, 30 (2): 75–93.
- Alejano, L. R., I. Gómez-Márquez, and R. Martínez-Alegría. 2010. "Analysis of a complex toppling-circular slope failure." *Eng. Geol.*, 114 (1): 93–104.
- Al-Rkaby, A. H., and Z. M. Alafandi. 2015. "Size effect on the unconfined compressive strength and Modulus of elasticity of limestone rock." *Electronic Journal of Geotechnical Engineering*, 20 (12): 1393–1401.
- Al-Zahrani, R. M. 2000. "A coupled discontinuous deformation analysis and boundary element method for two-dimensional elastostatic problems." *Ph. D. thesis, University of Pittsburgh*.
- Alzo'ubi, A., C. Martin, and D. Cruden. 2010. "Influence of tensile strength on toppling failure in centrifuge tests." *Int.J.Rock Mech.Min.Sci.*, 47 (6): 974–982.
- Amini, M., M. Golamzadeh, and M. Khosravi. 2015. "Physical and theoretical modeling of rock slopes against block-flexure toppling failure." *Int.Journal of Mining & Geo-Engineering*, 49 (2): 155–171.
- Amini, M., A. Majdi, and Ö. Aydan. 2009. "Stability analysis and the stabilisation of flexural toppling failure." *Rock Mech Rock Eng*, 42 (5): 751–782.
- Amini, M., A. Majdi, and M. A. Veshadi. 2012. "Stability analysis of rock slopes against block-flexure toppling failure." *Rock Mech Rock Eng*, 45 (4): 519–532.
- Ashby, J. 1971. "Sliding and toppling modes of failure in models and jointed rock slopes." *M.Sci.Thesis, London Univ., Imperial College*.
- ASTM D7012, A. 2014. "Standard Test Method for Compressive Strength of Dimension Stone."
- Augarde, C. E., S. J. Lee, and D. Loukidis. 2021. "Numerical modelling of large deformation problems in geotechnical engineering: A state-of-the-art review." *Soils and Foundations*, 61 (6): 1718–1735. Elsevier.
- Aydan, O., and T. Kawamoto. 1987. "Toppling failure of discontinuous rock slopes and their stabilization." *J Min Metall Inst Jpn*, 103: 763–770.
- Aydan, Ö., and T. Kawamoto. 1992. "The stability of slopes and underground openings against flexural toppling and their stabilisation." *Rock Mech Rock Eng*, 25 (3): 143–165.
- Aydan, Ö., Y. Shimizu, and Y. Ichikawa. 1989. "The effective failure modes and stability of slopes in rock mass with two discontinuity sets." *Rock Mech Rock Eng*, 22 (3): 163–188.
- Babiker, A. F. A., C. C. Smith, M. Gilbert, and J. P. Ashby. 2014. "Non-associative limit analysis of the toppling-sliding failure of rock slopes." *Int.J.Rock Mech.Min.Sci.*, 71: 1–11.
- Benvenuti, L. 2016. "Identification of DEM Simulation Parameters by Artificial Neural Networks and Bulk Experiments/eingereicht von Luca Benvenuti." PhD Thesis. Universität Linz.
- Board, M. 1989. "UDEEC (Universal Distinct Element Code) Version ICG1. 5 Vol. 1-3." *US, NRC, NUREG= CR-5429, September*.
- Bobet, A. 1999. "Analytical solutions for toppling failure." *Int.J.Rock Mech.Min.Sci.*, 36 (7): 971–980.
- Brideau, M.-A., and D. Stead. 2010. "Controls on block toppling using a three-dimensional distinct element approach." *Rock Mech Rock Eng*, 43 (3): 241–260.
- Brooks, G. R. 2001. *A Synthesis of Geological Hazards in Canada*. Geological Survey of Canada, Geol Surv Can Bull 548.

- Carlà, T., P. Farina, E. Intrieri, K. Botsialas, and N. Casagli. 2017. "On the monitoring and early-warning of brittle slope failures in hard rock masses: examples from an open-pit mine." *Engineering Geology*, 228: 71–81. Elsevier.
- Cruden, D. M., and C. D. Martin. 2006. "A century of risk management at the Frank Slide, Canada." *The Geological Society of London, UK* :1-7.
- Cruden, D., and D. F. VanDine. 2013. "Classification, description, causes and indirect effects - Canadian technical guidelines and best practices related to landslides: a national initiative for loss reduction." *Geol Surv Can Open*,7359: 2013
- Cundall, P. A. 1971. "A computer model for simulating progressive, large scale movement in blocky rock systems." *InProceedings of the international symposium on rock mechanics*, 9: 129-136.
- Cundall, P. A., and R. D. Hart. 1992. "Numerical modelling of discontinua." *Eng.Comput.*, 9 (2): 101–113.
- Cundall, P. A., and O. D. Strack. 1979. "A discrete numerical model for granular assemblies." *Geotechnique*, 29 (1): 47–65.
- Cundall, P., J. Marti, P. Beresford, N. Last, and M. Asgian. 1978. *Computer Modeling of Jointed Rock Masses*. Dames and Moore (0404)
- Dabirmanesh, H., and Zsaki A.M. 2023. "A discrete element method-based simulation of block-flexural toppling failure. " *Arabian Journal of Geosciences* 16(12): 634. [https://DOI : 10.1007/s12517-023-11723-4](https://doi.org/10.1007/s12517-023-11723-4)
- Dabirmanesh H., Zsaki A.M. 2024. "A discrete element method-based simulation of block toppling failure on an inclined surface. " *In:Geo-Congress 2024* (pp.101-110).
- Dabirmanesh H., Zsaki A.M., and Li, B. 2024 "Application of Discrete Element Particle-Based Method to Simulate Toppling Failure: A Case Study. " *Geotechnical and Geological Engineering* 1:22. <https://doi.org/10.1007/s10706-024-02756-x>
- De Freitas, M., and R. Watters. 1973. "Some field examples of toppling failure." *Geotechnique*, 23 (4): 495–513.
- Dou, W., X. Geng, and Z. Xu. 2019. "Experimental investigation and numerical simulation of the orthogonal cutting based on the smoothed particle hydrodynamics method." *Journal of Manufacturing Processes*, 44: 359–366. <https://doi.org/10.1016/j.jmapro.2019.06.010>.
- Eberhardt, E. 2003. "Rock slope stability analysis—utilization of advanced numerical techniques." *Earth and Ocean sciences at UBC*.
- Elmo, D., D. Stead, B. Yang, G. Marcato, and L. Borgatti. 2022. "A new approach to characterise the impact of rock bridges in stability analysis." *Rock Mechanics and Rock Engineering*, 55 (5): 2551–2569. Springer.
- Evans, S. G. 2007. *Landslides from massive rock slope failure*. Springer Science & Business Media.
- Fakhimi, A., and T. Villegas. 2007. "Application of dimensional analysis in calibration of a discrete element model for rock deformation and fracture." *Rock Mechanics and Rock Engineering*, 40 (2): 193–211. Springer.
- Goodman, R. E., and J. W. Bray. 1976. "Toppling of rock slopes." 201–234. ASCE.
- Goodman, R. E., and D. S. Kieffer. 2000. "Behavior of rock in slopes." *Journal of geotechnical and geoenvironmental engineering*, 126 (8): 675–684. American Society of Civil Engineers.
- Hammah, R. E., T. E. Yacoub, and J. H. Curran. 2009. "Probabilistic slope analysis with the finite element method." *43rd US Rock Mechanics Symposium & 4th US-Canada Rock Mechanics Symposium*. OnePetro.

- Harmon, J. M., K. Karapiperis, L. Li, S. Moreland, and J. E. Andrade. 2021. "Modeling connected granular media: Particle bonding within the level set discrete element method." *Computer Methods in Applied Mechanics and Engineering*, 373: 113486.
- Harrison, J., and J. Hudson. 2000. "Part 2: Illustrative worked examples." *Engineering Rock Mechanics*, Pergamon, Oxford.
- He, L., X. An, G. Ma, and Z. Zhao. 2013. "Development of three-dimensional numerical manifold method for jointed rock slope stability analysis." *Int.J.Rock Mech.Min.Sci.*, 64: 22–35.
- Hittinger, M. 1978. "Numerical analysis of toppling failures in jointed rock." *Ph. D. thesis*, University of California, Berkeley
- Hsieh, Y.-M., H.-H. Li, T.-H. Huang, and F.-S. Jeng. 2008. "Interpretations on how the macroscopic mechanical behavior of sandstone affected by microscopic properties— Revealed by bonded-particle model." *Engineering Geology*, 99 (1–2): 1–10. Elsevier.
- Hu, Y., X. Li, Z. Zhang, J. He, and G. Li. 2020. "Numerical investigation on the hydraulic stimulation of naturally fractured Longmaxi shale reservoirs using an extended discontinuous deformation analysis (DDA) method." *Geomech. Geophys. Geo-energ. Georesour.*, 6 (4): 73. <https://doi.org/10.1007/s40948-020-00195-5>.
- Huang, H. 1999. *Discrete element modeling of tool-rock interaction*. University of Minnesota.
- Ishida, T., M. Chigira, and S. Hibino. 1987. "Application of the distinct element method for analysis of toppling observed on a fissured rock slope." *Rock Mech Rock Eng*, 20 (4): 277–283.
- Itasca, P. 2004. "2D 3.1 Manual (3.) Itasca Consulting Group." *Inc., Minneapolis*.
- Itasca, U. 2000. "User's Guide (Version 3.1)." *Itasca Consulting Group Inc., Minneapolis*.
- Jing, L. 1998. "Formulation of discontinuous deformation analysis (DDA)—an implicit discrete element model for block systems." *Eng.Geol.*, 49 (3): 371–381.
- Jing, L. 2003. "A review of techniques, advances and outstanding issues in numerical modelling for rock mechanics and rock engineering." *Int.J.Rock Mech.Min.Sci.*, 40 (3): 283–353.
- Jing, L., and O. Stephansson. 2007. *Fundamentals of Discrete Element Methods for Rock Engineering: Theory and Applications: Theory and Applications*. Elsevier.
- Koyama, T., and L. Jing. 2007. "Effects of model scale and particle size on micro-mechanical properties and failure processes of rocks—a particle mechanics approach." *Engineering analysis with boundary elements*, 31 (5): 458–472. Elsevier.
- Lanaro, F., L. Jing, O. Stephansson, and G. Barla. 1997. "DEM modelling of laboratory tests of block toppling." *Int.J.Rock Mech.Min.Sci.*, 34 (3–4): 173. e1-173. e15.
- Le Pennec, J.-L., J.-L. Bourdier, J.-L. Froger, A. Temel, G. Camus, and A. Gourgaud. 1994. "Neogene ignimbrites of the Nevsehir plateau (Central Turkey): stratigraphy, distribution and source constraints." *Journal of Volcanology and Geothermal Research*, 63 (1): 59–87. [https://doi.org/10.1016/0377-0273\(94\)90018-3](https://doi.org/10.1016/0377-0273(94)90018-3).
- Li, X., H. Tang, C. Xiong, J. Wartman, and Y. Yin. 2015. "Dynamic Centrifuge Modelling Tests for Toppling Rock Slopes." *Engineering Geology for Society and Territory-Volume 2*, 769–774. Springer.
- Lian, J.-J., Q. Li, X.-F. Deng, G.-F. Zhao, and Z.-Y. Chen. 2017. "A Numerical Study on Toppling Failure of a Jointed Rock Slope by Using the Distinct Lattice Spring Model." *Rock Mech Rock Eng*, 1–18.
- Lin, C. T., B. Amadei, J. Jung, and J. Dwyer. 1996. "Extensions of discontinuous deformation analysis for jointed rock masses." 671–694. Elsevier.

- Lisjak, A., and G. Grasselli. 2014. "A review of discrete modeling techniques for fracturing processes in discontinuous rock masses." *Journal of Rock Mechanics and Geotechnical Engineering*, 6 (4): 301–314.
- Liu, C., M. Jaksa, and A. Meyers. 2008a. "A transfer coefficient method for rock slope toppling." *Canadian Geotechnical Journal*, 46 (1): 1–9.
- Liu, C., M. Jaksa, and A. Meyers. 2008b. "Improved analytical solution for toppling stability analysis of rock slopes." *Int.J.Rock Mech.Min.Sci.*, 45 (8): 1361–1372.
- Liu, G., J. Li, and F. Kang. 2019. "Failure mechanisms of toppling rock slopes using a three-dimensional discontinuous deformation analysis method." *Rock Mechanics and Rock Engineering*, 52 (10): 3825–3848. Springer.
- Majidi, A., and M. Amini. 2011. "Analysis of geo-structural defects in flexural toppling failure." *Int.J.Rock Mech.Min.Sci.*, 48 (2): 175–186.
- Martin, C. D. 1993. "The strength of massive Lac du Bonnet Granite around underground opening." *Ph. D. thesis, University of Manitoba*.
- Mas Ivars, D., D. Potyondy, M. Pierce, and P. Cundall. 2008. "The Smooth-Joint Contact Model." 8th World Congress on Computational Mechanics/5th European Congress on Computational Methods in Applied Sciences and Engineering, Venice. Paper No. a2735. B.A. Schrefler and U. Perego, Eds. Barcelona, Spain: CIMNE
- Meng, J., J. Huang, S. Sloan, and D. Sheng. 2018. "Discrete modelling jointed rock slopes using mathematical programming methods." *Comput.Geotech* 96:189-202.
- Michalowski, R. 1995. "Slope stability analysis: a kinematical approach." *Geotechnique*, 45 (2): 283–293.
- Mishra, B. K. 2003. "A review of computer simulation of tumbling mills by the discrete element method: part I—contact mechanics." *International journal of mineral processing*, 71 (1–4): 73–93. Elsevier.
- Morris, J., L. Glenn, and S. Blair. 2003. "The distinct element method—application to structures in jointed rock." *Meshfree Methods for Partial Differential Equations*, 291–306. Springer.
- Müller, L. 1968. "New considerations on the Vaiont slide." *Rock Mechanics & Engineering Geology* 6:1–91.
- Munjiza, A. 2004. *The Combined Finite-Discrete Element Method*. England: John Wiley & Sons Ltd.
- O’Sullivan, C. 2011. *Particulate Discrete Element Modelling: A Geomechanics Perspective. Applied Geotechnics*. Spon Press/Taylor & Francis.
- Pierce, M., P. Cundall, D. Potyondy, and D. M. Ivars. 2007. "A synthetic rock mass model for jointed rock." *1st Canada-US Rock Mechanics Symposium*. OnePetro.
- Pierce, M., D. Mas Ivars, and B.-A. Sainsbury. 2009. "Use of Synthetic Rock Masses (SRM) to Investigate Jointed Rock Mass Strength and Deformation Behavior." *In Proceedings of the International Conference on Rock Joints and Jointed Rock Masses 1:7*.
- Potyondy, D., and P. A. Cundall. 2004. "A Bonded-Particle Model for Rock." *International Journal of Rock Mechanics and Mining Sciences*, 41: 1329–1364. <https://doi.org/10.1016/j.ijrmms.2004.09.011>.
- Pritchard, M., and K. Savigny. 1990. "Numerical modelling of toppling." *Canadian Geotechnical Journal*, 27 (6): 823–834.
- Rackl, M., C. D. Görnig, K. J. Hanley, and W. A. Günthner. 2016. "Efficient calibration of discrete element material model parameters using latin hypercube sampling and kriging." *Proceedings of ECCOMAS 2016 (VII European Congress on Computational Methods in Applied Sciences and Engineering)*.

- Sagaseta, C. 1986. "On the modes of instability of a rigid block on an inclined plane." *Rock Mech Rock Eng*, 19 (4): 261–266.
- Sagaseta, C., J. Sanchez, and J. Canizal. 2001. "A general analytical solution for the required anchor force in rock slopes with toppling failure." *Int.J.Rock Mech.Min.Sci.*, 38 (3): 421–435.
- Sari, M. 2009. "The stochastic assessment of strength and deformability characteristics for a pyroclastic rock mass." *International Journal of Rock Mechanics and Mining Sciences*, 46 (3): 613–626. Elsevier.
- Sari, M. 2021. "Secondary toppling failure analysis and optimal support design for ignimbrites in the Ihlara Valley (Cappadocia, Turkey) by finite element method (FEM)." *Geotechnical and Geological Engineering*, 39 (7): 5135–5160. Springer.
- Scholtès, L., and F. V. Donzé. 2015. "A DEM analysis of step-path failure in jointed rock slopes." *Comptes Rendus Mécanique, Mechanics of granular and polycrystalline solids*, 343 (2): 155–165. <https://doi.org/10.1016/j.crme.2014.11.002>.
- Scholtès, L., and F. V. Donzé. 2012. "Modelling Progressive Failure in Fractured Rock Masses Using a 3D Discrete Element Method." *International Journal of Rock Mechanics and Mining Sciences*, 52 (1): 18-30.
- Shi, C., W. Yang, J. Yang, and X. Chen. 2019. "Calibration of micro-scaled mechanical parameters of granite based on a bonded-particle model with 2D particle flow code." *Granular Matter*, 21 (2): 38. <https://doi.org/10.1007/s10035-019-0889-3>.
- Shi, G., and R. E. Goodman. 1985. "Two dimensional discontinuous deformation analysis." *Int.J.Numer.Anal.Methods Geomech.*, 9 (6): 541–556.
- Wang, R., W. Zhao, T. Nian, C. Liu, and H. Wu. 2022. "Centrifuge Model Test on Anti-dip Rock Slopes with Unequal Thicknesses Subjected to Flexural Toppling Failure." *KSCE J Civ Eng*, 26 (6): 2575–2587. <https://doi.org/10.1007/s12205-022-2214-7>.
- Wu, J.-H., Y. Ohnishi, G.-H. Shi, and S. Nishiyama. 2005. "Theory of three-dimensional discontinuous deformation analysis and its application to a slope toppling at Amatoribashi, Japan." *International Journal of Geomechanics*, 5 (3): 179–195.
- Wyllie, D. C. 1980. "Toppling rock slope failures examples of analysis and stabilization." *Rock mechanics*, 13 (2): 89–98.
- Wyllie, D. C., and C. W. Mah. 2004. *Rock slope engineering: civil and mining*. London:UK: Spon Press.
- Yang, B., Y. Jiao, and S. Lei. 2006. "A study on the effects of microparameters on macroproperties for specimens created by bonded particles." *Engineering Computations*. 23(6):607-31
- Zanbak, C. 1983. "Design charts for rock slopes susceptible to toppling." *J.Geotech.Eng.*, 109 (8): 1039–1062.
- Zhang, H., L. Li, X. An, and G. Ma. 2010. "Numerical analysis of 2-D crack propagation problems using the numerical manifold method." *Eng.Anal.Boundary Elements*, 34 (1): 41–50.
- Zhang, J., Z. Chen, and X. Wang. 2007. "Centrifuge modeling of rock slopes susceptible to block toppling." *Rock Mech Rock Eng*, 40 (4): 363–382.
- Zhang, Z., G. Liu, S. Wu, H. Tang, T. Wang, G. Li, and C. Liang. 2015. "Rock slope deformation mechanism in the Cihaxia Hydropower Station, Northwest China." *Bull.Eng.Geol.Env.*, 74 (3): 943–958.
- Zhao, G.-F. 2015. "Modelling 3D jointed rock masses using a lattice spring model." *Int.J.Rock Mech.Min.Sci.*, 78: 79–90.
- Zheng, Y., C. Chen, T. Liu, H. Zhang, and C. Sun. 2019. "Theoretical and numerical study on the block-flexure toppling failure of rock slopes." *Engineering Geology*, 263: 105309. Elsevier.



- Zhou, C., C. Xu, M. Karakus, and J. Shen. 2018. "A systematic approach to the calibration of micro-parameters for the flat-jointed bonded particle model." *Geomechanics and Engineering*, 16 (5): 471–482. Techno-Press.
- Zhu, C., M. He, M. Karakus, X. Cui, and Z. Tao. 2020. "Investigating Toppling Failure Mechanism of Anti-dip Layered Slope due to Excavation by Physical Modelling." *Rock Mech Rock Eng*, 53 (11): 5029–5050. <https://doi.org/10.1007/s00603-020-02207-y>.
- Zsaki, A. 2009. "An efficient method for packing polygonal domains with disks for 2D discrete element simulation." *Comput. Geotech.*, 36 (4): 568–576.